A simulation study for future satellite gravimetry missions

Miragaia Gomes Inacio, P.

DOI
10.4233/uuid:6b6f6ab4-0849-4bda-a024-9b06305e3b3c

Publication date
2020

Document Version
Final published version

Citation (APA)
Miragaia Gomes Inacio, P. (2020). *A simulation study for future satellite gravimetry missions*. [Dissertation (TU Delft), Delft University of Technology]. https://doi.org/10.4233/uuid:6b6f6ab4-0849-4bda-a024-9b06305e3b3c

A simulation study for future satellite gravimetry missions

A simulation study for future satellite gravimetry missions

Proefschrift

ter verkrijging van de graad van doctor
aan de Technische Universiteit Delft,
op gezag van de Rector Magnificus Prof. dr. ir. T. H. J. J. van der Hagen,
voorzitter van het College voor Promoties,
in het openbaar te verdedigen op donderdag 10 september 2020 om 15:00 uur

door

Pedro MIRAGAIA GOMES INÁCIO

Master of Science in Aerospace Engineering bij de Technische Universiteit Delft
geboren te Ovar, Portugal.

Dit proefschrift is goedgekeurd door de promotor:

Prof. dr. ing. habil. R. Klees

Copromotor: Dr. P. Ditmar

Samenstelling promotiecommissie:

Rector Magnificus,	voorzitter
Prof. dr. ing. habil. R. Klees,	Technische Universiteit Delft, promotor
Dr. P. Ditmar,	Technische Universiteit Delft, copromotor

Onafhankelijke leden:

Prof. dr. L.L.A. Vermeersen	Technische Universiteit Delft
Prof. Dr.-Ing. Torsten Mayer-Gürr	University of Graz
Prof. Dr. ing. habil. Jürgen Kusche	University of Bonn
ir. Roger Haagmans	European Space Agency
Dr. João Encarnação	The University of Texas at Austin
Prof. dr. ir. R. Hanssen,	Technische Universiteit Delft, reservelid

Keywords: GRACE · Temporal aliasing errors · Satellite formations · Satellite geodesy · Future gravity missions

Printed by: printenbind.nl

Front & Back: Illustration of a hypothetical Gamma mission over the Earth with a Milky Way background.

ISBN 978-94-6366-311-3

An electronic version of this dissertation is available at
http://repository.tudelft.nl/.

To my wife Daša and my friend Rúben. Only two of the many people I could not have made it this far without.

Contents

Summary

The Gravity Recovery and Climate Experiment (GRACE), launched in 2002, was the first low-low satellite-to-satellite tracking (ll-SST) satellite gravity mission. One of its primary objectives was to monitor the redistribution of mass in the Earth's system, which is of vital importance not only to the scientific community, but also to society in general. GRACE allowed for the mass redistribution monitoring at much smaller spatial scales than ever before. The data collected by the mission lead to a proliferation of researches in many scientific domains.

The GRACE mission, completed in 2017, was considered as an outstanding success. Consequently, the GRACE Follow-On (GFO) mission was launched in 2018 to continue its legacy. With the GFO mission underway, it is now timely to look into the future of satellite gravimetry.

The major goal of this thesis was to design and benchmark a set of ll-SST mission concepts with the potential to deliver unprecedented accuracy of mass redistribution estimates. The approach taken was to develop a simulation tool capable of handling arbitrarily complex satellite mission designs. In the first instance, this tool was used to analyze the error budget of the GRACE mission. A combination of simulated errors from various sources showed a very good agreement with observed noise in the GRACE inter-satellite acceleration data. Noise in the frequency range between 1 and 9 mHz, the origin of which was previously unknown, was explained by a combination of positioning, acceleration and ranging errors and errors in the atmosphere and ocean de-aliasing model (cf. Chapter 6).

A good agreement between simulated and actually observed noise was only possible by properly accounting for the propagation of errors through the computed reference orbits. I called this error propagation mechanism the indirect effect. I formally defined the indirect effect and demonstrated that it propagates differently in different types of ll-SST missions (cf. Chapter 3).

Next, the error budget of future missions which replicate GRACE was simulated. I confirmed that temporal aliasing errors are the ones that limit the performance of these missions. A better instrumentation will not improve the performance of those missions in any significant way. New mission concepts are required in order to surpass the performance level of the current ones.

Afterwards the tool was used to run small-scale simulations in order to gain insight into the mission design aspects which determine the performance of the mission. Small-scale simulations consider relatively short timespans (between 2 and 5 days) and the obtained solutions are typically computed up to a relatively low maximum SH degree (normally between 40 and 60). Using small-scale simulations, I could identify mission design aspects which impact the temporal and spatial resolution of ll-SST missions (cf. Chapter 7) . Considering different gravity gradient directions as observables, I have shown that collecting multiple observables from

a single formation greatly increases the spatial resolution of the mission compared to the single-observable case. This discovery begs the consideration of formations consisting of more than two satellites in order to maximize the spatial resolution. I have also considered missions consisting of multiple formations. For these, I have shown that temporal aliasing errors can be minimized by orienting the polar orbital planes of the satellite formations such that they equipartition 3-D space. Specifically, for two-formation missions, the orbital planes should be perpendicular, while for three-formation missions they should be set 60° apart.

On the basis of the small-scale simulations, I have proposed a set of satellite missions, which were benchmarked with full-scale simulations (cf. Chapter 8). The missions were designed to combine multiple observables in a single or multiple formations. In the latter case, their orbital planes were correctly oriented in order to minimize temporal aliasing errors. Of the proposed concepts, missions which considered along-track/pendulum (which I called gamma) and along-track/cartwheel (which I called sigma) combinations were found to yield the lowest total errors. Of those, I selected the single-formation along-track/pendulum combination (gamma) mission as the most promising for future ll-SST mission. I have shown that this concept yields large improvements in terms of spatial and temporal resolutions. At the same time, the gamma mission avoids the complexities of the cartwheel pair of satellites and, given that it considers a single satellite formation, it is potentially cheaper and less complex than the other alternatives which considered two. The gamma mission shows substantially lower errors compared to existing ll-SST missions, which may be further reduced when used as the basis for a multi-formation constellation of satellites.

Samenvatting

De GRACE-satellietmissie (Gravity Recovery and Climate Experiment: Zwaartekracht- en Klimaatexperiment), was gelanceerd in 2002 en was daarmee de eerste missie in een lage baan waarbij de onderlinge satellietafstand werd gemeten, de zogeheten ll-SST-techniek (low-low satellite-to-satellite tracking). De missie maakte het mogelijk om de ruimtelijke herverdeling van massa te monitoren op een nog niet eerder vertoonde wijze. Dientengevolge heeft de data die hierbij werd verzameld geleid tot een stroomversnelling van het onderzoek in verschillende wetenschappelijke disciplines. Het is duidelijk gebleken dat het in kaart brengen van massabewegingen op onze planeet uitermate belangrijk is, niet alleen voor de wetenschap, maar ook voor de maatschappij in bredere zin. De GRACE-missie was een groot succes en recentelijk is de opvolger GRACE Follow-On (GFO) gelanceerd om daarmee de continuïteit te waarborgen. Nu de GFO-missie gaande is, is het een goed moment om stil te staan bij de toekomst van satellietgravimetrie.

De doelstelling van dit proefschrift is het ontwerpen en testen van een aantal ll-SST-concepten die mogelijk tot veel grotere nauwkeurigheden in staat zijn dan de GRACE- en GFO-missies. De aanpak in dit proefschrift is de ontwikkeling van een simulatie die in staat is om te gaan met vergaand complexe satellietmissie-ontwerpen. Ik gebruik deze techniek vervolgens om met kleinschalige simulaties inzicht te verkrijgen in die ontwerpaspecten die bepalend zijn voor de missieprestaties. Op basis van geïdentificeerde ontwerpaspecten, doe ik een voorstel voor een aantal missieconcepten die potentieel beter presteren dan huidige missies. Vervolgens heb ik de voorgestelde concepten getest op prestaties en de best presterende heb ik geselecteerd als geschikt startpunt voor toekomstige gravimetriesatellietmissies.

Tevens heb ik de simulatietechniek gebruikt om het foutenbudget van de GRACE-missie te valideren. De gesimuleerde ruis vertoont goede overeenkomsten met de geobserveerde ruis uit de intersatelliet-acceleratiedata van GRACE. De geobserveerde ruis in het 1-9 mHz frequentiebereik, voorheen van onbepaalde herkomst, kan verklaard worden als combinatie van positionering-, acceleratie- en afstandsbepalingsfouten en fouten in de atmosfeer- en oceaanmodellen die gebruikt worden om vouwvervorming (aliasing) tegen te gaan (zie hoofdstuk 6). De goede overeenkomst is alleen mogelijk wanneer rekening wordt gehouden met de propagatie van fouten in de bepaling van referentiebanen. Deze wijze van foutenpropagatie benoem ik als indirecte effecten. Ik geef een formele definitie van de indirecte effecten en illustreer hoe deze fouten op verschillende wijzen doorwerken voor verschillende type ll-SST-missies (zie hoofdstuk 3).

De analyse van de foutenmarges van de GRACE-missie en die van toekomstige opvolgers bevestigt dat de prestatie van deze missies wordt beperkt door tijdsafhankelijke vouwvervorming. Verder laat de analyse ook zien van verbeteringen in

instrumenten geen significante verbetering te verwachten valt voor de prestatie van de missies. Nieuwe missieconcepten zijn noodzakelijk om tot een prestatieverbetering te komen ten opzichte van de bestaande missies.

Gebruikmakende van kleinschalige simulaties, kan ik die ontwerpaspecten van missies uitlichten die bepalend zijn voor de tijdsafhankelijke en ruimtelijke resolutie van ll-SST-missies (zie hoofdstuk 7). Ik laat zien dat het meten van meerdere observabelen bij een enkelvoudige satellietformatie een grote verbetering in de ruimtelijke resolutie betekent in vergelijking met het geval van een enkele observabele. Deze vaststelling vraagt om een overweging van missies bestaande uit complexere formaties om daarmee de ruimtelijke resolutie te maximaliseren. Daarnaast laat ik zien dat de tijdsafhankelijke vouwvervormingsfouten geminimaliseerd kunnen worden door de oriëntatie van de polaire banen van de satellietformaties dusdanig te kiezen dat deze de ruimte tussen de baanvlakken gelijk verdeeld. Meer specifiek, voor missies bestaande uit twee formaties zouden de baanvlakken loodrecht op elkaar moeten staan, bij missies van drie formaties moeten de baanvlakken onder hoeken van 60° staan.

Op basis van deze uitgangspunten heb ik een voorstel gedaan voor een aantal satellietmissies en hiervan de prestaties onderzocht (zie hoofdstuk 8). Deze zijn zodanig ontworpen dat meerdere observabelen gecombineerd kunnen worden in een enkele formatie en, wanneer meerdere formaties in aanmerking komen, zijn de baanvlakken zodanig georiënteerd dat de tijdsafhankelijke vouwvervorming minimaal is. Van de conceptuele voorstellen presteren de, enkel- en tweevoudige formatie, sigma- en gamma-missies als beste. Van de genoemde concepten heb ik de gamma-missie als enkelvoudige formatie gekozen als veelbelovendste toekomstige ll-SST-missie, ofwel als opzichzelfstaande formatie, ofwel als basis voor een constellatie van satellieten bestaande uit meerder formaties.

1

Introduction

1.1. Background

Gravity field models provide invaluable information for a wide array of geophysical applications with great benefits for the society. Satellite gravimetry derived data has been used in the prediction of river basin flood potential with several months lead time (Reager et al., 2014), and was shown to be a indicator of extreme drought events, such as the one over Texas in 2011 (Long et al., 2013). Satellite gravimetry data is fundamental in the monitoring of ice-mass loss over the polar regions (Didova, 2017; Shepherd et al., 2012; Velicogna et al., 2014). Furthermore, ice mass loss on land is one of the major contributors to the sea level rise; several publications dedicated to the assessment of global and regional sea level rise (Dangendorf et al., 2017; Frederikse et al., 2017; Kleinherenbrink et al., 2017) rely on satellite gravimetry data. Satellite gravimetry data is used to study earthquakes (Fuchs et al., 2013), volcanoes (Battaglia et al., 2008), the Earth's lithosphere (Bouman et al., 2015), to estimate glacial isostatic adjustment (X. Wu et al., 2010), dynamic ocean topography (Knudsen et al., 2011), ocean tides (Han et al., 2005), height datum unification (Rummel, 2012), etc.

Determining a global gravity field model requires a set of gravity measurements distributed over the surface of the Earth. The most practical way to obtain these measurements is from space-borne instruments. Four gravity-dedicated satellite missions have been launched since the year 2000:

- **Cha**llenging **M**inisatellite **P**ayload (CHAMP)
- **G**ravity **R**ecovery and **C**limate **E**xperiment (GRACE)
- **G**ravity Field and Steady-State **Oc**ean **E**xplorer (GOCE)
- **G**RACE **F**ollow-**O**n (GFO)

Importantly, a continuous time-series of global gravity measurements allows for the tracking of mass changes over time. To that effect, the GFO mission has been

recently launched to continue the GRACE data series. This was the motivation to launch the GFO mission, which extends the GRACE time-series into the future and is certainly not the last satellite gravimetry mission. Moreover, the need for satellite gravimetry data will likely increase in the future. Future missions are expected to deliver even more accurate data, which will improve the scientific outcomes of existing and open the way for new scientific applications.

This brings about the question of how should future missions be designed in order to achieve such improvements. The main purpose of this thesis is to answer this question by proposing a candidate mission with the greatest potential to monitor the mass transport signal. Fundamental to the design of future satellite missions is the understanding of the performance limitations of the current ones. Therefore, a prerequisite to the stated goal is to close the knowledge gaps on the errors limiting the performance of current satellite gravimetry missions. One additional motivation to better understand the errors in the current missions is that, in doing so, it might become possible to correct part of these errors and thus improve the quality of existing models.

After the launch of the GRACE mission, it became apparent that noise in its data was larger than previously expected. Over the years, several authors have researched different possible causes for the observed errors with limited success. Ditmar et al. (2012) is one of the major publications dealing with the error budget of the GRACE mission. The authors concluded that, in the frequency range below 1 mHz, errors in the satellite orbits are the main error source is errors in the satellite orbits. These propagate as centrifugal accelerations into the computed residual inter-satellite accelerations. Furthermore, the authors also concluded that the source of observed errors in the frequency range between 1-9 mHz remains unexplained.

In an attempt to close the error budget of the GRACE mission, I identified a two topics which could potentially explain the observed errors in the mission. They are *indirect effect* errors and *star camera* errors.

Indirect effect errors arise in the computation of the reference orbits and ultimately affect the computed solutions. The reference orbits are computed through the numerical integration of the laws of motion. Any perturbation in the force model used will cause the computed orbits to deviate from the true ones. Even relatively small perturbations, grow over time as random-walk noise, resulting in computed orbits which increasingly deviate from the true ones. Afterwards, these orbits are used to compute the reference quantities, at which point, these errors propagate into the residual quantities used for gravity field solution computation.

Star cameras are satellite instruments which are used to measure the attitude of the spacecraft w.r.t. the inertial frame. Star-camera data is required to translate the 3D accelerometer measurements into the inertial frame, essential to the computation of high quality orbits. Furthermore, star-camera data is required to relate the ranging instrument measurements to the center of mass of the GRACE satellites. Errors in star camera data propagate through both these operations with consequences on the quality of the computed gravity fields.

Beyond the errors affecting the current missions, the performance of all satellite

gravimetry missions is limited by spatial instability errors, temporal aliasing errors, and spatial aliasing errors. Spatial instability errors arise in the computation of gravity field parameters. For a given set of globally distributed measurements, estimating gravity field parameters of increasingly smaller spatial scales will result in large amplification of measurement noise in the estimated parameters. Without considering pre- and post-processing filtering procedures, spatial instability errors set a hard limit on the spatial resolution of the mission. They are intrinsically linked with the distribution of measurements and the level of noise in the data.

Spatial aliasing errors are a consequence of the SH degree at which the computed gravity field solutions are truncated. The signals which a satellite gravimetry mission measures are composed by an infinite number of SH degrees. In the estimation of a gravity field solutions, those degrees above the selected truncation degree will map down to the set of estimated ones and result in spatial aliasing errors.

Finally, satellite gravimetry data also suffer from temporal aliasing errors. Satellite gravimetry missions require measurements to be gathered over a certain period of time in order to attain a sufficiently dense global coverage. Mass transport signals over timescales shorter than this period will not be correctly represented in the gathered data, which manifest in the solutions as temporal aliasing errors.

With the recent launch of the GFO mission, it is now time to reflect about the future of low-low satellite-to-satellite tracking (ll-SST) gravimetry. The wealth of data provided by the GRACE mission allows us to learn what the drawbacks of the mission are what are the limitations of its performance. It is expected that future ll-SST gravimetry missions be able to deliver more accurate mass transport models at smaller spatial scales in order to potentiate new and existing scientific applications.

While one of the objectives of the GFO mission is to validate a new type of ranging instrument, it is for the most part a replica of the GRACE mission. Looking into the future, it is important to find out whether additional replications of the GRACE mission are an appropriate way to design the missions of the future or whether this GRACE-legacy should be deprecated.

Ultimately, the performance of future satellite missions depends on their ability to mitigate the above discussed errors. Given that any specific satellite mission can be stated as a set of parameters, the way to design a maximum performance mission is to search the parameter space in order to find the ones which are most effective at reducing these errors. The major difficulty in this endeavor is the vast number of parameters that need to be considered along with the computationally demanding task of computing gravity field models up to sufficiently high SH degrees.

In order to tackle this challenge my approach was split in two parts. Firstly, I took the simplest possible mission configurations and, or different types of errors, I analyzed which of the mission parameters affected the considered errors the most. Once the knowledge about the most important mission design aspects was gathered, I systematically designed a set of ll-SST missions with the potential to greatly outperform the current missions and I benchmarked them in order to identify the best candidate for the future generations of ll-SST satellite gravimetry.

1

1.2. Research Objectives

1. *Explain the error budget of the GRACE mission.* On the basis of the a simulation tool and a realistic noise model, the error budget of the GRACE mission can be explained by comparing synthetic and observed errors in real data. This is an important step towards predicting and comparing the performance of different future mission concepts. Closing the error budget of GRACE requires three sub-objectives to be fulfilled.

   (a) *Build a simulation tool and a realistic noise model to assess the performance of satellite gravimetry missions.* The variety of error sources and the non-trivial manner in which orbits, measurements, errors and gravity field parameters interact excludes the possibility of analytically predicting the performance of a given mission design. These interactions can only be realistically modeled by simulating all the required data products and by inspecting the propagation of errors through them. Once a realistic noise model is available, it can be validated against error realizations of current satellite missions and afterwards to predict the performance of future ones.

   (b) *Describe and predict the propagation of indirect effect errors.* Indirect effect errors are a poorly understood error propagation mechanism, in which errors propagate into gravity field solutions through the computation of reference satellite orbits. Because these errors play an important role in the quality of the recovered gravity field solutions, it is important to understand them.

   (c) *Quantify the impact of star camera errors in the GRACE data.* Preliminary inspection of these errors lead to unexpected findings with the potential to improve the quality of GRACE solutions. The error budget cannot be closed until these errors have been thoroughly analyzed.

2. *Quantify the performance of future GRACE-type missions.* The GFO mission was recently launched as using the same satellite formation and orbits as the original GRACE mission. While it is convenient to build upon proven technologies, one must wonder whether continuing to replicate the GRACE-platform is the right approach for the future.

3. *Identify the set of mission design parameters that have the largest impact on spatial aliasing, spatial instability and temporal aliasing errors.* These errors are known to limit the performance of satellite gravimetry missions. Starting with a set of simple mission concepts, a search through the parameter space will reveal which ones are effective at mitigating those errors. This knowledge can then be used to drive the design of future satellite missions.

4. *Compare the performance of a comprehensive set of mission concepts to identify the best candidates for next-generation satellite gravimetry missions.* On the basis of the knowledge gathered in the previous task, a set of missions

will be proposed and benchmarked in order to identify the concepts with the most potential to improve the accuracy of computed gravity field solutions.

1.3. Thesis outline

In Chapter 2, an in-depth analysis of the literature on the topic of future satellite mission is detailed. In Chapter 3, indirect effect errors are defined and illustrated for a selection of satellite mission concepts. A detailed overview of the simulation tool used to assess the performance of satellite mission is presented in Chapter 4. Also in this Chapter, the error scenarios which may affect the current and future satellite missions are presented. A analysis of star camera errors in the GRACE mission is presented Chapter 5. In Chapter 6, the simulation tool and the considered error scenarios are validated by comparing their synthetic noise realizations with observed ones in real data of the GRACE mission.

Chapter 7 deals with finding the mission design parameters which are determinant at mitigating spatial instability, spatial aliasing and temporal aliasing errors. Chapter 8 is dedicated to the assessment of the performance of future satellite gravimetry missions. In this chapter a set of future mission concepts is proposed and benchmarked leading to the selection of the best candidate mission. Chapter 9 is reserved for the conclusions.

2

Literature review

At the end of Chapter 1, I have stated that the focus of this thesis is the evaluation of the performance of future ll-SST mission concepts. In this Chapter, I will introduce the tools and concepts which are required to accomplish this task. Then I will introduce the basic concepts regarding satellite orbits, repeat orbit design and the elementary satellite formations. After that, I will present an overview of all publications on errors in ll-SST data, future satellite mission concepts and the associated spatio-temporal resolution. At the end of this Chapter, the reader will understand the concepts upon which ll-SST missions rely, will be aware of the state-of-the-art and will understand the tools that I will use to analyse the performance of future missions.

2.1. Background on gravity field modelling

In this section, background information regarding gravity field modelling is provided along with the set of tools which are commonly used to analyse gravity field models and gravimetry observations.

2.1.1. Spherical harmonics

The Earth's gravitational potential $V(r,\theta,\lambda)$ is a harmonic function outside the domain of the attracting mass, It is defined as

$$V(r,\theta,\lambda) = \frac{GM}{R}\sum_{l=0}^{\infty}\left(\frac{R}{r}\right)^{(l+1)}\sum_{m=-l}^{l}\bar{C}_{lm}\bar{Y}_{lm}(\theta,\lambda) \quad , \tag{2.1}$$

where

- l – spherical harmonic degree
- m – spherical harmonic order
- GM – product of the universal gravitational constant G and the mass of the earth M
- R – an arbitrary constant, typically the equatorial radius of the Earth.

Functions $\bar{Y}_{lm}$ are known as *surface spherical harmonics*. Their general form is

$$\bar{Y}_{lm}(\theta,\lambda) = \begin{cases} \bar{P}_{lm}(\cos\theta)\cos m\lambda & \text{for } m >= 0 \\ \bar{P}_{l|m|}(\cos\theta)\sin|m|\lambda & \text{for } m < 0, \end{cases} \tag{2.2}$$

where

$\bar{P}_{lm}$ – fully-normalized associated Legendre functions of the first kind.

The exact definition of the associated Legendre functions can be found in, e.g., Heiskanen et al. (1967). The constants $\bar{C}_{lm}$ are known as *spherical harmonic coefficients* (SH), *geopotential coefficients* or *Stokes coefficients*. This set of coefficients can be used to fully describe the gravity field of the Earth. In practice, the maximum degree of the spherical harmonic expansion is limited to a certain value l_{max}.

2.1.2. Mass anomalies

For the most part, the movement of mass in our planet takes place in the atmosphere, oceans and shallow subsurface. Therefore, the mass transport signal is confined to a relatively thin near-surface layer, which is roughly 10 km thick. Then, the mass transport can be represented by variations of surface density $\delta s(\theta,\lambda)$ within this thin layer. As with any continuous function defined on a sphere, the surface density variations can be represented in terms of coefficients $\bar{C}^{\delta s}_{lm}$. It can be shown that the relationship between the Stokes coefficients and the surface density variation ones is,

$$\bar{C}_{lm} = \frac{3(1+k'_l)}{R\rho_{av}(2l+1)}\bar{C}^{\delta s}_{lm}, \tag{2.3}$$

where

k'_l – are the load Love numbers, which account for the Earth's elastic deformation under load, Wahr et al. (1998)

ρ_{av} – is the average density of the Earth, approximately equal to 5500 kg m^{-3}.

Another common way to express surface density variations is in terms of equivalent water height (ewh) $h_w(\theta,\lambda)$, which represents the height of the water column required to cause the observed surface density variation. The corresponding spherical harmonic coefficients can be computed as

$$\bar{C}^{\delta h_w}_{lm} = \frac{\bar{C}^{\delta s}_{lm}}{\rho_w}, \tag{2.4}$$

where

ρ_w – is the density of water, equal to 1000 kg m^{-3}.

Finally, one more common unit used to express mass anomalies is geoid height. The relation between Stokes coefficients and spherical harmonic coeffifients in terms of geoid height is straightforward,

$$\bar{C}_{lm} = \frac{1}{R}\bar{C}^{\delta g}_{lm} \quad . \tag{2.5}$$

It is often useful to convert SH coefficient in terms of geoid heights into ewh (and vice-versa). Taking into account Eqs. 2.3, 2.4 and 2.5, the relation between the two is,

$$\bar{C}_{lm}^{\delta g} = \frac{3(1+k_l')\rho_w}{(2l+1)R\rho_{av}} \bar{C}_{lm}^{\delta h_w} \quad . \tag{2.6}$$

2.1.3. Triangular plots

A common way to analyse a gravity field model is to look at the individual spherical harmonic coefficients. This is normally done by making a 2-D plot where the values of the coefficients are plotted row-wise starting from the lowest degree up to the maximum degree. Because the number of orders increases linearly with the degree (m is defined from $-l$ to l), plots of this type are called thereafter triangular plots. An example is shown in Figure 2.1.

Due to the typical characteristics of the gravity signals, the magnitude of the spherical harmonic coefficients rapidly decreases with increasing degree, where as typical errors rapidly increase at high degrees. Therefore it is also common to plot the logarithm of the absolute value of each coefficient.

This type of plot, found throughout this thesis, is useful to reveal internal structures in the considered model and to analyse the distribution of "energy" through the spatial scales. This type of plot is similar to the plot of power spectral density in time-series analysis.

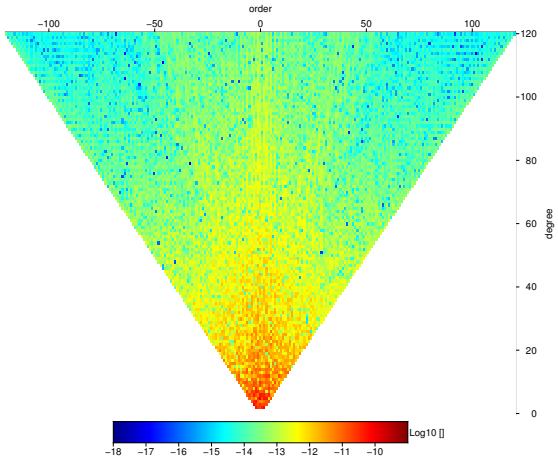

Figure 2.1: An example of a triangular plot. Depicted is the DMT2 monthly gravity field solution for March 2009, month in which ESA's GOCE mission was launched. This monthly solution is the residual field w.r.t. the DGM-1S long-term average field (Farahani et al., 2013).

2.1.4. Degree variance

The Degree Variance (DV) plot is commonly used to compare different gravity field models. The DV $\sigma^2(l)$, for a given degree l, is computed as

$$\sigma^2(l) = \sum_{m=-l}^{l} \bar{C}_{lm}^2 \quad . \tag{2.7}$$

Also useful is the cumulative DV (CDV), $\tilde{\sigma}^2(l)$, defined as

$$\tilde{\sigma}^2(l) \equiv \sum_{l'=0}^{l} \sigma^2(l') = \sum_{l'=0}^{l} \sum_{m=-l'}^{l'} \bar{C}^2_{l'm} \quad . \tag{2.8}$$

The DV plot is useful because it shows how the energy is distributed over different wavelengths. The wavelength λ associated with a certain SH degree is obtained by dividing equatorial circumference of the Earth by the corresponding SH degree: $\lambda = \frac{2\pi R_E}{l} \approx 40000/l$ km. The CDV shows the cumulative signal energy up to the considered degree and for $l = l_{\text{max}}$ the CDV represents the total variance of the considered signal.

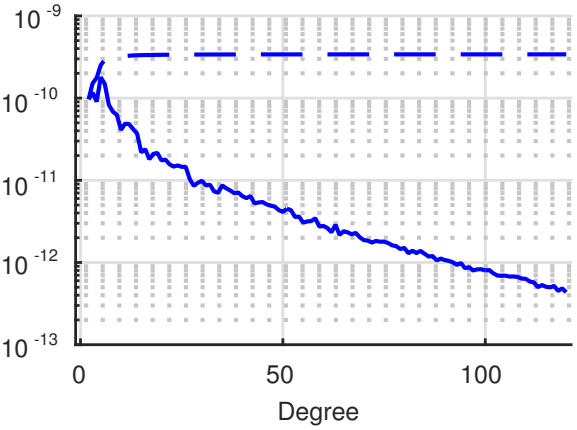

Figure 2.2: An example plot depicting the DV and CDV of the DMT2 monthly gravity field solution for March 2009, month in which ESA's GOCE mission was launched. This monthly solution is the residual field w.r.t. the DGM-1S long-term average field (Farahani et al., 2013).

The DV and CDV plots are very useful because they summarize the features of a two-dimensional set of coefficients into a single dimension. This makes the comparison of multiple spherical harmonic models easier. This characteristic is also the major disadvantage of this analysis tool. Because the DV plot averages much of the information, it must be used with care. Signals which are not evenly distributed over the orders might be misrepresented in DV plots. For example, the solutions computed from the GRACE mission typically contain striations caused by the amplification of noise in near-sectorial coefficients. Inspecting the DV plot of a GRACE solution will show very large errors for most degrees, because, at each degree, the near-sectorial orders will contribute the most to the DV.

2.1.5. Spatial RMS

Another useful metric to compare different gravity field models is the distribution of energy in the spatial domain. Parseval's identity states the equivalence of the total variance in the spatial and spectral domains, such that for an arbitrary continuous

function defined on the unit sphere,

$$\sigma^2 \equiv \frac{1}{4\pi} \| f \|^2 = \sum_{l'=0}^{l} \sum_{m=-l'}^{l'} \bar{C}_{l,m}^{f\,2}.$$

Just as it is useful to use the DV to inspect the distribution of energy over the different wavelengths, it is also useful to look into the energy distribution over different geographical regions. Starting from a spherical harmonic model, mass anomalies values $\delta s(\lambda_j, \theta_i)$ can be computed over an equiangular grid of appropriate dimensions. Then, the spatial RMS of the considered mass anomalies is simply the RMS of all the grid values weighted by the area corresponding to each grid cell,

$$\delta s_{\text{RMS}} = \sqrt{\frac{\sum_i \sum_j \delta_s(\lambda_j, \theta_i)^2 A_{i,j}}{A_{\text{sphere}}}} \quad . \tag{2.9}$$

The area of each equiangular grid cell only depends on the latitude and for an equiangular grid, the expression can be simplified as

$$\delta s_{\text{RMS}} = \sqrt{\frac{\sum_i \cos\theta_i \sum_j \delta s(\lambda_j, \theta_i)^2}{N_j \sum_i \cos\theta_i}} \quad , \tag{2.10}$$

where

N_j – is the number of meridians in the considered grid.

When analyzing the propagation of errors in ll-SST mission, it is likely that errors propagate differently in different regions of the globe and at different spatial scales. In order to quantify such differences it becomes also important to analyze the signal RMS in specific geographic regions. The regional RMS can be similarly computed using the above equations as long as the considered grid refers to the geographic region of interest. Various geographic regions are interesting to the scientific community because of specific phenomena occurring at these locations. For example, gravity signal over Greenland and Antarctica is dominated by ice mass loss, while hydrology is the main signal of interest over the Amazon river basin. This motivates the need to understand how errors propagate into these specific regions.

2.1.6. Power Spectral Density

In this thesis, an important analysis tool is the *Power Spectral Density* (PSD). I use this tool to analyse the distribution of energy over the frequencies that compose the signal (or noise) in a time-series of satellite gravimetry observations.

When analysing the propagation of errors, this tool allows one to identify the frequency bands where errors are the largest, and by comparison with the desired signal, to identify the spectral bands with low (or high) signal-to-noise ratios.

In the literature, several approaches to estimate the power spectral density can be found, from the classical periodogram to the modified periodograms which provide improved variances at the cost of reduced frequency resolution. In this thesis

we use the *Lomb-Scargle periodogram* (Scargle, 1982). It is formally equivalent to the least squares fitting of sine waves to the input data. Its advantages are that it does not require evenly spaced data and that the periodogram can be directly computed from an analytical expression. For an arbitrarily sampled signal $X_i \equiv X(t_i), i = 1, 2, \ldots, N$, the periodogram $P_X(\omega)$ can be computed as,

$$P_X(\omega) = \frac{1}{2}\left\{\frac{\left[\sum_j \cos\omega(t_j-\tau)\right]^2}{\sum_j \cos^2\omega(t_j-\tau)} + \frac{\left[\sum_i \sin\omega(t_j-\tau)\right]^2}{\sum_j \sin^2\omega(t_j-\tau)}\right\} \quad , \tag{2.11}$$

where τ is defined as

$$\tan 2\omega\tau = \frac{\sum_j \sin 2\omega t_j}{\sum_j \cos 2\omega t_j} \quad . \tag{2.12}$$

2.2. Satellite Orbits

In this section an introduction to satellite orbits is given. I will provide background information regarding the orbital elements, the design of repeat orbits and the existing types of stable satellite formations.

2.2.1. Orbital elements

As mentioned in Section 2.1.1, a satellite in the Earth's gravity field experiences an acceleration **a**, directed approximately towards the centre of mass of the Earth. The satellite orbit can be computed by integrating the Newton's laws of motion. Six variables are required to describe the three-dimensional position and velocity of the satellite at each epoch. This means that, in order to describe a satellite's orbit, one needs a list of six-element items composed of satellite position and velocity as functions time. Because this is inconvenient, an alternative representation of satellite orbits is commonly used, known as *orbital elements* or *keplerian elements* referring to the astronomer Johannes Kepler.

Kepler discovered that the orbit of any celestial body could be described by an ellipse where the attracting mass is located at one of its focci. This means that, instead of describing the orbit as a collection of positions and velocities, one may use only six orbital elements. They are:

- a – the semi-major axis of the orbit
- e – the eccentricity of the orbit
- i – the inclination of the orbit
- Ω – the Right Ascension of the Ascending Node (RAAN)
- ω – the argument of the perigee
- ν – the true anomaly.

The RAAN, the inclination and the argument of periapsis define the orientation of the orbital plane in space. The RAAN is the longitude in the celestial frame at which the satellite crosses the equatorial plane in the ascending direction. The inclination is the angle between the equatorial plane and the orbital plane. The argument of the periapsis (or perigee, since we are concerned about the Earth) is the angle

along the ellipse between the RAAN and the point at which the ellipse is the closest to the Earth. The semi-major axis and the eccentricity define the shape of the ellipse. Finally, the true anomaly defines the angular position of the satellite along the ellipse.

Of course, it is important to keep in mind that an orbit stays Keplerian only if the attracting body behaves as a point mass and other attracting bodies are absent.

2.2.2. Design of repeat orbits

In the design of satellite missions, the concept of repeat orbits is frequently used. A repeat orbit is an orbit which follows the same ground-tracks after a specified amount of time. The condition that defines any repeat orbit β/α is that the satellite must complete an integer number β of revolutions in the same time as the Earth completes another integer number α of revolutions. The time it takes for the Earth to complete one full revolution is a *nodal day* or *sidereal day* (23.93 h).

For the design of any realistic repeat orbit, one must further take into account two secular drift parameters that are caused by the oblateness of the Earth: the precession of the orbital plane $\dot{\Omega}$ and the precession of the perigee $\dot{\omega}$. The condition that defines a β/α repeat orbit can be written as (Wiese, 2011),

$$\beta(n + \dot{\omega}) = \alpha(\Omega_E - \dot{\Omega}), \quad \alpha, \beta \in \mathbb{N} \tag{2.13}$$

where

$$n = \sqrt{\frac{\mu}{a^3}} + \frac{3}{4}\sqrt{\frac{\mu}{a^7}}\frac{J_2 R_E^2 (3\cos i^2 - 1)}{(1-e^2)^{\frac{3}{2}}} \tag{2.14}$$

$$\dot{\Omega} = -\frac{3}{2}\sqrt{\frac{\mu}{a^7}}\frac{J_2 R_E^2 \cos i}{(1-e^2)^2} \tag{2.15}$$

$$\dot{\omega} = \frac{3}{4}\sqrt{\frac{\mu}{a^7}}\frac{J_2 R_E^2 (5\cos i^2 - 1)}{(1-e^2)^2} \quad . \tag{2.16}$$

All the unique repeat orbits are defined by α and β pairs which are co-prime, i.e. having no common divisor greater than 1. The mean motion n is a smooth function of the semi-major axis. For the range of useful satellite altitudes, say between 200 and 500 km, the number of satellite revolutions per nodal day is roughly equal to 16. This fact can be used to restrict the search space for (α, β) pairs of co-prime numbers to the range $15 < \frac{\beta}{\alpha} < 17$.

Equation (2.13) is a 7th degree polynomial in $\sqrt{a}$,

$$C_7 a^{\frac{7}{2}} + C_4 a^{\frac{4}{2}} + C_0 = 0 \quad , \tag{2.17}$$

with,

$$C_7 = \frac{\alpha}{\beta}\Omega_E \tag{2.18}$$

$$C_4 = -\sqrt{\mu} \tag{2.19}$$

$$C_0 = \frac{3}{4}\frac{\sqrt{\mu}J_2R_E^2}{\left(1-e^2\right)^2}\left[\frac{2\alpha}{\beta}\cos i + 1 - 5\cos^2 i - \left(3\cos^2 i - 1\right)\cdot\sqrt{1-e^2}\right] \quad . \tag{2.20}$$

Only circular orbits will be considered below, so that $e = 0$. For a selection of (α, β) co-prime integers and the desired inclination i, there is only one real positive solution in a larger than the radius of the Earth. This solution is then the radius a of the desired repeat orbit.

Once the semi-major axis a is known, all the rotation rates that describe the motion of the satellite in inertial space can be computed. This allows for the analytical computation of the osculating orbital elements at any point in time which can then be converted into position and velocity (Curtis, 2008).

2.2.3. Elementary satellite formations

A brief introduction to the topic of stable satellite formations can be found in M. A. Sharifi et al. (2007) and a more complete reference is Schaub et al. (2009). In this Section, I highlight the main results, which allows me to derive the types of stable satellite formations that I will refer to throughout this thesis.

A satellite formation consists of at least two satellites, a *chief* and one or more *deputy* satellite(s). The motion of a deputy satellite relative to the chief is described in the local orbital reference frame, or *Hill frame* defined with the origin at center of mass of the chief satellite, the x and z axis in the along-track and radial directions and the y-axis to complete a right-handed coordinate system, thus defining the cross-track direction. General expressions for the relative motion in this coordinate frame are known (M. A. Sharifi et al., 2007). By restricting the general case to only circular orbits, one obtains the so-called *linearised Hill equations* (Hill, 1878), describing the motion of the deputy satellite,

$$\begin{aligned} \ddot{x} + 2n\dot{z} &= 0 \\ \ddot{y} + n^2 y &= 0 \\ \ddot{z} - 2n\dot{x} - 3n^2 z &= 0 \end{aligned} \quad , \tag{2.21}$$

where n is the mean motion (cf. Eq. (2.14)). These equations are valid as long as the distance between the two satellites is relatively small in comparison with the semi-major axis of the orbit.

We are interested in finding out the types of satellite formations which are stable. Thus, assuming no disturbing forces act on the satellites, the linear system of differential equations 2.21 can be solved analytically. This yields (Schaub et al.,

2009):

$$\begin{aligned} x(t) &= -2A_0 \sin(nt + \alpha) - \frac{3}{2} nt\Delta z + \Delta x \\ y(t) &= B_0 \cos(nt + \beta) \\ z(t) &= A_0 \cos(nt + \alpha) + \Delta z \quad , \end{aligned} \tag{2.22}$$

where Δz and Δx represent an offset between the satellites in the radial and along-track directions; A_0 and B_0 are the amplitudes of cyclic motion at the fundamental frequency n; α and β represent phase shifts in this cyclic motion.

From Equation 2.22, one sees that, if there is a radial offset between the two satellites, their separation in the along track direction grows linearly with time. Therefore, any stable satellite solution requires that $\Delta z = 0$, i.e., there are no stable formations with satellites at different mean altitudes. Another interesting conclusion is that the motion in the cross-track direction is decoupled from the motion in the orbital plane.

The set of parameters $[\Delta x, A_0, B_0, \alpha, \beta]$ defines the relative motion of formation satellites. On the basis of these equations, three elementary formations may be defined. The idea behind all the elementary formations is that each accounts for relative motion along one of the x, y and z directions.

An *along-track* formation is the one where the two satellites are separated by a constant offset in the along-track direction. A *pendulum* formation is the one where the deputy satellite oscillates back and forth in the cross-track direction. A *cartwheel* formation is the one where the deputy satellite has a cyclic motion in the orbital plane. Due to the coupling between the along-track and radial directions, the amplitude of the motion in the along-track direction is twice as large as the amplitude in the radial direction. Table 2.1 presents the elements of each elementary formation.

Other combinations of the formation parameters allow for more complex relative motion. For example, in M. A. Sharifi et al. (2007), the authors consider the LISA formation. After selecting $B_0 = \sqrt{3}A_0$ and matching the α and β phases, the deputy satellite moves in a circular path around the chief satellite with motion along all three axes.

Formation	Δx	A_0	B_0	α	β
Along-track	x_{off}	0	0	0	0
Pendulum	0	0	B	0	β
Cartwheel	0	A	0	α	0

Table 2.1: Key parameters for each of the considered elementary satellite formations.

2.3. CHAMP, GOCE, GRACE and GFO

The measurement of the Earth's gravity field is a long-standing scientific goal with applications in diverse scientific and societal domains. In recent year, advances in

satellite technology have lead the quest for the precise measurement of gravity to space. Several gravity-dedicated satellite missions have been launched, and active research, including the present work, is carried out to design future ones.

The Challenging Minisatellite Payload (CHAMP) mission (Reigber et al., 1996) was launched in 2000. The mission was successfully completed in September 2010 and it was the first example of the high-low satellite-to-satellite tracking (hl-SST) concept in the context of satellite gravimetry. The hl-SST concept relies on the continuous tracking of a satellite placed in a low-altitude orbit by a constellation of GNSS satellites in high-altitude orbits, hence the term *high-low*. To allow for continuous tracking, CHAMP was equipped with a GNSS receiver. The acceleration of the satellite was completely determined by the net force acting on it, which ultimately allowed for the recovery of the Earth's gravity field. However, the motion as tracked by the GNSS receiver was also affected by non-gravitational forces acting on the satellite, e.g., atmospheric drag and solar radiation pressure. Before the gravity field could be recovered, the non-gravitational accelerations had to be removed from the observations. In order to accomplish this, the satellite was also equipped with an accelerometer, which allowed for the precise measurement of the non-gravitational accelerations.

The Gravity and Ocean Circulation Explorer (GOCE) mission (Drinkwater et al., 2006) was launched in 2009. It was equipped with the first gravity gradiometer instrument, which allowed for the precise measurement of the gravity gradient tensor, a measuremente principle known as satellite gravity gradiometry (SGG). The gradiometer was, in essence, an array of six accelerometers arranged in three sets of two accelerometers. The two accelerometers in each set were located at an offset of roughly 50 cm from each other on opposite sides of the satellite's centre of mass. The sets were aligned in three orthogonal directions, which allowed for the measurement of 3-D differential accelerations along different axes, i.e., the gravitational tensor. These characteristics made the GOCE mission extremely sensitive to the fine details of the Earth's gravity field.

Unlike CHAMP, SGG data of the GOCE mission did not need to rely on the differences between GNSS and accelerometer measurements to discard non-gravitational accelerations. The gradiometer instrument alone is capable of distinguishing the two kinds of accelerations. For each pair of accelerometers, the common-mode signal, i.e., the average of both accelerometer measurements, was the non-gravitational acceleration while the differential-mode signal, i.e., the difference between the two accelerometer measurements contained the gravitational signal of interest.

The mission was aimed at improving the Earth's gravity field by reaching a very high spatial resolution, which required the mission to be flown as low as possible. To that end, the mission was executed at the very low altitude of about 250 km. To maintain this low altitude, the satellite was equipped with a new drag-free propulsion system, which continuously compensated for the along-track component of the significant drag force acting on the satellite. Due to that system, the mission lasted for 4 years and ended in October 2013.

The Gravity Recovery and Climate Experiment (GRACE) mission (B. Tapley, 1997), which was launched in 2002, consisted of two twin satellites and was the first

demonstration of the low-low satellite-to-satellite tracking (ll-SST) concept. The two satellites, travelling at a nominal distance of about 200 km from each other, were equipped with a microwave ranging system (K-band ranging instrument, KBR), which continuously tracked their relative position variations. The major advantage relative to CHAMP was the accuracy to which the (relative) motion of satellites could be tracked; while the accuracy of GNSS measurements is at the mm level, the KBR instrument delivered range measurements at the µm level. Similar to CHAMP, each of the GRACE satellites was equipped with an accelerometer in order to account for non-gravitational accelerations in the measurements.

The GRACE mission provided significant improvements to models of the Earth's gravity field. For example, in Farahani et al. (2013), the DGM-1S gravity field model was computed on the basis of a combination of GRACE and GOCE data. Other examples of gravity field models which used GRACE data are the EIGEN (Förste, Christoph et al., 2014), GGM (Ries, J. et al., 2016) and GOCO (Pail et al., 2010) model series. In this combination, GRACE data is essential for the estimation of long to medium wavelength features of the gravity field, to which the GOCE mission is less sensitive. Conversely, the GOCE mission greatly outperforms GRACE in the high-frequency part of the spectrum.

A major scientific objective of the GRACE mission was to recover the time-variable gravity field of the Earth. Indeed, GRACE has demonstrated the ability to directly measure those variations and associated mass redistribution in the Earth's system from space. In particular, the redistribution of water could be observed, which is critical for monitoring key climate indicators such as ice-sheet mass balance, terrestrial water-storage change, sea-level rise and ocean circulation. Examples of the application of GRACE data in these domains are abundant over the past few years. For instance, GRACE data has been used to quantify extended groundwater losses in various regions, e.g. India, Northern Iraq or the Middle East (Chinnasamy et al., 2015; Joodaki et al., 2014; Mulder et al., 2015). Other examples include the estimation of ice mass losses in Antarctica (B. C. Gunter et al., 2014); estimates of groundwater storage variations at the river basin scale (Tangdamrongsub et al., 2015); estimation of steric sea level variations (Lombard et al., 2007); estimates of regional and global sea level rise trends (Purkey et al., 2014); and variations in large-scale ocean circulation (B. D. Tapley, 2003). Furthemore, new approaches were proposed to estimate geocenter motion (Swenson et al., 2008) and the dynamic oblateness of the Earth (Sun et al., 2015) using the GRACE data as input. Applications of GRACE data extend also to the domain of the solid Earth. For example, GRACE data was used to improve glacial isostatic adjustment models (B. C. Gunter et al., 2014) and to estimate mass displacement triggered by megathrust earthquakes (Broerse et al., 2014).

The GRACE mission ended on October 2017, after being operational for more than 15 years. Due to the vital importance of the data provided by GRACE, the scientific community mobilized to ensure the continuity of those observations with the GRACE Follow-On mission.

The GRACE Follow-On (GFO) mission (Flechtner et al., 2014b) was launched on May 2018. The primary objective of the GFO mission is to continue the time series

of high-resolution monthly gravity field solutions for an additional period of at least 5 years. The secondary objective of the GFO mission is to validate the effectiveness of a laser ranging interferometer (LRI) instrument, which was developed to improve the accuracy of ll-SST measurements. The LRI instrument is expected to improve the accuracy by a factor between 5 and 50, in comparison with the KBR instrument of GRACE. Another significant difference with respect to GRACE is a new star-camera assembly consisting of three star-cameras, instead of the two used in the GRACE mission. In all other major aspects, the GFO mission is similar to the GRACE mission.

While the expected improvements in terms of ranging accuracy delivered are definitely welcome, there are indications that these will not map into equivalent improvements in terms of monthly gravity field solutions.

Loomis et al. (2011) made a comparison study, where a GRACE-type pair of satellites was compared with a similar formation equipped with a modern drag-free system and laser ranging instruments, the latter similar to those carried by the GFO mission. The authors concluded that technology improvements alone do not significantly improve the accuracy of the recovered gravity field and that future work should focus on improving the background geophysical models, mission design and data processing criteria in order to minimize temporal aliasing errors.

More recently, Flechtner et al. (2016) predicted that improvements brought by the GFO mission will be small when compared to GRACE, in terms of filtered monthly gravity field solutions. The authors argued that the limiting factor in the GFO mission would be accelerometer errors, as well as errors in ocean tide models and in non-tidal atmosphere and oceanic mass transport models.

First results of the GFO mission are imminent at the time of writing. Preliminary reports indicate that the accuracy of the LRI instrument has greatly exceeded the specification. At the same time, there are indications that one of the accelerometers onboard on of the GRACE satellites is not meeting the requirements. Soon, new publications will shed some light on the actual performance of the GFO mission.

While awaiting first results from the GFO mission, one may look back and realize the many achievements of the GRACE mission. The scientific ramifications of the application of GRACE data are an impressive statement on both, the usefulness and the need for better gravity field modelling. In this sense, GRACE has become a vital component of a global observation system, which monitors the Earth. Despite its many successes, the GRACE mission has also revealed its limitations.

2.3.1. Limitations of GRACE

The performance of the GRACE mission is limited by its *spatial resolution* and its *temporal resolution*. Formally, the spatial resolution can be interpreted as the wavelength of the maximum spherical harmonic degree of a gravity field solution. This straightforward definition is however not meaningful; a more realistic definition must take into account the existence of errors in the observations. In the GRACE mission, errors in the observations become larger than the gravitational signal at a certain spatial frequency (see Section 2.4). As a consequence, the spherical harmonic coefficients above this frequency become noisy. Therefore, the spatial resolution is in fact defined by the smallest wavelength of the spherical harmonic

coefficients estimated under favourable noise conditions. Until noise in the computed solutions is quantified, the actual spatial resolution of the mission remains unknown.

In the GRACE mission, the limitations in terms of spatial resolution are further aggravated by two phenomena: inaccurately known reference orbits and anisotropic sensitivity. Recovery of gravity field solution from GRACE data requires the removal of references quantities (ranges, range-rates or range-accelerations). The reference quantities are obtained from reference orbits, which are computed on the basis of a background force model. Deficiencies in the force model will cause errors in the reference quantities, thus increasing the overall error level and further limiting the spatial resolution.

Anisotropic sensitivity is related to the direction along which the observations in the GRACE mission are made. Inter-satellite ranging is performed in the along-track direction, which due to the near-polar orbits of GRACE satellites, is parallel most of the time to the North-South direction. As a consequence, GRACE's sensitivity in the East-West direction is greatly reduced. This lack of sensitivity means that a poor signal-to-noise ratio is achieved for near-sectorial coefficients in the recovered solutions. This is the mechanism responsible for the appearance of vertical stripes, or *striations*, typically seen in unfiltered GRACE solutions.

The performance of GRACE is also limited by its temporal resolution. In order to calculate a gravity field solution, observation data has to be accumulated for a certain period of time, until the inversion into a gravity field solution up to sufficiently high degree is possible. For GRACE, the accumulation period is typically 1 month. Mass transport signals occurring at shorter-time scales than one month, will map, or alias, as *temporal aliasing* errors into the solutions. In paricular, there are rapid mass transport signals caused by atmospheric and oceanic processes with time-scales from few hours to weeks. In the case of GRACE, if left uncorrected for, these would cause large temporal aliasing errors (Flechtner et al., 2014a). A set of background models that represent rapid mass transport signals is used to remove their influence from the satellite measurements. However, those models are not perfect; they fail to represent the actual processes accurately, which causes temporal aliasing errors in the computed monthly gravity field solutions. Background models and their errors are further discussed in Section 2.5.2.

The GFO mission, while expected to have significantly lower instrumentation errors, is similarly affected by the same limitations as those of the GRACE mission. Future ll-SST missions must effectively tackle these limitations in order to significantly surpass the performance of the GRACE and GFO missions. One final concern, when predicting the performance of future satellite missions, is the fact that, after the end of the GRACE mission, a complete understanding of the errors in the GRACE data is still missing.

2.4. Incomplete error budget

Before the launch of the GRACE mission, Kim (2000) presented an in-depth study on the propagation of instrument errors into gravity field solutions. This result became known as the *GRACE baseline*. After the GRACE launch, it soon became

apparent that the observed noise was several times larger than expected. First investigations into the matter (Frommknecht et al., 2006; Gerlach et al., 2004) showed that the level of noise in GRACE Level-1 A (L1A) data was, for the most part, close to the specification, with the exception of the accelerometers. After these first investigations, research efforts then went in a different direction; Ray et al. (2006) and Thompson (2004) investigated the impact of temporal aliasing errors (up to then not considered relevant), caused by innacuracies in background force models, and showed that these could potentially be larger than instrument errors. Still, temporal aliasing errors could not explain the observed noise in real GRACE data. After this point, specific error sources were further investigated: attitude control thruster pulses (Meyer et al., 2012), magnetic torquer induced signals (Peterseim et al., 2012) and errors from star camera instruments (Bandikova et al., 2012; Horwath et al., 2011; Inácio et al., 2015).

Ditmar et al. (2012) is the latest publications which tackle the full budget of noise in the GRACE mission. The authors examined GRACE data noise in different frequency bands and compared it with synthetic realizations of errors from different sources. That publication was also the first to consider errors in the computed reference orbits. The authors concluded that errors in frequencies above 9 mHz are well explained by KBR ranging errors. They attributed errors in the frequency range below 1 mHz to the limited accuracy of the reference orbits. The origin of noise observed in the frequency range between 1 and 9 mHz remained to be explained.

With an outlook into the future, it becomes clear that understanding the errors in GRACE data is an essential requirement to predict the performance of future satellite gravimetry missions. In Section 6.1, I will complete the GRACE errors budget and explain the sources of the errors that remained to be explained. For now, in the next sections, an overview is provided of the publications which addressed specific error components in data from the GRACE mission.

2.5. Signal and errors in ll-SST data

The performance of a satellite gravimetry mission depends on the signal-to-noise ratio as a function of frequency. There are several error sources that play a role in ll-SST satellite missions. The error sources can be divided in two categories: *instrumentation* and *temporal aliasing* errors. Instrumentation errors refer to the noise generated by the instruments on-board typical ll-SST satellites. Temporal aliasing errors, which were already mentioned in Sec. 2.3.1, refer to errors in the background models that are used to remove mass transport signals at short time scales from the observations. Ocean tides as well as non-tidal mass transport in the ocean and atmosphere are the two largest contributors to those errors.

2.5.1. Signal

To simulate a satellite mission it is necessary to have a representation of the mass transport signal to be recovered. In this thesis, I use as signal the ESA's Earth System Model for Gravity Mission Simulation Studies (ESM) (Dobslaw et al., 2014a). This model is the subject of several related publications (Bergmann-Wolf et al.,

2014, 2015; Dobslaw et al., 2014b, 2015).

The ESM model is an attempt of designing a realistic model of all the mass transport signal components of the Earth system. It addresses the needs of simulation studies of future satellite missions (such as this thesis) in order to suitably benchmark different mission concepts. The ESM model aims at providing a representation of real mass transport signal over all temporal scales; sub-daily to weekly mass variability in the atmosphere and oceans is required to properly take into account the impact of temporal aliasing errors while signal at monthly and yearly timespans, particularly at small spatial scales, is essential to assess the performance of future ll-SST missions in terms of signal recovery.

The ESM is a collection of spherical harmonic solutions for a period of 12 years with a timestep of 6 h. The ESM signal is composed of 5 components: *A*tmosphere, *O*cean (non-tidal), *H*ydrology, *I*ce and *S*olid Earth.

As I mention in Section 2.3.1, the major sources of rapid mass transport signal are the Atmosphere and Oceans. The signal of that origin are typically removed from the satellite measurements with the help of models, in order to mitigate temporal aliasing errors. Therefore, I consider only H, I, and S (HIS) components as the signal to be recovered.

Mean mass transport signal

Even after removing the AO components, the HIS mass transport signal is by no means static. As a consequence, the variations in the HIS signal will similarly cause temporal aliasing errors in the solutions. In order to isolate the signal of interest from errors, I consider the mean mass transport signal (HIS) over the *data accumulation period* of the mission to be the signal one wishes to recover. DAP is the period needed to collect the observations which are used to compute a gravity field solution. As it is already mentioned above, the typical DAP of the GRACE mission is 1 month. Deviations of the recovered solutions from this mean signal are interpreted as noise.

2.5.2. Temporal aliasing errors

Temporal aliasing errors are caused by phenomena that occur on shorter time-scales than the DAP. There are three major sources of temporal aliasing errors: dynamic mass transport signal (see below), ocean tides and non-tidal mass transport signal in the atmosphere and oceans. In the following sections, a description of the considered temporal aliasing error sources is given.

Dynamic mass transport signal

While the mean HIS is the signal to be recovered, the instantaneous deviation of the HIS signal from this mean is one of the error sources to be considered. The dynamic mass transport signal is simply defined as the total HIS minus the mean HIS over the DAP of the mission.

Errors in ocean tide models

The tides on Earth are primarily caused by the gravitation of the Moon and the Sun. Other planets' gravitation is negligible. The Sun and the Moon create the

Variable	Description	Period
τ	The lunar day	$T = 1.04$ days
s	The sidereal month	$T = 27.3$ days
h	The tropical year	$T = 365.24$ days
p	The moon's perigee	$T = 8.85$ years
N'	The regression of the moon's nodes	$T = 18.6$ years
p'	The perihelion	$T = 20942$ years

Table 2.2: Doodson's astronomical variables (given as phases) and the corresponding periods (Huess, 2001)

tide generating potential. Tidal forces periodically deform the shape of our planet. Tidal deformation can be split into solid earth tides and ocean tides. Both types must be taken into account in the context of gravimetry data. While solid earth tides are quite accurately modelled, ocean tides are much more complex to do so, especially in shallow water areas and polar regions. Nonetheless, tidal deformation of the oceans accounts for extremely large surface mass variations which must be accurately removed from the gravimetry data.

The tide is the elevation of the sea surface relative to the mean sea surface in response to the tide generating potential. Another important parameter is the *equilibrium tide*, which is defined as the theoretical elevation of the sea if the Earth were fully covered by water, and the water responded instantaneously to the tidal force. The real tide and the equilibrium tide differ because of the non-instantaneous response of the ocean to the tide generating potential, due to friction at the sea bottom, the presence of continents, etc. The equilibrium tide serves as a reference for the calculation of the real tide.

The tide generating potential can be split in different harmonics, or *tidal constituents*. The Doodson argument, θ_f, is commonly used as a representation of a specific tidal constituent f. It is a linear combination of the six astronomical variables that describe the motion of the moon around the Earth and the motion of the Earth around the Sun (Doodson, 1921). Each variable is a phase relative to the Greenwich meridian. The six variables are listed in Table 2.2 along with their corresponding periods. These six variables constitute the fundamental frequencies of the Earth-Moon-Sun system and every frequency of the tide generating potential can be expressed as a linear combination of these fundamental ones, such that,

$$\theta_f(t) = i_f\tau + j_f s + k_f h + l_f p + m_f N' + n_f p' \tag{2.23}$$

where i_f, j_f, k_f, l_f, m_f, n_f are the integers known as the Doodson numbers that define a certain tidal constituent f.

The tidal height ξ at any point of the Earth's surface (φ,λ) at time t can be computed as (IERS, 2010),

$$\xi(\varphi,\lambda,t) = \sum_f Z_f(\varphi,\lambda)\cos(\theta_f(t) - \psi_f(\varphi,\lambda)) \tag{2.24}$$

Where
f – is a certain tidal constituent
Z_f – is the amplitude of constituent f
θ_f – is the Doodson argument
ψ_f – is the phase at Greenwhich Mean Sidereal Time $t = 0$

Ocean tide models have one of three origins: empirical, hydrodynamic or assimilation. Empirical models are based on sea level observations like tide gauges and sea level altimetry records. This approach is purely data-driven. Hydrodynamic models are computed by applying the tide generating potential to a model of the oceans containing the ocean boundaries, sea bottom topography, friction with sea bottom and tidal currents. This is a physical approach where no measurements of the ocean are used. Assimilation models are a mix of both methods, where the dynamic models of the ocean assimilate sea level observations to combine both theoretical and observed information.

Ocean tide models are used in GRACE data processing to remove the influence of the ocean tides from the observations. The tidal signal is increasingly well modelled, partly due to the ever increasing amount of radar altimetry data.

Currently, the most commonly used ocean tide models in the field of satellite gravimetry are the EOT11a (Bosch et al., 2009) models and, more recently, FES2014 Carrère et al. (2016). At the beggining of my research the FES2014 model was not available, therefore, in this thesis I considered the older version FES2004 (Lyard et al., 2006).

In order to estimate tide model errors, I assume that these are adequately represented by the differences between these two models: FES2004 (Lyard et al., 2006) and EOT11a (Bosch et al., 2009). FES2004 is an assimilation model that combines several years of altimetry data with a hydrodynamic model. EOT11a is a successor of FES2004 in the sense that it is released as an increment to FES2004; it is an empirical model estimated from the residuals of FES2004. EOT11a model is reported to provide improvements in specific areas of the globe, e.g., in shallow water areas where tidal dynamics are non-linear (Bosch et al., 2009).

The assumption that errors in ocean tide models are defined as the difference between two alternative models suffers from an obvious weak point. Since both models are roughly based on the same datasets, their differences could underestimate the magnitude of the errors, especially in certain areas where observations are scarce. An evidence of this has been observed by Quinn et al. (2011) when analyzing variances of ocean bottom pressure records. Despite this fact, the current definition of errors is seen as adequate for the purpose of comparing the performance of future satellite mission concepts.

The two considered ocean tide models consist of a set of tidal constituents. In EOT11a, each constituent is defined by a quadrature and in-phase component. In FES2004, each constituent is defined by amplitude and phase components. In Table 2.3, a summary of the constituents in each tide model is given. Eqn. (2.24) can be expanded into in-phase and quadrature components by expanding the cosine

Table 2.3: List of tidal constituents in each of the considered tidal models

	Tide	Doodson	FES2004	EOT11a
Long-period	M_m	065.455	✓	✓
	M_f	075.555	✓	✓
	M_{tm}	086.455	✓	✗
	M_{sqm}	093.555	✓	✗
Diurnal	Q_1	135.655	✓	✓
	O_1	145.555	✓	✓
	P_1	163.655	✓	✓
	S_1	164.555	✗	✓
	K_1	165.555	✓	✓
Semi-diurnal	$2N_2$	235.555	✓	✓
	N_2	245.755	✓	✓
	M_2	255.655	✓	✓
	S_2	273.555	✓	✓
	K_2	275.555	✓	✓
Quarter-diurnal	M_4	455.555	✓	✓

term:

$$\xi(\varphi,\lambda,t) = \sum_f Z_f(\varphi,\lambda)\cos[\psi_f(\varphi,\lambda)]\cos[\theta_f(t)] + Z_f(\varphi,\lambda)\sin[\psi_f(\varphi,\lambda)]\sin[\theta_f(t)] \quad , \quad (2.25)$$

where $Z_f\cos(\psi_f)$ and $Z_f\sin(\psi_f)$ are the *in-phase* and *quadrature* components, which are typically provided in the form of gridded data.

Models of non-tidal rapid mass transport in the atmosphere and ocean and their errors

Aside from mass redistribution caused by tides, other phenomena cause short-term mass variability. Evolving synoptic weather systems result in significant variations of surface atmospheric pressure. Heavy precipitation events cause significant accumulation of water over continental regions. Winds associated with cyclonic pressure systems may cause the re-distribution of oceanic water masses thus impacting the ocean bottom pressure (Flechtner et al., 2014a).

The Atmosphere and Ocean De-aliasing Level-1B product (AOD1B) (Dobslaw, Henryk et al., 2016) is used to subtract these non-tidal rapid mass transport signals from the GRACE data. Currently in its 6th release, it is the official de-aliasing product of the GRACE and GRACE Follow-On missions.

The product contains a set of combined atmosphere and ocean spherical harmonic coefficients complete up to degree and order 180 with a time sampling of 3 hours. For the atmospheric component, it uses analysis and forecast data out of the operational high-resolution global numerical weather prediction (NWP) model from the European Center for Medium-range Weather Forecast (ECMWF). For the

oceanic component, the global ocean circulation model MPIOM (Jungclaus et al., 2013) is used, which is consistently forced with ECMWF atmospheric data.

In a recent publication by Bergmann-Wolf et al. (2015), the authors have built a realistic realization of errors in the previous release RL05 of the AOD1B model. The authors model those errors as the sum of a set of distinct error components. Each component might differ from the others in terms of regional extent, temporal scale and whether it refers to a continental or oceanic region. The authors show that the overall variability of AOD errors is explained by large-scale errors over the oceans with particularly high magnitudes in the Arctic Ocean and in the vicinity of the Antarctic Circumpolar Current. Finally, the authors argue that errors at small spatial scales provide only a minor contribution to the overall AOD errors. In this thesis, I use this product as an estimation of the AOD model errors.

2.5.3. Instrumentation Errors

There are four instrumentation error sources that I will consider: star-cameras, accelerometers, positioning and ranging.

Positioning

One of the products required in ll-SST data processing is the kinematic orbits derived from GNSS receivers on-board the satellites. In the processing of ll-SST data, kinematic orbits are used as observations during the computation of the reference orbits. State-of-the-art accuracy of kinematic orbits derived from space-borne receivers is at the level of 3 cm (Zhou et al., 2019).

Ranging

The GRACE and GRACE Follow-On satellites are equipped with a KBR instrument, which continuously monitors range variations between the two satellites. Errors of the KBR instrument have two components: system noise and oscillator noise. System noise is modelled as white noise and oscillator noise shows a $1/f$ behaviour, where f is the frequency. Above the frequency of 2 mHz, the system noise is dominant with a PSD$^{\frac{1}{2}}$ specification of $1\,\mu\mathrm{m}\,\sqrt{\mathrm{Hz}}^{-1}$ (Gerlach et al., 2004).

Star cameras

A star-camera (SC) is an instrument comprising a digital camera, a microprocessor, software, and a star catalogue (Liebe, 2002). The star catalogue contains information about the positions of the stars in the celestial sphere. The SC views a small portion of the sky and pinpoints the brightest stars in its field of view. The pattern formed by the brightest stars is compared with the internal star catalogue allowing the instrument to recognize the stars in the field of view. The SC instrument uses advanced algorithms to compute the (sub-)pixel coordinates of the centres of the stars in the field of view. Knowing the location of the brightest stars in the camera's internal reference frame, the attitude of the SC instrument and consecutively that of the spacecraft can be determined.

The origin of the SC internal reference frame is the centre of the optical system's field of view. Its orientation is defined with a *boresight* axis (typically the *z*-axis)

crossing the centre of the field of view and pointing perpendicular to it. The *x*- and *y*-axes are coplanar to the field of view and are typically named *cross-boresight* axes. The rotation between this reference frame and the science reference frame (SRF) is obtained through calibration procedures, and is provided as the quaternion product QSA1B (Case et al., 2010).

The distinction between boresight and cross-boresight is motivated by the fact that acuraccy of the SC data is anisotropic (Liebe, 2002). Typically, SCs are more sensitive to rotations about the cross-boresight axes than about the boresight axis. Rotations around the cross-boresight axes are seen by the optical system as a translation of all the stars in the field of view. The displacement of the stars is uniform across the whole image. On the other hand, rotations around the boresight axis result in rotations of the stars around the centre of the field of view. Stars close to the centre show much smaller displacements than those at the edge. As a result, the ratio between the accuracy of the cross-boresight and the boresight axes of typical SCs is somewhere between 6 and 20 (Liebe, 2002). For GRACE SCs, the accuracy of rotations about the cross-boresight axes is better than that of rotations about the boresight axis by a factor of 8 (S.-C. Wu et al., 2006, Appendix J).

It is a common practice that satellites use two (or more) SCs, looking at different parts of the sky. This has two advantages; first of all, combining data of several SCs improves the accuracy of attitude information. Secondly, several cameras provide redundancy; should one of the sensors fail or look towards the Sun or the Moon, the others are still available to provide attitude information. Regarding the GFO mission, the star camera assembly configuration has been upgraded to a total of three star cameras for improved redundancy and accuracy.

The GRACE satellites are equipped with two SCs each, which provide attitude information with 1 s sampling. They are referred to as *primary* and *secondary* SC, respectively. Fig. 2.3 depicts the relative orientation of each SC reference frame and the SRF.

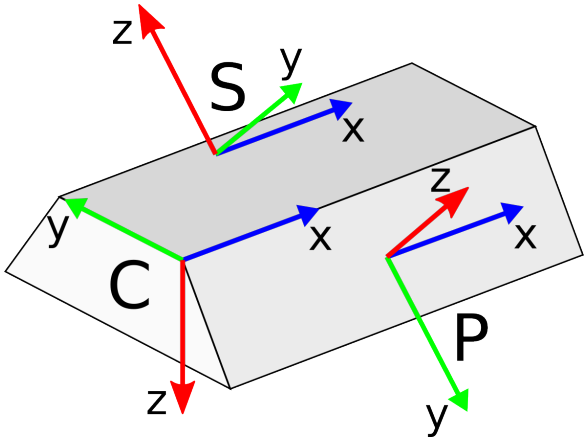

Figure 2.3: Primary SC (P), secondary SC (S) and science (C) reference frames. *x*-, *y*- and *z*-axis are represented by blue, green and red color, respectively. The z-axis in the SC reference frames is the boresight axis. Both SCs are assembled at $\pm 135°$ rotation angle about the *x*-axis in the science reference frame (SRF).

Accelerometers

All recent satellite gravimetry missions (CHAMP, GRACE, GOCE and GFO) carried three-axis capacitive accelerometers for the measurement of non-gravitational accelerations. In the case of CHAMP and GRACE and GFO, the accelerometers were located at the centre of mass of the satellite. The SuperSTAR accelerometers used in GRACE and GFO missions were roughly one order of magnitude less sensitive in the cross-track direction w.r.t. the other two directions.

Errors in accelerometer data may be be categorized as: *noise intrinsic* to the instrument, *interference noise* and *orientation errors*. Intrinsic noise reflects the limits of every measurement instrument. Interference noise is caused by other instruments on-board the satellite or by changes in the physical processes related to the spacecraft, e.g., temperature variations or deformations. Finally, orientation errors are caused by inaccurately known attitude of the spacecraft relative to inertial space. These deviations, in turn, affect the accuracy of the reference orbits.

Current accelerometer technology makes use of a free-floating proof mass within a metallic enclosure. The proof mass is kept at the centre of the enclosure (i.e., the centre of mass) by applying an electrostatic force which reproduces the total non-gravitational one acting on the satellite. The voltage that is proportional to the applied electrostatic force constitutes the raw acceleration measurement.

Associated with each raw measurement is an error resulting from the combination of several effects. Accelerometer measurements must be converted from voltages into acceleration units. This conversion requires a set of parameters which must be estimated by calibration procedures, e.g., using in-flight manoeuvres. Deviation of the estimated parameters from the instantaneous instrument state will result in errors in the measurements. Furthermore, the measured acceleration vector in the instrument frame must be related to the physical non-gravitational acceleration of the satellite in the inertial frame. This requires the orientation of the accelerometer instrument with respect to the satellite and of the satellite with respect to the inertial frame. The orientation of the accelerometer frame w.r.t the satellite must be estimated from calibration procedures. Any inaccuracy will cause misalignment errors in the accelerometer measurements. Additionally, the accelerometer instrument is not perfectly built, and its three axes are not perfectly orthogonal, which introduces cross-talk errors in the measurements. Finally, the location of the proof mass slightly deviates from the centre of mass. This introduces a centrifugal acceleration term in the measurements caused by the rotation of the spacecraft. All these effects cause systematic errors, which are largely removed from the measurements through proper modelling and calibration procedures. These are well documented in Kim (2000).

In a general sense, quantifying the in-flight performance of accelerometers is a troublesome task due to the scarcity of complimentary data. Similarly, it is also difficult to distinguish between intrinsic noise and interference noise (Peterseim et al., 2012).

In the context of the GRACE, analysis of accelerometer data has revealed several issues which likely affected the performance of the mission. The requirement for the accelerometer instruments of the GRACE and GFO missions along the most

sensitive axes was that the $\mathrm{PSD}^{\frac{1}{2}}$ of noise is below (Flury et al., 2008)

$$\sqrt{1+\frac{0.005}{f}}\cdot 10\times 10^{-10}\,\mathrm{m^2\,s^{-1}\,\sqrt{Hz}^{-1}} \quad . \tag{2.26}$$

Gerlach et al. (2004) examined the $\mathrm{PSD}^{\frac{1}{2}}$ of *relative* L1A accelerations between the GRACE satellites along the line-of-sight (LoS) direction. This method reveals errors in accelerometer data, but limited to the frequency ranges where noise is larger than signal, i.e., the high-frequency part of the spectrum (above 30 mHz). The authors found that in this frequency range, L1A accelerometer noise was at the level of $6\times 10^{-9}\,\mathrm{m\,s^{-2}\,\sqrt{Hz}^{-1}}$, i.e., a factor of 60 above the specification.

Upon close inspection, it seems that accelerometer data above 30 mHz were contaminated with *thruster events*, *twangs* and *spikes*. Thruster events were caused by firing of satellite thrusters used to control the attitude of the satellite. They come into play by a combination of thruster misalignments and small deviations of the accelerometer instrument from the satellite's CoM. However, thruster events reflect for the most part real linear accelerations of the satellite, i.e., they should not be considered as errors (Frommknecht et al., 2006). Twangs are described as strong signal impulses (up to $2\times 10^{-5}\,\mathrm{m\,s^{-2}}$) followed by a damped oscillation with a duration of up to 10 s, occurring very frequently (about 30% of the data) in the radial accelerometer component and less frequently (about 1-3%) in the other two components. Twangs are hypothesized to be caused by an uneven expansion of a radiator foil at the bottom of each satellite (Flury et al., 2008; Gerlach et al., 2004). Spikes are smaller in amplitude ($1\times 10^{-7}\,\mathrm{m\,s^{-2}}$) and shorter in duration (1 s to 3 s) but occurring much more frequently (in 30 to 40% of data) along all three accelerometer axes. They are found to be caused by frequent heater switching used to regulate temperature on-board the GRACE satellites (Flury et al., 2008). In a later publication, Peterseim et al. (2012) have shown that a part of the observed spikes were caused by the magneto-torquer instruments. Apart from these features, the actual sensor performance seems to be close to the requirements (Flury et al., 2008; Frommknecht et al., 2006; Gerlach et al., 2004). However, because these features were so strong and so frequent, they degraded the overall data quality significantly. While the 35 mHz low-pass filter applied to the L1A data removes most of the noise in the high-frequency part of the spectrum, several authors warn about the unknown impact of the effects discussed above in the low-frequency range (Frommknecht et al., 2006; Gerlach et al., 2004). This impact may not be negligible, since the occurrence of twangs is correlated with the orbital frequency and the spikes also seem to exhibit certain periodicities (Gerlach et al., 2004). As a consequence, Gerlach et al. (2004) and more recently Peterseim et al. (2012) state that, although unlikely, it cannot be theoretically excluded that some of these effects may have an influence in the gravity field determination.

2.6. Future of satellite gravimetry missions

With the GFO mission underway, it is time to look into the future of satellite gravimetry missions. In Rummel et al. (2003), the authors began by mapping all the different phenomena that compose the gravity signal in terms of their spatial and temporal spans. The authors proceeded to evaluate the potential of four different mission concepts to measure all these phenomena: very high altitude orbit missions, gradiometry missions and ll-SST formations. The authors used a relatively simple simulations in order to quantify the accuracy and spatial resolution of each concept. While limited in its scope, (e.g., no temporal resolution was determined), several interesting ideas arose from that publication. The authors showed that very high altitude orbit missions are limited in the spatial resolution they can achieve, irregardless of the improvements in terms of instrumentation noise. Envisioning future technological developments, the authors argue that the along-track SST missions similar to GRACE have the potential to significantly improve the achievable spatial resolution, enabling these types of missions to completely observe several geophysical phenomena of interest. The authors also showed that, while GOCE is unable to contribute to the study of temporal gravity field variations, future gradiometer-type missions have tremendous potential to measure those variations, as long as the orbits can be made significantly lower and/or the gradiometer accuracy is increased by at least an order of magnitude. Finally, SST formations are proposed, where satellite pairs work as a very long gradiometer-arm instrument. Several satellite pairs may observe the gravity gradient simultaneously over several directions. This concept is also shown to potentially bring major improvements and new scientific applications of satellite gravimetry data.

In the following years, the study of alternative satellite (multi-)formation missions became of general interest with several publications dedicated to this topic. In the following, I will discuss the relevant publications that deal with single-formation missions. Then, I will proceed to discuss the missions which combine two satellite formations.

2.6.1. Elementary satellite formations

In two closely related publications, M. A. Sharifi et al. (2007) and Sneeuw et al. (2008) analysed the performance of the three elementary satellite formations: along-track, pendulum and cartwheel, along with that of the LISA concept. The authors concluded that the along-track formations are relatively poor in signal-to-noise ratio and that both the cross-track and radial directions contain stronger gravity signal. The authors concluded that the inclusion of cross-track information may be helpful to mitigate temporal aliasing errors. They highlighted the importance of reducing the anisotropy of future missions and that proper design of multi-formation missions should allow for full-tensor gravity gradiometry, since different pairs of satellites may work together as very long gradiometer arms oriented in perpendicular directions.

In Wiese et al. (2009), an analysis of four candidate missions was carried out. The authors used 30 days of data and two simulations per mission concept, at 250 km and 400 km altitude. The considered missions were: one along-track pair

of satellites in polar orbits, two along-track pairs in polar orbits, a cartwheel formation and a mission with two cartwheel formations along the same orbits with perpendicularly oriented baselines. In the absence of temporal aliasing errors, the double cartwheel is an order of magnitude better than the GRACE mission. However, in the presence of these errors, all missions performed at the similar level. Another interesting conclusion was that the choice of the mission altitude did not have a significant impact on the level of temporal aliasing errors. The authors highlighted the need to reduce temporal aliasing errors by using better background models and by making use of multiple formations to improve the overall temporal resolution of the mission.

Elsaka (2010) presented an extended study of future satellite gravimetry concepts. Elsaka analysed several concepts based on the elementary satellite formations: along-track, pendulum and cartwheel (the author addressed the latter as radial-wheel). The author showed that the pendulum and cartwheel concepts performed better than the along-track concept both in terms of static and temporal gravity field recovery. The author argued that, due to the limitations of inter-satellite ranging technology, the pendulum missions are very challenging to design. As such, the author recommended the cartwheel type of missions to be considered for the future.

More recently, Elsaka et al. (2013) proposed and compared seven concepts of future satellite missions, consisting of single or dual satellite formations. The comparison was made under the same error scenarios. Regarding the single-formation concepts, the authors concluded that the pendulum-type formations are desirable. The authors showed that the so-called *advanced pendulum* formations exhibit the best performance. Advanced pendulums are pendulum-type missions where the LoS direction is tilted by up to a maximum of 45° relative to the cross-track direction. The authors warned that such type of pendulums are technologically hard to accomplish due to the large values of the inter-satellite velocity. The authors then recommended a *moderate pendulum* mission, with a maximum LoS tilt of 25°, which is already regarded as feasible. This mission, despite a poorer performance, still shows significant improvements relative to the along-track concept.

In Encarnação (2015), a complete analysis of the errors in the elementary satellite formations was given. The author considered an extended set of ll-SST errors, including those not taken into account in any previous work. The analysis of the performance of the elementary formations lead to the conclusion that the pendulum formations are the best. The author also concluded that the accuracy of the pendulum formations is limited by ranging noise. Another noteworthy conclusion was that the cartwheel mission is very sensitive to orbit errors.

When looking into the future, taking into account the foreseeable performance of drag-free and laser-ranging technologies, it seems that temporal aliasing errors are the major limitation. Regarding single-formation missions, there seems to be consensus that, from a simulation point of view, both the cross-track and cartwheel concepts are superior compared to the along-track formation. They are more isotropic, which significantly reduces the level of errors in the solutions. Additionally, the performance of the pendulum concept is shown to increase with

increasing tilt of the LoS direction relative to the along-track direction. Increasing tilt however results in an increase in the inter-satellite velocities, in which existing inter-satellite ranging technology is limited, rendering concepts with an tilt larger than 30° technically difficult to realize (Elsaka et al., 2013). Due to the same limitation and additionally due to the highly dynamic behaviour of their LoS direction, the cartwheel formations are also deemed as extremely difficult to implement in practice. Apart from choosing the proper type of formations, several additional ways have been pointed out to mitigate temporal aliasing errors even further: the use of better-quality background models, better data processing and the inclusion of additional satellite formations in order to improve the overall temporal resolution of the mission. The latter has also been a topic of extensive research.

2.6.2. Multi-formation concepts

P. L. Bender et al. (2008) proposed the concept which is nowadays referred to as *Bender mission*. The authors stated that temporal aliasing errors are likely one of the limiting factors of the GRACE mission and that such limitation will not vanish even if the measurement accuracy is significantly improved. Same conclusion was similarly made by Loomis et al. (2011). The Bender mission attempts to solve this problem with the addition of another pair of along-track satellites. The second pair of satellites result in another set of observations which both improve the temporal resolution of the mission and provide observations with a East-West component resulting in a more isotropic sensitivity of the mission as a whole. The authors argued that the second pair also provides a high density of ground-tracks at mid-latitudes each day. Furthermore, the authors suggested that the many crossings of the two pairs would allow for significant improvements of the combined solution. It was the first example of an attempt to improve the spatio-temporal resolution achieved by GRACE by including an additional pair of satellites.

Capitalizing on the idea behind the Bender mission, Wiese (2011) analyzes the future of satellite gravimetry. One of the pillars of this thesis was the optimization of the parameters that define the Bender mission. The author analyzed different parameters of the formation: the mission length, the maximum solved degree, the inclination of the second pair, the choice of repeat periods, etc. The author concluded that the best possible Bender-type mission consists of two pairs of satellites in 13-day repeat period orbits. The first pair of satellites is placed in a polar orbit at an altitude of 299 km. The second pair is placed at an inclination of 72° and an altitude of 290 km. The author proceeded to compare the expected performance of the designed Bender mission with two other mission concepts: a single along-track pair in a polar orbit and two along-track pairs in polar orbits. The author showed that the designed Bender mission is the best.

In Elsaka (2010), the author analyzed, alongside the already discussed elementary formations, a few multi-formation concepts. The author considered a so-called *GRACE-pendulum* formation, consisting of three satellites which realize two independent formations. A chief satellite takes simultaneous part in two formations: in an along-track formation with another satellite and in a pendulum formation with the remaining third satellite. The author considered also the so-called *Multi-GRACE*

mission concepts, where two along-track pairs of satellites are combined in two different ways in order to improve the spatial or the temporal resolution of the mission. Both in terms of static and time-variable gravity field recovery, the author showed that the GRACE-pendulum mission consistently performs better in comparison with all other considered concepts. As mentioned previously (see Section 2.6.1), the author warned, however, that this concept is technologically challenging to implement.

Elsaka et al. (2013) compare the performance of several single formations with a Bender-type of mission. After excluding alternative concepts due to their technologically difficult nature, the authors recommended the Bender mission and showed that it is able to reduce the overall error by at least an order of magnitude relative to GRACE and GFO mission, with significant improvements in the short and medium frequency ranges.

A radically different idea was proposed in B. Gunter et al. (2011), where the authors proposed the inclusion of a gravimetry payload in the recently deployed 2nd generation Iridium constellation. This constellation consists of 66 operational satellites at an altitude of 780 km. The authors showed that, if certain positioning requirements could be achieved, such gravimetry constellation would allow for continuous monitoring of large-scale time-variable gravity field on a sub-monthly time scale. This is an example of a very high altitude gravimetry constellation, which as predicted in Rummel et al. (2003) is fairly limited to the measurement of the long-wavelength features of the gravity field.

In retrospect, the consensus about what a future satellite gravimetry mission should be seems to be gathering around the Bender-concept. Several publications remark on the advantages of the Bender-mission relative to all the elementary satellite formations, given that the cartwheel and pendulum concepts are deemed as difficult to implement.

Already at this point we can identify a gap in the literature. Several publications have identified that pendulum formations offer significant improvements over the along-track concept. Therefore, one wonders, whether a multi-pendulum concept could deliver similar improvements as the ones brought by the Bender-type missions.

Finally, from an overview of the existing literature it becomes clear that the performance of the GRACE and GFO missions is limited by the sub-optimal along-track concept, which suffers from highly anisotropic sensitivity. It has been shown that, with inclusion of information along other directions (radial or cross-track), these limitations are for the most part removed. Then, taking into account the new generation of ranging instruments already available for the GFO mission, it has been shown that the limitations of future satellite mission concepts are mostly related to temporal aliasing errors. Therefore, when designing future mission concepts, it becomes crucial to deal with the concept of temporal resolution.

2.7. Spatio-temporal resolution

Reubelt et al. (2010) introduced the so-called *Heisenberg rule* of satellite gravimetry, which relates the spatial and temporal resolution of a mission. The authors assumed

a single-sensor mission (i.e., single satellite or a ll-SST pair) in a β/α repeat orbit. The authors defined the spatial resolution of the mission as the equatorial ground-track spacing, $D_{\text{space}} = \frac{2\pi}{\beta}$[1], while the temporal resolution was defined as the repeat period of the orbit, $D_{\text{time}} = \alpha$. For a given satellite gravimetry mission, the product of the spatial and temporal resolution is,

$$D_{\text{space}} \cdot D_{\text{time}} = \frac{2\pi\alpha}{\beta} = 2\pi T_{\text{rev}} \quad . \tag{2.27}$$

This product is approximately constant because, for typical altitudes of low earth orbiters, the orbital revolution period T_{rev} is practically constant and approximately equal to 90 min.

Reubelt et al. (2010) tested the validity of the Heisenberg rule by simulating various single- and multi-formation missions. The authors discussed several possibilities of placing multiple satellite formations. They presented a Δt-shift to improve temporal resolution, where one formation is delayed in time over the same ground-tracks, and a $\Delta\lambda$-shift to improve the spatial resolution, where one formation is placed at 1/2 ground-track spacing from the other. A third option, a $\Delta\Omega$-shift (i.e., a relative shift in the RAAN of the satellite-pair orbits) was also discussed, where the authors predicted that $\Delta\Omega \approx 90°$ is likely beneficial for reducing temporal aliasing errors.

Other studies of multi-formation missions have selected formation orbital planes which are roughly co-planar, i.e., $\Delta\Omega \approx 0°$ or $\Delta\Omega \approx 180°$. In Elsaka (2010), the author simply considers the second formation to be placed at a $\Delta M = 180°$ from the first, in order to mitigate temporal aliasing errors. A ΔM-shift, i.e., a shift in the orbital mean anomaly, does not change the orbital plane, meaning that the RAAN shift between the two formations is $\Delta\Omega$=0. In the case of Wiese (2011), the author analysed simulation results made at various $\Delta\Omega$-shifts. He claimed an overall better performance for satellite missions with $\Delta\Omega = 180° + \epsilon$, where ϵ is a small increment which interleaves the ground-tracks of the second pair in-between the ones of the first pair. Also in this situation, both satellite formations are nearly co-planar.

The definitions of spatial and temporal resolution used in the Heisenberg rule, are based on the properties of the repeat orbits. In the context of satellite gravimetry, we are concerned not with repeat orbits, but with gravity field determination. Therefore, to quantify the spatio-temporal resolution of a mission, one must find the link between the orbits and the gravity field solution. This link has been established in Colombo (1983), one of the fundamental works in the field of satellite gravimetry. In that work, the author was concerned with the problem of efficiently solving a system of linear equations relating residual inter-satellite velocities and gravity field parameters. At the time, solving a large system of equations was a serious task, and much of the work done by Colombo was in designing the type of orbits which cause a sparse normal matrix with a block-diagonal structure. The inversion of such normal matrices is greatly simplified, which allowed for the calculation of a solution in a reasonable amount of time.

[1] for a repeat orbit, β is the number of revolutions while α is the number of nodal days, see also Sect. 2.2.2

Colombo (1983) assumed that the two ll-SST satellites are placed in circular polar orbits and that a gravity field solution is computed up to degree and order $N_{\max}$ on the basis of N_d days of data. One of the fundamental contributions made by Colombo was the relation $N_r > N_{\max}$ between the number of orbital revolutions of the repeat orbit N_r and the maximum degree of the spherical harmonic solution. A few years later, Schrama (1990) showed that the block-diagonal structure is obtained as long as all lumped coefficients overlapping at the same frequencies can be avoided. This was shown to require the number of satellite revolutions N_r to be larger than $2N_{\max}$. This inequality is what is nowadays referred to as the *Colombo-Nyquist rule*.

Together, the Heisenberg and the Colombo-Nyquist rules are commonly used to discuss the temporal and spatial resolutions of satellite missions, e.g., in Wiese (2011) and Iran Pour et al. (2013). However, it should be clear that these rules, while certainly valid, must be regarded with care when designing satellite gravimetry missions. Firstly, the definitions of temporal and spatial aliasing as stated in the Heisenberg rule are arbitrary. The authors themselves hint at the fact that they represent "worst-case numbers", and that in reality, the spatio-temporal constant might be better than what is predicted by the rule.

Furthermore, the temporal resolution, as defined in the Heisenberg rule, is translated into an equivalent gravity field temporal resolution through the Colombo-Nyquist rule. Because of the way Colombo decided to parametrize the gravity field, which I refer as the *standard parametrization*, the temporal resolution of the solution becomes N_d days, i.e., the length of the dataset used to compute a single set of spherical harmonic coefficients. However, this value by no means reflects the potentially achievable temporal resolution of the mission; this limit is simply imposed by the choice of parametrization. A different choice of parametrization is likely to result in significant improvements in terms of temporal resolution. One such example of an alternative parametrization is documented in Wiese (2011, Chap. 4), where the author investigated the possibility of co-estimating, alongside a full monthly gravity field solution, low-degree coefficients over daily and two-day periods as an attempt to minimize the propagation of temporal aliasing errors into the monthly gravity field solutions. The authors show that, for a Bender-type mission, co-estimating a daily set of spherical harmonic coefficients up to degree and order 18 reduces the overall temporal aliasing errors in the mission by 33%. Further evidence of the effectiveness of this approach in the Bender formation is presented in Daras et al. (2017). Another example of alternative parametrization is found in Kurtenbach et al. (2009), where the authors employed a Kalman filter approach to estimate daily gravity field solutions complete up to degree and order 40.

While the discussion of alternative parameterizations is of potential interest for gravity field modelling, further discussion of this topic is outside of the scope of this thesis. The focus of this thesis is on the performance of future satellite mission using the standard parametrization, i.e., , where a single set of spherical harmonic coefficients complete up to degree and order $N_{\max}$ is obtained from observations made over a period of N_d days.

The Colombo-Nyquist rule has been developed for the efficient inversion of the

normal matrix. Over the 35 years since Colombo published his work, computing power has grown dramatically. Many of the assumptions that allowed Colombo to compute a gravity field solution in limited time are, nowadays, no longer a requirement. In Visser et al. (2012) the authors revisit the Colombo-Nyquist rule. The authors show that, indeed, the quality of the gravity field solution is homogeneous only up to maximum degree $N_{\max} < N_r/2$ as originally stated. More importantly, the authors show that the *maximum resolvable degree* is actually equal to $N_{\max} = kN_r + 1$, where k is 1, 2 or even 3 depending on the combination of observations used. Furthermore, in Weigelt et al. (2013), the authors show that this rule applies only to the order, not to the degree.

This result is remarkable. It adds a new dimension to the problem of satellite gravimetry. It tells us that, by combining different observations, the achievable spatial resolution may be doubled or even tripled. At first, this might seem irrelevant; after all, noise in the observations prevents us from increasing the maximum spherical harmonic degree by a factor of three in comparison to what is already possible with e.g., GRACE. However, taking into account the Heisenberg rule, one realizes that this increase in spatial resolution can be traded by temporal resolution, i.e., by combining additional observations, one could potentially solve up to the same maximum degree (allowed by the noise in the data) in a third of the time. This remarkable result is yet to be applied to the design of future satellite missions. This means that conclusions drawn by previous studies might be sub-optimal considering that this new result has not been taken into account. The application of the modified Colombo rule to future satellite concepts is one of the pillars of this thesis and is tackled in Chapter 8.

The modified Colombo-Nyquist rule has already prompted a new investigation in terms of so-called *sub-Nyquist* gravity field recoveries (Iran Pour et al., 2013). In that publication, the authors relied on the fact that it is possible to solve a gravity field solution up to a higher degree than predicted by the original Colombo rule. They investigated what are the mission parameters that have the largest impact on the quality of these sub-Nyquist solutions. The authors concluded that the repeat orbits which avoid large unobserved gaps in their ground-track evolution pattern show the best performance. The concept of sub-cycle, also introduced in this publication, has been later researched in some detail of which the latest examples are Iran-Pour et al. (2018) and Purkhauser et al. (2020).

The two rules discussed so far are useful in the design of satellite mission due to their simplicity. This simplicity however means that many important details that determine the real spatial resolution of the mission are left out, such as the actual geometry of the orbits and the signal-to-noise ratio of the observations.

Regarding the geometry, important aspects are the existence of polar gaps and the distribution of observations. The Colombo-Nyquist rule is stated for (near-)polar, circular orbits and it formalizes the notion that a sufficiently dense global coverage with observations is required to solve for a set of spherical harmonic coefficients up to a specified degree and order. New mission concepts, like the Bender mission, propose satellite orbits with significant inclinations. Non-polar orbits result in a circular region around the poles where no observations are available. Regarding

the distribution of observations, polar orbits are not ideal either; they do not have the most homogeneous distribution of measurements over the latitudes, since all ground-tracks converge to the poles, increasing the density of observations in the polar areas (Iran Pour et al., 2013).

The geometry of the orbits, despite being crucial to the performance of the satellite gravimetry mission, is not the only factor that limits the spatio-temporal resolution of a gravity field solution. The other factor that determines the achievable spatial resolution is the signal-to-noise ratio of the observations. In essence, computing a gravity field solution relies on isolating in the observations all the frequencies that correspond to each spherical harmonic coefficient (Schrama, 1990). This is always guaranteed, as long as the observations are distributed densely enough. However, if at any of these frequencies, the noise in the observations is larger than the signal, the estimated coefficients will simply contain noise. In the case of GRACE, while the geometry of the observations allows for high-degree solutions, the signal-to-noise ratio of a large chunk of near-sectorial coefficients is too low. This is the mechanism through which striations appear in the GRACE solutions. This highlights the fact that the spatial resolution of a mission *is not* the maximum degree of the spherical harmonic solution computed from its data. Here lies the connection between errors in data from existing ll-SST missions, as discussed in Section 2.4, and the performance of future mission concepts. One cannot evaluate the performance of future missions without adequate knowledge of the errors in the data, since these limit the achievable spatio-temporal resolution.

There are three main conclusions from this discussion, which will be further addressed in Chapter 8:

- Not only the equatorial ground-track spacing, but the complete geometry of the orbits as well as the orientation and the combination of the observations are crucial aspects that ultimately determine the performance of the mission.
- The trade-off between spatial and temporal *resolution* in the orbital domain does not directly translate into a trade-off in terms of spatial- and temporal *aliasing errors*. The performance of a mission depends (among other errors) on the latter and not on the former.
- Due to the complex interaction between orbits, observations and noise, the only way to evaluate the performance of future satellite missions is to properly simulate the impact of all these factors, including their interactions.

2.8. Summary

In this Chapter, I have provided background information required to understand the bulk of this thesis. In Section 2.1, I have given an overview of the framework of tools which are commonly used to evaluate the performance of satellite gravimetry missions. Then, in Section 2.2, I have introduced the concepts of satellite orbits, orbital elements, repeat orbit design and stable satellite formations.

Following with Section 2.3, I have given an overview of the past and present satellite gravimetry missions with an emphasis on the GRACE mission. I have dis-

cussed the success of GRACE and highlighted its limitations. These limitations are partly caused by errors in the observations. In Sections 2.4 and 2.5, I reviewed the literature that deals with errors in the GRACE mission, taking into account both errors in the satellites' instruments and errors in the background models. I have pointed out that previous publications have not fully taken into account the propagation of errors through the reference orbits. I also concluded that nowadays, even after the end of the GRACE mission, we still cannot fully explain the errors in the observations. Full understanding of the GRACE error budget is required to reliably predict the performance of future ll-SST missions. In Section 6, I will complete the error budget of GRACE.

Section 2.6 deals with the research regarding future mission concepts. First, I have discussed single-formation missions and then missions consisting of multiple formations. The literature shows that along-track formations suffer from anisotropic sensitivity and that the alternative elementary formations are likely to perform better. Several authors also argue that, due to the limitations of exiting ranging technology, despite their increased performance, cartwheel and pendulum formations with large tilt angles are difficult to implement.

Multi-formation missions concepts are aimed at improving the spatio-temporal resolution, as compared to that of a single-formation one. An example of this is the Bender concept, which was reported by several publications as a good candidate for a future satellite mission. An additional benefit of the Bender mission is the inclusion of observations in another direction, which effectively reduces the anisotropy compared to the along-track formation.

Then, in Section 2.7, I have presented the fundamental framework that is used to predict the temporal and spatial resolution of a given mission concept. I have argued that the Heisenberg and the Colombo-Nyquist rules are too simplistic to serve as the basis for the design of future missions. An important insight of this literature study is that the performance of future missions depends on the complex interaction between orbits, observations and noise. These interactions can only be properly evaluated with adequately complex simulations. In Chapter 8, I will present a performance comparison of different future satellite formation concepts.

3

Indirect effect of force model perturbations in ll-SST observations

At least five approaches to estimate a gravity field solution from ll-SST data have been developed to this date; they are the *energy balance approach* (Gerlach et al., 2003; Han, 2004; Jekeli, 1999), the *variational equations approach* (Beutler et al., 2010; Jäggi et al., 2010; Prange et al., 2008; Reigber, 1989; Reigber et al., 2002, 2003; B. Tapley et al., 2005), the *short-arc approach* (Mayer-Gürr, 2006; Mayer-Gürr et al., 2005, 2010), the *point-wise acceleration approach* (Reubelt et al., 2003, 2006) and the *average acceleration approach* (Ditmar et al., 2004, 2006; Liu, 2008; Liu et al., 2010). Encarnação, 2015, Chap. 2.5 provides a comprehensive discussion of the advantages and disadvantages of each approach.

The two latter approaches share similarities in that they link the satellites' acceleration vector to the gradient of the gravitational potential through Newton 2nd law of motion (Ditmar et al., 2004). They differ in the way in which the satellite acceleration is obtained from ll-SST data. In this thesis I use the average acceleration approach (Liu, 2008).

In real data processing of ll-SST data with the average acceleration approach, residual range combinations (RRC) are the observations used for the computations of a gravity field solution. The RRC is obtained from the differences between the ranges measured by the satellites and the ranges computed from purely dynamic orbits (PDO). PDOs are computed solely from an initial state vector and a force model. The initial state vector is a set of 6 parameters describing the initial position and velocity of the satellite. The force model accounts for all the forces acting on the satellite. The PDO is then computed by numerical integration of the laws of motion. In this thesis, all PDOs are computed with the PANDA software (Zhao, 2004).

The background force model is intended to account for all the forces acting on the satellite, to the best of possible extent, in order to isolate the signal of interest. The force model is used to compute reference quantities and it is precisely from the residuals between the reference and observed quantities that the signal of interest is estimated. Similarly to the signal, any errors in the force model also propagate into the RRC observable by means of the computed quantities and later into the computed gravity fields. It is important to fully understand the mechanism of how these errors propagate into the observations because these errors play an important role in the quality of the recovered gravity field solutions.

A perturbation in the force model will manifest itself in two different ways in the RRC. The perturbation at a particular geographic location directly propagates into the computed inter-satellite acceleration affecting the RRC in the vicinity of observation points. This is a very *local* propagation mechanism which I refer to as *direct effect*. Besides that, the very same perturbation will additionally cause the computed orbits to deviate from the true ones. This happens because computed orbits are obtained in a numerical integration procedure of the laws of motion. Due to the nature of this procedure, even relatively small perturbations, grow over time as random-walk noise in the computed orbits. In this manner, errors propagate not only locally, but also far beyond the region of the perturbation. I refer to this as the *indirect effect*.

At this point, it is necessary to clarify why the indirect effect is important. Notice that the unknown gravity field (i.e., the signal of interest) is nothing more than a perturbation to the force model used to compute the reference orbits. The functional model of the average acceleration approach i.e., Newton's 2nd law, only applies to the direct effect component of the RRC observations. The indirect effect is a signal distortion which maps into the solutions as noise, even though it is caused by the signal of interest. This distortion is a poorly understood error source with an unknown impact on the quality of the solutions.

The indirect effect is not likely to be limited to the average acceleration approach. It emerges in the computation of reference quantities from PDOs. It is likely to play a role and similarly have an unknown impact in the gravity field solution of any inversion approach which requires the computation of PDOs.

In this chapter, I will formally define the indirect effect and its constituents, and will provide a meaningful example that illustrates it.

3.1. Average inter-satellite accelerations

According to Newton's 2nd law, the instantaneous acceleration $\mathbf{a}_i \equiv \begin{bmatrix} a_x & a_y & a_z \end{bmatrix}^T$ experienced by a satellite S at time instant i caused by gravitational potential V can be computed as

$$\mathbf{a}_{s,i} = \nabla V|_{\mathbf{r}_i^s}, \tag{3.1}$$

i.e., it is the gradient of the potential field V evaluated at the satellite position $\mathbf{r}$. The instantaneous inter-satellite acceleration $\Delta\mathbf{a}$ between a pair of satellites A and

B directly follows:

$$\Delta \mathbf{a}_i = \nabla V|_{\mathbf{r}_i^a} - \nabla V|_{\mathbf{r}_i^b} \quad . \tag{3.2}$$

Average accelerations $\Delta\bar{\mathbf{a}}$ can be derived by applying the so-called averaging filter $\mathbf{f} \equiv \begin{bmatrix} f_{-N} & \dots & f_0 & \dots & f_N \end{bmatrix}^T$ to a set of 2N+1 consecutive acceleration measurements centred around time instant i (Ditmar et al., 2004),

$$\Delta\bar{\mathbf{a}}_i = \begin{bmatrix} \Delta\mathbf{a}_{i-N} & \dots & \Delta\mathbf{a}_i & \dots & \Delta\mathbf{a}_{i+N} \end{bmatrix} \cdot \mathbf{f} \quad . \tag{3.3}$$

Taking the projection onto the satellites line-of-sight (LOS) and expanding Eq. (3.2) yields

$$\Delta\bar{a}_{i,\mathrm{LOS}} = \mathbf{e}_i^T \cdot \begin{bmatrix} \nabla V|_{\mathbf{r}_{i-N}^a} - \nabla V|_{\mathbf{r}_{i-N}^b} & \dots & \nabla V|_{\mathbf{r}_{i+N}^a} - \nabla V|_{\mathbf{r}_{i+N}^b} \end{bmatrix} \cdot \mathbf{f} \quad , \tag{3.4}$$

where $\mathbf{e}_i \equiv \begin{bmatrix} e_x & e_y & e_z \end{bmatrix}^T$ is the instantaneous LOS unit vector.

Eq. (3.4) directly relates a gravitational potential with the average inter-satellite acceleration caused by it. Importantly, a computation of the latter requires knowledge of both the potential and the satellite orbit, which are not known exactly during real data processing. In real data processing, RRCs are the observations used.

3.2. Residual Range Combinations

The RRC methodology is based on the 3-point range combinations (3RC) (Liu, 2008). This methodology has been applied in the production of the Delft Mass Transport (DMT) monthly gravity field solutions from GRACE data. This approach aims at recovering the perturbing gravity field from the ll-SST data converted into average inter-satellite accelerations $\bar{\ddot{\rho}}$. The latter are computed as (Liu, 2008, eq. 5.34)

$$\bar{\ddot{\rho}}_i \equiv \mathbf{e}_i^T \cdot \bar{\ddot{\mathbf{r}}}_{12,i} = \frac{\xi_i^- \cdot \rho_{i-1} - 2\rho_i + \xi_i^+ \cdot \rho_{i+1}}{\Delta t^2} \quad , \tag{3.5}$$

with

$$\xi_i^{\pm} \equiv \mathbf{e}_i^T \cdot \mathbf{e}_{i\pm1} \quad , \tag{3.6}$$

$$\rho \equiv \| \mathbf{r}_{12} \| \quad , \tag{3.7}$$

$$\mathbf{r}_{12} \equiv \mathbf{r}_2 - \mathbf{r}_1, \tag{3.8}$$

where

- $\bar{\ddot{\rho}}$ – is the range combination
- ρ_i – is an inter-satellite range at time instant i
- $\mathbf{e}_i$ – is the inter-satellite unit vector at time instant i.

The 3RC is computed on the basis of the ranging measurements and is equal to the projection onto the line-of-sight at the central epoch of a 3-point double numerical differentiation (Liu, 2008). As a consequence, in the absence of non-conservative forces acting on the satellites, the 3RC is also equal to the projection

onto the line-of-sigth at the central epoch of the average inter-satellite acceleration caused by the gravity field (Ditmar et al., 2004). This is the link which allows for the calculation of the DMT monthly gravity field solutions from GRACE ll-SST data.

In order to recover the *perturbing* gravity field from ll-SST data, the residual form of the 3RC functional model, the *residual range combinations* $\delta\bar{\rho}$ (Liu, 2008, eq. 5.35), are used as observations.

There are two equivalent ways of computing RRCs, both of which rely on reference orbits computed on the basis of the a-priori gravitational field. RRCs can be computed as the difference between the 3RC and the average inter-satellite accelerations yielded during reference orbit computation. Alternatively, RRCs can also be obtained by applying Eq. 3.5 to the residual inter-satellite ranges $\delta\rho$,

$$\delta\ddot{\bar{\rho}}_i = \frac{\xi^-_{i,c}\cdot\delta\rho_{i-1} - 2\delta\rho_i + \xi^+_{i,c}\cdot\delta\rho_{i+1}}{\Delta t^2} \quad , \tag{3.9}$$

where

$$\delta\rho_i \equiv \rho_i - \rho_{i,c} \quad . \tag{3.10}$$

The residual inter-satellite range $\delta\rho$ is the deviation of the measured range ρ from the computed reference range ρ_c. The computed reference ranges ρ_c, along with the LOS unit vectors $\mathbf{e}_c$, are computed quantities derived from the reference orbits.

3.3. Indirect effect and its constituents

Let us first setup a formalism to properly define the concept of indirect effect. Let V be the a-priori reference potential field and T a perturbation to it, such that the true potential field is $V+T$. Consider a pair of satellites in a ll-SST mission orbiting in the $V+T$ potential and having orbits $\mathbf{r}_{V+T,a}$ and $\mathbf{r}_{V+T,b}$. Because the true potential field and the true satellite orbits are unknown, PDOs are computed on the basis of V yielding reference orbits $\mathbf{r}_{V,a}$ and $\mathbf{r}_{V,b}$.

In this scenario, the total acceleration of satellite A is, according to Eq.(3.2),

$$\mathbf{a}_i = \nabla(V+T)\big|_{\mathbf{r}^a_{V+T,i}} , \tag{3.11}$$

while, the residual acceleration $\delta\mathbf{a}$ caused by the residual field T is similarly given by,

$$\delta\mathbf{a}_i = \nabla T|_{\mathbf{r}^a_{V+T,i}} . \tag{3.12}$$

Therefore the projection of the residual average inter-satellite acceleration $\Delta\delta\bar{a}_{i,\mathrm{LOS}}$ caused by the perturbing field T along the true satellite orbits is defined by Eq. (3.4) provided that V is replaced with T.

$$\Delta\delta\bar{a}_{i,\mathrm{LOS}} = \mathbf{e}^T_{V+T,i}\cdot\Big[\nabla T|_{\mathbf{r}^a_{V+T,i-N}} - \nabla T|_{\mathbf{r}^b_{V+T,i-N}} \cdots \nabla T|_{\mathbf{r}^a_{V+T,i+N}} - \nabla T|_{\mathbf{r}^b_{V+T,i+N}}\Big]\cdot\mathbf{f} \tag{3.13}$$

Let ρ be the inter-satellite range, $\mathbf{e}$ be the unit vector along the LOS of the satellites and $\mathbf{m}$ the mid-point between the two satellites. The absolute position of either satellite is easily obtained as

$$\mathbf{r} \equiv \mathbf{m} \pm \frac{\rho}{2}\mathbf{e}. \tag{3.14}$$

Using this relation, each of the terms $\mathbf{r}$ in Eq. (3.13) can be expanded in terms of these new quantities. In order to keep the nomenclature compact and to highlight the dependence on the relevant quantities T, $\mathbf{m}$, $\mathbf{e}$ and ρ, let ,

$$\begin{aligned} g_i(T)\left|\begin{matrix}\rho_{V+T}\\ \mathbf{e}_{V+T}\\ \mathbf{m}_{V+T}\end{matrix}\right. &\equiv \Delta\delta\bar{a}_{i,\mathrm{LOS}} \\ &= \mathbf{e}^T_{V+T,i}\cdot\Big[\nabla T|_{\mathbf{m}_{V+T,i-N}-\frac{\rho_{i-N}}{2}\mathbf{e}_{V+T,i-N}} - \nabla T|_{\mathbf{m}_{V+T,i-N}+\frac{\rho_{i-N}}{2}\mathbf{e}_{V+T,i-N}} \cdots \\ &\qquad \nabla T|_{\mathbf{m}_{V+T,i+N}-\frac{\rho_{i+N}}{2}\mathbf{e}_{V+T,i+N}} - \nabla T|_{\mathbf{m}_{V+T,i+N}+\frac{\rho_{i+N}}{2}\mathbf{e}_{V+T,i+N}}\Big]\cdot\mathbf{f} \end{aligned} \tag{3.15}$$

Let us further think of the RRC as the operator h taking inter-satellite ranges and LOS unit vectors as input. The RRC as defined in Eq. (3.9) can then be rewritten as

$$\delta\ddot{\bar{\rho}}_i \equiv h_i\left|\begin{matrix}\delta\rho_V\\ \mathbf{e}_V\end{matrix}\right. = \frac{1}{\Delta t^2}\begin{bmatrix}\mathbf{e}^T_{V,i}\cdot\mathbf{e}_{V,i-1}\\ -2\\ \mathbf{e}^T_{V,i}\cdot\mathbf{e}_{V,i+1}\end{bmatrix}^T\cdot\begin{bmatrix}\delta\rho_{V,i-1}\\ \delta\rho_{V,i}\\ \delta\rho_{V,i+1}\end{bmatrix} \tag{3.16}$$

The RRC is linear in terms of inter-satellite ranges,

$$\delta\ddot{\bar{\rho}}_i = h_i\left|\begin{matrix}\rho_{V+T}\\ \mathbf{e}_V\end{matrix}\right. - h_i\left|\begin{matrix}\rho_V\\ \mathbf{e}_V\end{matrix}\right. \tag{3.17}$$

The problem with RRC produced with Eq. (3.17) is that it is evaluated over the reference LOS unit vector. The reference LOS unit vector is obtained from the PDOs which deviate from the true orbits. The RRC is computed in this way because, in real data processing, there is no better way to obtain the true LOS unit vectors. This fact underpins a deficiency in the RRC approach, which plays a role in the propagation of errors in ll-SST missions.

In realm of simulations, where the true LOS unit vectors are known, one can define a *simulated RRC*, $\delta\ddot{\bar{\rho}}^*$, which takes into account the disturbances caused by the unknown gravity field T not only in terms of the inter-satellite ranges, but also in terms of the LOS unit vectors $\mathbf{e}$. From this point on, let us drop the index i for simplicity. In this case, the simulated RRC is defined as,

$$\delta\ddot{\bar{\rho}}^* = h\left|\begin{matrix}\rho_{V+T}\\ \mathbf{e}_{V+T}\end{matrix}\right. - h\left|\begin{matrix}\rho_V\\ \mathbf{e}_V\end{matrix}\right. . \tag{3.18}$$

With this formalism, one can quantify the modelling error δp, i.e., the impact of not taking the changes in terms of LOS unit-vectors into account,

$$\delta p \equiv \delta\ddot{\bar{\rho}} - \delta\ddot{\bar{\rho}}^* = h\left|\begin{matrix}\rho_{V+T}\\ \mathbf{e}_V\end{matrix}\right. - h\left|\begin{matrix}\rho_{V+T}\\ \mathbf{e}_{V+T}\end{matrix}\right. . \tag{3.19}$$

Due to the equivalence between the 3RC and the projection onto the LoS of the average inter-satellite accelerations, Eq. (3.18) can be written as

$$\begin{aligned}\delta\bar{\ddot{\rho}}^{*} &= g(V+T)\begin{vmatrix}\rho_{V+T}\\ \mathbf{e}_{V+T}\\ \mathbf{m}_{V+T}\end{vmatrix} - g(V)\begin{vmatrix}\rho_{V}\\ \mathbf{e}_{V}\\ \mathbf{m}_{V}\end{vmatrix}\\ &= g(T)\begin{vmatrix}\rho_{V+T}\\ \mathbf{e}_{V+T}\\ \mathbf{m}_{V+T}\end{vmatrix} + g(V)\begin{vmatrix}\rho_{V+T}\\ \mathbf{e}_{V+T}\\ \mathbf{m}_{V+T}\end{vmatrix} - g(V)\begin{vmatrix}\rho_{V}\\ \mathbf{e}_{V}\\ \mathbf{m}_{V}\end{vmatrix} \quad . \end{aligned} \tag{3.20}$$

The first term in Eq. (3.20) is by definition the residual inter-satellite acceleration caused by the perturbing field T over the true orbits. This term is the so-called *direct effect*, which was previously empirically defined. Let this term be denoted as δd. The last two terms in Eq. (3.20) represent the *orbital effect*, i.e., the residual inter-satellite accelerations caused by evaluating the static field V at two different sets of orbits. Let this effect be denoted as δo.

Taking Eqs. (3.19),(3.20) into account, one can write

$$\delta\bar{\ddot{\rho}} = \delta d + \delta o + \delta p \tag{3.21}$$

with

$$\begin{aligned}\delta d &\equiv g(T)\begin{vmatrix}\rho_{V+T}\\ \mathbf{e}_{V+T}\\ \mathbf{m}_{V+T}\end{vmatrix}\\ \delta o &\equiv g(V)\begin{vmatrix}\rho_{V+T}\\ \mathbf{e}_{V+T}\\ \mathbf{m}_{V+T}\end{vmatrix} - g(V)\begin{vmatrix}\rho_{V}\\ \mathbf{e}_{V}\\ \mathbf{m}_{V}\end{vmatrix}\\ \delta p &\equiv h\begin{vmatrix}\rho_{V+T}\\ \mathbf{e}_{V}\end{vmatrix} - h\begin{vmatrix}\rho_{V+T}\\ \mathbf{e}_{V+T}\end{vmatrix} \quad . \end{aligned}$$

Eq. (3.21) shows that the RRC observation is constituted by the direct effect (δd), an orbital effect (δo) and a modelling effect (δp) components. The modelling and orbital effects are always errors and their sum is in fact the *indirect effect*. Regarding the δd component, whether it represents signal or noise depends on the nature of the perturbation T. If T is caused by e.g., a real mass anomaly on the surface of the Earth, then δd represents the signal of interest. On the other hand, if T represents an error in the AOD model, then δd is an error.

The orbital effect component can further be divided in three components,

$$\begin{aligned}\delta o \equiv g(V)\begin{vmatrix}\rho_{V+T}\\ \mathbf{e}_{V+T}\\ \mathbf{m}_{V+T}\end{vmatrix} - g(V)\begin{vmatrix}\rho_{V}\\ \mathbf{e}_{V}\\ \mathbf{m}_{V}\end{vmatrix} &\approx \left(g(V)\begin{vmatrix}\rho_{V+T}\\ \mathbf{e}_{V}\\ \mathbf{m}_{V}\end{vmatrix} - g(V)\begin{vmatrix}\rho_{V}\\ \mathbf{e}_{V}\\ \mathbf{m}_{V}\end{vmatrix}\right)\\ + \left(g(V)\begin{vmatrix}\rho_{V}\\ \mathbf{e}_{V+T}\\ \mathbf{m}_{V}\end{vmatrix} - g(V)\begin{vmatrix}\rho_{V}\\ \mathbf{e}_{V}\\ \mathbf{m}_{V}\end{vmatrix}\right) &+ \left(g(V)\begin{vmatrix}\rho_{V}\\ \mathbf{e}_{V}\\ \mathbf{m}_{V+T}\end{vmatrix} - g(V)\begin{vmatrix}\rho_{V}\\ \mathbf{e}_{V}\\ \mathbf{m}_{V}\end{vmatrix}\right) \quad . \end{aligned} \tag{3.22}$$

I denote these three terms as geometric ($\delta\rho$), orientation (δe) and mid-point effects (δm). They correspond to the residual inter-satellite accelerations caused by evaluating the a-priori gravity field at two sets of orbits which differ only in their ranges, LOS direction and mid-points, respectively.

It is worth pointing out that the geometric effect ($\delta\rho$) can be computed and corrected for during ll-SST data processing. This only requires the true inter-satellite ranges, which are accurately observed by the ranging instrument. The modelling, orientation and mid-point effects cannot be corrected for in real data processing because that requires knowledge of the true orbits of the satellites.

Finally, numerical integration errors δn are one additional error source, which appears in the RRC observations arising from the computation of the PDOs. For completeness, Eq. (3.21) can be expanded then into

$$\delta\bar{\rho} = \delta d + \delta\rho + \delta e + \delta m + \delta p + \delta n. \tag{3.23}$$

The present analysis continues the previous work presented in Ditmar et al., 2012 and Encarnação (2015). The authors treated correction, orientation and position noise as stochastic phenomena. Having understood the general physics of how these errors propagate into the observations, real GRACE data was used to estimate the expected magnitude of each and to extrapolate them onto future satellite missions.

The content of this chapter improves on previous work by adopting a deterministic propagation of orbital perturbations into observation noise. Given a specific perturbation T, e.g., in the form of a spherical harmonics model, Eqs. (3.19) and (3.22) exactly predict the corresponding errors in terms of RRC observations independently of the considered satellite formation. Unfortunately, there is no one-to-one correspondence between the terminology adopted in the present study and the one in Encarnação, 2015. Previous ”orientation noise” corresponds here to ”modelling effect”; previously termed ”correction noise” is here referred to as ”orientation effect”, while previous ”positioning noise” comprises both ”geometric effects” and ”mid-point effects”.

3.4. Indirect effect: Along-Track

In order to illustrate the importance of the indirect effect, a simulation was performed. The objective of this exercise is to illustrate the indirect effect and its constituents, and to compare them to the signal of interest. The idea is to introduce a Dirac-like type of perturbation and visualize how each of the elementary satellite formation responds. A 1000 Gt mass anomaly is introduced over the Pacific Ocean. The mass anomaly was defined over an equiangular grid and thereafter converted into a SH representation up to SH deg 120. I modelled the mass anomaly as Gaussian bell shape in the spatial domain with an adequately small radius in order to minimize the ringing effecs in the SH domain. The static gravity field is defined as the DGM-1s model, which is complete up to degree and order 250.

Three quantities are computed and plotted: RRCs, the direct effect and the indirect effect. The RRCs are computed following the procedure used to handle

real data by applying Eq. (3.9). It requires the inter-satellite ranges and LOS unit vectors of the reference orbits, i.e., the orbits computed with on the basis of the unperturbed DGM-1s gravity field. Additionally, *observed* inter-satellite ranges are required. These are derived from the true satellite orbits, which are computed in a consistent manner on the basis of the sum of DGM-1s model and the considered mass anomaly.

The direct effect is computed by directly applying Eq. (3.4). The mass anomaly and the true satellite orbits are used as input. The indirect effect is simply the difference between the RRCs and the direct effect.

An along-track satellite formation is considered, at an altitude of 272 km and an inter-satellite distance of 200 km. The altitude was chosen in order to yield a 24-day repeat period orbit. These will cover the Earth with homogeneously distributed observations with sufficient density to compute solutions up to SH 120, the maximum degree of the SH representation of the mass anomaly.

In Figure 3.1, in the left panel, inter-satellite accelerations for one orbital arc are shown. The green line denotes the direct effect of the considered perturbation over the satellites reference orbits. One can see a distinctively large negative peak around 16 h and two very small similar peaks at roughly 14.5 h and 17.5 h. These features correspond to three moments in which the satellites' ground-tracks come into the vicinity of the introduced perturbation, the closest one being responsible for the largest peak. The right panel of Figure 3.1 presents a zoom-in on the largest acceleration peak. It reveals the shape of the inter-satellite acceleration caused by the considered gravity field perturbation.

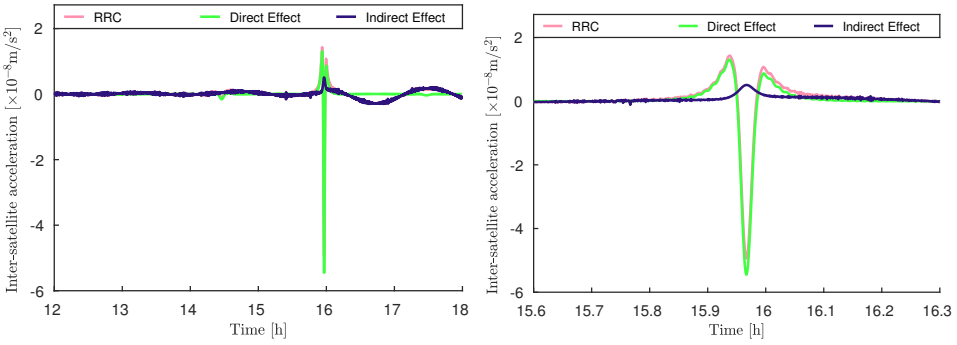

Figure 3.1: Inter-satellite accelerations for the Along-Track formation caused by a localized mass anomaly in terms of direct effect (in green), total effect (in pink) and indirect effect (in blue). These are shown in the left panel for the duration of one arc. The right panel presents a zoom-in on the largest acceleration peak.

In both panels, the residual inter-satellite accelerations computed on the basis of the RRC are depicted in pink. The RRC matches the direct effect up to the first peak at 14.5 h. After this point, the RRC begins to oscillate away from the direct effect. The oscillation becomes larger after the largest perturbing peak at 16 h. In the right panel of Figure 3.1, one can see that the peak magnitude of RRC is smaller than that of the direct effect. The introduced mass anomalies are reflected in the

collected RRC data along with two types of distortions: low-frequency oscillations and a dampening of the peaks.

Figure 3.2 presents the corresponding PSD$^{\frac{1}{2}}$ of the RRC, direct and indirect effects. One can see that most of energy of the direct effect is in the frequency band between 1 and 10 mHz. The RRC however exhibits most of the energy in the very-low frequencies: below 0.1 mHz. This is the frequency range in which the satellites' orbits react to the introduced perturbation far beyond the vicinity of the perturbing mass.

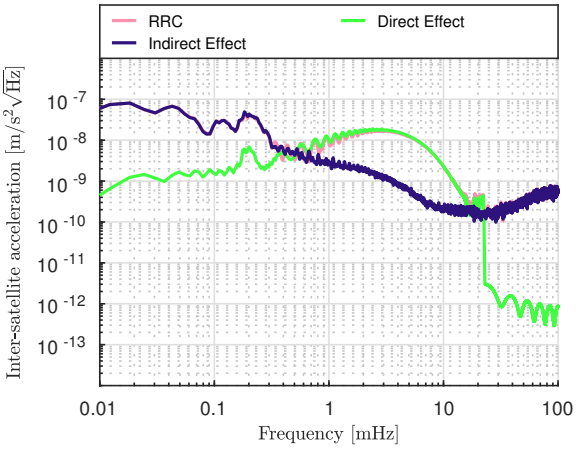

Figure 3.2: Breakdown of the RRC into direct and indirect effects in terms of PSD$^{\frac{1}{2}}$ of inter-satellite accelerations of the along-track formation.

In Section 3.3, it was shown that the indirect effect can be split into modelling and orbital effects. These are shown in the left panel of Figure 3.3, in the frequency domain. It becomes clear that the orbital effect is predominant in the low-frequency range, below 0.1 mHz. The ascending tail shown in the high-frequency part of the spectrum of the modelling effect is attributed to numerical integration noise generated in the orbit computation. Numerical integration noise has been kept at a minimum level by using the orbit computation software with quadruple precision. As a consequence, numerical noise is only visible above 20 mHz, with a magnitude well below other error sources considered in this thesis. Figure 3.4 shows the modelling and orbital effects in the time domain, for the duration of one orbital arc and zooming in on the observed peak, in the left and right plots, respectively.

In Section 3.3, I have also shown that the orbital effect can be decomposed in three components. Though it is possible to correct for the geometric effect in real data processing of ll-SST data it is worth investigating how strong this component is. In the right panel of Figure 3.3, the three orbital effect components are depicted in the frequency domain. The geometric component dominates the orbital effect and correcting for it will reduce the indirect effect in the low- to medium-frequency bands.

Apart from the indirect effect errors in terms of inter-satellite accelerations, it is also interesting to see how those errors propagate into gravity field solutions. It is important to notice however, that the results of such analysis depend on the

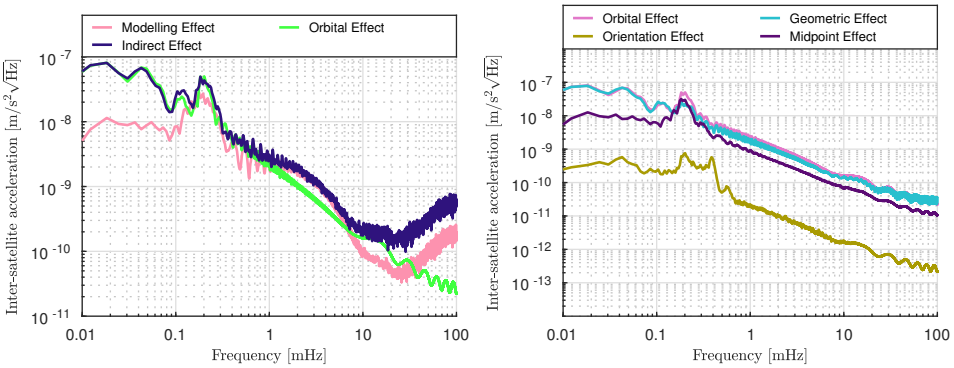

Figure 3.3: PSD$^{\frac{1}{2}}$ of inter-satellite accelerations for the along-track formation caused by a localized mass anomaly. In the left panel a breakdown of the indirect effect into orbital and modelling effects. In the right panel, a break down of the orbital effect into geometric, orientation and midpoint components.

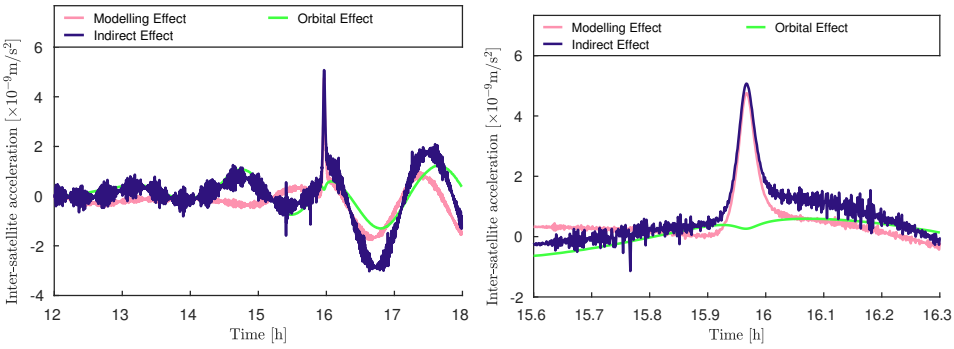

Figure 3.4: Inter-satellite accelerations for the along-track formation caused by a localized mass anomaly in terms of modelling and orbital effects. These are shown in the left panel for the duration of one arc. The right panel presents a zoom-in on the largest acceleration peak.

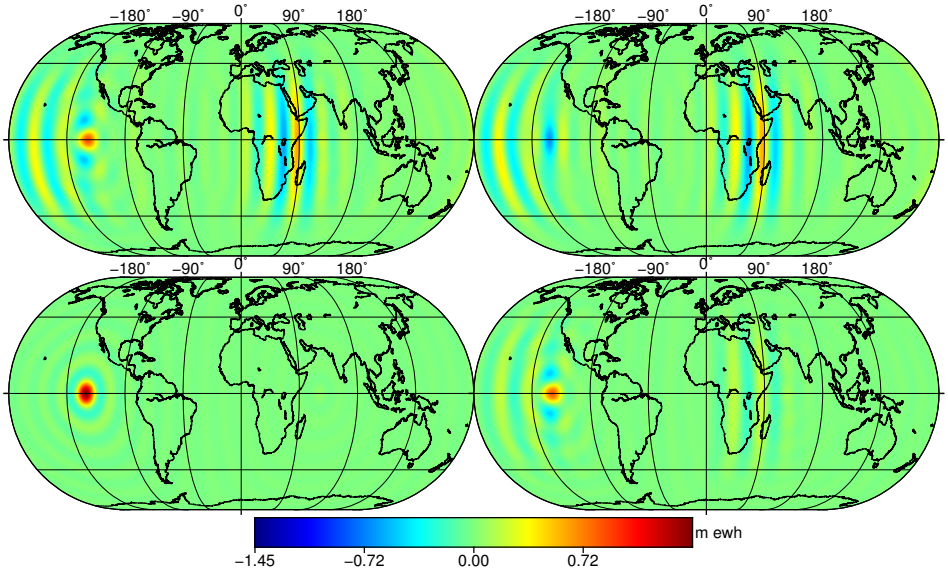

Figure 3.5: Gravity field solutions recovered with the average acceleration approach for the along-track type of mission. On the top-left, the solution computed from the RRC data; on the bottom-left the direct effect; the difference between the two is the indirect effect which is plotted on the top-right panel; in the bottom-right panel the solution computed from the RRC data after applying the geometric correction.

considered gravity field recovery approach. Therefore, the following results are valid in the context of the average acceleration approach.

After comparing maps of gravity field solutions from several simulations, it became clear that, for visualization purposes, a better illustration of indirect effect errors is obtained when the SH expansion of the introduced mass anomaly is limited to a relatively low SH degree. This is because, when solving to large SH degrees, indirect effect errors manifest as very narrow spatial features, oriented in the North-South direction, with large magnitudes, which are hard to visualize and interpret. Therefore, in order to better visualize indirect effect errors in terms of gravity field solutions, the input perturbation and recovered solutions have been limited to maximum SH degree 24.

The resulting fields are shown in Figure 3.5; the top-left panel depicts the recovered gravity field on the basis of the RRC data, while the bottom-left panel shows the direct effect field. The output direct effect field is equal to the input mass anomaly disturbance up to numerical precision. One can see that the RRC solution is able to capture the perturbing mass anomaly, however there are significant striations in the computed solution. The recovered perturbation is also lower in magnitude than the original perturbation, which is consistent with the observations made in the time-domain plots.

The difference between the top-left (RRC solution) and bottom-left (direct effect solution) plots is the indirect effect, as shown in the top-right plot. Here we see

that the indirect effect manifests itself as a vertical striping pattern superimposed on the perturbing gravity field.

Finally, the bottom-right plot shows the solution computed on the basis of the RRC data after the geometric correction has been applied. The geometric correction succeeds at partially removing the striping pattern, although significant differences still remain compared to the direct effect field.

Having illustrated the propagation of indirect effect errors in ll-SST data for the along-track mission, I proceed with an investigation of how these errors propagate when considering pendulum and cartwheel-type formations.

3.5. Indirect effect: Cartwheel

A cartwheel pair of satellite was considered under similar conditions as previously: a circular polar 24-day repeat period orbit with a mean altitude of 272 km and a maximum inter-satellite distance of 200 km. As a consequence of the selected inter-satellite distance (chosen to be consistent with the other formations) the satellites' altitude oscillates between 222 km and 322 km. Figure 3.6 shows the breakdown of the RRC into direct and indirect effects for the cartwheel pair. One can see that the RRC is increasingly distorted by the localized mass anomaly. The distortion is very different from the one shown for the along-track formation due to the very different orbital dynamics of the inter-satellite baseline. The inter-satellite acceleration peaks caused by the mass anomaly are relatively small in comparison with the acceleration from the resulting orbital disturbances. The right panel shows a zoom-in on the largest acceleration peak caused by the localized mass anomaly.

The corresponding PSD$^{\frac{1}{2}}$ is shown in the left panel of Figure 3.7 also reveals significant differences between the two formations. The indirect effect is significantly larger than the direct effect between 0.1 and 2 mHz. Above 2 mHz and up to 11 mHz, both components have similar magnitude. The right panel of the same Figure shows the breakdown of the orbital effect, into its constituents. One can see that for the most part of the spectrum, the orientation effect is the largest contributor although the magnitude of the geometric effect is similar.

In Figure 3.8, the top-right panel shows that the indirect effect introduces a large number of features with a magnitude larger than the introduced perturbation. Furthermore, the bottom-right panel shows that, unlike the along-track formation, there is no significant improvement after applying the geometric correction to the RRC.

3.6. Indirect effect: Pendulum

Similarly to the previous sections, a pendulum pair of satellites was considered in a circular polar 24-day repeat period orbit with an altitude of 272 km and a maximum inter-satellite distance of 200 km. In the pendulum configuration, the inter-satellite distance cycles between the minimum at the poles, where the two satellites come in close proximity, and the maximum over the over the equator, where the two satellites are the furthest apart. In Figure 3.9, the RRC is shown in the time-domain for the pendulum formation. The gaps in the RRC data correspond to the regions

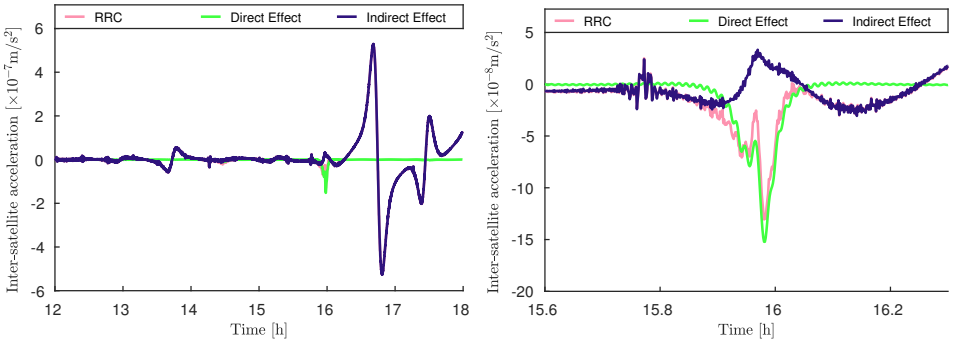

Figure 3.6: Illustration of the indirect effect caused by the considered mass anomaly for a cartwheel type of mission. These are shown in the left panel for the duration of one arc. The right panel presents a zoom-in on the largest acceleration peak. Notice how the mass anomaly shakes the satellites' orbits introducing relatively large inter-satellite acceleration signal in the low-frequency part of the spectrum, whose magnitude grows over time.

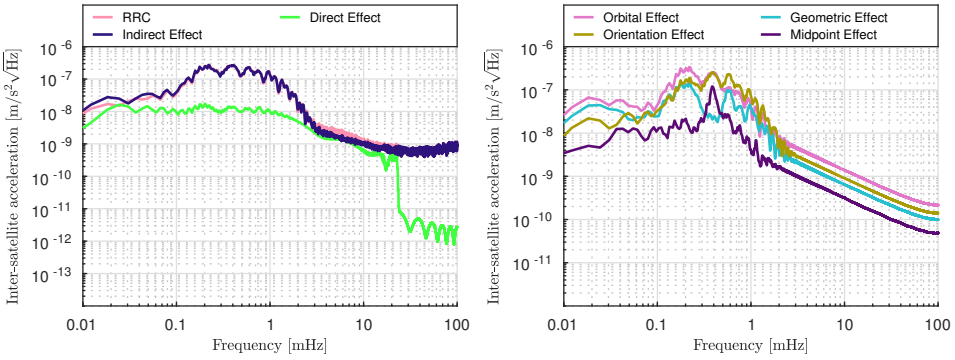

Figure 3.7: PSD$^{\frac{1}{2}}$ of inter-satellite accelerations of the cartwheel formation. In the left panel, breakdown of the RRC into direct and indirect effects. The right panel shows the breakdown of the orbital effect into its components.

where the two satellite orbits cross over, such that the inter-satellite distance shrinks to (nearly) zero. These outliers are removed at the pre-processing stage. Notice how the indirect effect errors are modulated by the orbital dynamics of the inter-satellite baseline of the pendulum formation. The first small peak at 13 h introduces low-frequency oscillations in the RRC observations, which are increasingly magnified after the following sharp perturbations at 15 and 16.5 h. A zoom-in on the largest acceleration peak is shown in the right panel.

The PSD$^{\frac{1}{2}}$ of the indirect effect is shown in the left panel of Figure 3.10. Up to 10 mHz indirect effect errors are, for the most part, smaller than the introduced mass anomaly depicted as direct effect. There is, however, a very clear resonance peak centered at 0.4 mHz (2cpr) where the indirect effect is larger than the direct effect. From 10 mHz onwards, indirect effect errors are dominant.

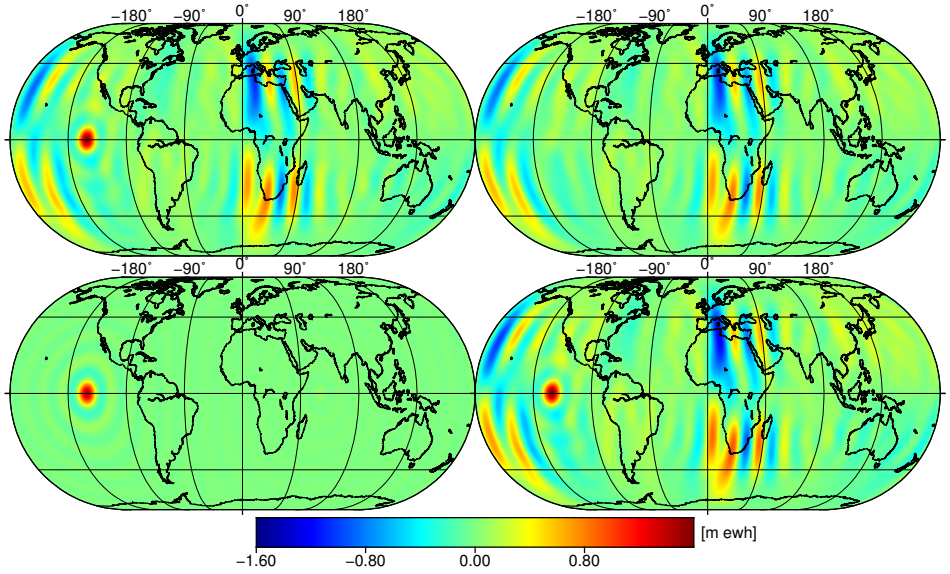

Figure 3.8: Gravity field solutions recovered with the average acceleration approach for the cartwheel type of mission. On the top-left, the solution computed from the RRC data; on the bottom-left the direct effect; the difference between the two is the indirect effect which is plotted on the top-right panel; in the bottom-right panel the solution computed from the RRC data after applying the geometric correction.

The right panel shows a breakdown of the orbital effect for the pendulum mission. The plot shows that the geometric effect is the dominant error source over the whole spectrum. Since the geometric effect can be corrected for, the remaining orbital effect will be the midpoint effect which is more than an order of magnitude smaller. This is unlike the previous two formations, where the geometric effect was found much closer in magnitude to other orbital components. Because of this, in the other formations, correcting for the geometric effect only yielded relatively small error reductions.

In terms of gravity field solutions, there are also significant differences compared to the along-track formation. The recovered fields are shown in Figure 3.11. A comparison between the RRC (top-left) and the direct effect solution (bottom-left) shows good agreement between the two. The difference between these is the indirect effect shown in the top-right. The indirect effect can be characterized as distortion mostly in large scale features. The bottom-right panel shows the recovered field from the RRC data after applying the geometric correction to the data. It shows that the geometric correction removes all of the indirect effect errors.

3.7. Discussion

The indirect effect shown in this chapter is a poorly understood source of error that arises in the processing of gravity data. One may argue that the indirect effect

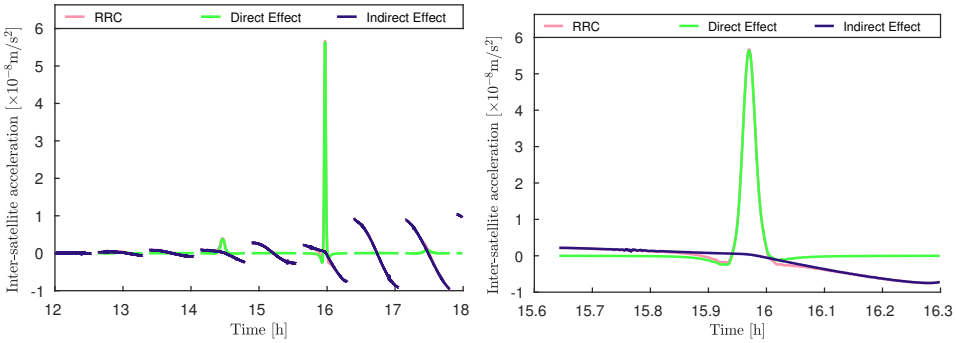

Figure 3.9: Illustration of the indirect effect caused by the considered mass anomaly for a pendulum type of mission. In the left panel, these are shown in the left panel for the duration of one arc. The right panel presents a zoom-in on the largest acceleration peak. The gaps in the data correspond to the periods where the satellite orbits cross over and the inter-satellite baseline shrinks to (nearly) zero. Notice how the mass anomaly affects the satellites orbits well beyond the geographical extent of the perturbation.

error is only relevant in the context of the average acceleration approach that I use to process ll-SST data. However, that is most likely not true. From a very general perspective, the indirect effect is a consequence of the increasing discrepancy over time between the real inter-satellite orbits and the computed ones. Any approach which relies on reference quantities derived from computed orbits are likely to be affected by indirect effect errors.

The present analysis shows that the considered elementary satellite formations are differently affected by indirect effect errors. Pendulum formations are only mildly affected and most of the distortions can be removed by applying the geometric correction to the RRC. Along-Track formations are more susceptible to indirect effect errors, which manifest themselves as vertical stripes in the solutions. Applying the geometric correction results in an overall improvement, although the resulting field still shows significant distortions. The cartwheel formation is the most sensitive to indirect effect errors. In that case, indirect effect errors manifest themselves as relatively large artifacts spread over the whole spatial domain. Furthermore, applying the geometric correction does not lead to noticeable improvements. The sensitivity of each formation to indirect effect errors shown in this chapter is consistent with the previous work (Encarnação, 2015, cf. Chap. 7).

Regarding the orbital effect, one can also see significant differences in each of the considered formations. For the along-track and pendulum formations, the geometric effect is the largest orbital errors component followed by the midpoint effect. However, the magnitude difference for these two errors is small for the along-track while it is rather large for the pendulum. As a consequence of this difference, it was shown that, after the geometric correction is applied, there are significant improvements in the pendulum mission, while only minor ones were obtained for the along-track. For the cartwheel mission, the orientation effect was found to be the largest orbital error component, and as a consequence the geometric correction

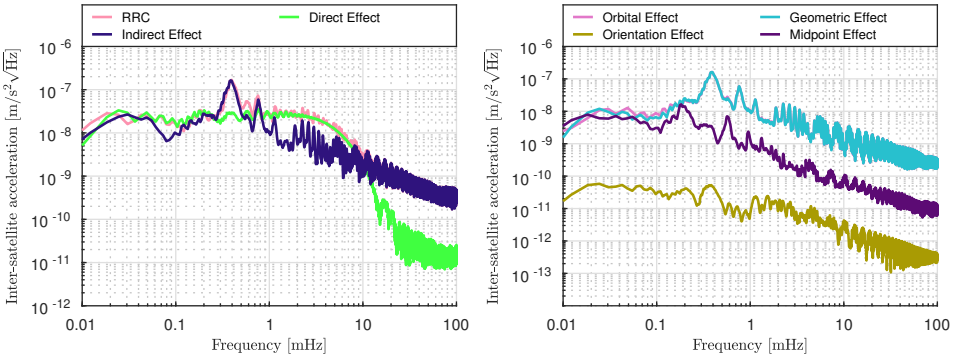

Figure 3.10: PSD$^{\frac{1}{2}}$ of inter-satellite accelerations caused by the considered mass anomaly for a pendulum type of mission. The left panel shows the breakdown of the RRC into direct and indirect effects. The right panel shows the relative magnitude of the orbital effect components.

yielded no significant error reduction.

Another characteristic of indirect effect errors is that, unlike e.g., accelerometer errors or ranging errors, indirect effect errors are not an error source themselves; rather, indirect effect errors are a mechanism which amplifies other existing error sources. Even in the absence of all errors, indirect effect errors are caused even by the signal itself. As a consequence, in building the error budget for a ll-SST mission, it is not possible to independently account for indirect effect errors alone. Indirect effect errors are accounted for as a part of each considered error source.

3.8. Summary

The indirect effect is a significant and poorly understood error source in ll-SST satellite missions. I have presented a formal definition of the orbital and modeling effects which constitute the indirect effect.

A simple simulation setup, where a mass anomaly is used as a perturbation, was defined to demonstrate the propagation of indirect effect errors in the three elementary types of satellite formations. It was shown that the cartwheel formation is very sensitive to indirect effect errors, that the along-track formation is affected to a lesser extent, while the pendulum formation is very resilient. This distinction emerges from the way orbital perturbations map into the inter-satellite baseline. These findings are fully consistent with the previously published works (Ditmar et al., 2012; Encarnação, 2015).

Nonetheless, the results obtained from this illustrative example are a simplification of reality. The introduced mass perturbation is very simple. Realistic mass anomalies will perturb the satellite orbits in a more complex manner. The complexity of the indirect effect errors prompts the need to properly account for them. In Chapter 6, I will take indirect effect errors into account when building the error budget of the GRACE mission.

There are likely several ways to reduce the level of indirect effect errors. The

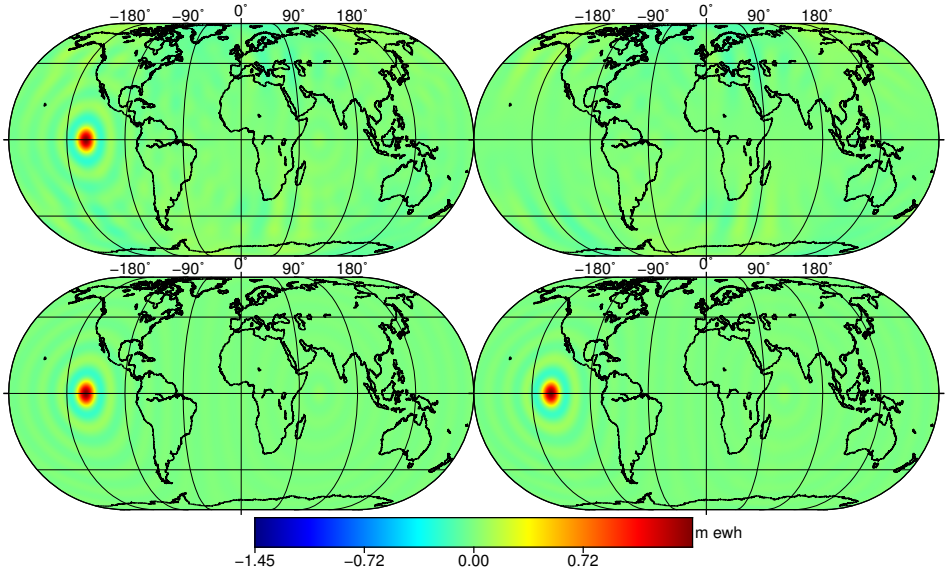

Figure 3.11: Gravity field solutions recovered with the average acceleration approach for the pendulum type of mission. On the top-left, the solution computed from the RRC data; on the bottom-left the direct effect; the difference between the two is the indirect effect which is plotted on the top-right panel; in the bottom-right panel the solution computed from the RRC data after applying the geometric correction.

most obvious way is to reduce the magnitude of the sources of indirect effect: better a-priori gravity field, lower accelerometer errors, better ocean tide model, etc. Additionally, by iterating the recovery procedure, it may be possible to decrease the discrepancy between the reference and true orbits. This should potentially reduce the level of indirect effect errors. One final approach that may be useful in reducing indirect effect errors is to constrain the computed reference orbits with additional information obtained from the real ones, such as inter-satellite ranging data.

The presented results, in terms of the recovered gravity field solutions, are specific to the average acceleration approach. The design of future satellite gravimetry mission should not be constrained by the drawbacks of any specific approach that is used to process the data. Therefore, it is desirable to evaluate the design of alternative concepts independently of any given approach. While it is likely that indirect effect errors are relevant in alternative approaches, it is difficult to quantify their impact in each of the existing (and future) approaches. Therefore, in Chapter 8, I opt to consider a best-case scenario, where no indirect effect errors are considered in order to evaluate and compare the performance of future candidate missions.

4

Methodology

In this chapter I will present the methodology that is used to evaluate the error budget of ll-SST satellite mission data. The chapter begins by motivating a simulation approach as a means to estimate the performance of a satellite gravimetry mission. Afterwards, I present an overview of the steps that are required to perform a simulation. I proceed to discuss the details involved in generating orbits and observations. Afterwards, I explain the computation of gravity field solutions from the orbits and observations and the filtering that is applied.

4.1. How to evaluate the performance of ll-SST missions?

In this thesis I set out to benchmark different satellite gravimetry mission concepts. The performance of a mission is defined by how accurately it is capable of recovering mass anomalies. In broad terms, a recovery involves estimating a set of gravity field model parameters from the observations collected by the mission. These observations are invariably contaminated by various types of errors, which affect the recovered gravity field. Ultimately, the performance of a satellite mission depends on the signal-to-noise ratio (SNR) and how it maps into the solutions. Therefore, to measure the performance of a mission, it is necessary to propagate both signal and errors into gravity field solutions. Furthermore, by quantifying individual error sources, it becomes possible to identify the errors that limit the accuracy of a given mission.

Quantifying errors which affect gravimetry missions is a complex endeavor. There are different types of errors originating at different stages of the data processing chain. An analytical treatment of each error source would be both impractical and likely tackling only a limited set of the systems' complexity. Instead, a simulation tool will be used to tackle the full complexity of the task. This allows for a unified approach to the propagation of errors from any sources. The availability of the software used to process GRACE data makes this approach very practical.

In order to identify the performance limitations of a given ll-SST mission, it is necessary to separate the impact of different errors in the solutions. This is done by propagating each individual error through the processing chain. To identify the compound effect of several error sources, i.e., the total error, the impact of the individual errors is added up. In order to do this, I assume that all errors compound additively in terms of observations and gravity field solutions. This is possible since gravity field solutions are obtained as solutions of a linear system of equations.

A general overview of the simulation procedure is as follows.

1. A simulation addresses a satellite constellation, with one or more formations of two or more satellites. Each pair of satellites in a formation may collect only one ll-SST dataset.
2. For each satellite in the mission, I generate the corresponding orbit. Orbit generation is discussed in Section 4.3.
3. For each ll-SST dataset, I simulate the observations. The observations are represented as a set of independent data vectors consisting of the signal to be recovered and the ensemble of errors sources considered. The types of observations are discussed in Section 4.4 and the error sources in Section 4.2.
4. A system of linear equations is set up; the normal matrix that relates all ll-SST datasets and the gravity field parameters is explicitly computed and stored. Once the normal matrix is available, the observations are inverted into a set of gravity field parameters. The set consists of independent fields for the signal and each of the error sources considered. In addition, a set of filtered solutions may be computed by applying the statistically optimal filter. The computation of gravity field solutions is discussed in Section 4.5.

A simulation is performed in one of two modes: complete or simplified. The difference between the two modes is simply whether the indirect effect is taken into account (complete) or not (simplified). Specific differences between the two modes are discussed in Section 4.6. Nonetheless, both modes share the same general steps as described above.

In the following sections, each of the major simulation steps is described in detail.

4.2. Noise scenarios for GRACE, GFO and future satellite gravimetry missions

In this section, I will define the error scenarios used to assess the performance of GRACE and of future ll-SST satellite gravimetry missions. The considered error sources are divided in three categories: instrumentation errors, temporal aliasing errors and filtering errors.

4.2.1. Instrumentation errors

Regarding instrumentation errors, two error profiles are defined: one emulating the errors in the GRACE mission and another with a conservative level of errors for

Table 4.1: Comparison of instrumentation errors for the GRACE and future ll-SST missions. All error sources are modeled as white noise. A sampling interval of 5 s is assumed, which is consistent with that of the GRACE mission ranging data.

Error		GRACE	Future ll-SST	Unit
Ranging	Microwave	0.8	–	$\mu m/\sqrt{Hz}$
	Laser	-	0.05	$\mu m/\sqrt{Hz}$
Accelerometer		1	0.1	$nm/s^2/\sqrt{Hz}$
Attitude	Roll, Pitch, Yaw	20,80,80	-	$\mu rad/\sqrt{Hz}$
	IS Pointing	1	-	mrad
Positioning		3	3	$cm/\sqrt{Hz}$

future ll-SST satellite gravimetry missions. I consider four instrument error sources: accelerometer, inter-satellite ranging, star-camera and positioning. Table 4.1 shows the differences between the GRACE and future missions' instrumentation error scenarios.

Accelerometer (ACC)

Accelerometer errors for the GRACE mission are reported to have a $PSD^{\frac{1}{2}}$ of $1\,nm/s^2/\sqrt{Hz}$ (Frommknecht et al., 2006). This value has been estimated from the high-frequency part of the spectrum of the differences between L1B data of the two satellites' accelerometers.

Differences in accelerometer measurements can also be explained by residual non-gravitational acceleration signals acting on the satellites, however these are limited to the low-frequency part of the spectrum. The high-frequency components are a representation of the accelerometer noise.

The considered level of accelerometer errors is unexpectedly high, about 10 times higher than the specification (JPL, 2000). While selected periods of accelerometer data can be found which comply with the specification, several systematic disturbances have been identified which cause the overall quality of the data to degrade (Flury et al., 2008; Gerlach et al., 2004; Peterseim et al., 2012).

Regarding future missions, recent publications assume a higher accuracy, at the level of $0.01\,nm/s^2/\sqrt{Hz}$, for two of the accelerometer axes (Hauk et al., 2020; Purkhauser et al., 2020). In this thesis, I will make the conservative assumption that the accelerometers of future ll-SST missions will meet the performance requirements of GRACE at $0.1\,nm/s^2/\sqrt{Hz}$.

Inter-Satellite Ranging (RNG)

Ranging errors represent intrinsic noise in the ll-SST ranging sensor. Particularly, ranging error might be defined for the K-band ranging (KBR) sensor used by the GRACE and GFO missions, or Laser Ranging Interferometer (LRI), which is used by the GFO and future ll-SST missions.

For the GRACE mission, Gerlach et al. (2004) estimated the noise in the ranging data to have a $PSD^{\frac{1}{2}}$ between 1 and $2.1\,\mu m/\sqrt{Hz}$. However, more recently, Ditmar

et al. (2012) showed that this value is a slight over-estimation. A comparison with real GRACE data noise observations has lead to an estimate of 0.81 $\mu m/\sqrt{Hz}$.

The major innovation of the GFO mission is the use of a new laser interferometer ranging system. The new instrument brings significant improvements in the accuracy of the ranging measurements. The noise level specification for the LRI instrument is 50 $nm/\sqrt{Hz}$ (Flechtner et al., 2014b). First data analysis from the LRI instrument on-board the GFO mission show that the instrument is performing much better than the specification, at the level of 1 $nm/\sqrt{Hz}$ (Abich et al., 2019). Despite the good initial performance, and partly due to the unknown evolution of the noise level throughout the GFO mission, I will assume the noise level specification 50 $nm/\sqrt{Hz}$ as conservative value for the LRI instrument for future ll-SST missions.

Star-camera (SCA)

Each of the GRACE satellites is equipped with two Star-Camera instruments. Star-camera errors propagate into errors in the satellite attitudes and then into errors in the measured ranges. This type of errors is discussed in detail in Chapter 5. In that chapter, an analysis of SC errors based on L1A GRACE data is made. SC errors are categorized in two components with different spectral features: a harmonic and a stochastic component. The harmonic component of star-camera errors has been explained and corrected for (Harvey, 2016). Therefore, only the stochastic component of star-camera errors is considered in the noise scenario. The standard deviation of attitude errors is set equal to 20, 80 and 80 µrad in terms of roll, pitch and yaw angles, respectively (see Table 5.2 for 2006/02, month with best SC performance).

As discussed in Section 5.4, attitude errors propagate into inter-satellite ranges because the long axes of the GRACE satellites slightly deviate from the LOS direction. The operational requirement for the GRACE mission is that the *inter-satellite pointing angle* is to be kept below 1 mrad in terms of standard deviation. Considering 2006/02, a month with good AOCS performance, the standard deviation value of the inter-satellite pointing angle was indeed found to be around 1 mrad.

Each GFO satellite is equipped with an extra star-camera, adding to a total of three star-camera instruments per satellite. The additional star-camera contributes to a significant improvement in the accuracy of the attitude determination system by dramatically reducing periods of single star-camera operation. Furthermore, the LRI has an additional advantage that the virtual measurement point is placed at the satellite CoM. As a consequence, no ranging correction needs to be applied to the LRI measurements, and therefore star-camera errors do not impact LRI data of the GFO mission. In the context of future missions, I will assume that the same configuration will be used, such that the collected LRI data will also be immune to star-camera errors.

Positioning (POS)

The computation of PDOs requires precise knowledge of the initial position and velocity of the spacecraft. GNSS observations are used to improve the estimate of

the initial state of the satellite. Therefore, errors in the GNSS observations perturb the initial state vectors which in turn perturb the PDOs.

Positioning errors reflect the accuracy of the GNSS receiver aboard the ll-SST satellites. For both GRACE and future ll-SST satellite missions, I consider the accuracy of the 3D absolute positioning of the GNSS receivers to be modeled as white noise with a standard deviation of 3 cm. This is consistent with reported RMS values of differences between kinematic GRACE orbits and SLR measurements (Zhao et al., 2010) and latest developments in kinematic orbit determination (Zhou et al., 2019).

Relative orientation errors

Knowledge of the the relative orientation of the spacecraft instruments (e.g. each star-camera instrument or each accelerometer) with respect to the spacecraft reference frame is required with great accuracy. In this thesis, I have made two assumptions:

1. the orientation of the instruments w.r.t. to the spacecraft does not change over time

2. it can be accurately estimated from on-ground and in-flight calibration to the point where it no longer plays a role in the mission performance

At first glance, these assumptions might seem optimistic. It is likely that thermal distortion of the spacecraft could cause relative displacement of the instruments within the spacecraft. For example, Siemes et al. (2019) show that the relative orientation of the star-camera instruments in GOCE changes over time, and after proper estimation and calibrations improvements could be observed in the computed gravity field solutions. However, in comparison with the other error sources considered, relative orientation are likely to have a relatively minor contribution to the total error budget, especially in the case of the GRACE mission.

Regarding the case for future mission, if such errors do play a role in the total error budget of existing missions, it is likely that they will be minimized by future spacecraft design with a better understanding of their dynamics. In general, I believe the impact of these errors in the total error budget is minor and therefore I chose to not include them in the presented mission scenarios.

4.2.2. Temporal aliasing errors

Any satellite gravimetry mission requires data to be collected over a a sufficiently long period of time before a set of spherical harmonic coefficients can be recovered. As it is mentioned in Sect. 2.5.1, I refer to this period of time as the *data accumulation period* (DAP). During this period, different mass transport phenomena unfold on the surface of the Earth. In spite of these variations, the mission can only recover the *mean* of the mass transport signal within this period. Signals (and errors) which change over the DAP will map as temporal aliasing errors in the solutions.

I consider three sources of temporal aliasing errors: ocean tide model errors (OTE), non-tidal atmosphere and ocean de-aliasing model errors (AOD) and dynamic mass transport signal (TMP). These will be explained in the following sections.

Atmosphere and Ocean De-Aliasing (AOD) Model Errors

In Bergmann-Wolf et al. (2015), the authors present a realistic realization of errors in the RL05 Atmosphere and Ocean De-aliasing product AOD1B, which was until recently officially used to process GRACE data. In this thesis, I use the AOD error product described in that publication as the realization of AOD errors for present and future satellite missions.

Dynamic Mass Transport Signal (TMP)

In this thesis, the mass transport signal used is based on the ESM model. The ESM model is composed of a set of mass transport components sampled at 6-hour intervals. The mass transport signal in my study is defined as the HIS (Hidrology, Ice and Solid Earth) components of the ESM model (cf. Section 2.5.1). The goal of a mission is to recover the mean of the mass transport signal within its data accumulation period. The dynamic (i.e., non-static) component of the signal maps into the observations in a non-trivial manner, causing temporal aliasing errors in the solution.

In order to quantify these errors, I adopt the following approach. First, the mean of all 6-hour HIS fields is computed over the data accumulation period of the considered simulation. Then, the resulting mean field is subtracted from each individual 6-hour field. As a result, a new, zero-mean, dynamic mass transport signal is obtained. This error source is used to evaluate the temporal aliasing errors caused by the continuously changing mass transport signal.

Ocean tide model errors (OTE)

Several alternative global ocean tide models can be found in the literature.

As discussed in Section 2.5.2, I define ocean tide model errors as the difference between the FES2004 (Lyard et al., 2006) and EOT11a (Bosch et al., 2009) tide models. To visualize the tide model errors, the differences between the two considered tide models were computed in terms of tidal heights over a 1° equiangular grid every hour for the time span of one month. In Figure 4.1, the RMS of the difference at each grid cell is shown. The depicted figure clearly illustrates the nature of ocean tide model errors. Just as concluded in Stammer et al. (2014), the differences between the EOT11a and FES2004 model reach values above 10 cm ewh. However, these large differences are confined to very specific regions where tides are hard to model, e.g., the southern tip of South America or the Hudson Straight. Apart from these difficult regions, the differences between the two models are very small, especially in the open oceans.

Static component of temporal aliasing error sources

In general, the average of the considered temporal aliasing error sources is not zero within any given DAP. I refer to this average as the *static component*. As soon as

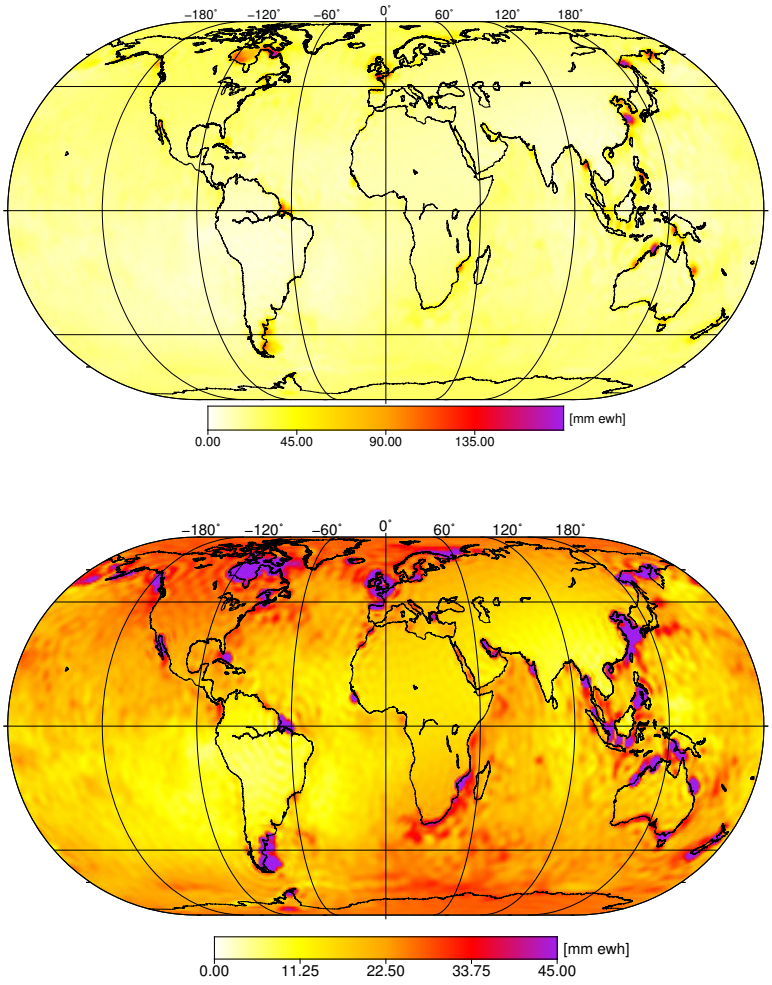

Figure 4.1: Each grid cell represents the RMS of the differences between the EOT11a and the FES2004 ocean tide models at hourly intervals for the duration of a month. Larger span of the colorbar in the top plot highlights the large localized features along the coastal areas. Narrower colorbar span in the bottom plot highlights the large-scale low magnitude error features.

the static component for a given DAP is removed, a zero-mean time-variable error source is left. This remaining component I refer to as the *dynamic component*.

Notice that by definition the dynamic mass transport source (TMP) only contains the dynamic component. However, the AOD and OTE error sources do contain a static component. When discussing AOD and OTE errors, I refer exclusively to the dynamic component of the AOD and OTE errors. I do not consider this static component as a source of temporal aliasing errors. At the first glance, this might seem strange. When dealing with satellite gravimetry data, normally we consider AOD and OTE signals as undesired; we make use of background models to remove them from the observations. As such, one would address the errors in these models simply as temporal aliasing erros. In my opinion, this would be a misuse of the concept temporal aliasing error. Temporal aliasing error should only apply to an error source which is changing in time. With that understanding, the static component of the AOD and OTE errors is not considered when discussing temporal aliasing errors.

The next question is whether the static AOD and OTE components should be considered as errors or as signal. On the one hand, background models are used to remove these signals from the observations to the extent possible. Therefore, we find these signals undesirable and if they show up in the solutions they should be considered as errors. On the other hand, the static AOD and OTE component is not fundamentally different from the static component of the hydrological or ice signals which we hope to recover from satellite gravimetry data. Therefore, I argue that the static component of AOD and OTE are not errors but signal.

4.2.3. Signal and other errors

Input mean mass transport model (ESM) and noise-free data (SGN)

The ESM model (see Section 2.5.1) is used to compute the mean mass transport signal over the DAP of the considered simulation. This mean signal (ESM) is then used as input in the simulation. Noise-free observations and solutions, labeled as SGN, are obtained from these input data and are compared to the considered errors sources in order to assess the signal-to-noise ratio.

High Pass Filtering (FLT) error and Regularization Bias (REG)

Apart from the considered error sources, additional error sources related to the data processing will be considered.

As will be shown in Section 6.1, where the error budget of the GRACE mission is presented, RRC data of the GRACE mission suffer from large low-frequency errors. In order to tackle these, a high-pass filtering procedure is routinely applied. This procedure is discussed in detail in Section 6.1.4. While the high-pass filtering procedure will result in an overall reduction of errors, it introduces a new error source which must be accounted for. The filtering error is computed as the difference between noise-free data and noise-free data after applying the high-pass filter.

Additionally, as will be discussed in Section 4.5, a regularization procedure may also be applied to the computed solutions. If one splits the ensemble of signal and errors as independent data vectors, then regularization procedure will effectively reduce the magnitude of all error realizations during the inversion procedure.

However, since the regularization modifies the linear system of equations, a signal distortion is unavoidable. The regularization bias is computed as the difference between the input mean mass transport signal (ESM) and the regularized solution computed from noise-free observations (SGN).

Indirect Effect Error (IEF)

Indirect effect errors (IEF) have been formalized in Chapter 3. Any perturbation in the background force model will cause the computed satellite orbits to deviate from the real ones causing indirect effect errors. For all considered errors sources in the previous sections the corresponding indirect effect error is taken into account.

However, the mean mass transport signal is also a background force model perturbation. Therefore, the mean mass transport signal causes a corresponding indirect effect error which has not yet been accounted for. The indirect effect (IEF) error source is used to represent this error.

4.3. True and reference orbit generation

A large part of simulating an ll-SST mission is the computation of PDOs on the basis of an initial state vector and a force model. All the components of the force model used for the orbit integration are described in Liu (2008). This is a crucial step; it is important to replicate in the simulations the approach followed during real data processing.

Typically, the data accumulation period ranges from a few days up to a month. For these relatively long timespans, PDOs are computed in independent arcs, each requiring an initial state vector. In real GRACE data processing, two inputs are required to obtain an initial state vector: a *kinematic orbit* (KO) and a *reduced dynamic orbit* (RDO). The KO have relatively large positioning errors in the data gathered by the GNSS receivers. Orbits computed on the basis of simple dynamic models are more accurate over short periods but they tend to accumulated large errors over time. RDOs couple data from the GNSS receivers with such models in order to better estimated the true satellite orbits. At this point, it is important to understand the role of these orbits in the computation of the PDO. The RDOs provide an estimate of the satellite's initial state vector. PDOs are very sensitive to errors in the initial state vector. Therefore, in order to minimize these errors, the initial state vector is adjusted using the KO as a set of observations. The procedure to generate a PDO is then as follows:

1. obtain the initial state vector from the RDO.
2. starting from the initial state vector, a trial PDO is computed.
3. then, the positions of the KO are used as observations and the parameters of the initial state vector are adjusted in a LS procedure in order to minimize the differences between the trial PDO and the KO. This procedure is called *orbit fitting*.
4. based on the the adjusted initial conditions, the PDO is computed.

PDOs in real data processing are used as the reference orbits.

In the context of simulations, in addition to the reference orbit, also the "true" orbits of the satellites need to be computed. The process of creating the "true" satellite orbits begins with defining the parameters of the true orbit, e.g., altitude, repeat period, inclination, etc. (see Section 2.2). The computation of a repeat period orbit immersed in a realistic gravity field model of the Earth is an extremely challenging task, which is well outside the scope of this thesis. It is, however, straightforward to generate the required orbit immersed in a Keplerian force field, i.e., assuming that the Earth is a point mass (see Section 2.2.2). In order to obtain a true satellite orbit which approximates the design criteria, the approach is the following (Encarnação, 2015),

1. Compute a Keplerian orbit according to the selected design criteria.
2. The Keplerian orbit provides the initial state vectors; a trial PDO orbit is computed on their basis with a realistic static gravity field.
3. The trial PDO is fitted to the Keplerian orbit, i.e., the initial state vectors are adjusted to minimize the deviations from the Keplerian orbit.
4. The adjusted initial state vectors are then used to compute the "true" orbit.

This procedure ensures that the "true" orbit is both realistic and matching the design criteria.

In order to compute the reference orbit, I use the "true" orbit to provide the initial state vector of each arc and, simultaneously, the observations in the orbit fitting procedure. In this manner, the "true" orbit plays the role of the RDO and KO in real data processing. In the absence of any perturbations, the computed reference orbit would be exactly equal to the "true" satellite orbit. Thus, any difference between the reference and true orbits is necessarily caused by an introduced error source. To study the impact of individual errors on the computed satellite orbits, I use different force models to generate the true and reference orbits.

By designing a set of error models, each considering a single error source, it becomes possible to analyze the full impact of each one on the computed orbits. Table 4.2 lists the types of error models which are used to generate PDOs.

Error Model 1 (EM1) is actually not perturbed by any error source. It simply uses a static gravity field model, a necessary requirement to generate any orbit. EM1 is exploited to generate the "true" orbits. Regarding the reference orbits, different versions are generated, each corresponding to a specific error source. EM2 is used to evaluate the impact of the mean mass transport signal. In this case, the differences between the true and reference orbits are caused by the differences between EM1 and EM2, i.e., by the mean mass transport signal. EM3 and EM4 make use of different ocean tide models. They are used to generate the "true" and reference orbits when I study the impact of differences between the considered ocean tide models on the computed orbits. Similarly, EM5 is applied to evaluate the impact of errors in the Atmosphere and Ocean De-Aliasing model. EM6 is used to evaluate errors in the accelerometer data, EM7 to evaluate positioning errors in

Table 4.2: Different error models considered for the numerical integration of orbits. Each error model (EM) represents a different force model used for the computation of a PDO. MMT represents the mean mass transport signal over the accumulation period of the mission, i.e., the signal to be recovered. OTE are errors in ocean tide models. AOD represents errors in the Atmosphere and Ocean De-aliasing model. ACC are errors in the accelerometer measurements. Finally, POS represents errors in the satellite orbits used to estimate the initial state vectors in the orbit fitting procedure. TMP refers to the dynamic mass transport signal.

	Static	MMT	OTE	AOD	ACC	POS	TMP
EM1	✓	✗	✗	✗	✗	✗	✗
EM2	✓	✓	✗	✗	✗	✗	✗
EM3	✓	✗	FES2004	✗	✗	✗	✗
EM4	✓	✗	EOT11a	✗	✗	✗	✗
EM5	✓	✗	✗	✓	✗	✗	✗
EM6	✓	✗	✗	✗	✓	✗	✗
EM7	✓	✗	✗	✗	✗	✓	✗
EM8	✓	✗	✗	✗	✗	✗	✓

the reference orbit and, finally, EM8 to quantify the impact of the dynamic mass transport signal. In Table 4.3, an overview of the error models used for each error source is shown.

Once the true and reference orbits of all the satellites for all the considered error sources have been obtained, it is time to compute the observations.

4.4. Observation generation

There are three types of ll-SST observations considered in the simulations, onto which the considered error sources may be propagated:

- synthetic ranges
- residual range combinations
- average inter-satellite accelerations.

Synthetic ranging noise

Synthetic ranging noise (NOI) is the simplest kind of observations. Its computation does not require any satellite orbits. It reproduces random errors that appear at the level of ranging data, specifically, from star cameras and a ranging sensor. These errors can be accurately modeled as random stationary noise defined by their PSD$^{\frac{1}{2}}$. In order to generate a noise realization, the phase corresponding to each frequency is randomized and the resulting complex spectrum is inverted back into the time domain.

To be consistent with the other types of observations, defined in terms of average inter-satellite accelerations, double differentiation is applied to the noise realizations. Consider a set of synthetic ranges sampled at time intervals Δt, where

ρ_i represents the inter-satellite range at the $i-$th time instant. The average inter-satellite acceleration $\ddot{\rho}_i$ is obtained by applying the 3-point numerical differentiation,

$$\ddot{\rho}_i = \frac{\rho_{i-1} - 2\rho_i + \rho_{i+1}}{(\Delta t)^2} \quad . \tag{4.1}$$

While the previous expression is strictly not consistent with the RRC (cf. Eq. 3.9), in practice it is adequate to generate error realizations of error sources which do not require satellite orbits to propagate into observations (e.g. ranging noise).

Average inter-satellite accelerations

Average inter-satellite accelerations (ISA) observations are directly linked to the differenced gravity field acting on the pair of ll-SST satellites, cf. Eq. 3.4. Computation of average inter-satellite accelerations requires the true orbits of the pair of ll-SST satellites. In the context of simulations, I use average inter-satellite accelerations because they allow me to compute the direct effect of each individual component of the force model. To compute the indirect effect the corresponding RRC observations are additionally required.

Residual Range Combinations

RRCs are computed on the basis of the residual ranges between two sets of orbits: the true and reference orbits and the LOS unit vectors corresponding to the reference orbits, cf. Eq. 3.9.

4.5. Generating Gravity Field Solutions

Once the set of true orbits is available, one can assemble the normal matrix that is needed to form the system of linear equations relating the observations and the Stokes coefficients. After the normal matrix is assembled, a solution is obtained for each error source.

Depending on the characteristics of the satellite mission, the quality of the obtained gravity field solution might not be homogeneous; e.g., the GRACE mission shows large errors in some near-sectorial coefficients, which result in the well-known vertical stripe pattern seen in unfiltered solutions. Several post-processing filters have been developed in the literature: gaussian filter (Wahr et al., 1998), de-striping filter (Swenson et al., 2006), de-correlating non-isotropic filter (Kusche et al., 2009) or the "fan" filter Zhang et al. (2009). In this thesis, I make use of the statistically optimal Wiener-type filter which is routinely applied to the DMT family of gravity field solutions Klees et al. (2008). The optimal filtering procedure is described in Liu et al. (2010). One of the ingredients of the optimal filter is the variance-covariance matrix of the mass transport signal to be recovered (Liu et al., 2010). This matrix has been computed on the basis of the ESM model and is applied consistently to all the solutions of all the simulations.

4.6. Simulation Modes

Indirect effect errors in the context of the RRC approach were introduced in Chapter 3, where simple simulations were presented to highlight their impact on the

gravity field solutions computed with the RRC approach. They are known to occur when PDOs are computed in the presence of force model disturbances. The way in which indirect effect errors propagate into observations and into gravity field solutions likely depends on the considered functional model. Even assuming that indirect effect errors affect all approaches, it is still unknown to what extent each approach is affected. In that case, the results presented in this thesis could be regarded as conditioned to the choice of methodology. Had a different methodology had been chosen, the results would likely be different. However, a comparison of indirect effect errors in all different functional models is beyond the scope of this thesis. In order to address this issue, the simulation of an ll-SST mission can be performed in one of two modes: *complete* or *simplified*. The difference between the two is that the complete mode accounts for indirect effect errors, while the simplified mode does not. The "simplified mode" implies a best-case scenario, where the impact of indirect effect errors is reduced to zero, while the complete mode can be regarded as a real-world example valid in the context of the average acceleration approach.

The complete mode will be used in Chapter 6 in order to compare simulated errors with observed inter-satellite residuals of the GRACE missions. The simplified mode will be used in Chapter 8, in the context of future satellite missions. In this chapter, comparing the relative performance of future mission concepts is more important than the specific data processing approach chosen to do so.

Importantly, the processing of real data is reproduced only in the complete mode. The simplified mode cannot be applied to real ll-SST data as it relies on the knowledge of the true orbits of the satellites. The major processing steps described in the previous sections refer to the complete simulation mode. This assumption that the true orbits are known leads to a number of simplifications when the simplified mode is used.

Since the "true" orbits are known, they can be directly used for the computation of residual average inter-satellite accelerations as in Eq. 3.4. Therefore, reference PDOs are no longer required and no RRC observations need to be considered. As a consequence of this, all indirect effect errors are excluded.

When indirect effect errors are excluded, two error sources disappear: positioning error and the indirect effect caused by the mean mass transport signal. Positioning errors (POS) can only propagate into ll-SST observations in the computation of reference PDOs which are no longer considered. The indirect effect errors caused by the mean mass transport signal (IEF) is also no longer considered by definition. Other error sources remain as they are directly evaluated over the true orbits instead of in terms of the RRC.

Tables 4.3 and 4.4 show an overview of all the errors sources, force models, orbits and observations considered in a ll-SST simulation for the complete and simplified simulation modes, respectively.

4.7. Summary

In this Chapter, I have given an overview of the methodology that is used to evaluate the performance of an ll-SST mission. In Section 4.2, I have presented the

Table 4.3: Overview of considered error sources, their orbits, observations and solutions for the *complete* simulation mode. The different error models (EM1, ... EM8) used for orbit integration are shown in Table 4.2. Regarding the observations column, ISA are inter-satellite accelerations (see eq. (3.4)), RRC are residual range combinations (see eq.(3.9)) and NOI are realizations of random noise. Other items in this column represent addition or subtraction of other error sources' observations. Regarding the solutions column, it lists whether a solution is computed from the observations or not. Alternatively, a solution may also be obtained as the addition of subtraction of other errors sources' solutions.

Source	**Orbits**		**Observations**	**Solutions**	**Description**
	True	Ref.			
SGN	EM1	✗	ISA	✓	Signal of interest: the direct effect caused by the mean ESM signal over the data accumulation period
TEF	EM1	EM2	RRC	✗	The total effect of SGN
IEF	✗	✗	TEF - SGN	✓	The indirect effect of SGN
RNG	EM1	✗	NOI	✓	Ranging sensor noise
SCA	EM1	✗	NOI	✓	Star-camera noise
ACC	EM1	EM6	RRC	✓	Accelerometer noise
POS	EM1	EM7	RRC	✓	Positioning noise
TIN	✗	✗	RNG + SCA + ACC + POS	✓	Total instrumentation error
AOD	EM1	EM3	RRC	✓	Atmosphere and Ocean De-aliasing model error
OTE	EM4	EM5	RRC	✓	Ocean Tide Model error
TMP	EM1	EM8	RRC	✓	Dynamic mass transport signal
TAL	✗	✗	AOD + OTE + TMP	✓	Total aliasing errors
SPT	EM1	✗	RRC	✓	Spatial aliasing: aliasing of input SH degrees above L_{max}
REG	✗	✗	✗	ESM - SGN	Regularization bias: bias introduced by the regularization procedure
FLT	✗	✗	ESM - SGN	✓	Filtering error: error introduced by the high-pass filtering procedure applied to ll-SST observations
TOT	✗	✗	TAL + TIN + IEF + SPT + FLT	TAL + TIN + IEF + SPT + FLT + REG	Total error
ESM	✗	✗	✗	✗	Mean ESM model over data accumulation period

Table 4.4: Overview of considered error sources, their orbits, observations and solutions for the *simplified* simulation mode. EMX error models used for orbit integration are shown in Table 4.2. Regarding the observations column, ISA are inter-satellite accelerations (see eq. (3.4)), RRC are residual range combinations (see eq.(3.9)) and NOI are realizations of random noise. Other items in this column represent addition or subtraction of other error sources' observations. Regarding the solutions column, it lists whether a solution is computed from the observations or not. Alternatively, a solution may also be obtained as the addition of subtraction of other errors sources' solutions.

Source	**Orbits**		**Observations**	**Solutions**	**Description**
	True	Ref.			
SGN	EM1	✗	ISA	✓	Signal of interest: the direct effect caused by the mean ESM signal over the data accumulation period
RNG	EM1	✗	NOI	✓	Ranging sensor noise
SCA	EM1	✗	NOI	✓	Star-camera noise
ACC	EM1	✗	NOI	✓	Accelerometer noise
TIN	✗	✗	RNG + SCA + ACC	✓	Total instrumentation error
AOD	EM1	✗	ISA	✓	Atmosphere and Ocean De-aliasing model error
OTE	EM1	✗	ISA	✓	Ocean Tide Model error
TMP	EM1	✗	ISA	✓	Dynamic mass transport signal
TAL	✗	✗	AOD + OTE + TMP	✓	Total aliasing errors
SPT	EM1	✗	ISA	✓	Spatial aliasing: input SH degrees above L_{max}
REG	✗	✗	✗	ESM - SGN	Regularization bias: bias introduced by the regularization procedure
TOT	✗	✗	TAL + TIN + SPT	TAL + TIN + SPT + REG	Total error
ESM	✗	✗	✗	✗	Mean ESM model over data accumulation period

error sources which are considered in the simulations. The errors are divided into instrumentation errors, temporal aliasing errors and others. The noise scenarios which apply to GRACE and future ll-SST missions were also presented, which only differ in terms of instrumentation errors.

Afterwards, the major steps in the simulation of a ll-SST mission were presented. In Section 4.3, the procedure to generate orbits is outlined in line with the background force models considered. In Section 4.4, the three types of observations used in the simulations were presented. In Section 4.5 the procedure to invert ll-SST observations into gravity field parameters is discussed. Finally, in Section 4.6, the two adopted simulation modes and their differences were addressed.

5

Star camera errors and their impact on GRACE's monthly gravity field models

In this chapter, I present the work published in Inácio et al. (2015) regarding the SC errors in GRACE's observations. The proper simulation of future concepts of ll-SST missions requires the development of a realistic simulation tool whose results must be validated against the data gathered by the GRACE mission. In order to accomplish this goal, a complete understanding of the errors present in the GRACE dataset is a prerequisite. Following this line of research, star camera errors were investigated and a number of interesting findings is documented below. The results presented in this paper have prompted the discovery of a minor software bug in GRACE's data processing chain with consequent improvement in the corresponding datasets (Harvey, 2016).

5.1. Introduction

The Gravity Recovery And Climate Experiment (GRACE) satellites (B. D. Tapley et al., 2004) were launched in 2002 with the aim to measure the static and time-variable gravity field of the Earth. The GRACE mission consists of two satellites, following each other in a low-earth orbit separated by a distance of about 200 km. The attitudes of the GRACE satellites are determined by two star cameras (SCs) on board each satellite. Errors in the SC measurements result in an inaccurate determination of the satellites' attitudes, which ultimately propagate into errors in monthly mass anomaly maps.

Simulation studies (Kim, 2000) done prior to the launch of the GRACE satellites predicted a noise level, which has not yet been matched by real data (Schmidt

Parts of this chapter have been published in Inácio et al. (2015).

et al., 2008). This discrepancy highlights the need to fully understand the overall error budget. This is a goal on its own but may also be relevant for future mission performance analysis depending on the overall mission concept. In a recent study, Ditmar et al. (2012) explain the major contributions to the GRACE noise budget in different spectral bands. They showed that low-frequency noise (<1 mHz) is caused by the limited accuracy of the computed GRACE orbits, while the K-band Ranging (KBR) sensor is the major contributor to noise at frequencies above 9 mHz. Noise in the frequency band between 1 mHz to 9 mHz (5.4 to 49 cycles per revolution, cpr) is less well understood. Although there is no one-to-one correspondence between frequencies in the KBR data and spherical harmonic degrees, it is very likely that relevant geophysical signal largely maps into this frequency range.

The fundamental observable of GRACE is the range between the satellites, which is measured by the KBR system. Since the launch of GRACE, advances in ranging technology allow the use of laser interferometers in satellites (Dehne et al., 2009). For instance, GFO carries both KBR and laser interferometric ranging instruments, the latter as a technological showcase. It is foreseen that laser interferometers will be able to improve the ranging accuracy by up to three orders of magnitude (P. Bender et al., 2003; Dehne et al., 2009). However, improvements brought by laser interferometry alone do not guarantee similar improvements in monthly gravity anomaly maps. Fully exploiting the new ranging technology requires all other relevant error sources to be controlled. Before GRACE's launch, pre-mission simulation studies had to rely on assumptions about error sources. At this point, real data of the GRACE mission can be used to understand the complete error budget. This knowledge may be important for the simulation and design of future GRACE-type missions.

Errors in attitude determination may propagate into GRACE-based gravity models either by causing errors in the orientation of the measured non-gravitational acceleration vector or by causing ranging errors.

In the context of the gravity field and steady-state ocean circulation explorer (GOCE) mission (Drinkwater et al., 2007), errors in satellite attitude are well understood. Pail (2005) documents a simulation study on attitude errors. He considers various scenarios of errors in the attitude product, and their impact on GOCE gravity gradients is shown. Frommknecht et al. (2011) provide details about the attitude reconstruction step of the GOCE data processing. They used the so-called *hybridization* approach to merge information provided by the gradiometer and the star tracker instruments using a Kalman filter. Building on this, Stummer et al. (2012) document improvements to the attitude reconstruction method, where a new FIR filter approach replaces the Kalman filter. All these publications rely on a-priori knowledge of the errors in the SC instruments aboard GOCE. A different approach was taken in Stummer et al. (2011), where an estimate of real errors in SC instruments is shown. More recently, Herceg et al. (2017) estimates thermal distortions of the star-camera assembly for the Swarm satellites. Similar idea was applied to the GOCE mission (Siemes et al., 2019), where a new method is presented to combine data from multiple scar-cameras along with an estimation of offsets to their relative orientation as a function of by temperature.

Regarding the GRACE mission, the impact of errors in the satellite attitudes has not yet been fully addressed. Inter-satellite accelerations (ISA) reflecting gravity field variations need to be corrected for non-gravitational accelerations. The latter are measured by accelerometers on board the GRACE satellites. The measurements refer to the Science Reference Frame (SRF) (Case et al., 2010), and need to be rotated to the Inertial Reference Frame (IRF) in which the ISAs are expressed. Attitude errors cause small deviations in the orientation of the non-gravitational acceleration vector in inertial space, which ultimately show up as errors in the ISAs.

Observed inter-satellite ranges refer to the antenna phase centres, but need to be reduced to the Centre of Mass (CoM) of each GRACE satellite. The corresponding correction is referred to as the antenna phase centre (APC) correction. This type of correction is applied to both the GNSS and KBR measurements. The APC is computed as the projection of the estimated antenna phase centre vector along the direction defined by the two CoM of the satellites. This computation requires the antenna phase centre vector to be rotated from the SRF to the IRF. Inaccuracies in the satellite attitudes introduce errors in reduced GNSS and KBR measurements. In this paper we focus only on the APC errors in the KBR ranging data.

The KBR ranging data and the corresponding APC are publicly available as the KBR1B product, which is part of the set of GRACE Level-1B (L1B) products (Case et al., 2010). Other relevant products are the KBR antenna phase centre vector product (VKB1B) and the orientation of each SC head with respect to the SRF (QSA1B). Horwath et al. (2011) identified biases in the pitch and yaw angles of L1B attitude data, which introduce errors in the APC. Horwath et al. also showed improvements in gravity field solutions when removing them. Bandikova et al. (2012) conducted a study on the inter-satellite pointing angles and found systematic effects with the potential to affect GRACE gravity field solutions. In 2012, a new release (RL02) of L1B data has been made available. Following up on the improvements proposed by Horwath et al., the new RL02 version benefits from a recalibration of the QSA1B and VKB1B products (Kruizinga et al., 2010). These results strongly support the hypothesis that errors in APC of KBR data may play a role in GRACE final products and motivate the need to better understand their propagation into gravity field solutions.

There are two main objectives of this study. The first objective is to estimate and model actual errors in GRACE SC data. Errors in SC data are obtained by exploiting the existing SC redundancy on board the GRACE satellites. SC data are part of the GRACE Level-1A (L1A) data products (Case et al., 2010). Using L1A SC data, we build models that describe errors along individual axes of GRACE SCs. These models allow us to propagate realistic SC errors into gravity field models and may be used to simulate SC errors under different scenarios.

The second objective is to assess the impact of estimated attitude errors on GRACE monthly gravity anomaly maps. Realizations of SC attitude errors are first propagated into KBR errors and then into ISA (Liu et al., 2010). From ISA, monthly mass anomaly maps are estimated using the procedure of Liu et al. (2010). The effect of attitude noise on the monthly mass anomaly maps is assessed by comparing them with monthly mass anomaly maps obtained in the presence of synthetic

SC noise.

SCs and their configuration in GRACE satellites have been described in Section 2.5.3. The structure of this section is as follows. In Section 5.2 we analyse real L1A SC data and quantify noise in individual SC axes. The noise realizations are then used in Section 5.3 to build models of attitude noise. In Section 5.4, we discuss the propagation of attitude errors into GRACE inter-satellite ranging data. In Section 5.5, we show the propagation of the SC error models into the satellite attitudes, ISA and monthly gravity field solutions. In Section 5.6, we provide a brief summary of the main findings of the study. Finally, in Section 5.7, we discuss the results obtained and discuss potential applications to future satellite gravimetry missions.

5.2. Attitude Errors

In this section, we provide the basic formalism of rotations and show how we exploit the data of the two independent SCs to quantify attitude errors. The presence of two SCs on board each GRACE satellite provides redundant measurements of the satellites' attitude. The difference between the SC measurements reflects the level of noise in the instruments. We will define the SC measurement errors as small-angle rotations. Then we show how noise in individual SC data propagates into the difference between primary and secondary SCs. This formalism allows us to estimate errors along individual SC axes based on the observed differences between SC measurements.

The relative orientation of two arbitrary reference frames can be modelled in different ways, using either direction-cosine-matrices (DCM), quaternions or angle-axis vectors. In Aerospace Engineering it is frequently needed to define rotations between the reference frame of a vehicle and some external reference frame. The most intuitive way to describe the rotation is to use Cardan angles: roll (α), describing the rotation around the *x*-axis, which in this paper is the along-track direction; yaw (γ) around the *z*-axis which is normally perpendicular (either up or down) to the horizontal plane of the vehicle, and pitch (β) around the *y*-axis, which is chosen to complete the right-handed system. These angles are most commonly used since they correspond to the types of rotations used to manoeuvre aircraft and spacecraft. This set of three rotations can be used to define the orientation of the spacecraft relative to some reference frame.

Each SC on board the GRACE satellites provides attitude information relative to the IRF. In the following, superscript C refers to the science reference frame (SRF), common to all star cameras, S_i to the i-th star camera reference frame, and I to the IRF. To the unacquainted reader, a short introduction to rotations is provided in Appendix A. Several specific references on the topic can be found, e.g., Jekeli (2001).

Let $\mathbf{R}_I^{S_i}$ be the DCM, which transforms vectors from the IRF to the *i*-th SC frame. Each SC measures this rotation with a small error $\boldsymbol{\varepsilon}_{\psi,i}$.

$$\tilde{\mathbf{R}}_I^{S_i} = \mathbf{R}(\boldsymbol{\varepsilon}_{\psi,i})\mathbf{R}_I^{S_i}, \tag{5.1}$$

where $\boldsymbol{\varepsilon}_{\psi,i} \equiv \begin{bmatrix} \varepsilon_{\alpha,i} & \varepsilon_{\beta,i} & \varepsilon_{\gamma,i} \end{bmatrix}^T$ is the vector representing the errors in the roll ($\varepsilon_{\alpha,i}$), pitch ($\varepsilon_{\beta,i}$) and yaw ($\varepsilon_{\gamma,i}$) angles in the measured rotation and where i can be P or S denoting the primary or secondary star camera, respectively. $\mathbf{R}(\boldsymbol{\varepsilon}_{\psi,i})$ is the DCM defined by the vector $\boldsymbol{\varepsilon}_{\psi,i}$, cf., Appendix A. The tilde denotes a measured quantity. The small angle errors $\boldsymbol{\varepsilon}_{\psi,i}$ in the SC frame are assumed to be stationary and well described by a Gaussian distribution.

The relative orientation of each SC with respect to the SRF is known (QSA1B product) and the $I \rightarrow C$ rotation can be written as

$$\tilde{\mathbf{R}}^C_{I,i} = \mathbf{R}^C_{S_i} \mathbf{R}(\boldsymbol{\varepsilon}_{\psi,i}) \mathbf{R}^{S_i}_I. \tag{5.2}$$

Both SCs measure the same rotation $\mathbf{R}^C_I$ and their differences expose the level of noise in the attitude determination system. Eq. (5.2) allows us to describe the differential rotation as a function of the errors $\boldsymbol{\varepsilon}_{\psi,i}$ and $\boldsymbol{\varepsilon}_{\psi,j}$ in the i-th and j-th SCs. The differential rotation between measurements of any two SCs is

$$\begin{aligned} \tilde{\mathbf{R}}^C_{I,i} \left(\tilde{\mathbf{R}}^C_{I,j}\right)^{-1} &= \mathbf{R}^C_{S_i} \mathbf{R}(\boldsymbol{\varepsilon}_{\psi,i}) \mathbf{R}^{S_i}_I \left(\mathbf{R}^C_{S_j} \mathbf{R}(\boldsymbol{\varepsilon}_{\psi,j}) \mathbf{R}^{S_j}_I\right)^{-1} \\ &= \mathbf{R}^C_{S_i} \mathbf{R}(\boldsymbol{\varepsilon}_{\psi,i}) \mathbf{R}^{S_i}_I \mathbf{R}^I_{S_j} \mathbf{R}(-\boldsymbol{\varepsilon}_{\psi,j}) \mathbf{R}^{S_j}_C \end{aligned} \tag{5.3}$$

Notice that $\mathbf{R}^b_c \mathbf{R}^c_a = \mathbf{R}^b_a = \mathbf{R}^b_d \mathbf{R}^d_a$. Therefore,

$$\tilde{\mathbf{R}}^C_{I,i} \left(\tilde{\mathbf{R}}^C_{I,j}\right)^{-1} = \mathbf{R}^C_{S_i} \mathbf{R}(\boldsymbol{\varepsilon}_{\psi,i}) \mathbf{R}^{S_i}_C \mathbf{R}^C_{S_j} \mathbf{R}(-\boldsymbol{\varepsilon}_{\psi,j}) \mathbf{R}^{S_j}_C$$

For small errors $\boldsymbol{\varepsilon}_{\psi}$, the approximation $\mathbf{R}(\boldsymbol{\varepsilon}_{\psi}) \approx \mathbf{I} - \boldsymbol{\Psi}$ holds (cf. Appendix A),

$$\begin{aligned} &= \mathbf{R}^C_{S_i} \left(\mathbf{I} - \boldsymbol{\Psi}^{S_i}_i\right) \mathbf{R}^{S_i}_C \mathbf{R}^C_{S_j} \left(\mathbf{I} + \boldsymbol{\Psi}^{S_j}_j\right) \mathbf{R}^{S_j}_C \\ &= \mathbf{I} - \mathbf{R}^C_{S_i} \boldsymbol{\Psi}^{S_i}_i \mathbf{R}^{S_i}_C + \mathbf{R}^C_{S_j} \boldsymbol{\Psi}^{S_j}_j \mathbf{R}^{S_j}_C - \mathbf{R}^C_{S_i} \boldsymbol{\Psi}^{S_i}_i \mathbf{R}^{S_i}_C \mathbf{R}^C_{S_j} \boldsymbol{\Psi}^{S_j}_j \mathbf{R}^{S_j}_C \end{aligned} \tag{5.4}$$

Neglecting second order terms, we obtain from Eq. (A.5),

$$\begin{aligned} \tilde{\mathbf{R}}^C_{I,i} \left(\tilde{\mathbf{R}}^C_{I,j}\right)^{-1} &\approx \mathbf{I} - \boldsymbol{\Psi}^C_i + \boldsymbol{\Psi}^C_j \\ &= \mathbf{I} - \Delta\boldsymbol{\Psi}^C_{ij} \\ &= \mathbf{R}(\Delta\boldsymbol{\varepsilon}^C_{\psi,ij}) \end{aligned} \tag{5.5}$$

where,

$$\Delta\boldsymbol{\varepsilon}^C_{\psi,ij} \equiv \boldsymbol{\varepsilon}^C_{\psi,i} - \boldsymbol{\varepsilon}^C_{\psi,j}.$$

For each GRACE satellite, equipped with primary and secondary SCs, the differential rotation between individual SC measurements can be computed as

$$\tilde{\mathbf{R}}^C_{I,P} \left(\tilde{\mathbf{R}}^C_{I,S}\right)^{-1} \approx \mathbf{R}(\Delta\boldsymbol{\varepsilon}^C_{\psi}). \tag{5.6}$$

In Eq. (5.6), the rotation $I \rightarrow C$ as measured by the primary SC is applied after the inverse rotation as measured by the secondary SC. If both SC measurements are error-free, this operation would result in the identity matrix. In reality, this operation yields a small angle rotation $\mathbf{R}(\Delta\boldsymbol{\varepsilon}_{\psi}^{C})$, which is caused by the measurement errors in the SCs. Eq. (5.6) shows that the measurement error $\Delta\boldsymbol{\varepsilon}_{\psi}^{C}$, in terms of roll, pitch and yaw angles, can be computed directly from the SC data.

Because of the anisotropy of the SC instruments it is important to understand how errors in each SC axis propagate into $\Delta\boldsymbol{\varepsilon}_{\psi}^{C}$, specifically in terms of their cross- and boresight axes. Eq. (5.5) shows that attitude errors $\Delta\boldsymbol{\varepsilon}_{\psi}^{C}$ in the C-frame equal the difference between errors in the individual SCs rotated to the C-frame. Using the approximate rotation matrix from each SC frame to the SRF (see Fig 2.3), we readily obtain

$$\Delta\boldsymbol{\varepsilon}_{\psi}^{C} = \mathbf{R}_{x}(-135°)\boldsymbol{\varepsilon}_{\psi,P} - \mathbf{R}_{x}(135°)\boldsymbol{\varepsilon}_{\psi,S}. \tag{5.7}$$

Notice that Eq. (5.7) is only valid when assuming that SC errors are small, i.e., in the range where $\sin\theta$ can be approximated by θ and $\cos\theta$ by 1. The following equalities hold: $\cos(\pm 135°) = -\frac{1}{\sqrt{2}}$, $\sin(\pm 135°) = \pm\frac{1}{\sqrt{2}}$, and Eq. (5.7) can be expanded into component-wise notation:

$$\begin{bmatrix} \Delta\varepsilon_{\alpha} \\ \Delta\varepsilon_{\beta} \\ \Delta\varepsilon_{\gamma} \end{bmatrix} = \begin{bmatrix} \varepsilon_{\alpha,P} - \varepsilon_{\alpha,S} \\ \frac{1}{\sqrt{2}}\left(-\varepsilon_{\beta,P} + \varepsilon_{\gamma,P} + \varepsilon_{\beta,S} + \varepsilon_{\gamma,S}\right) \\ \frac{1}{\sqrt{2}}\left(-\varepsilon_{\beta,P} - \varepsilon_{\gamma,P} - \varepsilon_{\beta,S} + \varepsilon_{\gamma,S}\right) \end{bmatrix}. \tag{5.8}$$

The right-hand side can be simplified by adding and subtracting the pitch and yaw errors,

$$\begin{bmatrix} \Delta\varepsilon_{\alpha} \\ \Delta\varepsilon_{\beta} - \Delta\varepsilon_{\gamma} \\ \Delta\varepsilon_{\beta} + \Delta\varepsilon_{\gamma} \end{bmatrix} = \begin{bmatrix} \varepsilon_{\alpha,P} - \varepsilon_{\alpha,S} \\ \frac{2}{\sqrt{2}}\left(\varepsilon_{\gamma,P} + \varepsilon_{\beta,S}\right) \\ \frac{2}{\sqrt{2}}\left(-\varepsilon_{\beta,P} + \varepsilon_{\gamma,S}\right) \end{bmatrix}. \tag{5.9}$$

Notice that the errors $\varepsilon_{\alpha,i}, \varepsilon_{\beta,i}$ correspond to the cross-boresight axes, while $\varepsilon_{\gamma,i}$ corresponds to the boresight axis of a SC. Boresight errors are expected to be a factor 8 larger than cross-boresight errors. Based on Eq. (5.9), we derive expressions for the attitude errors of each SC, where we neglect the cross-boresight terms in the second and third lines:

$$\begin{bmatrix} \varepsilon_{\alpha,P} - \varepsilon_{\alpha,S} \\ \varepsilon_{\gamma,P} \\ \varepsilon_{\gamma,S} \end{bmatrix} = \begin{bmatrix} \Delta\varepsilon_{\alpha} \\ \frac{\sqrt{2}}{2}\left(\Delta\varepsilon_{\beta} - \Delta\varepsilon_{\gamma}\right) \\ \frac{\sqrt{2}}{2}\left(\Delta\varepsilon_{\beta} + \Delta\varepsilon_{\gamma}\right) \end{bmatrix}. \tag{5.10}$$

Under the assumption of independent and identically distributed errors in primary and secondary SC data, Eq. (5.10) allows us to relate differences between SC measurements with errors along the boresight axis of each SC ($\varepsilon_{\gamma,P}$ and $\varepsilon_{\gamma,S}$) and

along a combination of one cross-boresight axis (the x-axes) of each SC. It can also be seen that the cross-boresight axes errors $\varepsilon_{\beta,i}$ (the y-axes) are not estimated. In the following we refer to the left-hand side as *SC error* and to the right-hand side as *SC error estimates*.

We analyse two months of L1A SC data: 2006/02 and 2006/05 and compute the SC error estimates. The statistics are shown in Table 5.1, columns "Obs". Notice that the mean SC error differs significantly from zero. Furthermore, the mean is not time-stationary and may change from month to month.

In Table 5.1, we assume a similar error level for both SCs, such that $\sigma_{\varepsilon_\alpha} = \frac{1}{\sqrt{2}}\sigma_{\varepsilon_{\alpha,P}-\varepsilon_{\alpha,S}}$. From this table, we see that the standard deviation of the first component of the SC error estimates (ε_α) is around 23 µrad. This value is at the edge of the single axis accuracy which is expected to be better than 24 µrad (E. Davis et al., 1999). The primary SC boresight axes error estimates have a standard deviation of 230-290 µrad. For both satellites, this value is seen to change from one month to another by up to 25 µrad. The secondary SC boresight axes error estimates have a standard deviation of about 160-170 µrad. They are therefore more accurate than the primary SC boresight axes. For both satellites, this value changes from one month to another by up to 3 µrad.

Table 5.1: Statistics of SC error estimates, fitted harmonic model and stochastic model in µrad. The mean value of the SC error estimates is attributed to the harmonic model. The stochastic model has zero mean. ε_α represent SC errors along the roll axis, assuming both SCs have the same level of noise along this axis. $\varepsilon_{\gamma,P}$ and $\varepsilon_{\gamma,P}$ represent SC errors along the boresight axis of the primary and secondary SCs, respectively.

µrad	GRACE-A				GRACE-B			
	Obs.		**Harm.**	**Stoc.**	**Obs.**		**Harm.**	**Stoc.**
2006/02	**mean**	**std**	**std**	**std**	**mean**	**std**	**std**	**std**
ε_α	27	23	18	13	2	24	19	14
$\varepsilon_{\gamma,P}$	97	263	198	158	-172	254	209	131
$\varepsilon_{\gamma,S}$	-168	162	124	98	264	170	130	103
2006/05	**mean**	**std**	**std**	**std**	**mean**	**std**	**std**	**std**
ε_α	-10	22	16	14	-16	25	18	16
$\varepsilon_{\gamma,P}$	-66	288	214	164	245	229	163	143
$\varepsilon_{\gamma,S}$	117	165	110	113	-234	167	122	101

If we consider the secondary SC boresight axes, the ratio between cross- and boresight axes accuracy is close to the expected value of 8. If we consider instead the primary SC boresight axes, then this ratio is higher than expected, with a value between 9 and 13.

A comparison of GRACE-A with GRACE-B reveals that the noise standard deviation is similar, except for the primary SC boresight axis, where GRACE-A shows higher standard deviations by up to 59 µrad.

5.3. Modelling SC errors

In this section we exploit Eq. (5.10) to build a model of SC errors based on L1A SC data for the months 2006/02 and 2006/05. They can be used to cover the existing data gaps. They can also be used to study the impact of SC errors on gravity field solutions, in months during which we have no SC data. Such model could also be used to investigate alternative configurations of the SC assembly.

Plotting and inspecting SC error estimates in the time domain reveals a cyclic pattern with a period matching the orbital revolution period of the GRACE satellites. This suggests that SC error estimates in the time domain can be better visualized when individual orbital revolutions are plotted side-by-side against the satellite's true anomaly, an approach first proposed by Bandikova et al. (2012).

Plotting the data in this manner reveals a dependency between the SC error estimates and the satellite's true anomaly. This is seen in Fig. 5.1 as a checkerboard pattern in the top plot and as a series of stripes in the two bottom plots. The SC error estimates can only be computed when measurements exist for both SCs. This explains the large amount of gaps in the SC error estimates. The black regions in Fig. 5.1 correspond to the periods of missing data in one of the SCs. They are caused by periods during which at least one of the star cameras is blinded by the sun or the moon shining in its field of view, either directly or through reflections in the optical camera baffle.

In Fig. 5.2 the square-root of the periodogram estimate of the power spectral density ($\mathrm{PSD}^{\frac{1}{2}}$) of one component of the SC error estimates is shown. The $\mathrm{PSD}^{\frac{1}{2}}$ reveals a set of very sharp, energetic frequencies closely related to multiples of the satellite's orbital period. These spectral peaks have also been observed in the SCs onboard GOCE (Stummer et al., 2011). These peaks are observed in both satellites and in all three components of the SC error estimates. They contain between 50-70% of the total energy.

Furthermore, the error pattern observed in Fig. 5.1 changes over time. A comparison of the error pattern during the first few and last few orbital revolutions shows slight differences in the error pattern. SC errors depend, among others, on the number and brightness of the stars in the field of view. For a given satellite anomaly, a similar pattern of stars is seen in consecutive satellite revolutions. This would explain the strong dependency of the errors with the orbital revolution frequency. Furthermore, the precession of the satellite's orbit causes a slow change in the pattern of stars. This could, in turn, explain the slow change observed in the error pattern depicted in the plots.

Another plausible explanation would be that thermal distortion of the SC assembly would cause measurable displacement of the SC heads. As GRACE's satellites drift through all local times, there are continuously changing sun/shadow configurations, not only during one orbit but also throughout the seasons. Similar thermal distortions have been reported for Swarm (Herceg et al., 2017), and even for GOCE (Siemes et al., 2019) to a lesser extent, since it is in a sun-synchronous orbit where the sun/shadow configuration is almost fixed. In any case, this error pattern indicates an influence of the satellites' environment on the SC measurements.

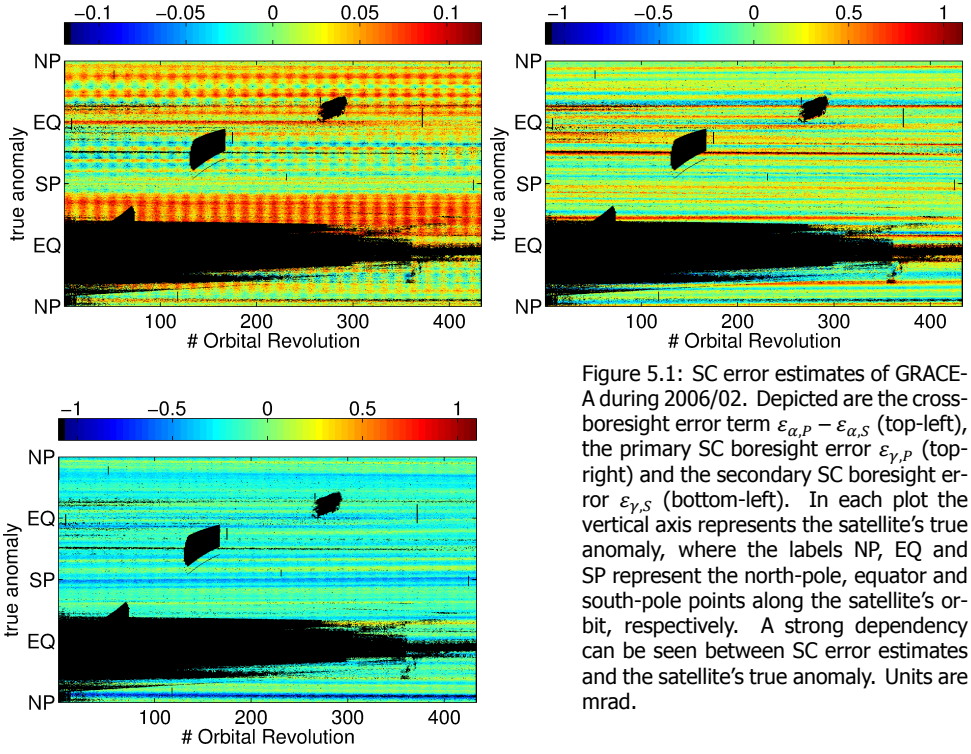

Figure 5.1: SC error estimates of GRACE-A during 2006/02. Depicted are the cross-boresight error term $\varepsilon_{\alpha,P} - \varepsilon_{\alpha,S}$ (top-left), the primary SC boresight error $\varepsilon_{\gamma,P}$ (top-right) and the secondary SC boresight error $\varepsilon_{\gamma,S}$ (bottom-left). In each plot the vertical axis represents the satellite's true anomaly, where the labels NP, EQ and SP represent the north-pole, equator and south-pole points along the satellite's orbit, respectively. A strong dependency can be seen between SC error estimates and the satellite's true anomaly. Units are mrad.

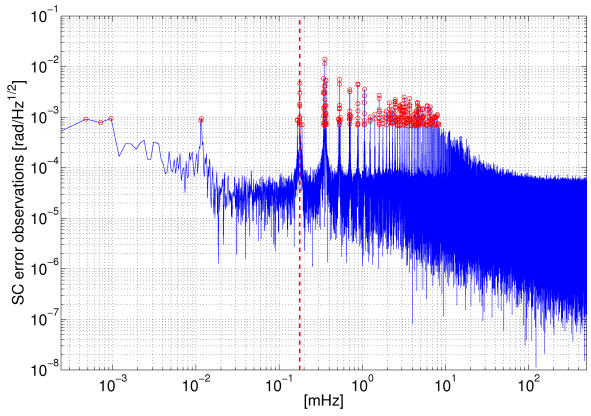

Figure 5.2: PSD$^{\frac{1}{2}}$ of the first component of SC error estimates ($\varepsilon_{\alpha,P} - \varepsilon_{\alpha,S}$) for GRACE-A during 2006/02. Sharp peaks of high magnitude can be seen in the plot, close to the harmonics of the orbital revolution frequency, marked with a dashed red line. They correspond to the periodic features observed in the spatial domain. Similar peaks are found for all axes and both months of data. Red dots highlight the 300 most energetic spectral components which are used to form a harmonic noise model. The zero-frequency component (bias, not shown) is always part of the harmonic model.

From Fig. 5.2 we conclude that SC error estimates reveal two distinct components. A random component with smooth spectral signature, and a systematic component with energy distributed over the harmonics of the satellite orbital frequency. We refer to these distinct SC error components as *stochastic* component and *harmonic* component, respectively. The distinction between these two components is purely based on their spectral properties; it is not implied that each of them can be attributed to a single specific error source or even that they must be caused by distinct error sources.

There are two reasons why it is necessary to separate such two components of the SC error estimates. Firstly, interactions of the satellite with its surrounding map presumably into harmonic errors, which means that potentially, one could be able to reduce such errors. For example, we could optimize the orbit to achieve a more uniform star distribution in the case of attitude errors; or one could chose a sun-synchronous orbit which would minimize thermal-load on the satellites in the case of (hypothetical) thermal errors. Therefore, the harmonic error component allows one to quantify the potential benefit of such improvements and whether they would be relevant in the context of gravity field modelling. Another reason to separate these two components is very practical. ARMA models have proven to be a very efficient tool to model random errors; they are now routinely used to model noise of satellite gravity data. However, for random errors with sharp spectral features, they are less suited unless the order of the ARMA model is chosen extremely high, which in turn reduces the numerical efficiency of the ARMA noise model. Separating the SC error estimates in harmonic and stochastic components allows the ARMA models to be efficiently used while keeping the overall noise spectrum realistic.

5.3.1. The harmonic component of SC errors

Because of their spectral characteristics, harmonic SC errors can be modelled by a relatively small number of sinusoids. Due to the presence of gaps in the SC measurement time series, we estimate the amplitude and phase of these sinusoids using the least-squares (LS) approach. We use the Inverse Discrete Fourier Transform (IDFT) as a functional model. Consider the input signal $y_i \equiv y(t_0 + i\Delta t), i = 0, 1, \dots, N-1$ and the set of complex Fourier coefficients Y_j, where N represents the total number of Fourier coefficients and the total number of points, such that,

$$\begin{bmatrix} y_0 \\ y_1 \\ \vdots \\ y_{N-1} \end{bmatrix} = \frac{1}{N} \begin{bmatrix} e^{\frac{i2\pi\cdot 0\cdot 0}{N}} & e^{\frac{i2\pi\cdot 0\cdot 1}{N}} & \cdots & e^{\frac{i2\pi\cdot 0\cdot (N-1)}{N}} \\ e^{\frac{i2\pi\cdot 1\cdot 0}{N}} & e^{\frac{i2\pi\cdot 1\cdot 1}{N}} & \cdots & e^{\frac{i2\pi\cdot 1\cdot (N-1)}{N}} \\ \vdots & \vdots & \ddots & \vdots \\ e^{\frac{i2\pi\cdot (N-1)\cdot 0}{N}} & e^{\frac{i2\pi\cdot (N-1)\cdot 1}{N}} & \cdots & e^{\frac{i2\pi\cdot (N-1)^2}{N}} \end{bmatrix} \begin{bmatrix} Y_0 \\ Y_1 \\ \vdots \\ Y_{N-1} \end{bmatrix}, \tag{5.11}$$

which is a linear and invertible system of equations.

The harmonic SC errors appear in the spectral domain as very sharp peaks with high energy. Only a small subset $\mathbf{Y}_m, \forall m \in [m_1, m_2, ..., m_M]$ with a total of M complex coefficients of the full set of Fourier coefficients $\mathbf{Y}_i, \forall i \in [0, ..., N-1]$ is required to model the harmonic SC errors. The complex coefficients to be used

in the model correspond to the M most energetic spectral components. They are selected from an initial, approximate, spectrum computed by filling the gaps in the original SC error estimates with zeros. This approximate spectrum is only used to determine which spectral components will be estimated.

The choice of how many coefficients should be used is a trade-off between the number of parameters used to describe the model and capturing enough energy to describe the harmonic error component. Selecting too many parameters leads to a leakage of stochastic errors into the harmonic model. This is undesirable because a more adequate model can be used to describe the stochastic SC errors, as will be discussed in Section 5.3.2.

Due to gaps in the SC data, only the subset $\mathbf{y}_l, \forall l \in [l_1, l_2, ..., l_L]$ with a total of L SC error estimates is available. Keeping only the L lines and M columns of Eq. (5.11) results in the following model,

$$\begin{bmatrix} y_{l_1} \\ y_{l_2} \\ \vdots \\ y_{l_L} \end{bmatrix} = \begin{bmatrix} e^{\frac{i2\pi \cdot l_1 \cdot m_1}{N}} & e^{\frac{i2\pi \cdot l_1 \cdot m_2}{N}} & \cdots & e^{\frac{i2\pi \cdot l_1 \cdot m_M}{N}} \\ e^{\frac{i2\pi \cdot l_2 \cdot m_1}{N}} & e^{\frac{i2\pi \cdot l_2 \cdot m_2}{N}} & \cdots & e^{\frac{i2\pi \cdot l_2 \cdot m_M}{N}} \\ \vdots & \vdots & \ddots & \vdots \\ e^{\frac{i2\pi \cdot l_L \cdot m_1}{N}} & e^{\frac{i2\pi \cdot l_L \cdot m_2}{N}} & \cdots & e^{\frac{i2\pi \cdot l_L \cdot m_M}{N}} \end{bmatrix} \begin{bmatrix} Y_{m_1} \\ Y_{m_2} \\ \vdots \\ Y_{m_M} \end{bmatrix}. \tag{5.12}$$

We assume that all observations are uncorrelated and have the same unknown standard deviation σ_y, so that the SC error estimates variance-covariance matrix is $\mathbf{C_y} \equiv \sigma_y^2 \mathbf{I}$. As seen in Fig. 5.1, gaps cluster in large regions, resulting in unstable linear system of equations, whose solutions show strong oscillations in the areas void of data. To mitigate this behaviour, we apply regularization (Tikhonov et al., 1977), in the form of a set of pseudo-observations, which are defined only over the gapped regions of the SC error estimates. Hence, the extended mathematical model is

$$\begin{bmatrix} \mathbf{y} \\ \mathbf{0} \end{bmatrix} = \begin{bmatrix} \mathbf{A} \\ \mathbf{A}_g \end{bmatrix} \mathbf{Y_m}. \tag{5.13}$$

The variance-covariance matrix of the pseudo-observations is $\mathbf{C}_g \equiv \sigma_g^2 \mathbf{I}$, where σ_g is the standard deviation of the noise in the pseudo-observations. Then, the regularized solution is obtained as,

$$\bar{\mathbf{Y}}_m = \left(\mathbf{A}^T \mathbf{A} + k \mathbf{A}_g^T \mathbf{A}_g\right)^{-1} \left(\mathbf{A}^T \mathbf{y}\right), \tag{5.14}$$

where $k = \frac{\sigma_y^2}{\sigma_g^2}$ is the regularization parameter. If the standard deviation of noise in the pseudo-observations is assumed to be large ($\sigma_g \to \infty$) then $k \to 0$. In this situation, no regularization is applied, resulting in potentially unstable LS solutions. On the other hand, if $\sigma_g = \sigma_y$, then $k = 1$, and, in this case, the pseudo-observations have the same weight as the observations. This is equivalent to assigning zero values to missing data, which, as we argued before, is undesirable. Thus, both extremes cases, $k = 0$ and $k = 1$, lead to sub-optimal results. A certain intermediate value of k corresponds to a solution which suitably represents the harmonic SC

errors. This solution is defined as the one which conserves the total energy of the *harmonic* component in the SC error estimates.

The total energy ξ' of the observed harmonic component, which contains data gaps, can be computed as

$$\xi' = \sum_m \| \mathbf{Y}_m \|^2 . \tag{5.15}$$

However, the fitted harmonic model contains no gaps. In view of Parseval's identity, the total energy of the observed and fitted harmonic components can only be compared if the observed harmonic component is up-scaled by the ratio $\frac{N}{L}$ between the total number and the number of valid SC error estimates. This means that Eq. (5.15) must be replaced by the expression for the up-scaled energy,

$$\xi = \frac{N}{L} \sum_m \| \mathbf{Y}_m \|^2 \tag{5.16}$$

The following procedure is used to fit a harmonic model to the gapped SC error estimates:

1. Assign zero values to the missing SC error estimates to compute an approximate PSD. This PSD is used to find the set of M most energetic frequency components in the SC error estimates. For one month of data, the PSD yields around 10^6 Fourier coefficients. However, only 100 to 300 most energetic components typically contain between 50%-70% of the total energy. In our models we chose the value of $M = 300$. This number is empirically chosen as a threshold beyond which adding more frequency components no longer significantly changes the total energy of the harmonic component. In Fig. 5.2 they are marked with red circles.

2. Compute the target total energy ξ of the harmonic model from the selected set of coefficients $\mathbf{Y_m}$, cf., Eq. (5.16).

3. An initial value of the regularization parameter is chosen and the regularized solution is computed.

4. The regularization procedure is iterated with different parameters k_i, until the obtained solution is within a threshold δ of the target total energy,

$$\left| \xi - \sum_m \| \bar{\mathbf{Y}}_m \|^2 \right| < \delta, \tag{5.17}$$

   If the total energy is too high, the solution needs more regularization ($k_i > k_{i-1}$). Otherwise the regularization parameter should be reduced ($k_i < k_{i-1}$).

This procedure yields a model for the harmonic error component. In the absence of information in gapped regions, it interpolates the information observed in the regions with measurements instead of assuming zero data in the gaps. We do not

state that such a model represents the real, unknown errors in the gapped regions. However, we can state that such a model is the one which, in the whole domain, most closely represents the harmonic error observed in the non-gapped regions.

The results of the outlined algorithm are shown in Fig. 5.3. Table 5.1 shows the statistics of the fitted harmonic models and of the respective residuals. It can be seen that the harmonic model, despite comprising only a small set of frequency components, contains ≈65% of the total SC error estimates energy.

The fitted harmonic model consists of one set of DFT coefficients for each component of the SC error estimates: $\mathbf{Y}_m^{\varepsilon_{\alpha,P}-\varepsilon_{\alpha,S}}$, $\mathbf{Y}_m^{\varepsilon_{\gamma,P}}$ and $\mathbf{Y}_m^{\varepsilon_{\gamma,S}}$. This model is used to generate a harmonic error realization for all axes of both SCs. Applying the IDFT operation to $\mathbf{Y}_m^{\varepsilon_{\gamma,P}}$ and $\mathbf{Y}_m^{\varepsilon_{\gamma,S}}$ yields the time-series of harmonic errors along the boresight axes of the primary and secondary SCs, respectively.

Regarding the cross-boresight model $\mathbf{Y}_m^{\varepsilon_{\alpha,P}-\varepsilon_{\alpha,S}}$, we assume that the magnitude of the error along each individual axis $\mathbf{Y}_m^{\varepsilon_{\alpha,P}}$ and $\mathbf{Y}_m^{\varepsilon_{\alpha,S}}$ is equally divided among both SCs and that they are orthogonal in the complex plane. This results in a solution,

$$\begin{aligned}\mathbf{Y}_m^{\varepsilon_{\alpha,P}} &= -\frac{\sqrt{2}}{2}e^{-i\frac{\pi}{4}}\mathbf{Y}_m^{\varepsilon_{\alpha,P}-\varepsilon_{\alpha,S}}\\ \mathbf{Y}_m^{\varepsilon_{\alpha,S}} &= \frac{\sqrt{2}}{2}e^{\frac{\pi}{4}}\mathbf{Y}_m^{\varepsilon_{\alpha,P}-\varepsilon_{\alpha,S}}.\end{aligned} \tag{5.18}$$

These two components are obtained as rotations in the complex plane by ±45° of the corresponding cross-boresight model, scaled to satisfy the observation in Eq. (5.10). The zero-frequency component (mean value) is not an imaginary value. Therefore, assuming that it is also equally divided among both SCs, $\mathbf{Y}_0^{\varepsilon_{\alpha,P}} = -\frac{1}{2}\mathbf{Y}_0^{\varepsilon_{\alpha,P}-\varepsilon_{\alpha,S}}$ and $\mathbf{Y}_0^{\varepsilon_{\alpha,S}} = \frac{1}{2}\mathbf{Y}_0^{\varepsilon_{\alpha,P}-\varepsilon_{\alpha,S}}$

The two remaining cross-boresight axes $\mathbf{Y}_m^{\varepsilon_{\beta,P}}$ and $\mathbf{Y}_m^{\varepsilon_{\beta,S}}$ are not observable, cf., Eq. (5.10). We assume that the magnitude of their DFT coefficients is the same as $\mathbf{Y}_m^{\varepsilon_{\alpha,P}}$ and $\mathbf{Y}_m^{\varepsilon_{\alpha,S}}$ while their phases are randomized.

5.3.2. The stochastic component of SC errors

The stochastic component of the SC error estimates is obtained by subtracting the harmonic model from the original SC error estimates. This yields the random measurement errors shown in the second column of Fig. 5.3. In this section, the power spectrum of the stochastic SC error estimates is computed. An Autoregressive-moving-average (ARMA) model is then fitted to the computed power spectrum (Klees et al., 2003). Using ARMA models to describe the random errors in SC measurements allows generating arbitrary long realizations with the same spectral signature.

We assume that all cross-boresight stochastic errors, $\varepsilon_{\alpha,P}$, $\varepsilon_{\beta,P}$, $\varepsilon_{\alpha,S}$ and $\varepsilon_{\beta,S}$ have the same power spectrum and are uncorrelated. Then $\mathrm{PSD}^{\frac{1}{2}}(\varepsilon_{\alpha,P} - \varepsilon_{\alpha,S}) = \sqrt{2}\,\mathrm{PSD}^{\frac{1}{2}}(\varepsilon_{\alpha})$, where $\mathrm{PSD}^{\frac{1}{2}}$ represents the square-root of power spectrum operator and ε_{α} represents the stochastic error along all cross-boresight axes. Applying the

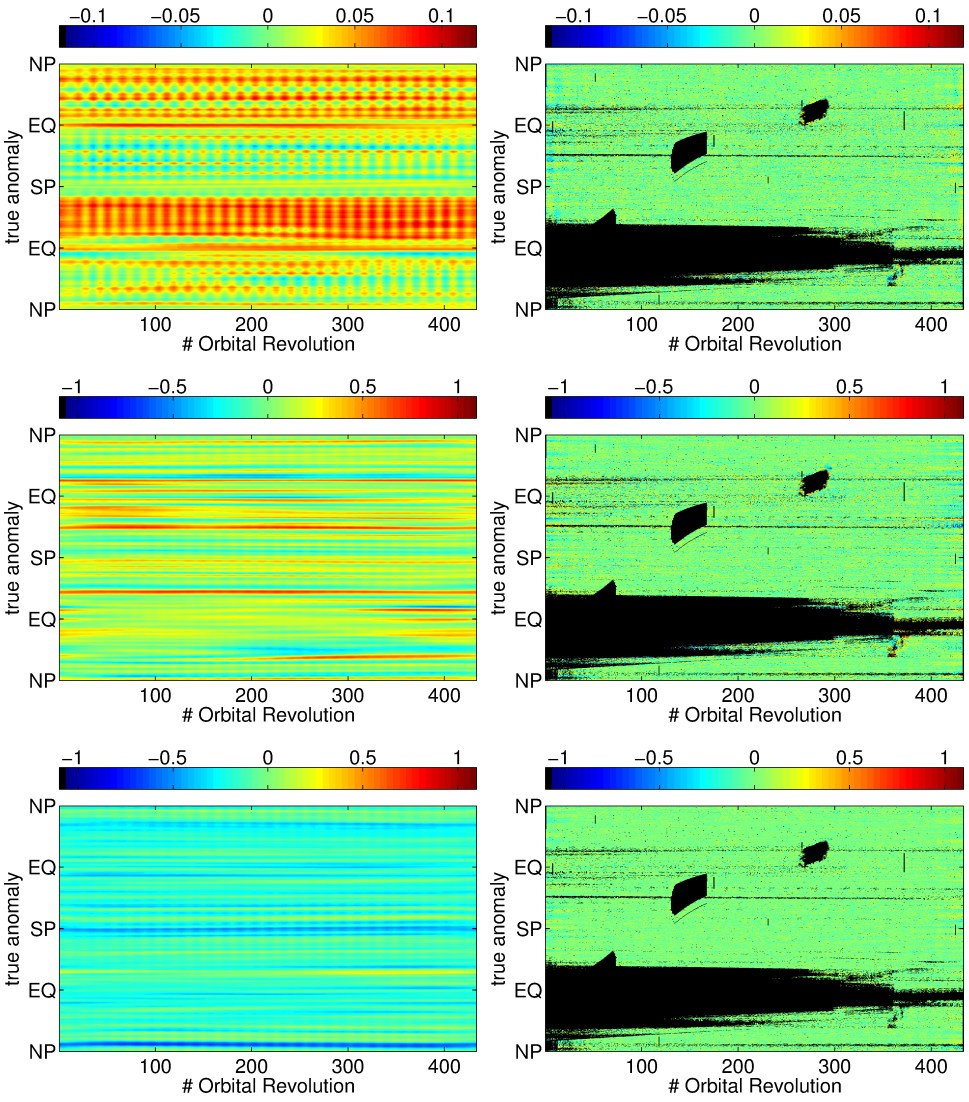

Figure 5.3: Fitted harmonic model (left), fit residuals (right). SC error estimates along the roll axis (top), pitch (middle) and yaw (bottom). Models were fitted using 300 complex Fourier coefficients. The residuals show random error, showing that the fitted harmonic models adequately describe observed patterns in SC error estimates (Fig. 5.1). Units are mrad.

operator $\mathrm{PSD}^{\frac{1}{2}}$ to Eq. (5.10) yields,

$$\begin{bmatrix} \mathrm{PSD}^{\frac{1}{2}}(\varepsilon_\alpha) \\ \mathrm{PSD}^{\frac{1}{2}}(\varepsilon_{\gamma,P}) \\ \mathrm{PSD}^{\frac{1}{2}}(\varepsilon_{\gamma,S}) \end{bmatrix} = \frac{\sqrt{2}}{2} \begin{bmatrix} \mathrm{PSD}^{\frac{1}{2}}(\Delta\varepsilon_\alpha) \\ \mathrm{PSD}^{\frac{1}{2}}(\Delta\varepsilon_\beta - \Delta\varepsilon_\gamma) \\ \mathrm{PSD}^{\frac{1}{2}}(\Delta\varepsilon_\beta + \Delta\varepsilon_\gamma) \end{bmatrix}. \tag{5.19}$$

Notice that, similarly to the harmonic component, the presence of gaps in the SC error estimates requires the power spectrum to be up-scaled by the ratio $\frac{N}{L}$.

Eq. 5.19 yields the power spectra of stochastic errors along the primary SC boresight axis ($\varepsilon_{\gamma,P}$), the secondary SC boresight axis ($\varepsilon_{\gamma,S}$) and all the cross-boresight axes of both SCs (ε_α). The ARMA models fitted to each component of the stochastic SC error are shown in Fig. 5.4.

The standard deviation of each SC error component is shown in Table 5.1. We see that the accuracy of the cross-boresight axes is similar for different months and for different satellites. Moreover, the standard deviation of the harmonic SC errors is higher than the standard deviation of the stochastic SC errors.

Generating a realization of stochastic SC errors along all the individual axes of both SCs is a matter of generating realizations of the fitted ARMA models. The error along the primary and secondary SC boresight axis is described by the ARMA models $\varepsilon_{\gamma,P}$ and $\varepsilon_{\gamma,S}$, respectively. As for the cross-boresight axes, we assume their accuracy to be similar. Therefore, we use different realizations of ARMA model ε_α for each cross-boresight axis: $\varepsilon_{\alpha,P}$, $\varepsilon_{\alpha,S}$, $\varepsilon_{\beta,P}$, $\varepsilon_{\beta,S}$.

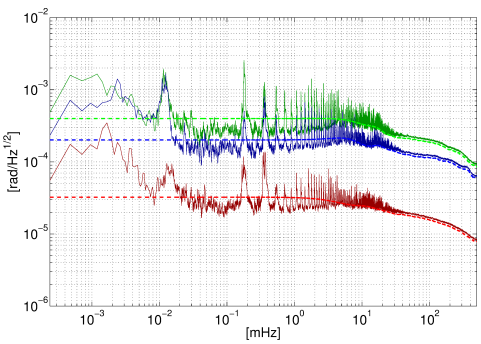

Figure 5.4: Spectra of fitted ARMA models and $\mathrm{PSD}^{\frac{1}{2}}$ of stochastic SC error estimates of GRACE-A during 2006/02. Red refers to the cross-boresight component (ε_α), blue to the secondary SC boresight error ($\varepsilon_{\gamma,S}$) and green to the primary SC boresight error ($\varepsilon_{\gamma,P}$). The solid lines represent the periodogram estimates of the square root power spectral density of stochastic SC error estimates. These have been smoothed to reduce noise in the high frequency part of the spectrum. The dashed lines represent the ARMA models fitted to each component. They have orders (100,0), (93,0) and (95,0) for the cross-boresight, primary SC boresight and secondary SC boresight, respectively.

5.4. Analysis of attitude error propagation

In this section we analyse how attitude errors introduce errors in the APC of KBR measurements. The APC λ is defined as the projection of the vector pointing from the CoM to the antenna phase centre onto the line-of-sight (LOS) direction (Fig. 5.5),

$$\lambda = \| \mathbf{p} \| \cos(\theta), \tag{5.20}$$

where $\mathbf{p}$ is the relative position of the antenna phase centre with respect to the satellite's CoM, and θ is the angle between $\mathbf{p}$ and **LOS**, i.e., the *inter-satellite pointing angle*.

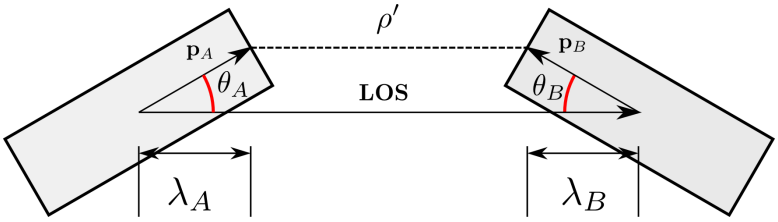

Figure 5.5: Illustration of antenna phase centre correction to KBR data. KBR system measures ρ', the distance between the antenna phase centres of the two GRACE satellites. The range ρ between the two CoMs is obtained by adding the APC of each satellite to the KBR measurement, $\rho = \rho' + \lambda_A + \lambda_B$. The inter-satellite pointing angles θ_i represent the angles between vectors $\mathbf{p}_i$ and the LOS, where i=A,B for GRACE-A and GRACE-B, respectively.

5

In the presence of attitude errors, the orientation of the antenna phase centre vector $\mathbf{p}^I$ in the IRF is determined inaccurately and the inter-satellite pointing angle θ is perturbed. Let us introduce the noisy quantities $\tilde{\theta} = \theta + \varepsilon_\theta$ and $\tilde{\lambda} = \lambda + \varepsilon_\lambda$, where we assume that ε_θ and ε_λ are normally distributed errors, in the pointing angle and APC, respectively. Linearisation of the APC around the nominal inter-satellite pointing angle yields

$$\sigma_{\varepsilon_\lambda} = \| \mathbf{p} \| \sin(\theta)\, \sigma_{\varepsilon_\theta}, \tag{5.21}$$

where $\sigma_{\varepsilon_\lambda}$ and $\sigma_{\varepsilon_\theta}$ is the standard deviation of the errors in the APC and inter-satellite pointing angles, respectively.

The inter-satellite pointing angle is actively controlled by the attitude and orbit control system (AOCS). GRACE AOCS is designed to keep these angles below $\theta < 4\,\mathrm{mrad}$ (Herman et al., 2004). In this range, $\sin(\theta)$ can be approximated by θ. Furthermore, we assume APC errors of both satellites to be uncorrelated and identically distributed, so that considering the contribution of both GRACE-A and B, yields the standard deviation

$$\sigma_{\varepsilon_\lambda} = \sqrt{2} \| \mathbf{p} \| \theta\, \sigma_{\varepsilon_\theta}. \tag{5.22}$$

Eq. (5.22) shows that the impact of attitude errors increases proportionally to i) the distance between the antenna phase centre and the CoM and ii) the inter-satellite pointing angle θ.

The distance between the antenna and the CoM is $\| \mathbf{p} \| \approx 1.5\,\mathrm{m}$ for both satellites. As will be shown in Section 5.5.1, the accuracy in the determination of the inter-satellite pointing angle is better than $\sigma_{\varepsilon_\theta} < 170\,\mu\mathrm{rad}$. Considering a worst-case scenario, according to Eq. (5.22), the corresponding standard deviation of the error in inter-satellite ranges is $\sigma_{\varepsilon_\lambda} = 1.4\,\mu\mathrm{m}$. The KBR accuracy is $10\,\mu\mathrm{m}$ (Kang et al., 2006), which means that the standard deviation of the attitude errors is about 7 times smaller than the standard deviation of the noise in the KBR ranging data.

On the other hand, the standard deviation alone does not provide a comprehensive understanding of propagated attitude errors. One should also analyse how the error is distributed over the spectrum. There might exist frequency bands at which the impact of attitude errors is more substantial than in average.

5.5. Error propagation

In this section we analyse to what extent SC errors contribute to the overall error budget of GRACE time-varying gravity field models. Section 5.5.1 describes the propagation of SC errors into satellite attitude data. The impact of data gaps in the SC time series is discussed in Section 5.5.2. In Section 5.5.3 the propagation of attitude errors into inter-satellite accelerations is discussed. In Section 5.5.4 we discuss the likely impact of degraded attitude control. Finally, in Section 5.5.5 we show how SC errors propagate into GRACE gravity field solutions.

5.5.1. Propagation of SC errors into satellite attitudes

In the presence of multiple SCs, it is necessary to compute an estimate of the satellite attitude from all available measurements. A description of the official combination method used by JPL can be found in Romans, 2003 and S.-C. Wu et al., 2006. In Appendix B, this method, originally developed for attitude quaternions, is re-written in terms of direction-cosine matrices.

A summary of the official procedure for combining SC measurements for GRACE is (S.-C. Wu et al., 2006):

1. Compute the small angle difference $\Delta\boldsymbol{\varepsilon}_{\psi}^{C}$ between both SC measurements, cf., Eq. (5.6)
2. The optimal correction to the first SC measurement is computed, cf., Eq. (B.7), as

$$\boldsymbol{\varepsilon}_{\text{opt}} = \left(\boldsymbol{\Lambda}_1^C + \boldsymbol{\Lambda}_2^C\right)^{-1} \boldsymbol{\Lambda}_2^C \Delta\boldsymbol{\varepsilon}_{\psi}^{C}, \tag{5.23}$$

where the information matrix $\boldsymbol{\Lambda}_i^C$ for each SC in the C-frame is defined as

$$\boldsymbol{\Lambda}_i^C = \mathbf{R}_x(\pm 135°)\mathbf{C}_i^{-1}\mathbf{R}_x(\mp 135°), \tag{5.24}$$

and the error variance-covariance matrix $\mathbf{C}_i$ for a single SC is defined as,

$$\mathbf{C}_i = \begin{bmatrix} 1 & 0 & 0 \\ 0 & 1 & 0 \\ 0 & 0 & \kappa^2 \end{bmatrix} \sigma^2, \tag{5.25}$$

with σ^2 being the variance of the errors along the SC cross-boresight axes and $\kappa = 8$ is the ratio between the standard deviation of errors along the boresight and the cross-boresight axes (Romans, 2003). It can be shown that

$$\left(\boldsymbol{\Lambda}_1^C + \boldsymbol{\Lambda}_2^C\right)^{-1} \boldsymbol{\Lambda}_2^C = \frac{1}{2}\begin{bmatrix} 1 & 0 & 0 \\ 0 & 1 & -\lambda \\ 0 & -\lambda & 1 \end{bmatrix}, \tag{5.26}$$

where

$$\lambda = \frac{\kappa^2 - 1}{\kappa^2 + 1}.$$

3. Compute the optimal satellite attitude $\mathbf{R}^{C}_{I,\text{opt}}$, cf., (B.8).

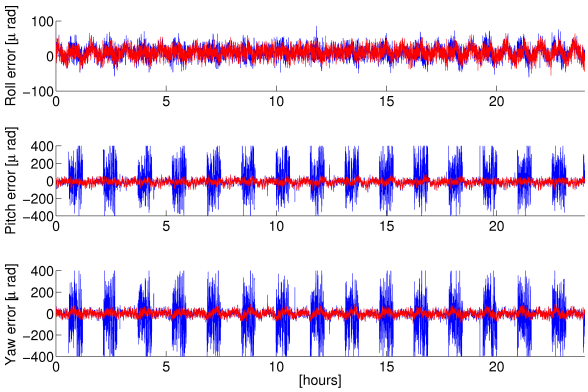

Figure 5.6: Propagated SC errors into GRACE-A attitude during 2006/05/01. Red line depicts hypothetical situation where both SCs are always active. Blue line takes into account periods in which one of the SCs is inactive.

The results of applying this SC measurement combination to synthetic realizations of SC errors for the months 2006/02 and 2006/05, are shown in Table 5.2. The red line in Fig. 5.6 shows the corresponding satellite attitude errors during one day of 2006/02. From Table 5.2, we conclude that the pitch and yaw angles of the satellite attitudes are less accurately determined than the roll angles. Errors in the satellites attitudes are therefore not isotropic.

5.5.2. Quantifying the impact of SC data gaps

There is a relatively large amount of gaps in the SC data (see Table 5.2). Gaps reduce the quality of attitude determination. The SC combination procedure described in Section 5.5.1 can only be applied when both SCs provide data. When one of the SCs is inactive, the data from the other SC are used to determine the attitudes. We quantify the impact of SC data gaps by comparing two error propagation scenarios; in one scenario both SCs are assumed to be constantly active and in the other we use real SC time series to flag time instants where one of the SCs is inactive.

Figure 5.6 shows the SC error propagation for both scenarios. It can be seen that, during periods in which only one SC is available, errors in the pitch and yaw angles are amplified by an order of magnitude. The roll angles are only slightly worse during single SC operation. Table 5.2 shows the overall standard deviation of satellite attitude errors with and without data gaps. Obviously, the existence of gaps in the SC data severely affects the accuracy of the attitude determination. For instance, during the month of 2006/05, the presence of data gaps amplifies the error level in the pitch and yaw angles by a factor of 4.

Table 5.2: Standard deviation of satellite attitude errors in µrad. Depicted two error propagation simulations; one which assumes both SCs are always active (nominal) and another where L1A SC data is used to flag periods when one of the SCs is inactive (gaps). ε_α, ε_β and ε_γ represent errors in the roll, pitch and yaw satellite attitude angles, respectively.

µrad		GRACE-A		GRACE-B	
		Gaps	**Nominal**	**Gaps**	**Nominal**
2006/02	% gaps	22%		21%	
	ε_α	17	16	18	17
	ε_β	65	29	70	30
	ε_γ	63	28	80	29
2006/05	% gaps	44%		48%	
	ε_α	17	15	20	17
	ε_β	101	27	119	31
	ε_γ	104	26	122	29

From Table 5.2, we can also conclude that the anisotropy of the errors in the satellite attitudes is accentuated by the amount of gaps in the SC data. Determination of the roll-axis direction is the least accurate, due to the worse accuracy of the pitch and yaw angles. Regarding the month of 2006/05, we can state that the attitude accuracy of GRACE satellites is better than $\sqrt{2} \cdot 120 = 170$ µrad. This value might be exceeded in other months, possibly with larger amounts of SC data gaps, not considered in this paper.

5.5.3. Propagation of attitude errors into inter-satellite accelerations

ISA are derived from inter-satellite ranges by means of numerical double differentiation. For details about the methodology, we refer to Liu et al., 2010. To quantify the impact of SC errors in terms of ISA, we compute the difference between the so-called *reference ISA residuals* and the *perturbed ISA residuals*.

The reference ISA residuals are obtained as the difference between the observed ISA and the modelled ISA. The modelled ISA are computed with state-of-the-art force models, which comprise the static gravity field model DGM-1S (Farahani et al., 2013), the corresponding mean monthly gravity field solution DMT-2 (data processing details in Farahani, 2013), tidal model EOT11a (Savcenko et al., 2012), the model of non-tidal mass-redistribution in the atmosphere and oceans AOD1B RL05 (Flechtner et al., 2014a), L1B RL02 products, and other tidal and relativistic effects. Because the monthly gravity field solution is included in the background force model, all known signals are removed from the reference ISA residuals. Therefore, we consider the remaining unknown "signal", i.e. the reference ISA residuals, as an estimate of the *total error* in GRACE data. Notice that the DMT-2 solutions are filtered (or regularized) to prevent propagation of data noise. This is the reason why the reference ISA residuals are not zero when the DMT-2 solution is included in the background force model.

As compared to DMT-1, a number of improvements are applied in the production

of DMT-2. Firstly, an accurate stochastic description of noise is obtained in the frequency domain on a monthly basis using ARMA models. Usage of these models allows for a proper frequency-dependent data weighting at the inversion stage. Furthermore, it facilitates an accurate computation of covariance matrices of noise in estimated spherical harmonic coefficients, which are used when unconstrained monthly solutions are subject to a statistically-optimal Wiener filter (Klees et al., 2008; Liu et al., 2010). Secondly, data prior to the inversion are subject to an advanced high-pass filtering, which uses a spatially-dependent weighting scheme, so that the low-frequency noise (which is caused by inaccuracies in satellites' orbits, Ditmar et al. (2012)) is primarily estimated based on data collected over areas with minor mass variations, e.g., oceans and deserts. On the one hand, this efficiently suppresses the noise and, on the other hand, preserves mass transport signals in data. Thirdly, DMT-2 benefits from the usage of the release 2 of GRACE level-1B data. Finally, latest background force models are taken into account when the DMT-2 model is produced.

To compute the perturbed ISA residuals, we generate synthetic SC errors and propagate them into satellite attitude errors. They are added to the measured satellite attitudes resulting in a custom SCA1B satellite attitude product. Furthermore, the generated attitudes are used to compute the corresponding KBR APC, resulting in a custom KBR1B ranging product. The perturbed ISA residuals are computed by the same procedure as the reference ISA residuals, but making use of the custom SCA1B and KBR1B products. The differences between the two ISAs reflect the impact of the synthetic SC errors, and provide an upper bound of the impact of SC errors in terms of ISA and later on in terms of monthly gravity field solutions.

Because both ISAs use real GRACE data, they contain real SC errors, which are present in the L1B data products. In fact, the perturbed ISA residuals contain SC errors twice; from the GRACE L1B data products and from the synthetic SC errors we add to the data. However, taking the difference between the reference and perturbed ISA residuals will cancel the real SC errors common to both, leaving only the impact of the synthetic SC errors.

Figure 5.7 shows the $\mathrm{PSD}^{\frac{1}{2}}$ of ISA errors, without any data gaps. The contribution of SC errors is flat up to 3 mHz, where double differentiation starts to amplify the high frequency noise. The stochastic error component is dominant in the frequency range above 10 mHz; the harmonic component is dominant in the frequency range 3-10 mHz. Overall, in terms of RMS, the total SC error accounts for 7% of the total noise.

In Section 5.5.2 we analysed the impact of SC data gaps on the attitude product. We have seen that SC data gaps cause non-stationary errors, for which the $\mathrm{PSD}^{\frac{1}{2}}$ is not a suitable representation. Therefore, to present the impact of SC data gaps in terms of $\mathrm{PSD}^{\frac{1}{2}}$, we compare two stationary total SC error realizations: full data gaps, where one SC is always inactive, and zero data gaps, where both SCs are always operational. They represent the upper and lower bounds on the impact of data gaps in ISA and are shown in the left plot in Fig. 5.8. Notice that the zero data gaps total SC error realization is the same as in Fig. 5.7. In the worst case

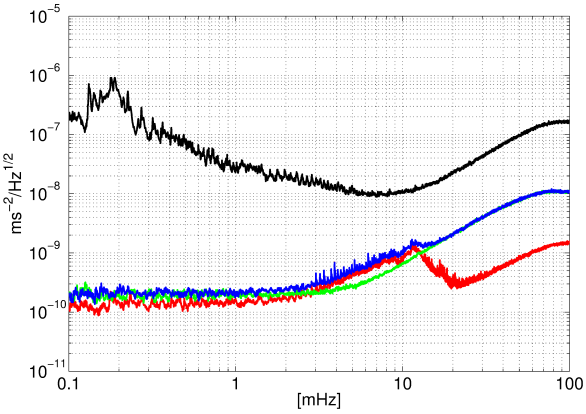

Figure 5.7: PSD$^{\frac{1}{2}}$ of errors in inter-satellite accelerations during 2006/05. Depicted are the total error (black), the harmonic SC error (red), the stochastic SC error (green) and the total SC error (blue). No SC data gaps are considered.

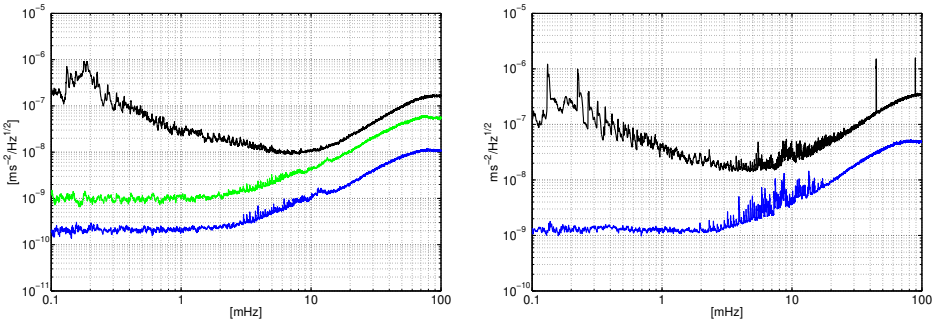

Figure 5.8: PSD$^{\frac{1}{2}}$ of ISA during 2006/05. *Left*: total error (*black*), total SC error in the absence of data gaps, (*blue*), total SC error with full data gaps (*green*). *Right*: depicted is total error (*black*) and total SC error without SC data gaps (*blue*) in 2003/04, month with very degraded attitude control.

scenario, i.e. full data gaps, the SC error is a factor of 5 larger when compared to the SC error in the absence of SC data gaps.

5.5.4. Impact of degraded attitude control

The inaccurate inter-satellite pointing causes errors in the APC ε_λ, cf., Eq. (5.22). These errors are proportional to the absolute value of the inter-satellite pointing angle θ, which is controlled by the AOCS. The GRACE AOCS is designed to keep the inter-satellite pointing angle below 4 mrad (Herman et al., 2004).

The left plot of Fig. 5.9 shows the inter-satellite pointing angle for both satellites during 2006/02. It can be seen that, most of the time, the satellites are kept pointing to each other to within 4 mrad. However, there is a period of a few hours, where inter-satellite pointing angles of both satellites exceed this level by up to an order of magnitude. During this period, errors in the APC are also amplified by an order of magnitude (cf., Eq. (5.22)) resulting in a degradation of the inter-satellite ranging quality.

An assessment of the impact of degraded attitude control requires an answer to

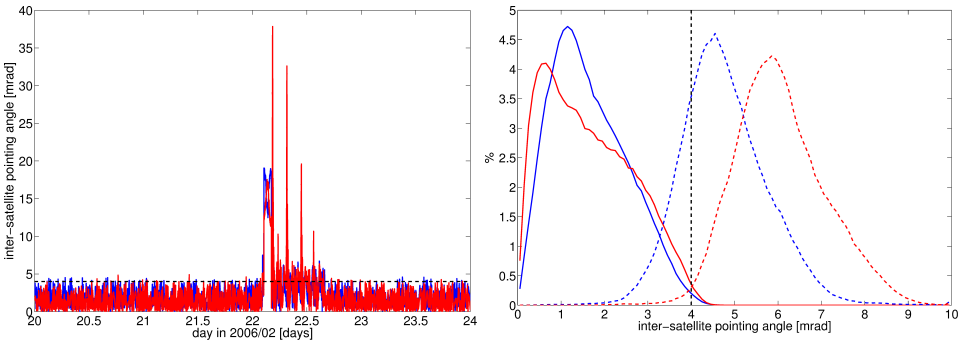

Figure 5.9: *Left*: Inter-satellite pointing angle during four days in 2006/02. GRACE-A is shown in blue and GRACE-B in red. Apart from the highlighted episode, the AOCS keeps the inter-satellite pointing angle below 4 mrad. *Right*: Histogram of inter-satellite pointing angles for GRACE-A (blue) and GRACE-B (red) during 2006/05 (solid line) and 2003/04 (dashed line). Black dashed line represents the AOCS inter-satellite pointing angle threshold. Attitude control is noticeably worse during 2003/04.

5

the question of how often periods of degraded attitude control occur in the GRACE time series. We define degraded attitude control by the condition $\frac{\theta_A+\theta_B}{2} > 4\,\text{mrad}$. Then, we compute the fraction of degraded attitude control measurements for each month in the GRACE time series. Table 5.3 summarizes the results.

Obviously, episodes of degraded attitude control happen frequently. During 2005/12, 5.3% of the measurements suffer from degraded attitude control. This is expected since, during this month, a satellite swap manoeuvre took place, which certainly affected the alignment of the satellites. More importantly, it can be seen that 2010/06 and months between 2003/02 and 2003/05 suffer from particularly bad attitude control.

To assess the impact of attitude errors on ISA in the worst case scenario, we have selected 2003/04, a month with particularly degraded attitude control performance. This choice is supported by the right plot of Fig. 5.9, where the histograms of inter-satellite pointing angles of 2003/04 are compared with the ones of 2006/05, a month with nominal performance of the attitude control.

We perturb the input data with realistic SC errors without SC data gaps and compute the differences observed in ISA in terms of $\text{PSD}^{\frac{1}{2}}$. The results are shown in the right plot in Fig. 5.8. SC errors in the presence of degraded attitude control increase by a factor of 5 when compared to a month with nominal attitude control, e.g. 2006/05.

We hypothesize that the peaks in the $\text{PSD}^{\frac{1}{2}}$ of the total error in 2003/04, particularly in the frequency range above 3 mHz, are likely caused by the combination of SC errors and degraded attitude control. However, it can be seen that the propagated SC errors for this month are both smaller, and present a different pattern of peaks with respect to the observed total error. The discrepancy in the magnitude could be explained by noticing that we simulated SC errors without taking into account possible gaps in SC data during this month. In the worst case scenario, as

Table 5.3: Fraction of measurements with degraded attitude control within each month in the period 2003-2010 in percentages. Degraded attitude control condition is defined as sum of inter-satellite pointing angles in excess of 8 mrad.

	Jan	Feb	Mar	Apr	May	Jun
2003	1.81%	**81.19**%	**87.13**%	**96.67**%	**43.05**%	0.01%
2004	0.11%	0.35%	0.41%	1.38%	5.32%	0.41%
2005	0.20%	3.16%	0.64%	0.06%	1.16%	0.06%
2006	1.16%	0.86%	0.02%	0.07%	0.02%	0.03%
2007	0.01%	0.68%	0.11%	1.01%	0.06%	1.51%
2008	0.25%	2.19%	0.81%	0.62%	0.62%	0.41%
2009	1.19%	1.57%	2.72%	1.67%	1.28%	3.08%
2010	1.04%	1.47%	1.78%	1.33%	2.01%	**21.02**%
	Jul	**Aug**	**Sep**	**Oct**	**Nov**	**Dec**
2003	0.44%	0.38%	1.24%	0.37%	0.99%	1.36%
2004	0.48%	0.87%	1.68%	0.36%	0.38%	1.56%
2005	0.02%	0.03%	0.54%	0.27%	0.49%	**5.29**%
2006	0.06%	0.24%	0.29%	1.08%	0.04%	0.01%
2007	0.10%	0.03%	0.07%	0.13%	0.55%	0.26%
2008	1.26%	0.81%	2.76%	1.05%	1.76%	1.79%
2009	1.19%	1.98%	1.32%	0.89%	0.93%	2.71%
2010	3.13%	1.22%	1.06%	2.80%	0.88%	0.53%

seen in the left plot of Fig. 5.8, SC data gaps might increase ISA errors by a factor of 5. Regarding the discrepancy in the peak pattern, notice that the collection of peaks in the frequency range 3-10 mHz represents the harmonic SC error, which was modelled on the basis of 2006/05 L1A SC data. This may explain the overall different shape of the spectra in this range.

5.5.5. Propagation into gravity field solutions: preliminary results

In this section, we propagate SC errors into monthly gravity field solutions in order to get an idea about their magnitude and the spatial pattern.

GRACE ISA are contaminated with a relatively strong noise in the range of low frequencies (below 1 mHz or 5 cpr). Before gravity field inversion and in order to eliminate this noise, we apply the same high-pass filter used in the production of DMT-2 model. We refer to Section 5.5.3 and Farahani (2013) for more details about this filter.

The results are presented in terms of equivalent water height (ewh) degree amplitudes in Fig. 5.10. It shows the total error during 2006/05 as well as total SC errors obtained with and without taking into account the real gaps in the SC data of this month. In the presence of SC data gaps, SC errors increase by a factor of 5-6 independently of the spherical harmonic degree. The plot also shows the total SC errors with no data gaps during the month of 2003/04, a month with

degraded attitude control. In this case, SC errors are amplified by a factor of 3 up to spherical harmonic degree 40, and by a factor of 6 above it, as compared to 2006/05. Fig. 5.11 shows various error components propagated into gravity field

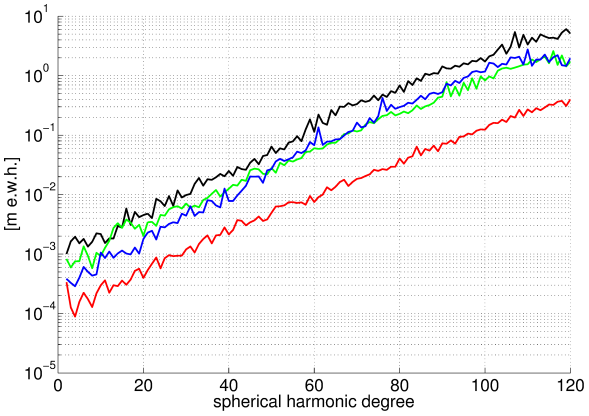

Figure 5.10: Propagated errors in the form ewh of degree amplitude spectrum. Depicted are the total error (black), the SC error with no gaps (red) and SC error amplified by real gaps in the SC data (green) during 2006/05. Also depicted is SC error with no gaps in 2003/04 (blue), month with degraded attitude control.

5

solutions in the spatial domain. All the solutions were post-processed by applying a Wiener filter (Klees et al., 2008; Liu et al., 2010) in order to stay more consistent with procedures for mass transport modelling from GRACE data. Fig. 5.11(a) shows the total error in 2006/05 as a filtered monthly gravity field solution. Figs. 5.11(b) and (c) present the SC errors in 2006/05 with and without taking into account gaps in real SC data, respectively. SC data gaps increase noise in the filtered gravity field solution by a factor of 5. In terms of RMS, both SC error realizations account for about 18% and 80% of the total error, respectively.

Fig. 5.11(d) shows the total error in 2003/04 as filtered monthly gravity field solution. Fig. 5.11(e) shows SC errors with no gaps in 2004/03. Comparing the RMS of the SC error solution in 2003/04 with the corresponding solution of 2006/05 (middle-left) allows one to conclude that degraded attitude control amplifies SC errors by a factor of 3. In terms of RMS, total SC errors in 2003/04 account for 31% of the total error.

The propagated SC errors in Fig. 5.11 are particularly high at places with significant geophysical signal, e.g., Greenland, Alaskan Glaciers, West Antarctica, etc. However, one should not wrongly conclude attitude errors themselves are significantly stronger at these regions. Larger propagated errors in these regions are caused by the use of the Wiener-filter to regularize the monthly gravity field solutions. The Wiener filter is defined based on the covariance matrix of known mass transport signal over an extended period of time. As a consequence, the filter is more aggressive in regions with small mass transport signal while it is more permissive in regions with large mass transport signal. Fig. 5.11 then shows how attitude errors propagate into Wiener filtered monthly gravity field models.

In Figs. 5.11(b), (c) and (e), SC errors propagate as horizontal stripes, a pattern already seen along the boresight axes of the SC error estimates, cf., Fig. 5.1. This finding is consistent with the results presented in Horwath et al., 2011. Similar horizontal stripes can also be observed in the total error solution of 2003/04. This

supports the conclusion that SC errors may be a significant error source in the gravity field solution of 2003/04.

5.6. Conclusions

We showed that the accuracy of the SCs cross-boresight axes is about 23 µrad which is close to the expected maximum of 24 µrad. In both satellites, the accuracy of the primary boresight axis is significantly worse compared with the secondary SC boresight axis. The ratio between the accuracy of the cross- and boresight axes matches the expected value of 8, if we consider the secondary SC boresight axes. If we consider the primary SC boresight axis, than this ratio is higher, indicating that errors are stronger along these axes. The SCs on board GRACE-A and GRACE-B have about the same accuracy except for the primary SC boresight axes, where GRACE-A is less accurate.

We observed two distinct types of error in SCs on board GRACE, i.e., random and harmonic. Harmonic errors are highly correlated with the satellite's true anomaly, indicating that they are caused by the environment of the satellite and not by the SC instruments themselves. We applied a custom estimation method to extract both components from a time series containing large amounts of clustered gaps. Considering different months, satellites and SCs, we showed that harmonic errors have a higher standard deviation than stochastic errors. In terms of PSD$^{\frac{1}{2}}$ of ISA, the stochastic error has a flat spectrum up to 10 mHz. The harmonic error is dominant in the frequency range 3-10 mHz.

SC errors alone account for about 18% of the total error in terms of filtered gravity field solutions. We showed that these errors are amplified in the presence of gaps in the SC data and during periods of degraded attitude control. Under these conditions, SC errors may become significant contributors to the error budget of GRACE.

We showed that pitch and yaw errors are amplified by gaps in the SC data, which increase the anisotropy in the accuracy of the satellite attitudes. In terms of RMS of filtered gravity field solutions, we showed that gaps in real SC data amplify SC errors by a factor of 5. This factor might even be larger for months with bigger amount of gaps in the SC data.

For the period 2003 to 2010, we identified several months with degraded performance of the attitude control system: 2010/06, 2005/12 and 2003/02 till 2003/05. A particularly bad month is 2003/04 when propagated attitude errors are amplified by a factor of 3 in terms of RMS of filtered gravity field solution. In this monthly solution, SC errors account for 31% of total error without considering any gaps in the SC data. The similarity between the spatial patterns of the two solutions suggests that this number is, in reality, even higher. This shows that a degraded performance of the attitude control system might have a significant impact on the quality of monthly GRACE solutions.

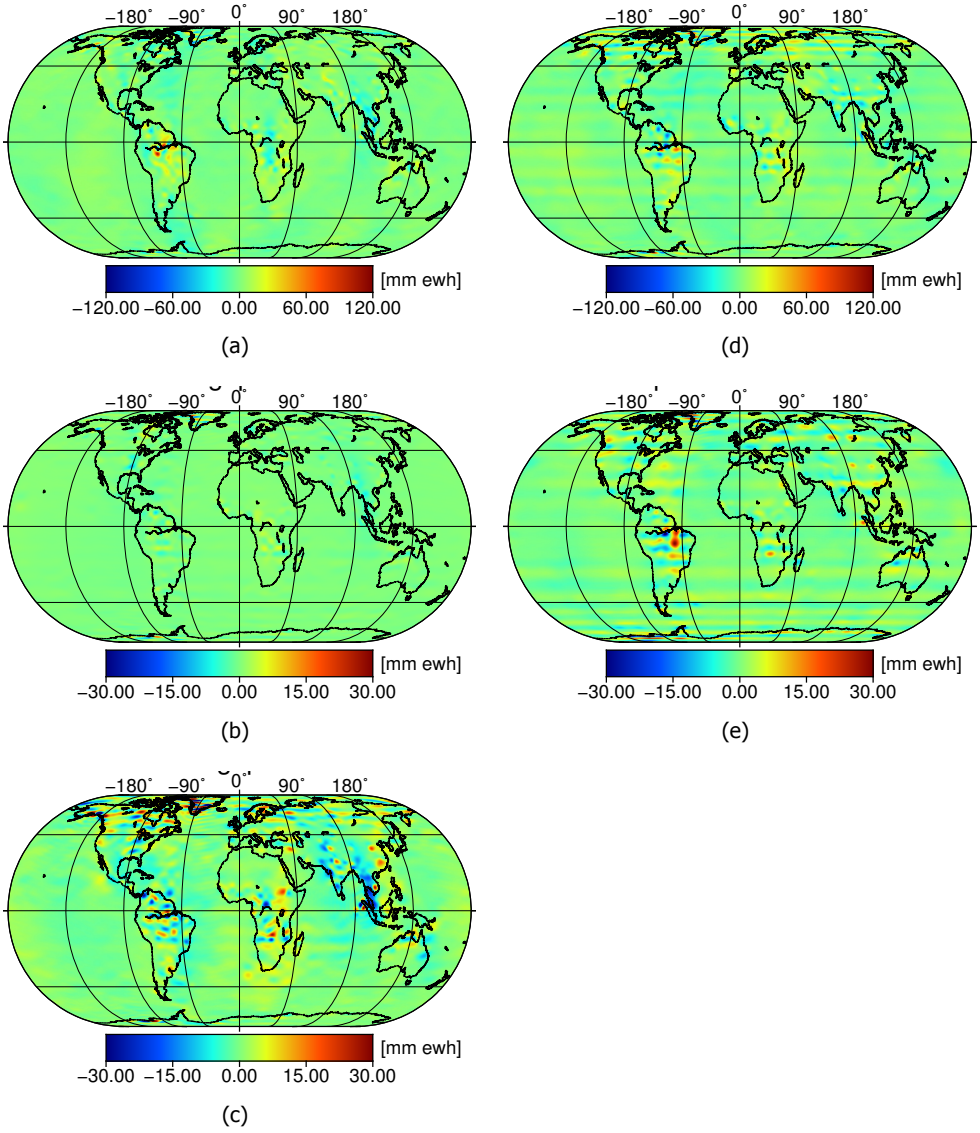

Figure 5.11: Propagation of errors into Wiener filtered monthly gravity field solutions in mm equivalent water height (ewh). *a*) total error in 2006/05 (RMS=6.1 mm ewh). *b*) SC errors in 2006/05 without considering SC data gaps (RMS=1.1 mm ewh). *c*) SC errors taking real SC data gaps into account (RMS=4.9 mm ewh). *d*) total error in 2004/03, month with degraded attitude control (RMS=9.6 mm ewh). *e*) SC error without SC data gaps amplified by degraded attitude control (RMS=3.0 mm ewh). To enhance the visibility of propagated SC errors, the colorbar of middle and bottom plots differs from the top plots.

5.7. Discussion: attitude determination errors and future satellite gravimetry missions

Throughout this paper we assumed that SC errors are observed in the difference between the SC measurements, which only contain the *differential* SC error. Errors *common* to both SCs are not observed. In fact, in this sense, we do not model the complete SC error, but only the differential part. However, it should be noticed that common SC errors are likely of less concern. There could be two types of common SC errors: time-invariant (static) common errors and time-variable (dynamic) common errors. Static common errors are eliminated by calibration of the attitude system with on-ground and in-flight manoeuvres, such that they are of no concern. Regarding dynamic common errors, one should keep in mind that each SC is an independent instrument making independent measurements; there is no obvious reason as to why their measurements should have a significant common error.

To compute the SC error estimates we make use of the QSA1B product specifying the relative attitude between each SC and the SRF. Despite of being accurately measured on-ground and calibrated with in-flight manoeuvres, the QSA1B product is not error-free. However, errors in the QSA1B are not fundamentally different from SC errors, and they are implicitly considered in the SC error estimates.

In this publication, we follow the methodology developed by Liu et al. (2010) to compute monthly gravity field solutions from GRACE ISA. Other methodologies exist, which instead make use of range and/or range-rate data. We propose, however, that our results are relevant independently of the chosen methodology. In one way or another, all methodologies use some form of KBR data, all contaminated by errors in the geometric correction. The conversion of ranges into range-rates or range-accelerations can be represented in the frequency domain as a multiplication with $i\omega$ and $-\omega^2$, respectively. Therefore, the signal-to-noise ratio at a given frequency would be the same for any type of observable. Furthermore, we employ a statistically-optimal inversion scheme, which takes the dependence of noise on frequency into account. Consistent results must be achieved for alternative methodologies, as long as they employ statistically-optimal inversion schemes, no matter whether ranges, range-rates, or range-accelerations are used as input (Ditmar et al., 2004).

Reducing errors in the attitude product of GRACE and future satellite gravimetry missions could be achieved by including information provided by the accelerometers on board the satellites. The accelerometers are able to measure the rotation of the proof mass. These measurements can be combined with SC data, potentially leading to improvements in attitude data in the high-frequency part of the spectrum. A similar approach has already been applied in the GOCE mission for the fusion of attitude data collected by the star camera and the gradiometer instruments (Frommknecht et al., 2011; Siemes et al., 2019; Stummer et al., 2011, 2012). It should be investigated, however, whether information collected by the accelerometers is accurate enough to substantially reduce noise in the attitude products.

Errors in the roll angle are not critical for the purposes of gravity field modelling. The opposite is true for errors in the pitch and yaw angles, which have a large

impact on the antenna phase centre correction. We have shown that the accuracy in the determination of the pitch and yaw angles is worse than that of the roll angle. Furthermore, pitch and yaw errors are amplified by gaps in the SC data, while the errors in roll are only slightly worse. This leaves space for an optimization of SC arrays in future low-low satellite-to-satellite tracking (ll-SST) gravity missions, so that the maximum accuracy for pitch and yaw angles is maintained even in the periods when only one SC is operational. An example of how this setup could look like is shown in Fig. 5.12. Because the roll angle determination is not critical, both (less accurate) boresight axes are oriented in the *x*-axis direction ensuring the full accuracy of both SC's for the determination of the much more critical pitch and yaw angles.

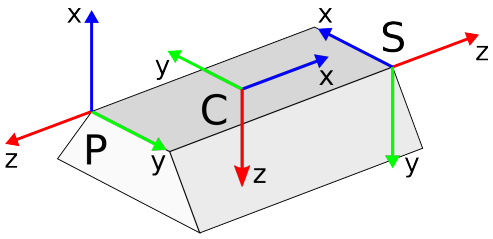

Figure 5.12: Possible SC configuration based on the single fact that roll angle determination is not critical for gravity field recovery. Blue represents *x*-, green represents *y*- and red represents *z*-axis, the least accurate boresight axis.

The cause of the harmonic error component in the SC measurements is not known to us. Further progress in SC design and data processing may reduce this error, which will also improve the accuracy of the satellite attitude determination. Reducing the harmonic error may improve the signal-to-noise ratio in the range of 3-10 mHz, where most of information about time-variable gravity signal is located. In this frequency range, no other sources of errors have yet been identified. Understanding and mitigating all sources of error in this range is of interest both for GRACE and future satellite gravity missions.

In our analysis we focused on the propagation of SC errors through the geometric correction of the KBR data. In the context of GRACE, this is likely the most critical way in which these errors propagate into estimates of the time-varying gravity field. In the context of future gravity missions, it is expected that they will make use of laser interferometers to measure inter-satellite ranges. The proposed architecture for the laser interferometer of GRACE-FO places the virtual measurement point at the position of the accelerometer proof mass (Sheard et al., 2012). Such an architecture is insensitive to SC errors as it does not require a geometric correction at all. However, in view of a higher overall accuracy of GRACE-FO, additional studies may be required to understand the propagation of attitude errors through the GNSS data and through the orientation of the non-gravitational accelerations. Then, a proper understanding of SC errors and how they propagate into the attitude are necessary.

6

Satellite gravimetry noise budget

After the end of the GRACE mission, its error budget remained incomplete. In previous studies, which addressed the error budget of the GRACE mission in the context of the RRC approach (Ditmar et al., 2012; Encarnação, 2015), the authors could not identify the sources of the observed noise in the GRACE data in the frequency range between 1 and 9 mHz. In this chapter, I will finally close the GRACE's error budget. I will describe an error model applicable to the GRACE mission, I will highlight the most important error contributors, and I will compare the total synthetic errors with observed errors in real GRACE observations. In Section 6.1, a prediction of the error budget of the GRACE mission is shown.

The GFO mission has been launched recently and, the first reports indicate that i) the accuracy of the laser ranging instrument has exceeded the expectations (Abich et al., 2019) ii) the accelerometer instrument on-board GRACE-D satellite is showing poor performance. The performance is so poor, that the data it collects have to be discarded and replaced by data transplanted from the other GFO satellite (Webb et al., 2019). Looking into the future, beyond the GFO mission, one wonders what more can be achieved on the basis of the *GRACE platform*, i.e. by continuing to replicate the GRACE-mission with updated hardware. In Section 6.2, I will predict the errors of future GRACE-type missions and I will compare them with the performance of GRACE.

Finally in Section 6.4, the concluding remarks of this chapter are gathered.

6.1. GRACE error budget

In order to investigate the error budget of the GRACE mission, real orbits of the GRACE satellites during 2006/02 were used as reference for the simulation. By using these orbits, I compare the synthetic realizations of errors to the observed errors of the GRACE mission in the same period (Section 6.1.4). The general overview of

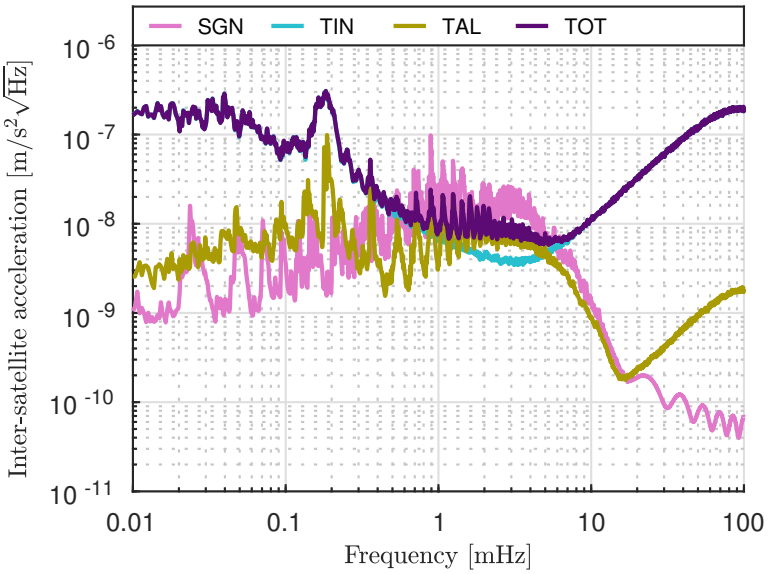

Figure 6.1: General overview of simulated errors in the GRACE mission in terms of inter-satellite acceleration. The total instrumentation error (TIN) and the total temporal aliasing error (TAL) are shown against the ESM mean monthly signal (SGN). The total error (TOT) is the sum of instrumentation and temporal

the simulation procedure is documented in Chapter 4.

In Figure 6.1, a general overview of simulated errors in the GRACE mission in terms of PSD$^{\frac{1}{2}}$ of inter-satellite accelerations is shown. The plot shows the total instrumentation error (TIN) and the total temporal aliasing error (TAL) in comparison with the ESM mean monthly signal (SGN). The signal is above the total error only in the 0.8 to 6 mHz frequency range. In this frequency range, temporal aliasing errors are dominant above 1.5 mHz, while instrumentation errors are dominant below this frequency.

6.1.1. Instrumentation errors in GRACE data

Instrumentation errors are shown in detail in Figure 6.2. The dominant error source up to 2 mHz is a combination of positioning and accelerometer error. Above 5 mHz, the ranging error becomes dominant.

6.1.2. Temporal aliasing errors in GRACE data

Temporal aliasing errors are presented in detail in the right panel of Figure 6.3. Over the whole spectrum, the atmosphere and ocean de-aliasing model error (AOD) is slightly larger than the other errors. Ocean tide model error (OTE) is slightly larger than the dynamic mass transport signal (TMP) over the whole spectrum.

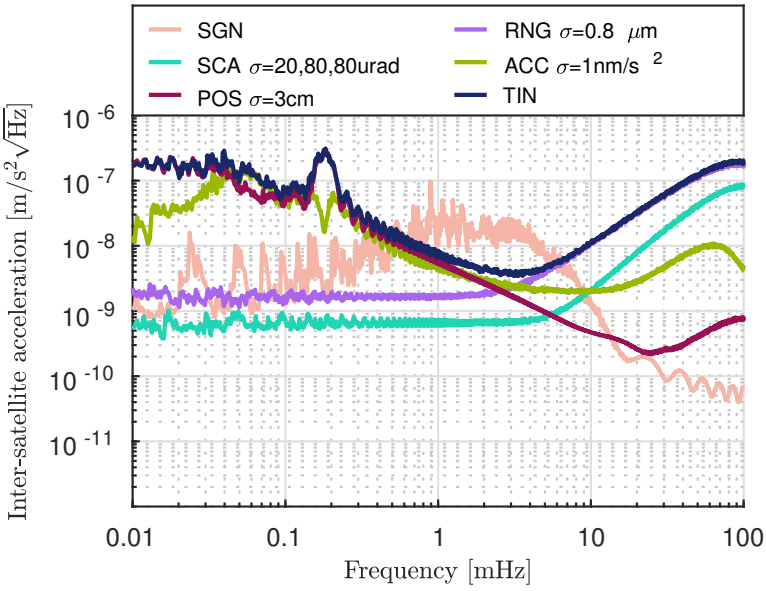

Figure 6.2: PSD$^{\frac{1}{2}}$ of simulated instrumentation errors for GRACE in terms of inter-satellite accelerations. See Table 4.3 in page 74 for the explanation of the used acronyms.

6.1.3. Comparison of total simulated error with observed noise in GRACE data

In the left panel of Figure 6.4, I show a prediction of total errors in GRACE's inter-satellite accelerations during 2006/02, as well as the observed total errors during the three consecutive months in 2006 in terms of inter-satellite accelerations. Depicted real data errors are the inter-satellite acceleration residuals at a third data processing iteration. The DMT-2 monthly gravity field model is estimated at the second iteration, therefore, the leftover residuals at the third iteration, are interpreted as an estimate of total error in the data.

The considered error model, despite its simplicity, does a remarkable job at reproducing the features of the observed noise in the data. The observed peak around 0.2 mHz is captured by the positioning error. While the accelerometer and positioning errors are similar in magnitude, this peak is not observed in the accelerometer error. The combination of accelerometer and positioning errors is in-line with the observed total error until about 0.8 mHz. Above this frequency, the AOD error becomes dominant, explaining the total error up to about 5 mHz. At this point, the ranging error becomes dominant and closely matches the observed total error.

This plot shows a very good agreement between the predicted errors and the observed ones in most of the spectrum. The noise observed in the frequency range between 1 and 9 mHz, with previously unknown origin (Ditmar et al., 2012), is now explained by a combination of positioning, acceleration, AOD and ranging error (cf. Section 4.2). Regarding the frequency range below 1 mHz, Ditmar et al. (2012)

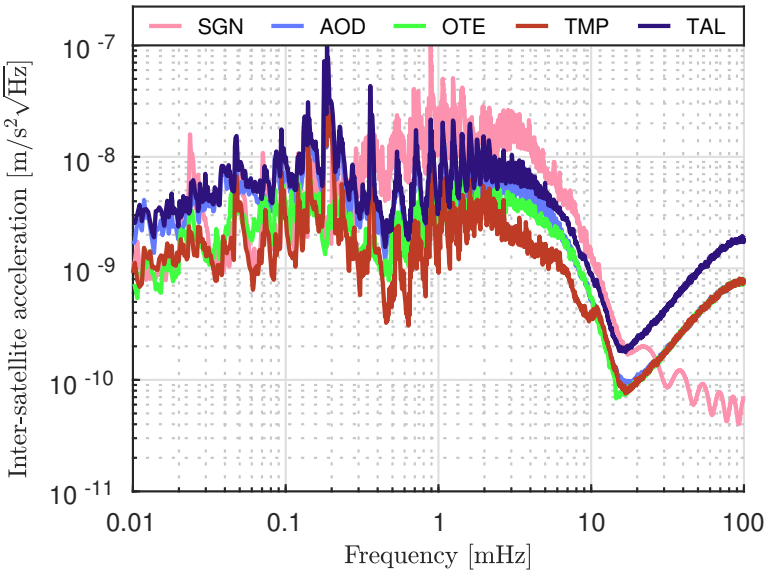

Figure 6.3: PSD$^{\frac{1}{2}}$ of simulated temporal aliasing errors for GRACE errors in terms of inter-satellite accelerations. See Table 4.3 in page 74 for the explanation of the used acronyms.

6

concluded that these errors are caused by inaccuracies in the reference orbits. While that is indeed the case, it is now shown that these inaccuracies are caused by the propagation of accelerometer and positioning noise into the computed reference orbits.

Despite the simple error model considered, it is now possible to capture the features present in the real data, provided that we take into account the indirect effect propagation of the considered error sources.

In conclusion, the good agreement between the considered error model and the observed total noise in real GRACE data shows that, in the context of the RRC approach, *GRACE's error budget is complete.*

6.1.4. Propagation of errors into gravity field solutions

The right panel of Figure 6.4 shows the DV curve for each instrumentation error propagated into a gravity field solution. In addition, I present the corresponding ESM mean mass transport signal in 2006/02. One can see that all error sources are orders of magnitude larger than the signal in terms of DV. This is not unexpected; it is known that unregularized solutions of the GRACE mission suffer from large North-South striations. There are two causes for the appearance of these striations: large amplitude of low-frequency errors and the anisotropic sensitivity of the GRACE mission.

Figure 6.2 shows that positioning and accelerometer errors in terms of inter-satellite accelerations are predominant in the low-frequency part of the spectrum (below 5 mHz). This low-frequency noise in the time domain will cause geograph-

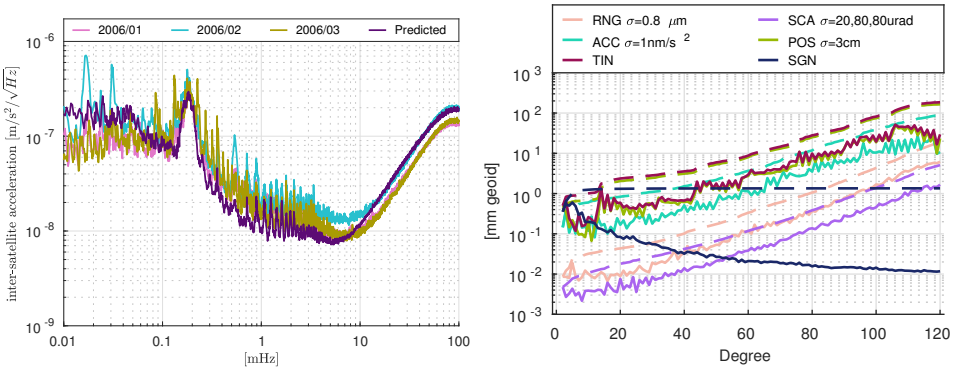

Figure 6.4: In the left panel, predicted total noise for 2006/02 is compared with real observed noise in the months from 2006/01 to 2006/03 in terms of PSD$^{\frac{1}{2}}$ of inter-satellite accelerations. The right panel, shows the contribution of instrumentation errors propagated into DV (solid) and CDV (dashed) error per degree. See Table 4.3 in page 74 for the explanation of the used acronyms.

ically adjacent regions in the East-West direction to exhibit random errors. This in turn leads to large estimated East-West gravity gradients in the solutions resulting in great amplification of observation errors on sectorial coefficients, especially at the higher spherical harmonic degrees.

On top of this noise amplification, the anisotropic sensitivity of the GRACE mission leads to uneven amplification of noise in different directions. An example of this can be seen in Figure 6.5, where ocean tide model errors are propagated into a mean monthly solution. Even though ocean tide model errors (OTE) are smaller than the mass transport signal (ESM) in terms of inter-satellite accelerations (see Fig. 6.3), the corresponding errors in terms of gravity field solutions are amplified well above the signal. Additionally, notice that there are no similarities between tidal model errors as plotted in Figure 4.1 and the corresponding mean monthly solution.

All these aspects are well known in GRACE data processing and, therefore, the solutions are typically filtered or regularized in order to maximize the signal-to-noise ratio.

Regularization procedure

In order to obtain useful results from the GRACE solutions, one must regularize them. The regularized solutions in this thesis are computed using the optimal filtering approach (Klees et al., 2008). In this approach, the filter is designed by including information about the mass transport signal in the form of its signal covariance matrix. Then, the filtering is formally equivalent to a regularization (Klees et al., 2008). This effectively stabilizes the solutions by suppressing noise, particularly, in the regions and spatial scales where no mass transport signal is expected. The regularization procedure is linear in terms of the observation data. Therefore, each error source can be regularized individually to build a regularized error budget.

For this thesis, I have computed the signal covariance matrix using a set of

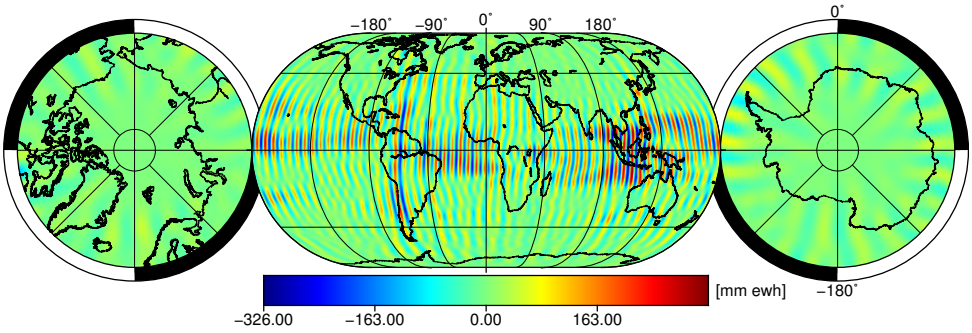

Figure 6.5: Unregularized solution based on the ocean tide model errors for the GRACE mission. An example of noise amplification due to the anisotropic sensitivity of the mission. In order to better depict the vertical stripes, the solution has been cropped to maximum SH degree 60.

monthly mean mass transport estimates computed on the basis of the ESM mass transport signal within the period contemplated by the model, i.e., from 1995 to 2006.

The impact of regularization applied can be tuned by scaling the signal covariance matrix as desired. This scaling is performed by changing the regularization parameter, which can be thought of as the ratio between the average total variance of noise in the data and average signal variance. In the simulations realm, the regularization parameter allows one to fine-tune the performance of a given mission. In the leftmost column of Table 6.1, a breakdown of global RMS of errors for the GRACE mission in terms of unregularized solutions is shown. This column shows very large RMS values for all error sources, reflecting the large amplification of errors in the unfiltered solutions.

Different regularization parameters will result in a different breakdown of errors in terms of global RMS. In Figure 6.6, an overview of the global error RMS for different regularization parameter values is shown. When no regularization is applied, the errors are orders of magnitude larger than the mass transport signal. As the amount of regularization increases, noise is increasingly suppressed at the expense of filtering out some of the mass transport signal. This is shown by the regularization bias error curve increasing with regularization parameter.

By applying different values of the regularization parameter, one finds the optimal point, where the total error is minimized. At this point, increasing the amount of regularization no longer leads to a performance gain, as the increase in regularization bias becomes larger than the corresponding decrease in the sum of all other error sources. Unfortunately, in the considered simulation, the maximum performance point occurs when the total error matches the level of the mass transport signal. In other words, the lowest level of total error is obtained when the filter suppresses everything. That means that under the considered set-up, no useful information can be obtained from the GRACE mission. This result is presented to show that the level of low-frequency errors in terms of inter-satellite accelerations

Table 6.1: Breakdown of GRACE's error budget in terms of global RMS in units of mm ewh for $l_{max} = 120$. From left to right, the second column presents unfiltered solutions; the third columns shows the noise reduction after high-pass filtering of inter-satellite accelerations; the fourth column shows error budget after regularizing the solutions with the ESM signal covariance matrix; the fifth column shows the lowest RMS error when both high-pass filtering and regularization procedures are employed.

High-pass Filter	✗	✓	✗	✓
Regularization	✗	✗	✓	✓
RNG	7933.33	7298.35	4.68	9.27
SCA	2147.96	2018.89	0.92	1.93
ACC	34773.10	7885.55	7.56	3.77
POS	65745.58	8759.58	12.84	3.46
TIN	74453.11	13636.15	17.68	11.05
AOD	162641.85	7466.21	106.00	4.24
OTE	5767.05	5249.99	3.68	4.56
TMP	161215.49	5302.84	105.91	3.26
TAL	322840.42	12593.05	211.97	8.26
FLT	✗	1059.13	✗	9.14
REG	✗	✗	34.84	30.31
TOT	345056.49	20176.64	216.96	35.71
SGN	65.29	65.29	65.29	65.29

in the GRACE mission is so overwhelmingly high that regularization alone is not sufficient to extract useful information.

High-pass filtering of inter-satellite accelerations

In order to prevent low-frequency errors in inter-satellite acceleration data from dominating the solutions, a high-pass filter with a cut-off frequency of ≈2 cpr (0.4 mHz can be applied to those data. This frequency was selected as a good compromise between the introduced signal distortion and the corresponding overall error reduction. The high-pass filter computes the Fast Fourier Transform (FFT) of the observations, sets to 0 all frequency components below the cut-off frequency and computes the Inverse FFT (IFFT) to obtain the filtered signal.

The left panel of Figure 6.7 shows PSD$^{\frac{1}{2}}$ of instrumentation errors after applying the high-pass filter. As expected, one can see that all errors in the low-frequency part of the spectrum have been significantly reduced compared to to their unfiltered counterparts, which are shown in Figure 6.2. Obviously, there is a price to pay; as a result of the filtering procedure, the mass transport signal is distorted as well, i.e., a new error source has been introduced due to the filtering procedure. This can be seen in the left panel of Figure 6.8. The gravity field signal is removed at frequencies below 0.4 mHz and above that it is left unchanged.

The right panel of Figure 6.8 shows instrumentation errors propagated into DV per degree. In comparison with Figure 6.4, the overall level of instrumentation errors is significantly lower. Especially the dominant positioning and accelerometer errors are smaller at all SH degrees.

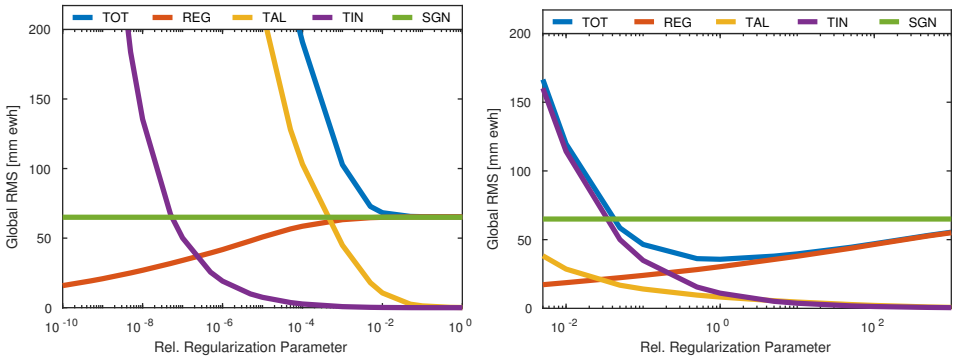

Figure 6.6: Errors in regularized solutions of the simulated GRACE mission as a function of regularization parameter. In the left panel, errors for the GRACE mission with no high-pass filtering applied. In the right panel, errors for the GRACE mission after high-pass filtering has been applied to remove low-frequency errors in terms of inter-satellite accelerations. Only relative values of the regularization parameter are shown with the value 1 being defined at the minimum total error.

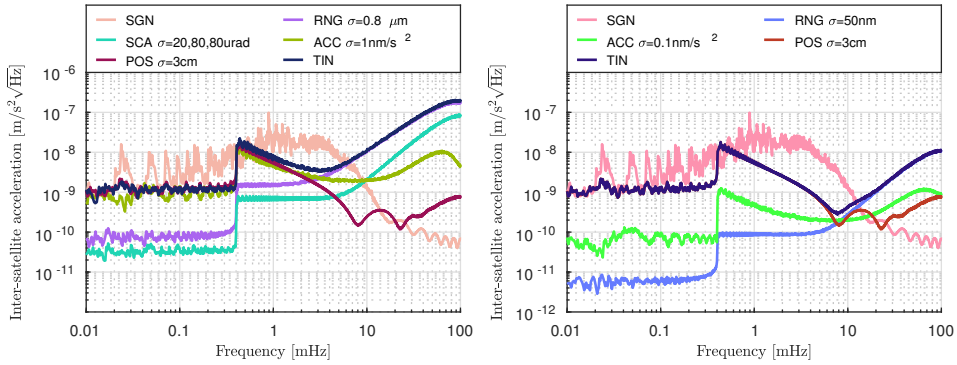

Figure 6.7: PSD$^{\frac{1}{2}}$ of inter-satellite accelerations. Instrumentation errors for the GRACE (left) and FGT (right) missions after high-pass filtering of the inter-satellite accelerations. See Table 4.3 in page 74 for the explanation of the used acronyms.

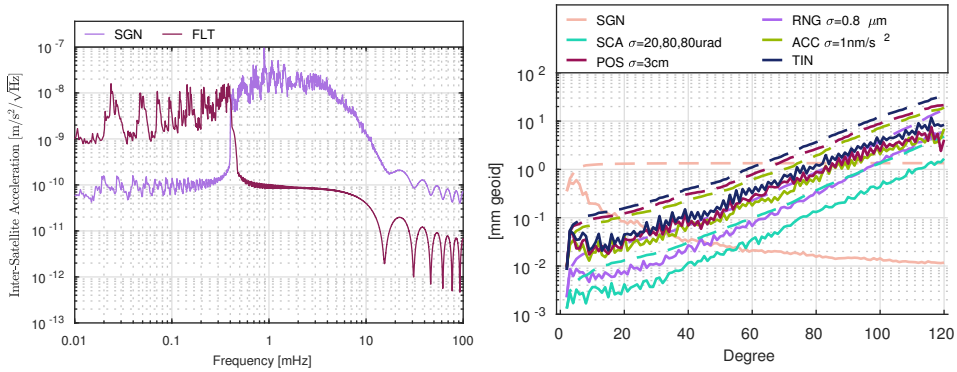

Figure 6.8: The left panel presents noise-free observations (SGN) simulated on the basis of the ESM signal along with the distortion (FLT) introduced by the high-pass filtering procedure. In the right panel, DV (solid) and CDV (dashed) of instrumentation errors in GRACE data after high-pass filtering of the inter-satellite accelerations. See Table 4.3 in page 74 for the explanation of the used acronyms.

In the top-left panel of Figure 6.9, a general comparison of instrumentation and temporal aliasing errors is shown in terms of DV error per degree. In addition, this plot presents the error introduced by the high-pass filtering procedure, which is the dominant error source up to SH degree 6 in terms of unregularized solutions and a considerable error up to SH degree 20, above which is becomes comparatively small. While the filtering error is a considerable error source below SH deg 20, this however should not be bluntly interpreted as a deficiency of the data processing approach. The filtering error reflects the intrinsic trade-off of any filtering procedure: when errors in the low-frequency part of the spectrum are reduced, the signal at these frequencies is reduced as well. The second column of Table 6.1 shows that, despite the fact that the filtering introduces a new error source, the RMS values of all other error sources have been dramatically reduced, leading to a net reduction of total errors in the solutions.

Appropriateness of units in SH solutions of gravimetry missions

Standard in the literature of satellite gravimetry is the use of DV plots in units of geoid height. In Chapter 8, I will use DV plots and global RMS values of SH solutions as metrics to compare the performance of future missions. In doing so, I found that geoid height units are not appropriate for this purpose.

So what is the appropriate metric to evaluate the performance of future satellite gravimetry missions? I propose that the appropriate metric is to consider the quantities typically considered by the end users of gravimetry data. Mass anomalies are the most relevant quantity to them and, in the rest of the thesis, I will opt for considering SH solutions in terms of ewh.

To motivate this choice, consider the relation presented in Eq. 2.6 relating the SH coefficients in terms of ewh with geoid heights. On the basis of this relation, a SH solution in terms of geoid height can be stated as a smoother version of the corresponding solution in terms of ewh. This can be explained by the $2l + 1$ term

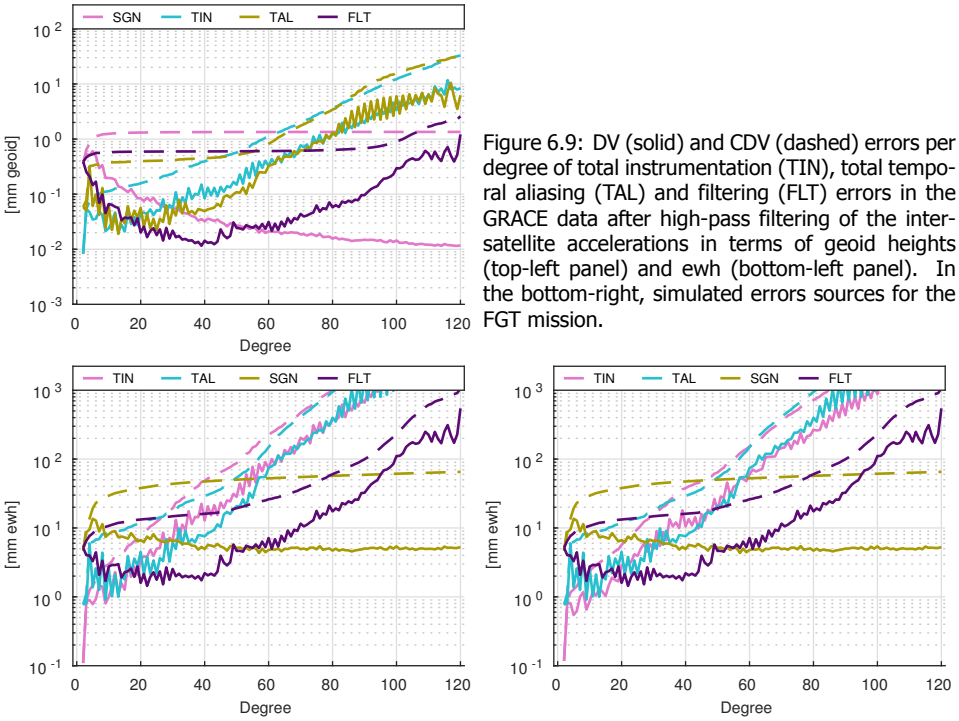

Figure 6.9: DV (solid) and CDV (dashed) errors per degree of total instrumentation (TIN), total temporal aliasing (TAL) and filtering (FLT) errors in the GRACE data after high-pass filtering of the inter-satellite accelerations in terms of geoid heights (top-left panel) and ewh (bottom-left panel). In the bottom-right, simulated errors sources for the FGT mission.

in the denominator of the relation between the two quantities, which considerably dampens the high SH degrees. As a consequence of this damping, typical SH solutions in terms of geoid height will have a global RMS value which is determined by the very low SH degrees. I propose that it is unreasonable to benchmark future gravimetry missions solely regarding their performance in the very low SH degrees. Even more so, since future satellite gravimetry missions are expected to significantly improve on the spatial resolution of current ones. Therefore, I concluded that it is unreasonable to analyze SH solutions in terms of geoid height and I decided to deviate from the standard practice in the literature.

The bottom-left panel of Figure 6.9 shows once more the general comparison of instrumentation and temporal aliasing errors for the GRACE mission, but now in units of ewh. A comparison with the left plot in the same Figure (in terms of geoid height) highlights the differences between the considered units. For example, consider the CDV of the input mean mass transport signal (SGN) on the right panel in terms of geoid height. Notice how the CDV curve becomes flat at about SH degree 10. This confirms that the global RMS value in terms of geoid height is determined by the first 10 SH degrees. On the other hand, the CDV curve never becomes flat in the case of ewh units. This means that the contribution of the very high SH degrees is also taken into account when computing the global RMS value of these solutions.

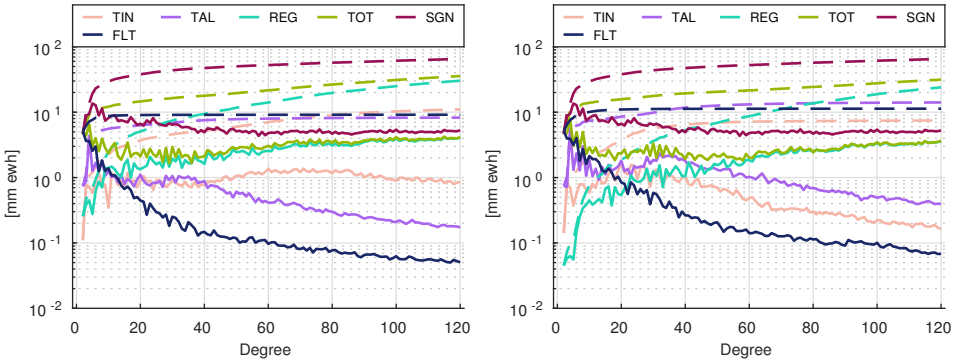

Figure 6.10: DV (solid) and CDV (dashed) of errors for the GRACE (left) and FGT (right) missions in terms of regularized solutions. See Table 4.3 in page 74 for the explanation of the used acronyms.

Propagation of errors into regularized gravity field solutions

Having shown the positive impact of the high-pass filtering procedure in terms of unregularized solutions, I proceed with the analysis of the error budget of GRACE in terms of regularized solutions. The presented solutions have been obtained after iterating the regularization parameter in order to minimize the total error. The total error as a function of the applied regularization parameter for the GRACE mission with high-pass filtering is shown in the right panel of Figure 6.6.

The left panel of Figure 6.10 shows the prediction of instrumentation (TIN), temporal aliasing (TAL), high-pass filtering (FLT) and regularization (REG) errors in the optimally filtered gravity field solutions during 2006/02 in terms of DV error per degree. Most noticeable differences compared to unregularized solutions are much lower magnitudes of all the errors, smaller than the signal of interest at all SH degrees, as well as a decrease in the error magnitudes with increasing SH degree. The largest error up to SH degree 10 is the high-pass filtering error. Above this degree, the regularization bias becomes dominant. The plot also shows that total temporal aliasing and total instrumentation errors are for all degrees smaller that the regularization bias.

A breakdown of the error budget in terms of global RMS of regularized solutions is shown in the rightmost column of Table 6.1. Here, it is shown that the largest error is the regularization bias (30 mm ewh). The high-pass filtering error (9 mm ewh) is also a considerable error source, at the same level of both instrumentation (11 mm ewh) and temporal aliasing errors (8 mm ewh).

At this point, it is important to discuss the obtained results in order to prevent possible misinterpretations. While it is a fact that the regularization error in terms of global RMS is the largest error source, it is **not correct** to state that the performance of the GRACE mission is limited by the applied regularization. The regularization procedure has been applied and optimized to yield the minimum total error, as was shown in the right panel of Fig. 6.6. Therefore, the performance of GRACE is still limited by the amount of temporal aliasing and instrumentation errors, which would be much larger without regularization. The same remark is

also valid for the high-pass filtering error.

Table 6.1 shows that the regularization and high-pass filtering procedures yield lower total error. A comparison between the last two columns in this table reveals that the high-pass filtering procedure reduced the level of instrumentation errors from 18 to 11 mm ewh. Even greater reductions can be seen for the level of temporal aliasing errors, which go down from 212 to 8 mm ewh. These improvements come at the expense of a new filtering error source with a magnitude of 9 mm ewh. While being a considerable error source in the budget, the filtering error is an acceptable price to pay for the corresponding increase in the signal-to-noise ratio. Similar comparison between the third and last column in the table reveals that the regularization procedure reduces the level of errors by orders of magnitude. And again, the introduced regularization bias of 30 mm ewh, which is the largest error source, brings massive error reductions to the otherwise unusable solutions.

In light of this argument, a more informed conclusion to this section is that instrumentation errors (11 mm ewh), and more specifically, the ranging error (9 mm ewh) is the largest contributor to the total error (36 mm ewh) in terms of global RMS. Temporal aliasing errors make nonetheless a considerable contribution (8 mm ewh), the largest component being the ocean tide model errors (5 mm ewh). All other considered errors are significantly smaller and do not limit the performance of the mission.

In Section 5.5.5, a preliminary analysis of attitude errors in terms of regularized gravity fields was presented. The discrepancy between the results presented in that section and the error budget in Table 6.1 requires an explanation. In that section, the global RMS in terms of regularized solutions for the considered month was 6.1 and 1.1 mm ewh for the total and star-camera errors, respectively. In Table 6.1, these are 35 and 1.9 mm ewh for the total and star-camera errors, respectively. Notice that the total error presented in this table includes the regularization bias and high-pass filtering errors. However, these components are not visible in the total error obtained from the inter-satellite acceleration residuals, as computed in Section 5.5.5. Therefore, a fair comparison requires the regularization bias and filtering error to be excluded. Then, a comparable total error can be obtained from the combined total instrumentation (8.2 mm ewh) and total temporal aliasing errors (11 mm ewh). This brings the total error from 35 down to $\sqrt{8.2^2 + 11^2} = 13.7$ mm ewh.

The remaining discrepancy between the presented numbers is explained by the regularization filter applied to the data. In Section 5.5.5, a signal covariance matrix based on the DMT-2b model was used as input for the regularization procedure. On the other hand, from this Chapter forward, a signal covariance matrix based on the ESM model is used for the same purpose. I adopted the ESM model since it is better suited at benchmarking the performance of future satellite missions. It has been designed to benchmark future satellite missions and it includes mass transport signal at small spatial scales which current missions are likely not sensitive enough to measure. Therefore, regularization based on the signal covariance matrix of the DMT-2 solutions is more aggressive at removing noise from the data in comparison with regularization based on the ESM model.

Beyond the choice of a-priori gravity field model, I do not expect that a this choice should significantly change the relative contributions of the errors sources. Indeed, the 18% (1.1 of 6.1 mm ewh) star-camera error contribution to the total error in Section 5.5.5 is similar to the 14% (1.9 of 13.7 mm ewh) presented here.

6.2. Future GRACE-type missions

In this section, I will predict the performance of future GRACE-type missions and compare it with the results obtained for GRACE, taking into account the updated instrumentation that may be used in the future.

Preliminary reports from the GFO mission showed that the LRI instrument has exceeded the expected level of accuracy. On the other hand, it has also been reported that the accuracy of the on-board accelerometer of GRACE-D satellite is not meeting the requirements. With the GFO mission well underway, it is interesting to look beyond GFO and into the future generations of ll-SST missions.

The recently launched GFO mission is, to a large extent, a replication of the GRACE mission with updated hardware. Considering a scenario where future ll-SST missions will keep replicating the original GRACE mission, one wonders what are the performance improvements one may expect from such missions. In the following sections, I will analyze the performance of a hypothetical future GRACE-type mission (FGT) which replicates the original GRACE mission.

The GFO mission has been launched into similar orbits as the ones of the GRACE mission. Therefore, I will assume that the FGT mission will also consider the same orbits. Consequently, the FGT mission has the same along-track formation with the same inter-satellite separation distance at GRACE.

Since the orbits are assumed to be the same, there is no difference between the two missions in terms of temporal aliasing errors. Therefore, the FGT mission differs from GRACE only in terms of its instrumentation errors. Those differences are summarized in the instrumentation error scenarios presented in Table 4.1.

6.2.1. Analysis of errors in terms of inter-satellite accelerations

The right panel of Figure 6.7 shows instrumentation errors for FGT mission in terms of PSD$^{\frac{1}{2}}$ of inter-satellite accelerations. A comparison with the corresponding errors of the GRACE mission (in the left panel), shows an overall error reduction. The total instrumentation error is dominated by positioning errors up to 10 mHz and by ranging errors from that frequency onwards. In the frequency range above 10 mHz, the instrumentation error is one order of magnitude smaller compared to GRACE which is expected due to the much better performance of the LRI instrument w.r.t. the KBR instrument (see Table 4.1 and Abich et al. (2019)).

The most significant reductions are due to the increased performance of the FGT accelerometers and the laser ranging instrument. Furthermore, LRI data from the FGT mission is also considered immune to star-camera errors, similarly to the LRI data of the GFO mission. As a consequence, the total instrumentation error is considerably lower that of the GRACE mission in the frequency range above 1 mHz.

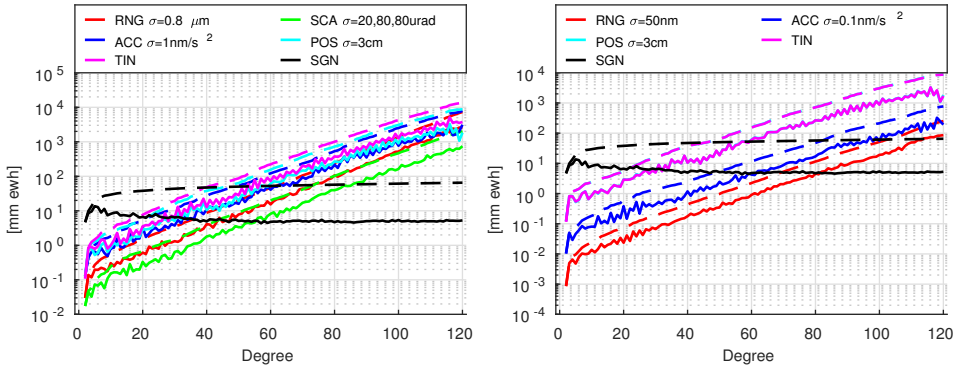

Figure 6.11: Instrumentation errors in terms of DV (solid) and CDV (dashed) of unregularized gravity field solutions for the GRACE and FGT missions in the left and right panels, respectively. See Table 4.3 in page 74 for the explanation of the used acronyms

However, below this frequency, the positioning error is equal for both missions, which means that there is no significant reduction in this frequency range.

A comparison of the total instrumentation error alone with the ESM mean mass transport signal shows a better signal-to-noise ratio for the FGT mission compared to GRACE, especially in the 3 to 11 mHz frequency range. However, the level of temporal aliasing errors is equal to that of GRACE, and is now the dominant error source.

6.2.2. Propagation of errors into gravity field solutions

Regarding the GRACE mission, instrumentation errors were found to be the major contributor to the error budget of unfiltered gravity field solutions. A comparison of instrumentation errors between the GRACE and FGT missions is shown in Figure 6.11. As expected, the FGT mission shows improvements in terms of individual instrumentation errors. However, the positioning error remains at the same level (compared to GRACE), which means that only an overall mild reduction of the total instrumentation error is achieved. Furthermore, temporal aliasing errors are the same as considered for the GRACE mission. These are shown in Figure 6.12. All three components of temporal aliasing error show equal level, the AOD model errors seem slightly larger than the other two from SH degree 70 onwards in terms of DV.

A general overview of the errors for the FGT mission is shown in the bottom-right panel of Figure 6.9 in terms of DV. A comparison with the corresponding plot for the GRACE mission (bottom-left panel of Figure 6.9) shows that, for the FGT mission too, the high-pass filtering error is the largest error up to about SH degree 16. Similarly, above SH degree 16, the total error results from a combination of instrumentation and total temporal aliasing errors. It can also be seen that, despite the better instrumentation assumed for the FGT mission, the total instrumentation error is only slightly smaller. This is explained by the positioning error, the same as considered for the GRACE mission.

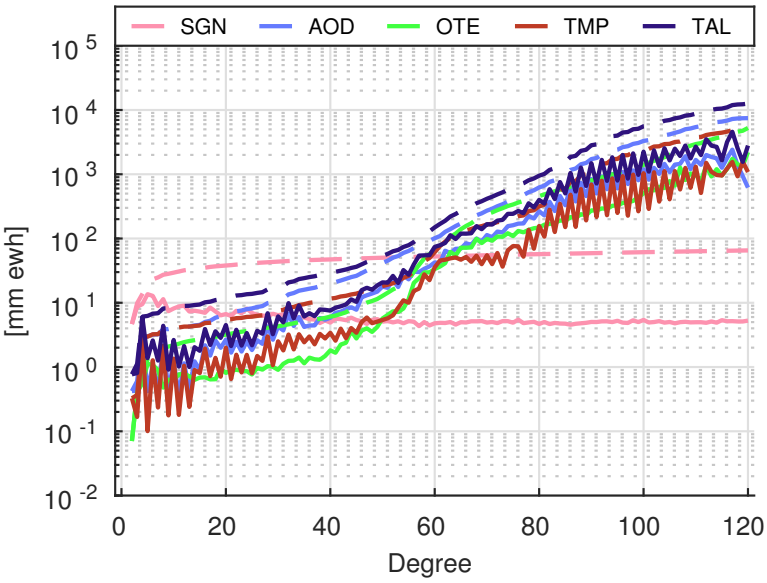

Figure 6.12: Temporal aliasing errors in terms of DV (solid) and CDV (dashed) of unregularized gravity field solutions for the GRACE and FGT missions. See Table 4.3 in page 74 for the explanation of the used acronyms

Regarding regularized gravity field solutions, the same optimization procedure as the one in the case of GRACE was used. The regularization procedure was iterated to yield the minimum total error. The right panel of Figure 6.10 shows the results for the FGT mission in terms of DV of regularized solutions. The high-pass filtering error is the largest error source up to SH degree 10. Above this degree the regularization bias becomes dominant. A comparison with the corresponding plot for the GRACE mission (in the left panel of Figure 6.10) reveals that the total error and regularization bias are smaller for the FGT mission. Due to a reduction of instrumentation errors in the data, a less aggressive regularization procedure is required. As a consequence, one see that the contribution of temporal aliasing errors to the error budget has increased compared to the GRACE mission. On the other hand, above SH degree 40, the total instrumentation error has become significantly smaller. Furthermore, above this degree, the total instrumentation error becomes smaller than the total temporal aliasing error. This is in contrast with the GRACE mission where the total instrumentation error was found to be larger than the total temporal aliasing error above SH degree 40. This shows that, after the regularization procedure, there is a significant improvement in the level of instrumentation errors of the FGT mission.

In Table 6.2, a comparison between the error budget of the GRACE and FGT missions in terms of global RMS of regularized solutions is shown. FGT shows a reduction of instrumentation errors compared to GRACE. The total instrumentation error goes down from 11.0 to 7.5 mm ewh. This is, for the most part, explained by

the reduction in ranging error, from 9.3 to 0.9 mm ewh. Despite this remarkable reduction of the ranging error, the total error shows only a relatively small reduction of about 12%: from 35.7 to 31.5 mm ewh in terms of global RMS. Flechtner et al. (2016) predicts an error reduction between 2-7% for regularized solutions of the GFO mission compared to GRACE. The presented results for the FGT mission confirm that a relatively small reduction of the total error is expected for missions which will replicate the GRACE platform.

Input temporal aliasing (TAL) and positioning (POS) errors are equal for the GRACE and FGT missions. The differences between these errors for the two missions (cf. Table 6.2) are explained by a different choice of the regularization parameter. The ratio between the regularization parameter of the FGT (7.8E-15) and that of GRACE (6.7E-14) is about 9. A lower regularization parameter means that a less aggressive regularization is required to minimize the total error. Therefore, the POS and TAL errors show a relative increase in their contributions to the total error. This is compensated by a relative decrease in the regularization bias (REG). The regularization bias can be stated as the portion of the input mass transport signal which is removed by the regularization procedure. The results obtained for the FGT mission send a clear message. Future satellite gravimetry missions will have to tackle, in the first instance, temporal aliasing errors.

Table 6.2: Comparison of individual error sources of regularized solutions for the GRACE and FGT missions in terms of global RMS [mm ewh]. See Table 4.3 for the explanation of the acronyms.

	RNG	SCA	ACC	POS	**TIN**	AOD	OTE	TMP	**TAL**	FLT	REG	**TOT**	SGN
GRACE	9.27	1.93	3.77	3.46	11.05	4.24	4.56	3.26	8.26	9.14	30.31	35.71	65.29
FGT	0.86	✗	0.91	7.50	7.46	8.73	6.62	6.01	14.09	11.31	23.99	31.53	65.29

6.3. Impact of indirect effect errors

As discussed in Section 4.6, it is likely that indirect effect errors affect existing approaches at gravity field recovery differently. However, it is outside the scope of this thesis to quantify the impact of indirect effect errors across all possible approaches. Therefore, I opted to consider a best-case scenario, where indirect effect errors are excluded. I present an additional comparison between GRACE and FGT missions in the simplified mode, i.e. excluding indirect effect errors. A comparison between the simplified and complete mode results will allow an estimation of the impact of indirect effect errors in the solutions of the considered satellite missions.

Excluding indirect effect errors is accomplished simply by computing reference orbits which are not perturbed by any error source. As a consequence, positioning errors are automatically excluded from the error budget, since they can only propagate into inter-satellite accelerations through the reference orbits. Regarding other errors, their realizations are generated directly in terms of inter-satellite accelerations instead of being used as inputs in the reference orbit computation.

Notice that there is no individual error source that accounts for indirect effect errors. All considered error sources, with the exception of ranging errors, perturb the computation of the reference orbits and, therefore, cause indirect effect errors.

Table 6.3: Comparison of individual error sources of regularized solutions for the GRACE and FGT missions without considering indirect effect errors in terms of global RMS [mm ewh]. See Table 4.3 for the explanation of the acronyms.

	RNG	SCA	ACC	**TIN**	AOD	OTE	TMP	**TAL**	FLT	REG	**TOT**	SGN
GRACE	10.86	2.41	1.70	11.20	4.39	4.23	2.30	6.99	✗	29.07	32.48	65.29
FGT	1.06	✗	0.46	1.19	9.48	5.75	5.57	13.25	✗	23.39	27.05	65.29

When excluding indirect effect errors, inter-satellite acceleration observations no longer suffer from large low-frequency errors. Therefore, the high-pass filtering procedure is no longer required. The comparison in terms of global RMS of regularized gravity field solutions follows the same procedure as previously; the regularization parameter is tuned to yield the lowest total error for each mission. The obtained results are presented in Table 6.3. A comparison of the presented error budget with the third column of Table 6.1, where no high-pass filtering was used either, shows that excluding the indirect effect results in a large reduction of errors in unregularized solutions.

Comparing the error budget of the GRACE mission with (see Table 6.2) and without indirect effect reveals that excluding indirect effect errors leads to total error reduction from 35.7 down to 32.5 mm ewh. This shows that indirect effect errors account for 9% of total error of the GRACE mission. Similar comparison for the FGT mission, shows a reduction in the total error from 31.5 to 27 mm ewh, meaning that indirect effect errors account for 14% of the total error.

Comparing the GRACE and FGT missions without indirect effect errors reveals that the total errors of the FGT mission (27.0 mm ewh) shows a more pronounced reduction of about 17% compared to GRACE (32.5 mm ewh).

It can also be seen that the level of temporal aliasing errors has increased from 7 to 13 mm ewh when the indirect effect is ignored. However, input temporal aliasing errors are in fact equal for GRACE and FGT missions. The difference between the output errors is again explained by the different choices of the regularization parameter value. The better performance of the FGT mission instrumentation allows for less aggressive regularization when minimizing the total error, which results in an apparent increase in the level of total temporal aliasing errors.

6.4. Summary

In this chapter, I have used the noise models presented in Section 4.2 to predict the error budget of GRACE and a future GRACE-type missions. The noise models for the instruments of the GRACE mission were built using simple white-noise assumptions and noise levels described in existing literature. Taking into account all the error sources, I have presented the complete error budget of the GRACE mission. A very good agreement is obtained between the simulated total errors and the total errors observed in real GRACE data, in terms of inter-satellite accelerations. An important finding is that errors in the frequency range between 1 and 9 mHz are caused by a combination of accelerometer, positioning, AOD and ranging errors.

In terms of regularized solutions, I have shown that instrumentation errors are

the dominant error source in the gravity field solutions based on the GRACE mission. Among them, ranging errors are the largest error source. Temporal aliasing errors have a slightly lower magnitude.

I have shown that the high-pass filtering of inter-satellite accelerations and regularization procedures are crucial to reduce the level of noise in the computed gravity field solutions. I also showed that a large regularization parameter (which implies a high regularization bias) is necessary to minimize the total error.

Having shown the error budget of the GRACE mission, I have analyzed the performance of a hypothetical future GRACE-type mission. Such a mission, similarly to the GFO mission, is assumed to follow the orbits and formation parameters of GRACE. I have shown that, despite some improvements in the instrumentation errors, the performance of the FGT mission will be only about 12% better than that of GRACE in terms of global RMS in mm ewh. The results have also shown that the performance of the FGT mission is limited by temporal aliasing errors, most significantly by the AOD error.

An additional set of simulations where indirect effect errors have been excluded showed that, under this specific setup, the FGT mission would perform 17% better than GRACE. A comparison between the error budgets of both missions with and without considering indirect effect errors showed that indirect effect errors for the RRC approach account for between 9% and 14% of the total error in terms of global RMS in mm ewh.

The presented results show that simply replicating the GRACE mission with updated hardware will only lead to marginal improvements on the performance of GRACE. Future ll-SST missions based on the GRACE platform will suffer from the same anisotropic sensitivity, thus requiring filtering and regularization procedures. Furthermore, replicating the GRACE mission does not improve in any way the level of temporal aliasing errors which were shown to limit the performance of the FGT mission. The future of ll-SST gravimetry lies in finding missions designs which can effectively tackle both these issues. In Chapter 7, I will search for a set of mission concepts with the potential to greatly improve the performance of the FGT mission.

7

Assessing limitations of ll-SST missions through small-scale simulations

In this chapter, I assess the limitations of different ll-SST concepts with the help of small-scale simulations. These simulations use idealized ll-SST formations and are designed to recover the Earth's gravity field to relatively low maximum spherical harmonic degree and over short periods of time. They are a quick way to explore the performance limitations of several different ll-SST concepts.

In Section 7.1, general considerations about the design of satellite missions are discussed. Looking into future, an overall reduction in the level of errors is fundamentally important in order to push the performance beyond what is currently achievable. In the following section, I make use of small-scale simulations in the simplified mode in order to pinpoint the crucial design parameters that influence the level of errors of a ll-SST mission. Section 7.3 is dedicated to spatial aliasing errors, section 7.4 to spatial instability errors and, finally, Section 7.5 deals with temporal aliasing errors

The final Section 7.6, is reserved for the conclusions of this chapter.

7.1. Satellite gravimetry mission design as a challenging optimization problem

The purpose of a satellite gravimetry mission is to map mass transport in the Earth's system. In order to select the best possible mission design, one may try to approach the problem as a general minimization problem to select the set of mission parameters which will yield the best performance. However, traditional minimization approaches over the full parameter space searching for the global minimum are not feasible for several reasons.

The major obstacle lies with the complexity of evaluating the performance of a selected mission concept. A large computational effort is needed to realistically evaluate the performance of a single ll-SST mission. One example of a Monte-Carlo optimization is found in Wiese et al. (2011), for the optimization of a mission consisting of two pairs of along-track satellites. The analysis was performed for a single mission concept. This was only possible after greatly reducing the parameter space to the three parameters deemed to be the most important. Even after that, the documented computational time used was large. Stepping back and contemplating the variety of other possible missions concepts, in practice, excludes a similar optimization approach. In order to tackle a larger variety of mission concepts, the necessary approach is to further restrict the parameter space to the smallest possible set of parameters.

There are many parameters to be defined. General parameters are: the maximum spherical harmonic degree $l_{\max}$ up to which the solutions are computed; the data accumulation period N_d; and the number of satellites N_s in the mission. ll-SST missions require pairs of satellites to track each other; therefore, for each chief satellite one must consider the six parameters that define its orbit (c.f. Section 2.2.1). In addition, for each deputy satellite, one must consider the five formation parameters that define the formation (c.f. Section 2.2.3). When considering multiple satellite formations, further parameters are required to define the relative placement of the different formations in inertial space. Despite the already rather complex set of parameters to consider, a further complication is that the total number of parameters is not fixed; e.g., it grows as additional satellites and formations are added to the mission. In order to tackle the complexity of the parameter space, my approach is to find appropriate constraints, which can be used to reduce the parameter set to a minimum. In Section 7.1.1, I will detail those constraints.

A further complication is due to the fact that certain parameters with large impact on the performance of the mission are tightly coupled: orbital inclination, satellite altitude, data accumulation period and the maximum spherical harmonic degree are all related to each other and greatly influence the performance of the mission. For example, both orbital inclination and satellite altitude define the ground track geometry of the mission, which in turn plays a role in the spatial resolution of the mission and the maximum spherical harmonic degree. On the other hand, the maximum spherical harmonic degree is also determined by the data signal-to-noise ratio, which in turn is influenced by the satellite altitude (again). At the same time, different data accumulation periods include different amounts of measurements, which influences the maximum spherical harmonic degree. These multiple inter-dependency loops are not simple to unravel in the context of a minimization problem.

After reaching a smaller set of parameters by means of reasoning or restricting the design to certain desirable configurations, a second round of parameter exclusion begins. This is done by looking at the simplest possible missions and finding the minimal set of design parameters which play a crucial role in the performance of the mission. Then, once it has been understood what are the relevant design parameters, the analysis of more complex mission designs can be focused on a

minimal set of parameters known to be critical to the mission performance.

A final difficulty is the lack of specific mission objectives leading to a difficulty in defining appropriate performance metrics. For instance, Wiese, 2011 explains how a mission oriented towards the monitoring of the hydrological cycle would give preference to low-latitude regions disregarding all measurements over the polar regions, thus rendering the mission useless for glaciology. In this thesis, I opt to use global and regional RMS of total errors over a variety of regions as a simple metric to compare the performance of different missions.

7.1.1. Constraining satellite gravimetry parameter space

As mentioned in the previous section, there are three general parameters: number of satellites N_s, maximum spherical harmonic degree l_{max} and data accumulation period N_d.

Regarding the number of satellites, I will only consider missions consisting of 2 to 4 satellites. ll-SST missions, such as GRACE and GFO, by definition require pairs of satellites to track their inter-satellite range, so that a minimum of 2 satellites is required. Three satellites arranged in a single formation can provide up to three inter-satellite links, which may prove to be a valuable topology for satellite gravimetry. Several publications have proposed missions consisting of 4 satellites arranged in 2 formations, a topology which is argued to bring multiple advantages over the single formation one (P. L. Bender et al., 2008; Wiese, 2011). Missions consisting of more than 4 dedicated gravimetry satellites are less likely to be implemented due to the associated high costs.

The other two parameters are intrinsically connected; it is well known that a larger data accumulation period allows for collecting more data, which in turn has the potential to increase the spatial resolution of the mission. I chose $l_{\text{max}} = 120$, a value which is a good compromise between the spatial resolution and computational time required to evaluate the performance of a mission. Having fixed the maximum SH degree, data accumulation periods between 8- and 24-day periods will be considered; I have found that there is a tendency for errors to grow large below 8-day periods, while error reductions above 24-day periods seem to become negligibly small.

Regarding the chief satellite of a formation, the six orbital parameters to consider are: inclination i, semi-major axis a, eccentricity e, right ascension of the ascending node Ω, argument of the perigee ω and true anomaly ν. Regarding the orbital altitude a, it is well known that lower satellite altitudes are extremely beneficial for satellite gravimetry. Of course, the problem with too low altitudes is exponentially increasing atmospheric drag, which severely impacts the mission lifespan. GOCE was the first satellite mission to implement a drag-free propulsion system, which allowed for maintaining a controlled orbital altitude at the expense of fuel. This technology enables relatively low altitude orbits to be considered for future ll-SST missions. However, depending on the selected data accumulation period, the strictly lowest possible altitude may be less than optimal. This is because repeat ground track orbits offer several advantages over otherwise non-repeat orbits. In Section 7.1.2 I will explain why I only consider repeat ground track orbits

and in Section 7.1.3 I will explain how I selected the minimum possible altitude for a satellite gravimetry mission to be 260 km. Regarding the altitude of any given satellite mission in this thesis, the rationale is to chose the lowest-altitude repeat-groundtrack orbit above the 260 km threshold that matches the selected data accumulation period in order to ensure the finest ground track coverage.

Regarding the eccentricity parameter, one may think of using an eccentric orbit to achieve lower satellite altitudes compared to an equivalent circular orbit with the same semi-major axis. However, this is unlikely to work for several reasons. Firstly, in a general sense, a satellite in a very elliptical orbit will be at very different altitudes during one revolution. This will lead to inhomogeneous measurement accuracy, since lower altitude measurements have higher signal-to-noise ratio than higher altitude ones. In turn, this likely leads to varying mission sensitivity at different regional and spatial scales, which is an undesirable feature. Furthermore, in an elliptical orbit, according to Kepler's 2nd Law, the satellite experiences the largest angular velocity in the vicinity of the perigee. This leads to two consequences; on the one hand, the fraction of measurements made at lower altitude would be relatively small, since the satellite rapidly flies over the orbital perigee. On the other hand, the large velocities at low altitudes would severely increase the drag acting on the spacecraft, with a consequent reduction of the mission timespan. Therefore, there seems to be little use for elliptical orbits. In the further study, I will consider only circular orbits.

Orbital inclination is important in defining the overall ground track geometry of the mission. Non-polar inclinations introduce a gap around the poles with no observations. A low inclination will lead to a large polar gap. On the other hand, for polar orbits all ground tracks converge to the poles, leading to a large concentration of observations in these regions and a sub-optimal observation distribution. In the satellite gravimetry literature, one finds that the main purpose of proposed lower-inclined orbits is to introduce East-West information in along-track mission concepts in order to mitigate the vertical striations error patterns, which are typical for these configurations (P. Bender et al., 2003; Wiese et al., 2011). As will be shown in later sections, different formation combinations will be used as a primary way to introduce East-West information in a satellite gravimetry mission concept. Therefore, for the most part I will make use of near-polar orbits with a 89.5° inclination. For the mission concepts where it is likely that lower inclination orbits are beneficial, such as the dual along-track mission in Section 8.4.1, the orbital inclination parameter will also be taken into account in accessing the mission performance.

If orbits are circular, the argument perigee ω and the true anomaly ν are not defined; in this case, the argument of latitude $u = \omega + \nu$ is normally introduced (cf. Wiese et al. (2011)). Together, u and Ω simply allow one to chose the latitude and longitude of the satellite at the beginning of the data accumulation period. Since the finest distribution of ground tracks will be ensured by using repeat orbits, the starting location of the satellites should be irrelevant. The only reason why one specific location could be better than any other can be attributed to a single instance of the ensemble of possible signal and noise realizations. Assuming we are concerned with the global performance of the mission, on average, any choice

of the argument of perigee and RAAN is as good as any other. In the presented mission concepts, I simply set the two parameters equal to 0°.

Regarding the deputy satellite in any satellite pair, there are only three configurations which are relevant, corresponding to the set of stable satellite formations, i.e., the elementary satellite formations. Any satellite pair will be in either an along-track, pendulum or cartwheel topology. Of the five formation parameters shown in Section 2.2.3, along-track formations only require one parameter, the along-track offset between the two satellites Δx. The pendulum formation only requires the cross-track amplitude B and the corresponding phase angle β. The cartwheel formation only requires the radial amplitude A and the corresponding phase angle α. For all the formations, I will consider the maximum inter-satellite distance to be 200 km; this is the same nominal inter-satellite distance as the one of the GRACE and GFO missions. This defines the aforementioned parameters as $\Delta x = 200$ km, $A = 100$ km and $B = 200$ km. The $A = 100$ km follows from the fact that, in a cartwheel formation, the along-track and radial relative satellite motion is coupled, such that along-track amplitude is twice the radial one. For the cartwheel mission, the α parameter can be used to define the orientation of the inter-satellite baseline. With $\alpha = 0°$, it is oriented in the along-track direction over the Equator and in the radial direction over the poles. For $\alpha = 90°$, it is vice-versa. For the pendulum formation, there exists the choice of adding an along-track constant offset between the two satellites. This configuration has been called in the literature an advanced pendulum (Elsaka et al., 2013). This offset allows the pendulum configuration to include some along-track information into its measurements. However, in the following sections I will not consider advanced pendulums since their potential advantages can be superseded by alternative mission concepts (see Section 8.2). Regarding the β parameter, which sets the phase of the pendulum oscillations, values which differ from 0° require a differential inclination between the two satellites in the formation. While a formation with two orbits with slightly different inclinations maybe stable over short periods of time, the differential inclination causes differential orbital precession, which over time inevitably will break the formation apart. Therefore, the β parameter of the pendulum formations must be set equal to 0°.

Regarding missions which consist of two formations, relevant parameters are: the repeat periods of each formation, the right-ascension angle difference between the orbital planes of the chief satellites $\Delta\Omega$, and the argument of latitude difference between the two chief satellites Δu. Regarding the repeat periods of each formation, they are already restricted to match the data accumulation period of the mission. Therefore, both formations are already assumed to have the same repeat periods. Iran Pour et al. (2013) showed an analysis of sub-Nyquist repeat-period orbits, however, I opt not to look into this type of configurations. Choosing repeat periods for the two formations that are different from the data accumulation period will have a major disadvantage: a repeat period shorter than the data accumulation one will result in a coarser than needed ground track coverage, while a longer one will not fully complete within the data accumulation period, which will result in an uneven ground track coverage and non-uniform coverage in each computed solution. On

the other hand, two formations with different repeat periods could be useful to co-estimate lower-degree shorter-period solutions in order to minimize the temporal aliasing of the mission. However, as argued before, alternative parameterizations of the gravity field are outside of the scope of this thesis. Finally, Δu can be used to adjust the relative latitude between the two chief satellites, while the $\Delta\Omega$ can be used to adjust the spacing between the ground tracks of both formations; in practice, $\Delta\Omega$ is used to interleave the ground tracks of one formation in-between the ground tracks of the other. In Section 7.4.2, an analysis of the best way to interleave formations' ground tracks is presented.

As an outcome of this discussion, the parameter space of the satellite gravimetry problem has been significantly reduced. There is only one general mission parameter to optimize, the data accumulation period N_d. Then, for each formation in the mission, one can choose the type of formation: along-track, cartwheel or pendulum and, when considering a cartwheel formation, the α parameter. When considering multiple formations, Δu should also be investigated. Furthermore, if the considered inter-satellite baseline of the formations is aligned in the same direction (as in e.g. the Bender mission), the orbital inclination of the additional formations may be relevant as well.

7.1.2. Making the case for repeat ground track orbits

There are two characteristics of repeat-groundtrack orbits (RGO) which make them desirable. Firstly, for an a-priori selected data accumulation period, the RGO with the corresponding repeat period ensures the finest possible global coverage of the Earth's surface (Koop, 1993, page 58). Secondly, the geometry of RGOs is constant in time, thus ensuring constant spatial resolution throughout the mission duration.

Despite their appealing characteristics, RGOs are by no means necessary to provide a gravity field solution. Given that satellite gravimetry missions, in general, require low altitudes, the presence of residual atmosphere causes significant drag and, consequently, the satellites' altitude decays over time, thus excluding the possibility of passively maintaining a target RGO.

GOCE was the first satellite mission equipped with a drag-free propulsion system, which maintained very low altitudes through the course of the mission. The ability to control the altitude over the whole mission timespan opens the possibility of using RGOs in future satellite gravimetry missions.

In the context of this thesis, one final motivation for the use of RGOs, is that by ensuring the finest possible coverage, it is possible to exclude the ground track geometry as one of the parameters limiting the performance of a given mission concept. Due to their advantages and their likely use in the future, in this thesis, all orbits are designed as RGOs.

7.1.3. Minimum altitude

It is a well-known fact that low-altitude missions are beneficial, especially for the recovery of signals at high spherical harmonic degrees (Meissl, 1971). On the other hand, the lower the satellite's orbit, the larger the atmospheric drag acting on the satellite with a severe impact on the mission timespan.

In a previous study, Wiese (2011) considered a minimum altitude of 290 km. This altitude was chosen on the basis of a requirement to achieve a mission lifetime of 10 years. Looking into the GOCE mission, the drag-free propulsion was turned on to keep a sun-synchronous orbit at an altitude of 254 km. The planned mission lifetime of GOCE was 20 months during a solar minimum, when atmospheric drag was relatively low. Towards the end of the GOCE mission, it was decided to lower the satellite's orbit in order to maximize the spatial resolution of the mission at the expense of the potential mission lifetime. In May 2013, GOCE was lowered just below 230 km, where it operated until the xenon propulsion fuel ran out in October 2013 (HSO-OEG) (2014).

The GOCE mission sets a lower bound on the scope of possible mission altitudes of future ll-SST missions. It may make sense to trade-off mission lifespan for performance improvements, just as was decided in the GOCE mission. Furthermore, on-going technological developments will likely make future drag compensation systems even more efficient, which is likely to alleviate the minimum altitude requirement.

An analysis of the altitudes of different polar repeat orbits, presented in the left panel of Figure 7.1, shows that an altitude of 290 km restricts the choice of repeat-period orbits. For example, the 12-day repeat-period orbit at 280 km is excluded, and the next possible 12-day orbit is at an altitude higher than 350 km. This means that by imposing a minimum altitude of 290 km, the 12-day repeat orbit is likely to perform worse than other repeat-period orbits. The same Figure shows that selecting a minimum altitude of 260 km is much less restrictive for repeat polar orbits above this value. Therefore, I select 260 km as the minimum altitude threshold to be used in the simulations.

For any considered repeat orbit, as the orbital inclination decreases, the required altitude decreases as well. As a consequence, lower inclinations bring many repeat orbits below the minimum altitude threshold. This is shown, for an inclination of 72°, in the right panel of Figure 7.1. In this case, either the next available higher altitude orbit has to be chosen or, alternatively, the inclination must be increased to keep the satellite altitude above the minimum threshold.

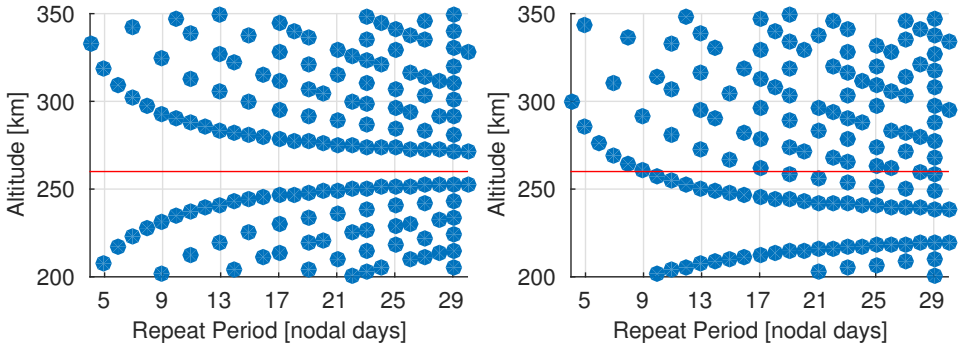

Figure 7.1: Possible altitudes of repeat period orbits for the inclination of 90° (left panel) and 72° (right panel).

7.2. Link between ll-SST formations and gradiometer observables

In the following sections, I will use a simplified set of simulations in order to identify the design parameters which limit the performance of ll-SST missions. The simplified simulations make use of gradiometer observations to analyze spatial aliasing, spatial instability and temporal aliasing errors. Both ll-SST missions and gradiometer instruments observe the same gravity gradients. Therefore, from a conceptual point of view, a given ll-SST satellite pair is equivalent to a single-axis gradiometer with a very long arm (M. Sharifi et al., 2005). On the other hand, simulating an ideal gradiometer instrument is simpler because that requires only one orbit to be calculated. Furthermore, the gradiometer instrument can be used to explore different combinations of gravity gradients without increasing the complexity of the simulation. Therefore, information gathered from analyzing the performance limits of the gradiometer instrument should provide valuable insights in the design of ll-SST missions as well.

A gradiometer instrument oriented in the local horizontal reference frame in a polar orbit is able to measure the xx, yy and zz gravity gradients. In this situation, the x-axis points in the along-track direction and is approximately aligned with the North-South direction, the z-axis points radially down and is aligned with the vertical direction, and the y-axis completes the orthogonal coordinate system and is approximately aligned with the East-West direction. The relation between different ll-SST mission concepts and an ideal gradiometer instrument is rather straightforward. The along-track concept is normally aligned in the North-South direction, such that the ll-SST observations collected will closely resemble the xx gradiometer component. The orbital inclination of the along-track concept can be modified, which will result in ll-SST data containing a combination of the xx and yy gradients. The pendulum concept is normally oriented in the East-West direction, such that its ll-SST observations map approximately to the yy gravity gradient. By adding an along-track offset, the pendulum can be modified to include xx information in the observations. Finally, the cartwheel formation collects ll-SST observations oriented in the vertical plane; the observations oscillate between the xx and the zz gravity gradient components.

In the following sections, I will compare the relative performance of missions which consider different gravity gradients as observations. Based on the above considerations, it will be possible to predict the relative performance of the corresponding ll-SST formations.

7.3. Spatial Aliasing

In practice, computing a gravity field solution from a set of measurements requires the choice of the maximum SH degree $l_{\max}$ to be solved for. The mass transport signal to be recovered from those observations is composed by an infinite number of harmonics. The signal harmonics which are above the chosen $l_{\max}$ will alias into the solutions as spatial aliasing errors. In this section, I will show the relation between spatial aliasing errors and the choice of $l_{\max}$, as well as the differences in

these errors between different gradiometer components.

The ESM model, which is used in this thesis as the input mass transport signal, is defined up to SH degree 180, while the bulk of the solutions computed will be cropped at $l_{max} = 120$. While the ESM model, unlike the real mass transport signal, does not contain infinite harmonics, SH degrees between 121 and 180 suffice to accurately represent the propagation of spatial aliasing errors.

Three different simulations are considered, each observing a single gradiometer component: xx, yy or zz. These are considered in order to evaluate the impact of spatial aliasing errors in each of the elementary formations. The considered simulations are set on 319/20[1] repeat orbit at an altitude of 403 km repeat orbits at an altitude of 275 km. The 20-day period was chosen as the minimum required to compute SH solutions up to $l_{max} = 120$.

The global RMS of spatial aliasing errors as a function of selected l_{max} for each simulation is presented in Table 7.1. For a selected l_{max}, the input field is composed of SH coefficients between $l_{max}+1$ and 180. It can be seen that there are significant differences between the considered simulations. The xx and yy simulations yielded relatively large global RMS of spatial aliasing errors (between 12 and 18 mm ewh), while the zz simulation yielded about an order of magnitude smaller errors (between 1 and 2 mm ewh). The yy simulation seems to be the worst of the three.

Figure 7.2 shows the DV of spatial aliasing errors with increasing l_{max}. This figure shows that the distribution of the spatial aliasing error over the SH degrees is also quite different for the considered gradients. While the xx gradient shows an exponential increase with SH degree, the spatial aliasing error of the yy and zz gradients is almost completely confined to the largest few SH degrees considered, as shown by the sharp increase of the plotted curves close to l_{max}.

Table 7.1: Global RMS of spatial aliasing errors for different choice of l_{max} [mm ewh]. First column shows the considered input SH degrees and the second column shows the selected l_{max}. Remaining columns on the table show global RMS of spatial aliasing errors for the considered gradiometer simulations.

Input	L_{max}	xx	yy	zz
41 to 180	40	12.37	12.52	1.85
61 to 180	60	14.12	17.17	2.12
81 to 180	80	12.57	14.89	1.67
101 to 180	100	12.81	14.81	1.46
121 to 180	120	13.45	14.55	1.57

Notice that, in general, the global RMS of spatial aliasing errors does not decrease monotonically with higher l_{max}. From the presented results, it seems that this error is constant with some random fluctuations. This finding is counter-intuitive. By increasing l_{max}, the number of harmonics in the aliased signal decreases and therefore one expects the corresponding spatial aliasing error to become smaller. To illustrate why this happens, I selected as input a constant portion of the ESM signal between SH degrees 121 and 140 and computed the corresponding spatial aliasing errors for different choices of l_{max} for all three simulations. The results are

[1] 319 revolutions in 20 nodal-days, cf. Section 2.2.2

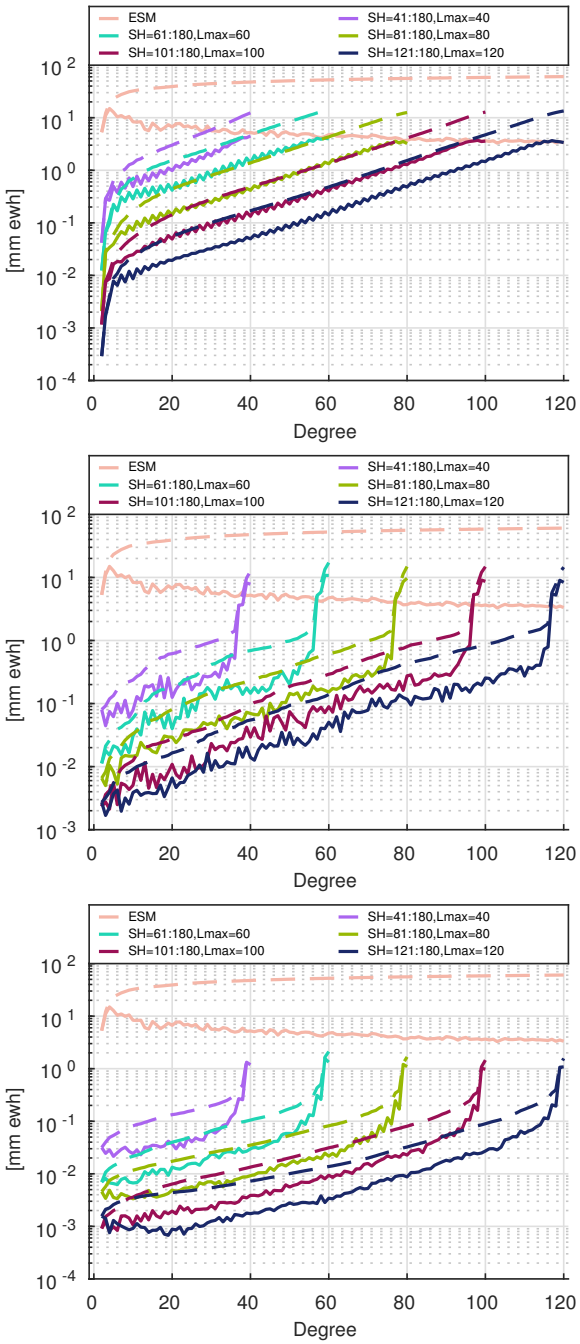

Figure 7.2: Spatial aliasing errors for the xx (top), yy (middle) and zz (bottom) simulations for different choice of l_{max}.

plotted in Figure 7.3 and they are consistent across all three considered simulations. For relatively low l_{max}, say 40 to 80, the input signal (between SH 121 to 140) triggers a negligible level of spatial aliasing errors. However for $l_{max} = 120$, immediately below the minimum SH of the considered input, the spatial aliasing error is now significantly larger than before. Similar behavior can be observed in Figure 7.2 by comparing the DV curves for consecutive l_{max}. For example, by comparing the range of SH degrees 0 to 40 corresponding to $l_{max} = 40$ and $l_{max} = 60$, one can see that spatial aliasing errors for the latter are significantly smaller than the former. This happens because, for $l_{max} = 60$, the range of SH degrees between 41 and 60 is no longer a part of the input fields. As a consequence, the level of spatial aliasing errors in the range between SH degree 0 and 40 goes down.

These results show that spatial aliasing errors are caused by the portion of the input signal corresponding to the SH degrees which are immediately above the selected l_{max}. Alternatively, one can say that input signals at SH degrees larger than $l_{max} + N$, where N is about 10, will not cause any significant spatial aliasing errors in the solutions. In turn, this explains why, an increase in selected l_{max}, which by definition reduces the power of the aliased signal, does not lead to a corresponding decrease in the global RMS of the spatial aliasing error.

Comparing the evolution of spatial aliasing errors with increasing l_{max} for the different simulation in Figure 7.3 reveals another relevant aspect in the choice of l_{max}. The different l_{max} curves of spatial aliasing errors of the yy simulation (for most SH degrees) overlap each other. The solution computed between SH degrees 10 and 30 does not change as a consequence of selecting higher l_{max}. This makes sense; given the same input signal, the output solution is not expected to change. However, one can see for xx simulation, that spatial aliasing errors, between any range of SH degrees, become larger with higher l_{max}. This illustrates the amplification of errors when solving a system of linear equations which becomes more ill-conditioned with increasing l_{max}. These spatial instability errors are another important aspect to consider in the choice of l_{max}; they will be further analyzed in Section 7.4.

In conclusion, spatial aliasing errors are significantly smaller for the zz compared to the yy or xx gradients. This means that, in principle one expects both along-track and pendulum missions to be rather sensitive to spatial aliasing errors. Considering that the observations provided by a cartwheel missions are partly oriented in along the radial direction means that they may be less sensitive to these errors compared to the other two concepts.

Furthermore, it was shown that spatial aliasing errors are mostly caused by the input signals immediately above the chosen l_{max}. Since the magnitude of the input mass transport signal decreases slowly (in mm ewh) with increasing SH degree, it is beneficial to choose higher l_{max}.

In general, the bulk of the spatial aliasing error is confined to the few largest considered SH degrees. This behavior is even more pronounced for the yy and zz gradients. While choosing large l_{max} may not significantly decrease the global RMS of the spatial aliasing errors, it will ensure that this error is almost completely allocated to the highest considered SH degrees which may be adequately filtered

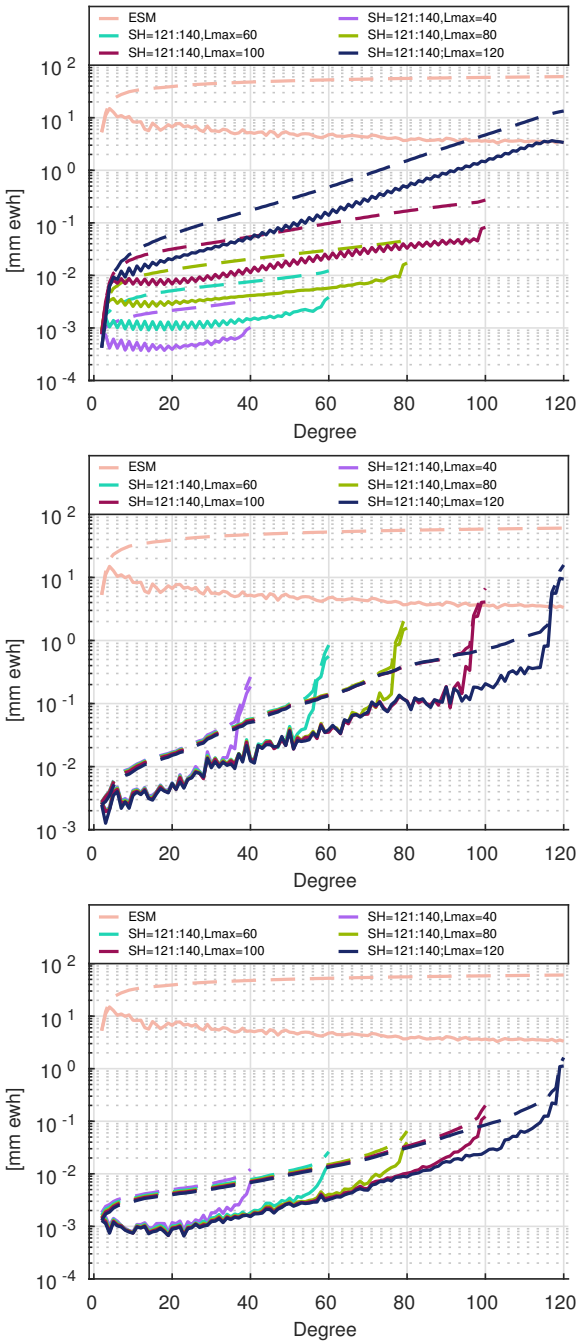

Figure 7.3: Spatial aliasing errors for the xx (top), yy (middle) and zz (bottom) formations for different choice of l_{max} caused by input signals between SH degrees 121 and 140 from the ESM model.

later on. The caveat exists however, that spatial instability errors are known to increase with l_{max}. Therefore, spatial instability errors must also be taken into account in the choice of l_{max}.

7.4. Improving spatial resolution

An increase in the spatial resolution is one of the desired improvements regarding the performance of future satellite gravimetry missions. In theory, in order to improve the spatial resolution of a mission all that is required is to compute a solution up to higher l_{max}. In practice, this is not possible. With increasing l_{max}, the system of linear equations to solve becomes ill-conditioned and a solution can no longer be computed. However, even before this point is reached, the downward continuation of the gravitational signal causes existing noise in the observations to be progressively amplified until it becomes much larger than the signal to be recovered. Once any source of noise in the data has been greatly amplified by this process, I refer to these errors as *spatial instability errors*. This term refers to the increasing instability of the solutions when solved up to an increasingly higher l_{max}. The spatial resolution of any gravimetry mission is affected by spatial instability errors. I claim that spatial instability errors are the best estimate of the spatial resolution of a mission. In this section, I will analyze what are the design parameters which play a role in mitigating these errors.

All simulations consist of a gradiometer instrument in a near-polar circular 31/2. Due to the 31 equidistant equator crossings of the orbit, the Colombo-Nyquist rule recommends the maximum degree of the solution to be $l_{max} < 31/2$, meaning that $l_{max} \leq 15$. To evaluate the spatial instability errors of each simulation, the normal matrices are assembled up to a significantly higher degrees. The choice of such short data accumulation period (and corresponding repeat orbit) is motivated by keeping the maximum SH degree of the normal matrices required to push the spatial resolution limits of the considered simulations below $l_{max} \leq 120$.

Spatial instability errors show up as an amplification of existing observation noise when solutions are computed to a too high SH degree. Therefore, in order to analyze the spatial instability errors, it is necessary to consider a noise source which will trigger it. In this section, I consider gradiometer noise modeled as simple white noise with a $\text{PSD}^{\frac{1}{2}}$ of $1 \times 10^{-5}\,\text{E}/\sqrt{\text{Hz}}$. This value has been chosen to be smaller than the mean mass transport signal (in the frequency range below 6 mHz), as one expects from a real ll-SST dataset. In the following sections this value plays no special role, since all conclusions will be based on a comparison of the spatial instability errors for different simulations affected by noise of the same level. All other errors sources are disregarded, including temporal aliasing errors.

To ensure a better comparability of the results, the same noise realizations are used in all simulations. Furthermore, for each simulation in this section (unless otherwise stated), the reported results are the aggregate of an ensemble of 9 different noise realizations. When presenting SH models, the aggregation of the different error realizations is done by computing the RMS error per SH coefficient. On the other hand, when presenting maps of errors, the aggregation is done by computing

the RMS per grid node.

Regarding the considered mass transport signal, it is the average of the HIS component of the ESM model over the 2 first days in May 2006 propagated into the gravity gradients along the 31/2 repeat orbit, which is considered in all the simulations. The selected time period has been randomly chosen, having no special significance. Furthermore, the mass transport signal in this section is plotted only to provide context of how strong errors are compared to a typical signal. Depending on the maximum inversion degree of the current simulation, the input mass transport signal will be consistently cropped to rule out spatial aliasing errors. Figure 7.4 shows a comparison of spatial instability errors with the typical mass transport signal in terms of PSD$^{\frac{1}{2}}$ of xx gravity gradients. In this plot, the input mass transport signal has been cropped to SH degree 40, which explains the sharp decay in signal at roughly 6 mHz.

7.4.1. Single formation

Single gradiometer component

To begin with, I present three simulations, each using a single gradiometer component as the observable, i.e., only the xx, yy or zz gradients are observed at a time. In this way, I investigate whether the choice of the observable orientation plays a role in the spatial resolution of the mission.

By considering a single gradiometer component and inverting the data up to an increasingly high SH degree, one can analyze the evolution of spatial instability errors as a function of l_{max}. The results for the xx component are shown in terms of DV in the right plot of Figure 7.4. Here one can see that errors gradually increase with increasing l_{max}. Between l_{max} 30 and 40, the DV of the computed solution jumps several orders of magnitude. Beyond $l_{\text{max}} = 40$, the normal matrix becomes ill-conditioned and solutions can no longer be computed. Notice that the considered plot does not conform to the Colombo-Nyquist rule (similar findings reported by (Visser et al., 2012)), which recommends a maximum $l_{\text{max}} = 15$; in fact, the plot shows that one may easily double l_{max} to 30 without introducing large spatial instability errors. Next, one may wonder whether there are significant differences between inverting observations of different gradiometer components. Two additional simulations were considered using the yy and zz gravity gradients. The solutions computed up to $l_{\text{max}} = 30$ are shown for each simulation in Figure 7.5. The zz gradient yields significantly lower errors for all SH degrees compared to the other two components. The xx gradient is just slightly lower than the yy up to SH degree 10, above which the yy gradient shows lower errors than xx. In terms of cumulative error, the xx gradient is slightly worse than yy.

Spatial instability errors for the three components are also shown as maps in Figure 7.6. The plot confirms that the zz gradient suffers from relatively low noise. The yy gradient shows a horizontal striation error pattern in the latitude range between $-45°$ and $45°$. The xx gradient suffers from the strongest noise, which shows up as a vertical striation pattern, being particularly pronounced around the $\pm 45°$ latitudes.

The presented results clearly show that the zz gradient is less sensitive to spa-

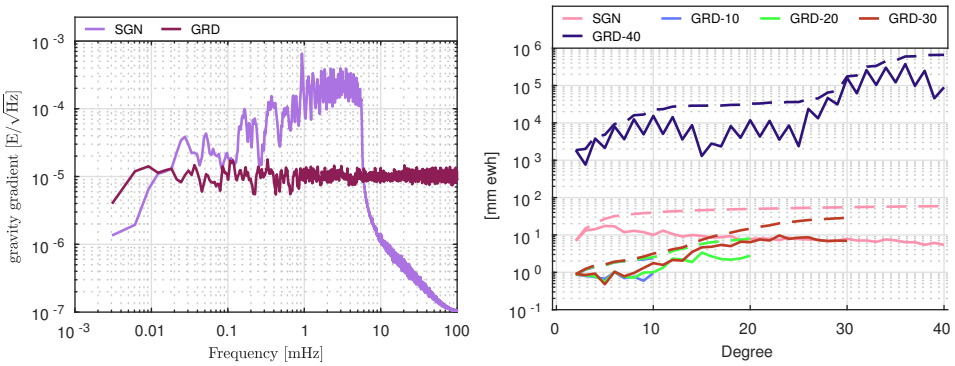

Figure 7.4: Left panel: a comparison of mass transport signal and introduced gradiometer white noise in terms of PSD$^{\frac{1}{2}}$ of xx gravity gradient. Right panel: DV plot of spatial instability errors up to increasingly high spherical harmonic degrees for xx gravity gradient observations.

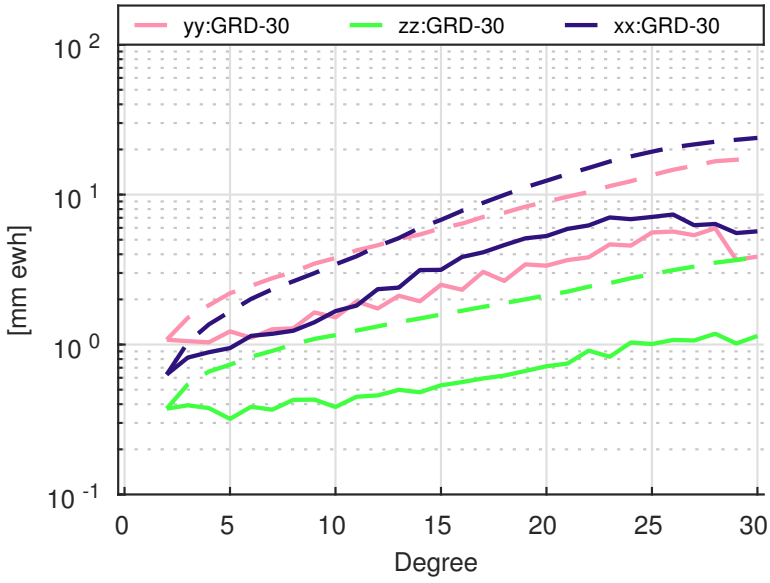

Figure 7.5: RMS per SH degree of 9 realizations of spatial instability errors for different gravity gradients: xx, yy and zz for $l_{max} = 30$.

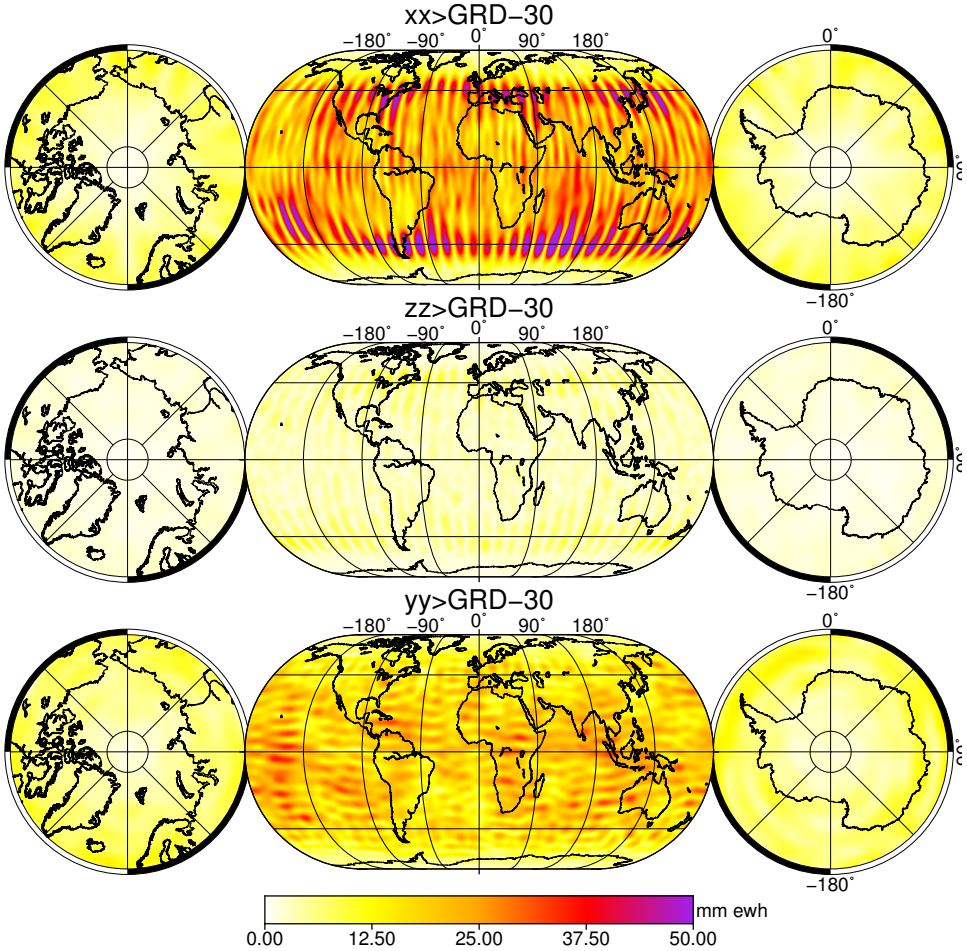

Figure 7.6: Spatial RMS of 9 realizations of spatial instability errors for different gravity gradients for $l_{\max} = 30$.

tial instability errors and conversely has the potential to deliver the highest spatial resolution.

Multiple gradiometer components

When considering the design of future ll-SST satellite missions, observables from different formations and/or different satellite pairs can be combined. Therefore, it is important to understand how spatial instability errors depend on different combinations of observables.

In the following sections, I will consider the xz gradiometer component in addition to the previous three. Despite the fact that there is no correspondence between the xz-gradient and a stand-alone ll-SST configuration, the inclusion of the xz gradient will lead to a few interesting findings which are relevant for satellite gravimetry in general. With the addition of the xz gradiometer, there are 6 possible combinations of 2 observables (xx+yy, xx+zz, xx+xz, yy+zz, yy+xz, and zz+xz), 4 combinations of 3 observables (xx+yy+zz, xx+yy+xz, xx+zz+xz, yy+zz+xz) and 1 combination of 4 observables (xx+yy+zz+xz).

Let us start with the combinations of 2 observables. Figure 7.7 shows the evolution of spatial instability errors for the xx+yy combination. Here we see that, unlike in the case of the single observable xx, spatial instability errors are below the mass transport signal up to $l_{\text{max}} = 50$, and only beyond $l_{\text{max}} = 70$ do spatial instability errors become orders of magnitude larger. This is a significant improvement over the single-observable setup; the spatial resolution of the mission is effectively doubled by the inclusion of another observable without any change of the ground track geometry.

Next, we compare the spatial instability errors of all 6 possible combinations for $l_{\text{max}} = 60$ (Fig. 7.8). All combinations show roughly similar performance, except for xx+xz, which performs worse than the others.

Finally, we inspect the evolution of spatial instability errors for the xx+yy+xz combination of three observables, shown in the left plot of Figure 7.9. It can be seen that the spatial instability errors increase gradually; at $l_{\text{max}} = 50$ they are below the mass transport signal for all SH degrees, and at $l_{\text{max}} = 70$, the cumulative spatial instability error is about the same as the cumulative mass transport signal.

Having selected $l_{\text{max}} = 70$, I compare all four combinations of three observables along with the single combination of four observables (Fig. 7.10). This is an interesting plot, as it shows that all the considered combinations, including the 4-observable combination, suffer from approximately the same level of spatial instability errors, except for the xx+yy+zz combination, which is orders of magnitude worse. The plot is fully consistent with the properties of the gravity field; gravitational potential is a harmonic function satisfying the Laplace's equation, so that each of the xx, yy and zz components can be written as a linear combination of the other two. Therefore, the addition of the zz component to a xx+yy combination does not yield any significant reduction of spatial aliasing errors. As a consequence, the xx+yy+zz combination is in fact similar to a 2-observable combination. For the same reason, the xx+yy+zz+xz combinations performs similarly to the 3-observable combinations, xx+yy+xz, yy+zz+xz and xx+zz+xz, since they all share the same amount of information.

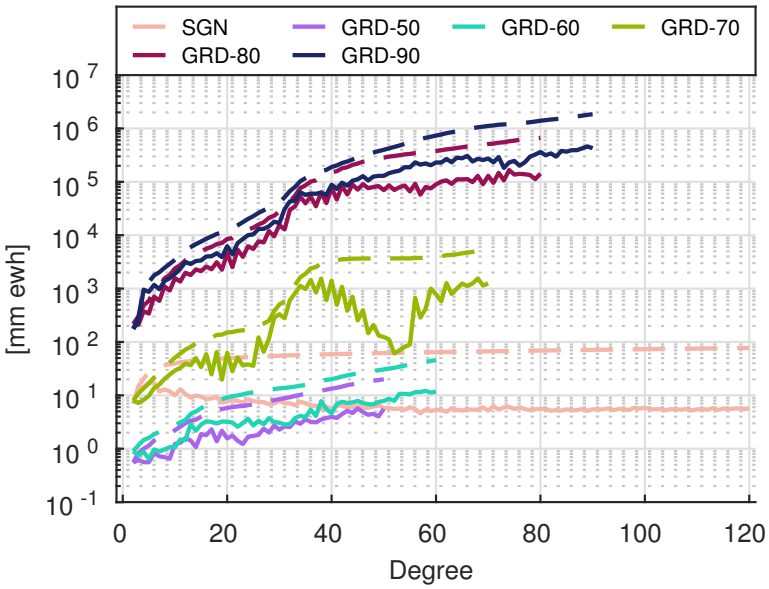

Figure 7.7: Evolution of spatial instability errors with increasing SH degree for the xx+yy combination.

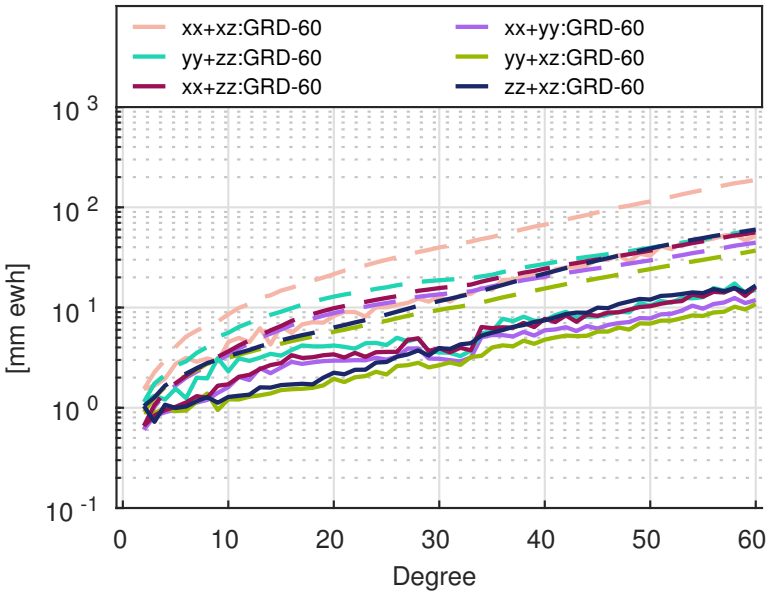

Figure 7.8: A comparison of all possible double-observable combinations for $l_{max} = 60$.

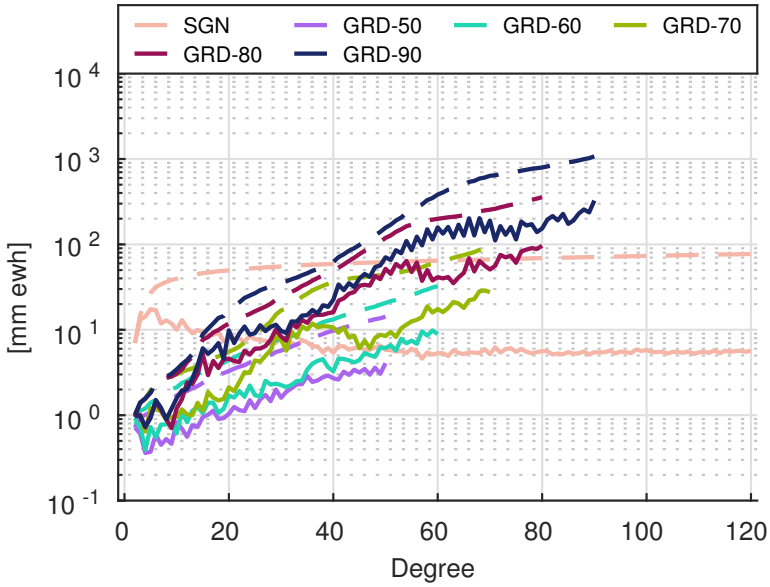

Figure 7.9: Evolution of spatial instability errors with increasing maximum SH degree for the xx+yy+xz combination.

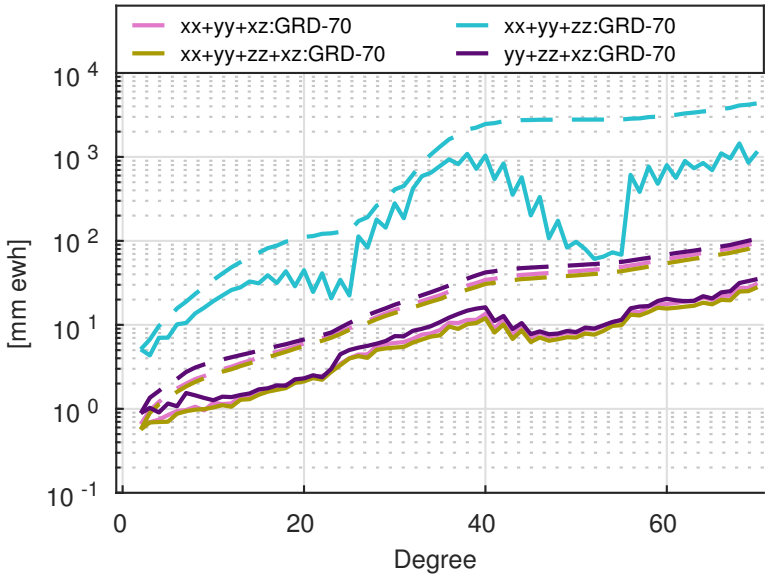

Figure 7.10: Comparison of all three- and four- component combinations of gradiometer observables for $l_{max} = 70$.

The presented result shows that adding more information to the system effectively increases the spatial resolution. This result is very important, since spatial resolution is likely a major bottleneck in the performance of future satellite missions. Spatial resolution is regarded as an unavoidable trade-off with temporal resolution of the mission, e.g. (Reubelt et al., 2010). As a consequence, discussions about improving spatial resolution are confined to either compromising the temporal resolution of a given mission or by launching additional satellites in order to reduce the overall ground track spacing of the mission. The presented results show that the spatial resolution of a mission is *not* uniquely determined by the ground track geometry.

Knowing that additional observables improve the spatial resolution of a given mission, one may also take advantage of this fact in the design of a mission in order to improve improve its temporal resolution. For a given target spatial resolution, the addition of another source of information relaxes the requirement on the data accumulation period, thus, potentially improving the temporal resolution. This aspect will be analyzed in detail in Section 7.5.

Colombo-Nyquist rule and its numerous reformulations

Visser et al., 2012 proposed the reformulation of the Colombo-Nyquist maximum solvable SH degree as

$$l_{\text{max}} = kn_r + 1, \tag{7.1}$$

where n_r is the number of satellite revolutions and k is the number of combined observation types. To validate this idea, I compare the spatial instability errors of three missions: a mission which collects a combination of three observables xx+zz+xz over a time span of 2 days, a mission collecting a zz+xz combination over a period of 3 days and one collecting only the zz component over a period of 6 days.

All three missions collect the same amount of data, since the product between linearly independent observations and days of data is always equal to 6. The standard Colombo-Nyquist rule predicts $l_{\text{max}} = 15$ for the xx+zz+xz on a 31/2 orbit, $l_{\text{max}} = 23$ for the zz+xz on a 47/3 orbit and $l_{\text{max}} = 47$ for zz scenario on a 95/6 orbit. According to Eq. 7.1, the maximum solvable SH degree should be about the same for all the considered scenarios: 93, 94 and 95 for xx+zz+xz, zz+xz and zz, respectively.

The corresponding spatial instability errors are shown in Figure 7.11 (in the left plot, for $l_{\text{max}} = 60$, and in the right plot, for $l_{\text{max}} = 90$). Both plots show that the three missions exhibit different levels of spatial instability errors. At $l_{\text{max}} = 60$, the 2-day xx+zz+xz mission already suffers from comparatively high errors, while the 3-day zz+xz mission is also worse compared to the 6-day zz mission. The discrepancies become even larger when considering $l_{\text{max}} = 90$. The results show that Eq. 7.1, while better than the original Colombo-Nyquist rule, is still inadequate for predicting the spatial resolution of different missions.

In Figure 7.12, a search for l_{max} was carried out to yield similar cumulative RMS of spatial instability errors. Here we see that the 6-day mission is solved to degree 95, the 3-day mission to degree 70 and the 2-day mission to degree 50. I propose

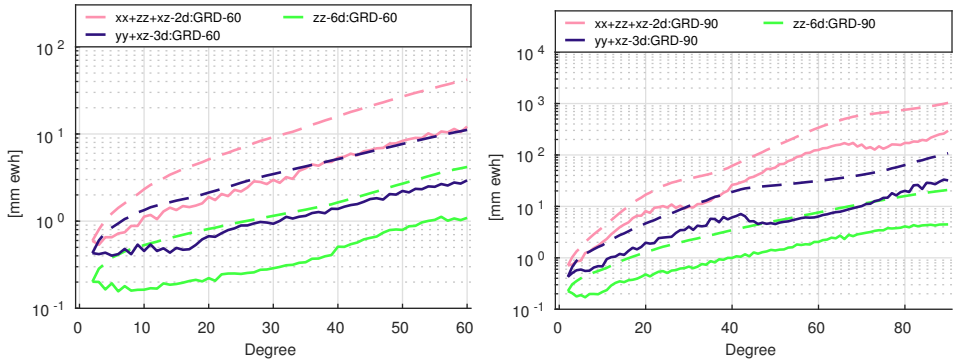

Figure 7.11: spatial instability errors for three missions with the same amount of data: a 2-day xx+zz+xz, a 3-day zz+xz and a 6-day zz mission. Left plot: spatial instability errors for $l_{\max} = 60$. Right plot: the same for $l_{\max} = 90$.

an improved empirical predictor for the maximum solvable degree of a satellite mission:

$$l_{\max} = n_r \cdot \left(1 + \frac{k-1}{c}\right) \quad , \tag{7.2}$$

where c is a constant scaling factor. This predictor is valid under the assumption that a repeat period orbit is used which matches the data accumulation period of the computed solutions and that the k combined observables are linearly independent sources of information.

What distinguishes this predictor from the previous ones is the realization that the spatial resolution benefits from the addition of observation components, but does not scale one-to-one with the number of observables or orbital revolutions. If c = 1, then the expression simplifies to $l_{\max} = n_r k$, which is close to Eq. 7.1. From the presented results, c is found to be between 1.6 and 2. The latter value means that an additional observable will increase the maximum SH degree by about half of the number of satellite revolutions. A simpler way to state this is that the spatial resolution of a 10-day mission collecting 2 observables is equivalent to a 15- or 16-day mission collecting 1 observable, and not to a 20-day mission collecting 1 observation as predicted Eq. 7.1.

Finally, it is important to state that such predictors are an oversimplification of the gravity field recovery problem They are very useful for a preliminary analysis of different satellite mission concepts but are no replacement for a proper assessment of mission performance through simulation.

Even- and odd-parity repeat-period orbits

As it is already mentioned above, geometry of the ground tracks is an important aspect determining the performance of a satellite gravimetry mission. A proof of that is the degradation of GRACE solutions when the satellites' orbits approach short repeat periods (Klokočník et al., 2008; Weigelt et al., 2013). Weigelt et al. (2013) noticed that, in some repeat orbits, the ascending tracks overlap the descending

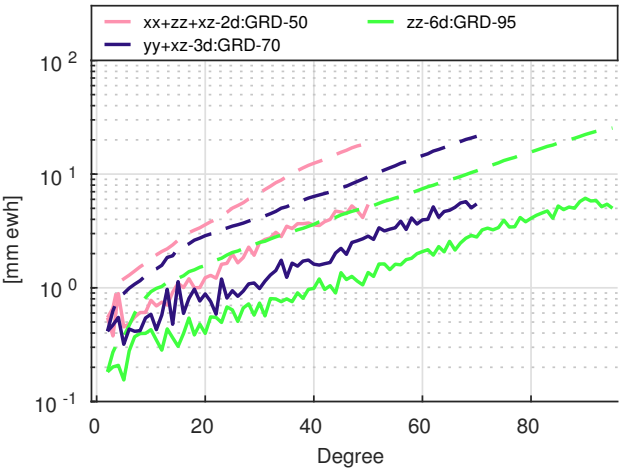

Figure 7.12: Spatial instability errors for three missions with same amount of data: a 2-day xx+zz+xz, a 3-day zz+xz and a 6-day zz mission. The l_{max} of each curve has been selected as to yield approximately the same cumulative spatial instability error.

tracks over the equator. This happens when the difference $\alpha - \beta$ is even, where α is the orbit repeat period in days and β is the number of satellite revolutions in that period (see also Section 2.2.2). This type of orbits are said to be of *even* parity, while orbits with no overlapping tracks over the equator are of *odd* parity. For brevity I will call these orbits *even orbits* and *odd orbits*, respectively.

A good illustration of this phenomenon is provided in Weigelt et al. (2013) and shown here as well in Figure 7.13. In the two left panels I present the ground tracks of two orbits of a 3-day repeat period: the leftmost is for an even 47/3 and the middle-left for an odd 46/3 repeat orbit. Despite the similar number of revolutions within the repeat period, it can be seen that the even orbit has two times less equator crossings than the odd one. This results in a significant degradation of the ground track spacing when compared to the odd type.

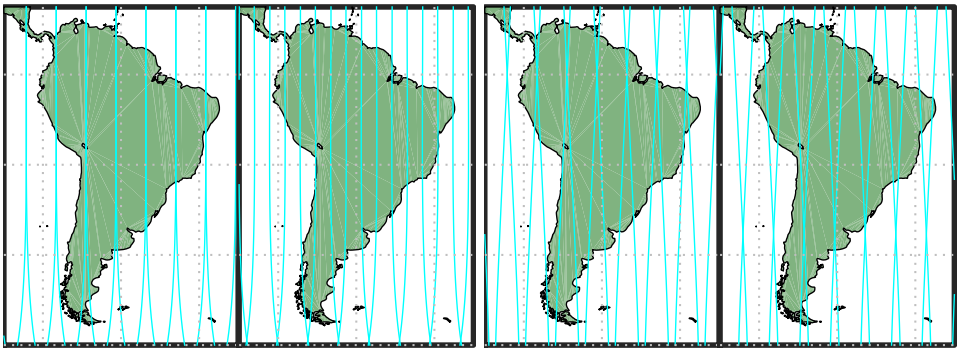

Figure 7.13: Odd- and even-parity 3-day repeat orbits with different inclinations. The two panels on the left depict 47/3 (even) and 46/3 (odd) repeat orbits with an inclination of 86.5°, respectively. The two right panels depict the same, but now with an inclination of 89.5°. For the 86.5° orbits, the ground track spacing of the even-parity orbit is noticeably worse than of the odd-parity one. The same is not true for other orbit inclinations, as shown by the example of 89.5° orbit.

One important detail missing in the analysis made by Weigelt et al. (2013) is that the two considered orbits have an inclination of 86.5°. This is important, because at this inclination, the East-West velocity of the satellites approximately matches the Earth's rotation speed, so that the ground tracks become meridional for the most part of the orbit. For other inclinations, the resulting ground track geometry is significantly different. In the two right panels in Figure 7.13, a similar pair of orbits is shown, but with an inclination of 89.5°. Regarding the equator crossings alone, the depicted orbits have the same characteristics: the even orbit has half of the equator crossings of the odd orbit. However, when one regards the full latitude domain, one sees that these two orbits are complementary; while the even orbit has a two-times larger ground track spacing at the equator, it has half ground track spacing at 30° S latitude.

In Figure 7.14, the spatial instability errors associated with the odd and even orbit at 89.5° inclination are shown for the xx gravity gradient observable. The figure reveals that the odd orbit shows an error reduction of about 50% with respect to the even one between SH degrees 10 and 20. Nonetheless the difference between them in terms of CDV at degree 40 is not significant.

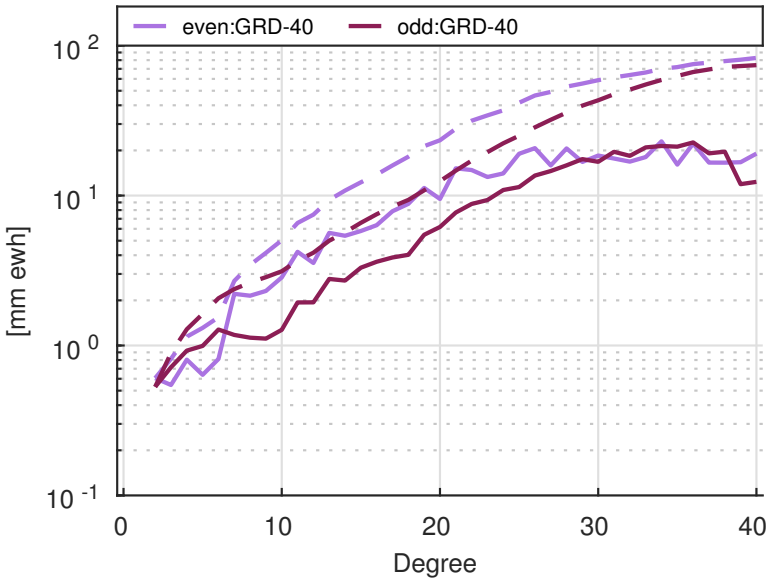

Figure 7.14: Averages of an ensemble of 9 realizations of spatial instability errors for odd and even parity orbits at 89.5° orbital inclination in terms of DV and CDV.

Considering the minimum altitude threshold of 260 km (cf. Section 7.1.3), Table 7.2 lists for each amount of nodal days α, the available repeat orbits until the first odd one. Notice that the lowest altitude available orbit for the odd α has even parity. If one would assume that even-parity orbits are significantly worse than odd ones, then for odd α one would have to chose the next higher altitude repeat orbit. This assumption would restrict odd α to have about 20 km higher altitude orbits

than necessary. In turn, this would probably result in a degradation of the performance at odd α. Given the relatively minor differences found in terms of spatial aliasing errors between even and odd orbits, I will use not only odd-parity orbits, but also even-parity ones ensuring that the lowest altitude repeat orbit available will be used.

Table 7.2: List of available repeat groundtrack orbits above 260 km in ascending altitude until the first odd-parity orbit for each α between 8 and 16-days. α represents the nodal days and β the number of satellite revolutions (cf. Section 2.2.2).

α	β	Parity	Altitude [km]
8	127	odd	296
9	143	even	292
	142	odd	323
10	159	odd	289
11	175	even	286
	174	odd	312
12	191	odd	284
13	207	even	282
	206	odd	304
14	223	odd	281
15	239	even	279
	238	odd	298
16	255	odd	278

7

7.4.2. Multiple formations

Multiple-formation mission concepts, such as the Bender constellation (P. L. Bender et al., 2008), are known from the literature (Elsaka et al., 2013; Wiese, 2011). Additional formations can reduce spatial instability errors in two ways: firstly, by increasing the amount of data collected in any time period and, secondly, by reducing the size of the gaps between ground tracks.

Interleaving ground tracks of multi-formation missions

When adding a second formation with the same repeat orbit, it may be desirable to design the ground tracks of the second formation to be interleaved with those of the first one in order to improve the overall ground track spacing and, ideally, the mission's spatial resolution. Then, the question is how to correctly interleave the ground tracks of multiple formations.

At the first glance, the answer is simple: shift the orbital plane of the second formation by half of the longitude difference between adjacent groundtracks $\delta\lambda$. More generally, the mission ground track spacing can be halved by shifting the second formation by an arbitrary multiple plus a half of this difference.

However, as discussed in Section 7.4.1, there is a relevant aspect in which even and odd repeat orbits differ. Regarding even orbits, the interleaving is straightforward; an even repeat orbit with β revolutions will have β unique equator crossings

equidistantly spaced in the longitude domain. The ground track spacing is $\delta\lambda = \frac{2\pi}{\beta}$. Therefore, when adding the second formation, it is sufficient to shift its RAAN by

$$\Delta\Omega = \left(k + \frac{1}{2}\right)\delta\lambda = \left(k + \frac{1}{2}\right)\frac{2\pi}{\beta}, \quad \forall k \in Z \quad . \tag{7.3}$$

For $k = 0$, interleaved ground tracks are obtained with $\Delta\Omega = \frac{\pi}{\beta}$.

The question is how to handle odd orbits. The ascending and descending tracks of odd orbits do not cross at the equator. There are 2β equidistant equator crossings. The ground track spacing *at the equator* is now $\delta\lambda = \frac{\pi}{\beta}$. Applying a $\frac{\pi}{\beta}$ shift will cause the ascending ground tracks of one formation to overlap the descending ground tracks of the other formations, thus resulting in no reduction of the equatorial ground track spacing. Thus, in order to interleave the groundtracks of multi-formation missions in odd repeat orbits the relative shift is

$$\Delta\Omega = \left(k + \frac{1}{2}\right)\frac{\pi}{\beta}, \quad \forall k \in Z \quad .$$

In Figure 7.15, two odd orbits with an inclination of 89.5° are plotted where two different shifts have been applied. In the left panel, the second orbit is shifted by $\frac{\pi}{2\beta}$, so that the new equator crossings are interleaved with the first orbit ones. One can see that, while the ground track spacing is indeed halved at the equator, at the latitude of $-30°$, where the ground track spacing is the coarsest, the addition of the second formation has not significantly improved the ground track spacing. If the second formation is shifted by $\frac{\pi}{\beta}$, the descending ground tracks of one formation overlap at the equator the ascending ground tracks of the other one, and the ground track spacing at the equator does not change. However, the ground track spacing at the coarsest location is now halved, resulting in a more uniform coverage overall. Looking at Figure 7.15, and assuming that the groundtrack spacing at the equator is not more important than at other latitudes, shifting odd orbits by $\frac{\pi}{\beta}$ seems more reasonable. This approach is also more convenient because one does not need to consider whether the orbits are even or odd. In the next experiment, I invert various combinations of synthetic data in order to quantify an improvement in the spatial resolution (if any) offered by the $\frac{\pi}{\beta}$ shift as compared to other options.

In the next section, spatial instability errors of the two alternative ways to shift odd parity orbits will be analyzed in the context of multi-formation missions.

Added value of additional formations

It was shown in Section 7.4.1 that combining different observables in the same formation effectively extends the spatial resolution of the mission. Now the question is whether a further increase can be obtained when the same amount of data is collected by distinct formations?

In general, a second satellite formation may improve the spatial resolution with respect to a single-formation mission for two reasons: more data and denser

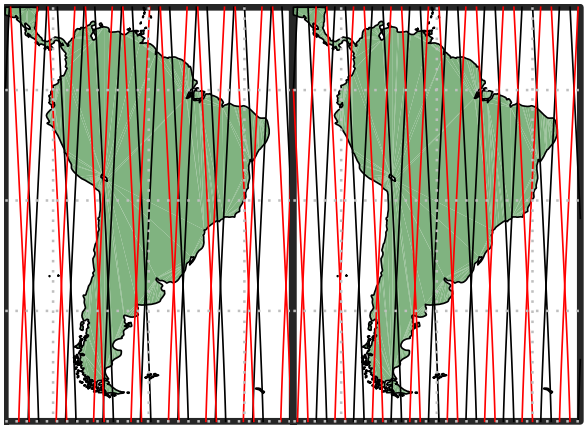

Figure 7.15: Two odd repeat orbits with interleaved ground tracks. The first orbit is represented in black. The second orbit, in red, is shifted by $\frac{\pi}{2\beta}$ in the left panel, and by $\frac{\pi}{\beta}$ in the right panel. In the right panel, even though the ground track spacing at the equator is not reduced, the overall geometry is more uniform.

groundtracks. It is trivial that more data is always beneficial. In previous sections, it was shown that it is also possible to design a single formation to acquire a higher amount of data by measuring different gravity gradient components. Therefore, I will isolate the added value of a second formation by keeping the amount of data constant when comparing single- and dual-formation simulations. The baseline mission is the yy+xz combination, which was shown in Figure 7.8 to be the 2-observable combination with the lowest spatial instability errors at maximum SH degree 60. To keep the amount of data constant, the yy+xz combination will be split in two different formations where one observes the yy and the other observes the xz component.

Four simulations will be analyzed, all consisting of formations on 31/2 odd-repeat orbits at an inclination of 89.5°:

- yy+xz: the baseline mission to compare improvements to.
- yy/xz: a dual-formation mission where the second formation is shifted by π/β, which, given that the considered orbit is odd, causes the equatorial ascending crossings of one mission to overlap the descending crossings of the other mission. As previously discussed, despite increasing the overall ground track density, this configuration does not decrease the equatorial ground track spacing, cf. the right plot of Figure 7.15.
- yy/xz-itv: a dual-formation mission where the second formation is shifted by $\pi/2\beta$, such that the overall equatorial ground track spacing is now halved, a configuration similar to what is shown in the left plot of Figure 7.15.
- yy/xz-ovl: shifts the second formation's ground tracks by $2\pi/\beta$ in order to overlap with the first formation's ones, so that there is no change in the overall ground track geometry relative to yy+xz.

A comparison of the spatial instability errors with the single-satellite yy+xz formation at maximum SH degree 60 is shown in terms of DV and CDV in the left

plot of Figure 7.16. Differences between the yy+xz and yy/xz-ovl simulations are hardly visible. These small differences can be explained by an accumulation of numerical errors during the numerical integration applied to compute the orbits. They represent a minimum threshold for any reduction of spatial instability errors to be meaningful in the context of ground track geometry design.

Regarding the yy/xz and yy/xz-itv simulations with improved ground track design, spatial instability errors are slightly smaller for both. The yy/xz is marginally better below spherical harmonic degree 30, while yy/xz-itv is better above that degree. Regarding the cumulative error, both configurations yield nearly the same spatial instability errors. Overall, there seems to be no significant difference between the two configurations in terms of spatial instability errors.

The spatial instability error reduction shown by the improved ground track simulations is underwhelming. There is no significant reduction of spatial instability errors which would allow for computing SH solutions up to a higher degree, thus increasing the spatial resolution of the mission. The Colombo-Nyquist rule applied to multi-formation missions (Reubelt et al., 2010) states that the maximum solvable spherical harmonic degree $l_{\max} = \text{floor}\left(\frac{\delta\lambda}{2}\right)$. Considering this rule, one could be tempted to imagine that halving the equatorial ground track spacing would effectively double the spatial resolution of the mission. This is true for multi-formation missions which consider the same observable in all the formations. However, the presented results show that the same is not generally applicable when different observables are considered.

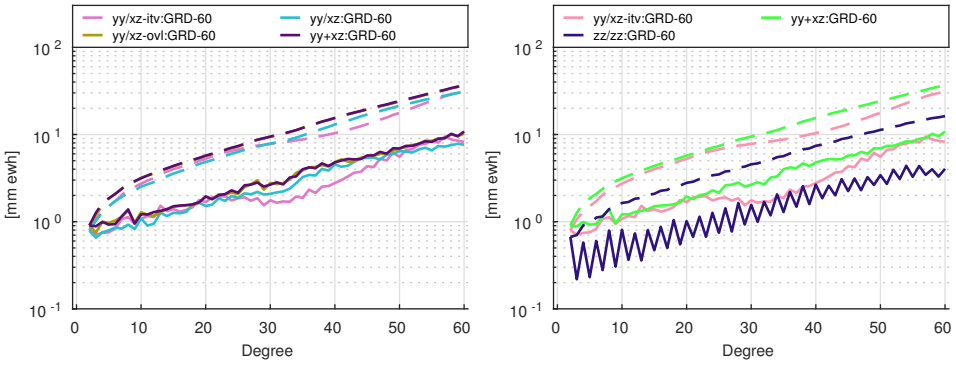

Figure 7.16: Left panel: comparison of the best 2-observable single formation mission, yy+xz, with three missions consisting of two formations observing the yy and xz components separately. Each of the three considered 2-formation missions shifts the ground track of the second formation differently; yy/xz ground track is shifted by $\Delta\Omega = \pi/\beta$, yy/xz-itv by $\Delta\Omega = \pi/2\beta$ and yy/xz-ovl by $\Delta\Omega = 2\pi/\beta$. Right panel: comparison of a single-formation mission collecting the yy+xz combination, a dual-formation mission yy/xz, where the formations collect yy and xz observables respectively and a dual-formation mission zz/zz, where both formations collect the same zz observable.

Type of observations

An additional simulation was performed to verify whether the improvements in spatial resolution can be obtained by selecting different combinations of observations.

The rationale is that, while on a single formation mission the only way to increase the amount of collected information is to combine orthogonal components of the gravity gradients, in multi-formation missions this limitation no longer applies. Taking into account that the zz observable has been shown to have the lowest spatial instability errors in the single-observable set of simulations, cf. Figure 7.5, perhaps a dual-formation mission where both formations observe the zz component is capable of improving on the yy/xz dual formation.

The zz/zz simulation shares the same orbits as the previously presented yy/xz simulation, so that the formation ground tracks are interleaved by $\Delta\Omega = \pi/\beta$. The comparison of the corresponding spatial instability errors is shown in the right plot of Figure 7.16. It can be confirmed that the zz/zz mission reduces the level of spatial instability errors. The observed improvement is even significantly larger than the improvement obtained by interleaving the ground tracks of the yy+xz mission. This shows that there is no need to ensure orthogonality of the collected observations in multi-formation missions in order to maximize the amount of information collected.

7.5. Improving temporal resolution

The concept of temporal resolution is clear for satellite missions which use direct observation methods, e.g. laser altimetry or radar. It is the amount of time between the satellite visits over the same geographical region. This amount of time is defined by design in the chosen satellite orbits. Temporal resolution in the context of a satellite gravimetry mission is not as clearly defined. This is a consequence of the fact that gravimetric measurements are not local in nature. Each measurement carries information about the Earth's gravity field as a whole and not only about the local geographical region.

Typically, a global gravity field solution is computed on the basis of data collected over a period of time. Temporal resolution can be defined as the amount of time between computed solutions, i.e. temporal resolution is equal to the data accumulation period. This is the definition proposed in the Heisenberg principle of satellite gravimetry (Reubelt et al., 2010). For a repeat orbit β/α, the temporal resolution of the mission is defined as $D_{\text{time}} = \alpha$. However, I argue that this definition is not useful in the design of satellite gravimetry missions. It does not take into account several aspects which play a role in the quality of the recovered solutions:

- the amount of data collected: under this definition, multi-formation missions would have the same temporal resolution as single-formation ones despite collecting much more data.
- the distribution of measurements: there are infinite number of possible orbits available to collect measurements and certainly some are worse than others. Under this definition of temporal aliasing, all of these would have the same resolution.
- the aliased error sources: the concept of temporal resolution is meaningless in the absence of the mass transport processes which cause temporal aliasing errors. The spatial distribution, temporal evolution of these processes and

how they map into the observations drives the temporal resolution of the mission.

Therefore, the design of a satellite gravimetry mission with enhanced temporal resolution requires a quantifiable definition of this concept. Conceptually, a satellite constellation could continuously observe all geographic regions. Over any pre-defined data accumulation period, it would allow one to perfectly recover the mean field. As a consequence, there would be no temporal aliasing errors and such a satellite network could be said to have an infinite temporal resolution. In any realistic scenario, this is not feasible, the temporal resolution will always be limited. Then, the mean field cannot be exactly recovered because temporal variations will map into the solutions as temporal aliasing errors. I state that the best metric for the temporal resolution of a mission is the level of temporal aliasing errors.

In Section 6.2, I have shown that temporal aliasing errors are one of the major limiting factors to the performance of the GRACE and GFO missions. Similarly to the analysis for the spatial resolution, I will use simulated gradiometer data to investigate the mission criteria which may play a role in minimizing the level of temporal aliasing errors.

The baseline mission has a 79/5 repeat orbit, polar inclination and an altitude of 317 km, from which temporal aliasing errors are propagated up to SH degree 40, well within the Colombo-Nyquist limit, in order to avoid any spatial aliasing issues. Temporal aliasing errors are caused by three components: dynamic mass transport signal (TMP), ocean tide model errors (OTE) and atmosphere and ocean de-aliasing model errors (AOD) (c.f. Section 4.2.2). The mean of the AOD and OTE error (i.e., the static component of the error) is, in general, non-zero within the data accumulation period of the mission. This static component, however, can be recovered exactly and does not cause temporal aliasing errors. Therefore, I subtract the static component from the input AOD and OTE errors. The TMP error consists by definition of only the non-static component of the mass transport signal.

When dealing with time-variable phenomena, it is naive to focus the analysis on a single period of time, since any conclusions made may be false if another period was chosen. In order to present robust conclusions, in this section, with the exception of 7.5.2, all temporal aliasing errors are an aggregate of 9 different error realizations at randomly selected dates in the range between 1995 and 2006[2]. Furthermore, the set of randomly selected dates is consistently applied to all simulations. This procedure ensures that the presented results are robust and not biased towards specific date.

In the following sections, I will compare different missions in terms of their temporal aliasing errors, using the simulation procedure presented in Chapter 4. I will analyze the impact of different parameters onto temporal aliasing errors. First of all, I will consider different gradiometer data components individually to check whether significant differences in temporal aliasing errors exist. Next, I will analyze different combinations of these components. Afterwards, the dependence of temporal

[2]this is the range spanned by the ESM mass transport model used in the simulations (Dobslaw et al., 2014b)

aliasing errors on the data accumulation period will be analyzed. Finally, multiple satellite formations will be considered. I will analyze the added value of a second formation, depending on the relative orbital shift and the type of observables used in the constellation.

7.5.1. Single formation

Impact of different observables

A set of missions equipped with an ideal gradiometer instrument is considered, differing by the gravity gradient component they observe: xx, yy or zz. The left panel of Figure 7.17 shows a comparison of the total aliasing error between the three considered gravity gradient observables. There are significant differences between observables. The zz observable shows the least errors overall, especially in the SH degree range from 10 to 30. The xx component is the best up to SH degree 10, above which it grows to reach the highest levels, being the worst one above SH degree 15. The yy observable shows relatively high errors below SH degree 10 and relatively low errors above this degree. In terms of cumulative error the observables can be sorted in increasing order as zz, yy and xx.

The right panel of Figure 7.17 shows the DV of each error source as recovered from the zz component, the one with the lowest cumulative temporal aliasing error. The plot reveals some interesting details. Firstly, it shows that TMP is the smallest contributor. This means that the dynamic mass transport signal is negligible in terms of temporal aliasing errors, at least at data accumulation periods of 5-days.

The remaining lines in the plot show that the total temporal aliasing error is dominated by a combination of OTE and AOD errors with roughly equal magnitudes. What is remarkable about this finding is that, despite having similar error magnitudes, OTE and AOD errors are differently distributed over the Earth. In particular, OTE errors are for the most part confined to a small fraction of the Earth's surface (c.f. Fig. 4.1).

A map comparing the spatial RMS of temporal aliasing errors as recovered by the three considered observables is shown in Figure 7.18. Notice how temporal aliasing errors are differently affected by the choice of observable. The overall error is much smaller for the zz- observable, being limited in geographical extent to a few particular regions, such as the North Sea, the Baltic Sea and the Southern Oceans. The yy observable also shows relatively small errors, although large localized features can be seen at the northern Australian coast, the coasts of East Asia and in the North Sea. As for the xx- observable, the geographical extent of the error is much larger; it is predominant over the oceans, where it manifests itself as the familiar vertical stripe pattern. Thus, the zz component seems to be less sensitive to temporal aliasing errors.

Combination of gradiometer components

It is also interesting to analyze the sensitivity of different combination of observables to temporal aliasing errors. In line with Section 7.4 dealing with spatial instability errors, I will consider the xz observable in addition to xx, yy and zz. All combinations of 2, 3 and 4 observables from the set xx, yy, zz and xz have been simulated, all

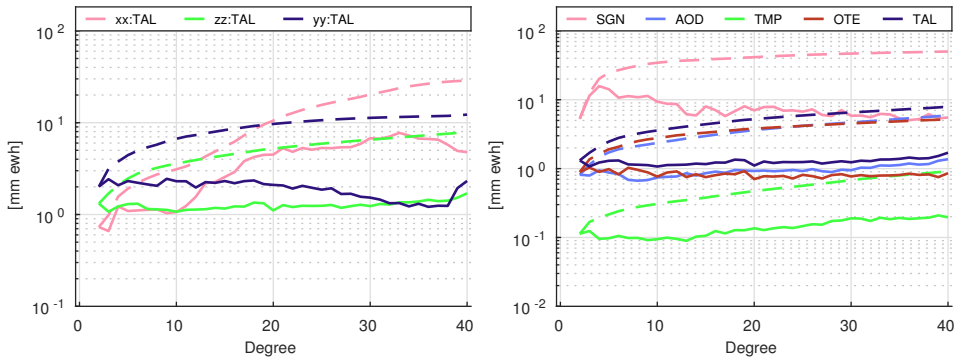

Figure 7.17: Analysis of temporal aliasing errors as recovered in a simulation of gravity gradient observables with a DAP of 5 days. Left panel: DV of the total temporal aliasing error (TAL) for different gravity gradient observables. Right panel: DV of different temporal aliasing error components as recovered by the zz observable simulation in comparison with the mass transport signal (SGN). The plotted curves are the aggregate of 9 different error realizations at randomly selected dates. The explanation of the used acronyms can be found in Table 4.4 in page 75.

yielding very similar results. The four combinations with the lowest level of temporal aliasing errors are shown in Figure 7.19. The plot shows that all combinations yield practically the same level of temporal aliasing errors. This means that, beyond considering the single xx or yy observables, the combination of additional gradiometer observables *does not lead* to a decrease in the amount of temporal aliasing errors relative to the single zz observable. This finding contrasts with what was shown in Section 7.4.1 where additional observables resulted in significant improvements in the context of spatial instability errors. Remarkably, the combination xx+yy shows the same level of errors as zz. This combination yields significant improvements compared to the single-component xx and yy cases.

7.5.2. Data Accumulation Period

Temporal aliasing errors will differ depending on the length of the data accumulation period (DAP). In this section, I will analyze the dependence of temporal aliasing errors on the DAP.

Increasing the DAP will obviously result in a larger amount of observations collected and, as a consequence, is likely to result in a reduction of temporal aliasing errors at the expense of temporal resolution. However, the amount of data is not the only relevant parameter that varies with the choice of DAP. There are at least three other factors which play a role in the level of temporal aliasing errors. In Section 7.1, I have restricted the orbits used in this study to have the same repeat period as the DAP. Therefore, by increasing the DAP, also the groundtracks become denser and the distribution of measurements over time changes. Notice that the time between revisits to the vicinity of a given geographic location is not the same for repeat-groundtrack orbits corresponding to different DAPs. Secondly, notice that the sources of temporal aliasing errors cannot be modeled as stationary random errors. Therefore, one can not assume that these errors will average out

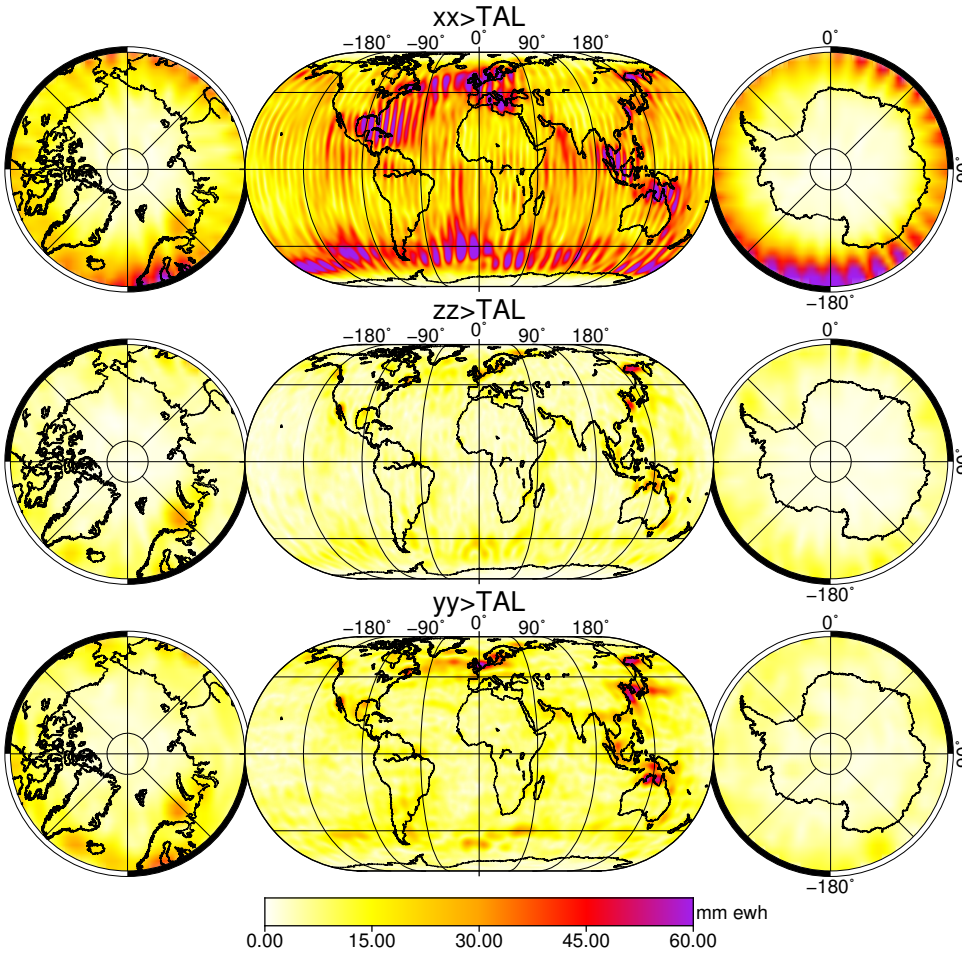

Figure 7.18: Spatial RMS of temporal aliasing errors as recovered in a simulation of different gravity gradient observables with a DAP of 5 days.

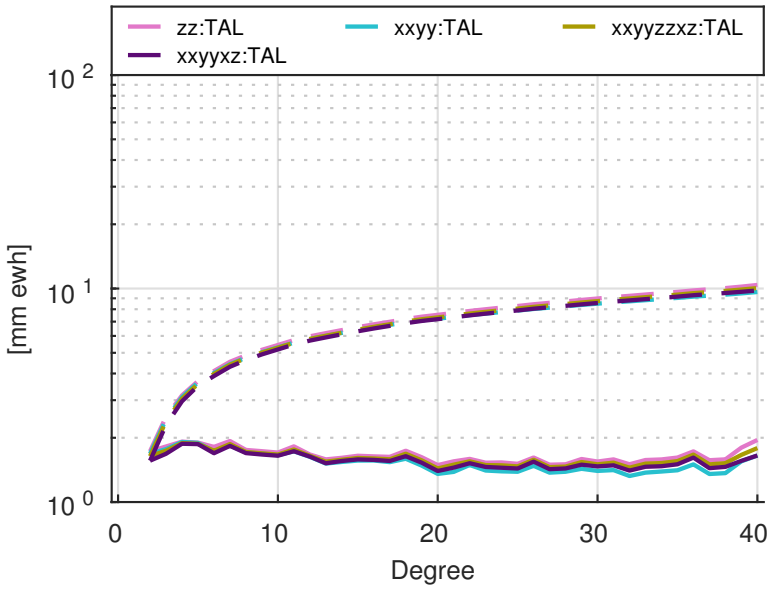

Figure 7.19: Comparison of total temporal aliasing (TAL) errors for a selection of different combinations of gravity gradient observables with a DAP of 5 days.

similarly as stationary errors will. Finally, the level of temporal aliasing errors in the observations depends on the orientation and combination of observables of the considered formation(s). Therefore, there is a possibility that a specific DAP may consistently yield lower temporal aliasing errors. All these are relevant aspects that play a role in the level of temporal aliasing errors, which motivates the study of their dependence on the DAP.

I select as the baseline the 5-day zz-only single-component mission presented previously, since that one has shown to have the lowest amount of temporal aliasing errors among all the single-component scenarios. Several different mission timespans, between 5- and 40-day long, are considered in order to compare the resulting temporal aliasing errors.

As shown in the right panel of Figure 7.17, AOD model errors and ocean tide model (OTE) errors are the major contributors of the total temporal aliasing errors. So, it is interesting to analyze how these two error sources evolve with longer DAPs. The left panel of Figure 7.20 shows AOD errors for DAPs between 5- and 40-day long. It can be seen that the level of AOD errors decreases monotonically with longer DAP periods, although with a diminishing rate at the longer timespans. The AOD error drops by about a factor of two between the 5- and 40-day DAP. A similar behavior can be seen for the OTE error component, as shown in the right panel of Figure 7.20. Not surprisingly, also the total temporal aliasing (TAL) error decreases with the increasing DAP, as presented in the left panel of Figure 7.21. Increasing the DAP from 5 to 15 days leads to a reduction in the the cumulative total aliasing error at SH degree 40 from 8 to about 5 mm ewh (38%). Furthermore, increasing

the DAP to 40 days further reduces the TAL error to ≈3.5 mm ewh (i.e., a total reduction of 56%).

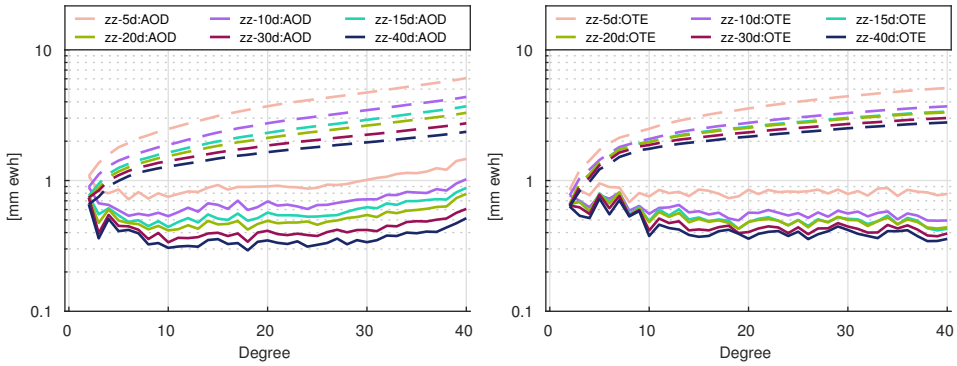

Figure 7.20: Left panel: RMS of AOD errors for zz-only single-component missions with DAPs between 5 and 40 days. Right panel: the same for the OTE errors.

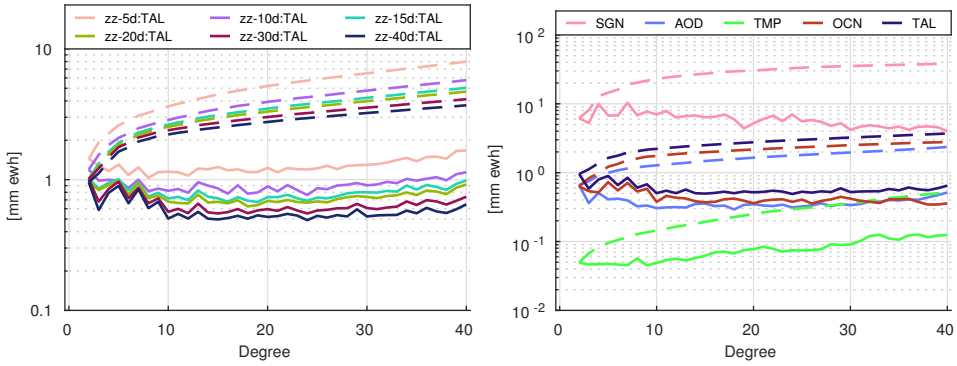

Figure 7.21: Left panel: RMS of the total temporal aliasing (TAL) error for zz-only single-component missions with different DAPs. Right panel: breakdown of TAL error for the mission with the longest DAP of 40 days.

At the 5-day DAP, the total temporal aliasing error is mostly composed of the AOD and OTE errors with similar magnitudes, as was shown in the right panel of Figure 7.17. The breakdown of the total temporal aliasing error for the 40-day timespan is shown in the right plot of Figure 7.21. Here, it can be seen that for the 40-day DAP, the OTE component is now slightly larger than AOD.

A breakdown of the of total temporal aliasing error in terms of spatial RMS map (together with the error itself) is shown for the 40-day DAP in Figure 7.22. The TMP component has been omitted, since not much information can be seen in the spatial plot due to it's relatively low magnitude. The regions which experience the largest temporal aliasing errors for each of the considered components can be easily identified. As shown previously, OTE is dominant in magnitude, with particularly

high levels in specific coastal regions. The AOD component is the second largest contributor, showing large magnitudes both in specific coastal regions and in large regions in the open ocean (in particular, the Southern Ocean).

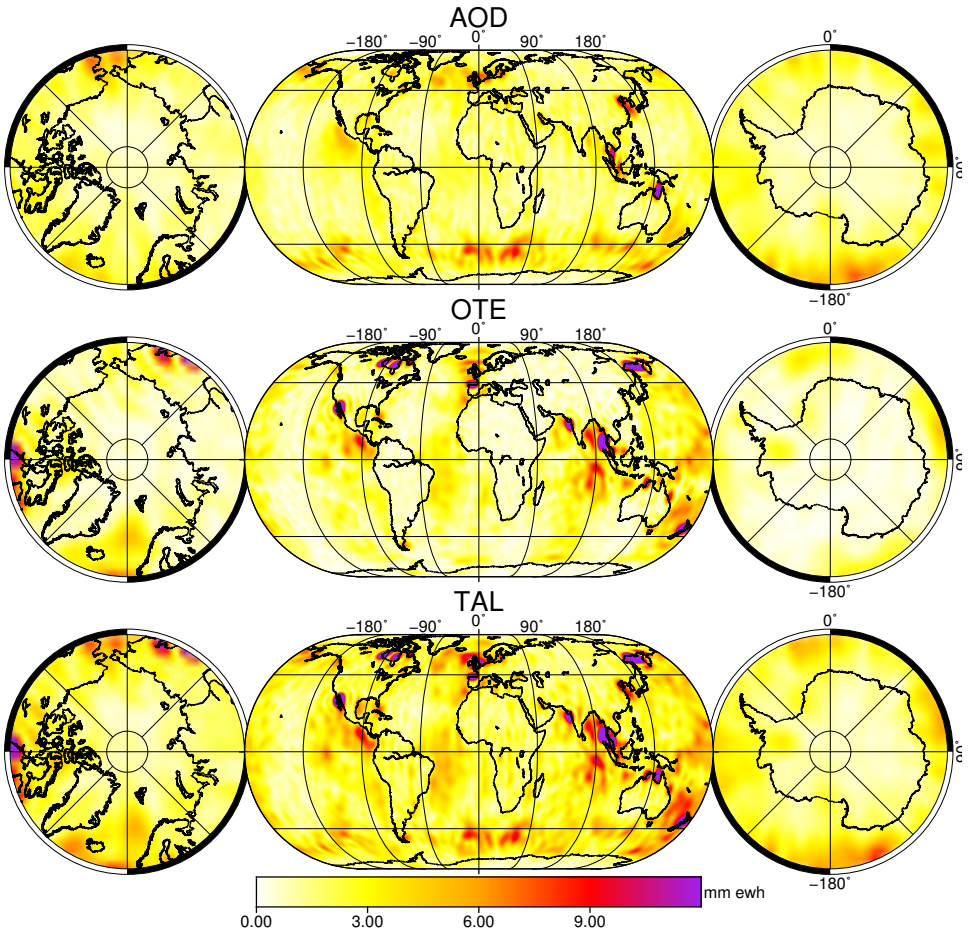

Figure 7.22: Spatial RMS of an ensemble of 9 different realizations of TAL error components and the entire TAL error for the zz-only single-component mission with the 40-day DAP.

Averaging Data Accumulation Periods

In the previous section, I found an overall reduction of temporal aliasing errors with increasingly longer data accumulation periods. This is explained by the averaging effect of the longer observation window. Now, let us assume that a relatively long time period is split into N sub-intervals, so that gravity field solutions are recovered for all of them and ultimately averaged. Then, an interesting question is: what is the optimal N which yields the lowest level of temporal aliasing errors?

I considered a timespan of 60 days and a set of simulations which consider the zz gravity gradient component with 5, 10, 15, 20 and 30-day DAPs. These yield a total of 12, 6, 4, 3 and 2 different solutions per set, respectively. Averaging the solutions within a set results in a single temporal aliasing error realization for the entire timespan. Because a set of solutions will be averaged for every DAP, in this section, unlike the previous ones, only one error realization is considered in each DAP instead of an ensemble of 9-realizations.

Figure 7.23 shows a comparison of the results for different DAPs. It shows that temporal aliasing errors per degree become smaller for longer data accumulation periods, although the differences between the resulting errors are not large. A similar behaviour is observed for cumulative errors, with the average of 2 30-day solutions showing the lowest value (3 mm ewh) and the average of 12 5-day solutions showing the highest value (4 mm ewh).

In Figure 7.24, maps of the averaged sets of solutions for the 5-, 15- and 30-day DAPs are shown, demonstrating a slight error reduction in the coastal areas of Australia, Indonesia and East Asia with increasing DAP. The presented results show that solutions computed with long DAPs yield lower temporal aliasing errors than the average of a set of solutions computed with short DAPs spanning the same period.

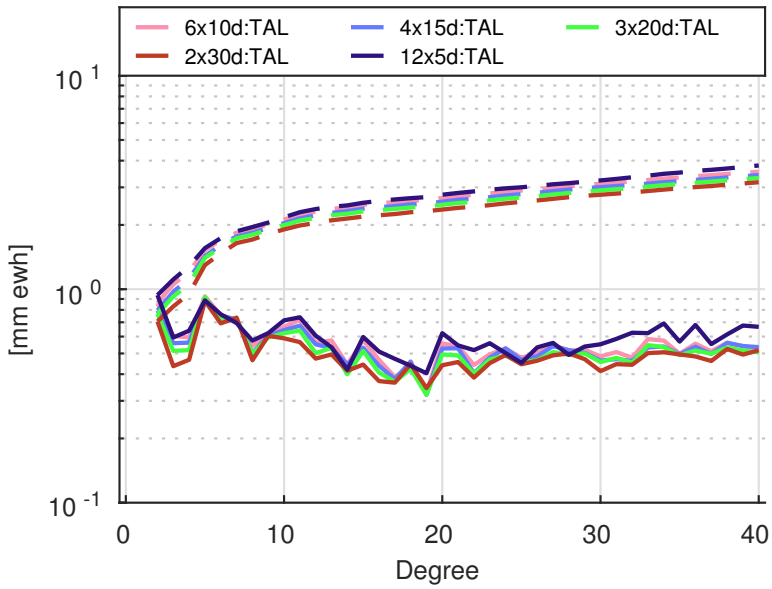

Figure 7.23: Temporal aliasing errors for several sets of solutions with different data accumulation periods averaged over a 60-day timespan.

7.5.3. Multiple formations

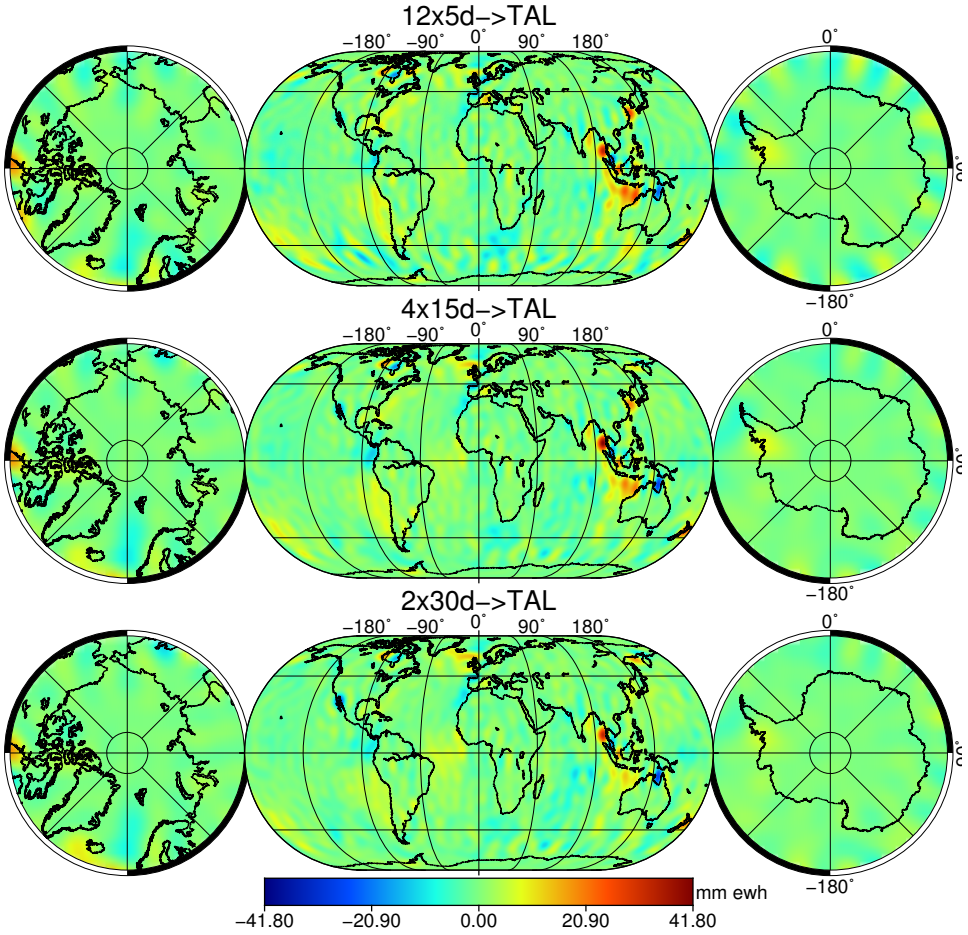

Figure 7.24: Maps of averaged temporal aliasing errors over a period of 60-days. On top, the average of 12 solutions with a 5-day DAP, in the middle the average of 4 solutions with a 15-day DAP and in the bottom the average of 2 solutions with a 30-day DAP.

Relative orbital shift

Introducing a second formation may improve the temporal resolution in comparison with a single-formation mission. The second formation can revisit the same geographic region in-between the visits of the first one, thus improving the temporal resolution. Recurring concepts in the literature on multiple satellite formations are *spatial and temporal shifts* (Reubelt et al., 2010). Considering a mission consisting of two formations, spatial shifts are intended to interleave the ground tracks of the second formation with respect to the first one, with the intent of doubling the spatial resolution of the combined constellation. In terms of temporal resolution, temporal shifts are used to half the revisit time of the first formation. This is done by keeping the same ground tracks and shifting the second formation in time by half of the orbit repeat period.

Spatial and temporal shifts are based on the idea that the spatial and temporal resolutions of satellite gravimetry missions are complementary and interchangeable, such that we can use temporal and spatial shifts to engineer a satellite constellation towards the target requirements. Spatial shifts were discussed in Section 7.4.2.

Time shifts, as I will proceed to illustrate, do not seem to be the best way of improving the temporal resolution of the mission. The time-shift approach is often considered in the literature, where it is used to halve the revisit time in order to double the temporal resolution of the mission. Revisit time is defined as the amount of time it takes the satellite to revisit the exact same geographic region; let this definition be called *exact revisit time*. Consider now the similar concept of a *wide revisit time*, i.e. the amount of time between the satellite coming, not exactly, but in the vicinity of a previously visited region. Assuming *wide revisit time* is a valid concept w.r.t. temporal resolution of a mission, then I can show that halving the exact revisit time results in a sub-optimal temporal resolution.

As an illustration, let us consider the left panel of Figure 7.25. It shows the equator crossings of two 63/4 repeat orbits, depicted in black and in red. The "black" formation starts at 0° longitude and circles the earth for 4 days before returning to the starting point. In order to half the exact revisit time of the first formation, the second one (in red) should have a time shift of 2 days. Notice that at 2 days, the first formation orbit crosses the 180° longitude, which should then be set as the starting point of the second formation. This can be achieved by rotating the orbital plane of the second formation by 180°. Notice in the left panel of Figure 7.25 that the distribution of equator crossings is far from ideal. The wide revisit time can be seen as the vertical distance between the dots contained in a given longitudinal band. The first formation revisits every $\approx 20°$ longitudinal band each half-nodal-day. The additional formation does not significantly improve wide revisit time; it flies over the vicinity of any region very shortly after the first formation, such that, during the remainder of the revisit cycle, this region remains unobserved.

An arguably better way to improve the temporal resolution is to set the second formation to revisit each longitudinal band within a quarter nodal day from the first formation, thus halving the wide revisit time. This can be done by shifting the RAAN of the second formation's orbit to be perpendicular to the first one. In the

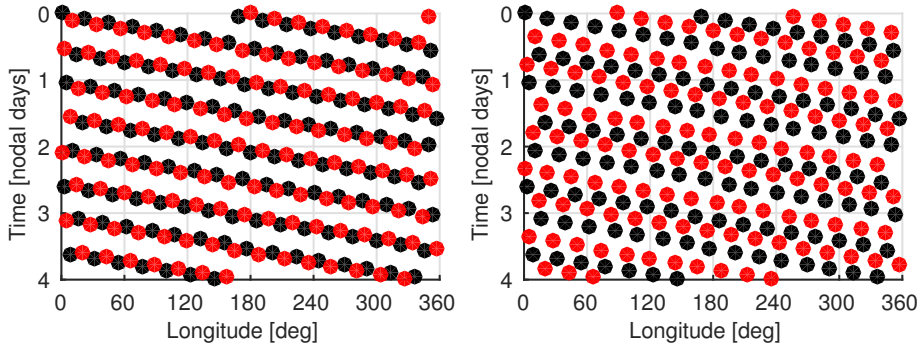

Figure 7.25: Equator crossings for two 63/4 repeat orbits with a $\Delta\Omega = 180°$ on the left and $\Delta\Omega = 90°$ on the right. The equator crossings of the first and second orbit are depicted in black and red, respectively.

right panel of Figure 7.25, the equator crossings for a mission with $\Delta\Omega = 90°$ are depicted, where the improvements in terms of wide revisit time can be clearly seen.

As it is shown in Figure 7.26, a simulation reveals that temporal aliasing errors are indeed smaller when the orbital planes of the two formations are perpendicular. Consider the zz/xz-180 and zz/xz-90 missions, where two satellite formations observe the zz and xz gravity gradient components, respectively. In the former case, a relative orbital shift of $\Delta\Omega = 180°$ is considered, and in the latter case, $\Delta\Omega = 90°$. The DV plot of the RMS of 9 different total temporal aliasing error realizations shows that the $\Delta\Omega = 180°$ brings no significant improvement compared to the single-formation scenario (legend *zz+xz: TAL*), while the $\Delta\Omega = 90°$ shift performs slightly better (≈15% in terms of CDV), especially below SH degree 20.

From this point, it is already possible to conclude that $\Delta\Omega = 90°$ is better than $\Delta\Omega = 180°$, however this becomes even more clearer in the next section, where the zz/zz combination is also introduced.

The notion of wide revisit time may have profound impact in the design of satellite orbits much beyond what I have considered in this thesis. Assuming wide revisit time as valid concept, allows one to redefine what a repeat period orbit is in the context of satellite gravimetry. This much less restrictive definition may allow for greater freedom in the design of future satellite gravimetry missions.

In this section, I have illustrated the concepts of exact and wide revisit time with the equatorial crossings of the considered orbits. In Section 7.4.2, I argued that groundtrack spacing at equator is not more important than at other latitudes in terms of mission coverage. However, on the one hand, notice that in this Section I refer to the time difference between passes over the same equatorial crossing and not about groundtrack spacing. Furthermore, I believe that similar analysis done at other latitudes would yield similar conclusions.

Types of observables

Another aspect worth investigating is whether there is any advantage in the combination of observations on missions with multiple formations. Notice that when

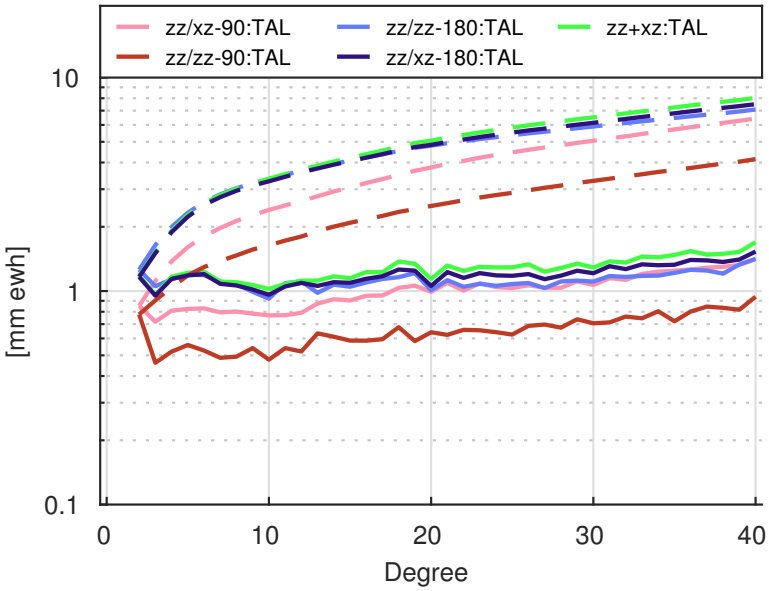

Figure 7.26: Comparison of five different simulations in terms of DV spectrum of the RMS of 9 realizations of temporal aliasing errors for 5-day repeat orbits. zz+xz is the single-formation mission observing the zz+xz gravity gradient combination. zz/xz-180 is a two-formation mission where the first formation observes zz and the second formation observes xz and is time-shifted by 2 days i.e., $\Delta\Omega = 180°$. zz/xz-90 is the same but now the second formation is on a perpendicular orbital plane, i.e., $\Delta\Omega = 90°$. zz/zz-180 and zz/zz-90 scenarios similar to the previous two, but both formations observe the zz component.

considering single-gradiometer observations, the zz component showed the lowest level of temporal aliasing errors. So, one wonders if two formations observing the same zz component will exhibit lower errors in comparison with the best two-observable combination zz+xz. The results are also presented in Figure 7.26. Regarding $\Delta\Omega = 180°$, we see that, similarly to the results obtained for the zz/xz scenario, there is only a marginal improvement w.r.t. the single-formation scenario zz+xz. In the $\Delta\Omega = 90°$ case, however, a clear reduction (≈40% in terms of CDV) of temporal aliasing errors is shown.

Two conclusions can be drawn from the presented results. Firstly, that for both considered combinations (zz/xz and zz/zz) $\Delta\Omega = 90°$ shifts are better than $\Delta\Omega = 180°$. Secondly, that it is better to combine the best single observable twice (zz/zz) than to consider the best two-observable concept (zz+xz). The zz/zz-90 simulation shows that these two characteristics combined lead to a significant reduction of temporal aliasing errors, while if they are independently considered (as in the zz/zz-180 and zz/xz-90 scenarios) there are little to no improvements.

Optimizing relative orbital shifts of two- and three-formation missions

Building on the results presented in Section 7.5.3, the goal now is to find the relative orbital shifts $\delta\Omega$ that minimize the temporal aliasing errors for missions consisting of two and three satellite formations. In the context of two-formation missions, in order to limit the domain of possible values, I consider only the values which ensure that the ground tracks of the two formations are interleaved. The simulations consist of two or three formations on a circular near-polar 79/5 repeat orbit at an altitude of 317 km. All formations observe the zz gravity gradient. Given that the considered repeat orbit is even, Equation 7.3 tells us that there are 79 unique possibilities for interleaved ground tracks. Furthermore this number can further be halved, by noticing the symmetry $\Delta\Omega = X = 2\pi - X$, such that only values $\Delta\Omega \leq 180°$ need to be considered.

From this reduced set of 40 possible $\Delta\Omega$ parameters, I started by considering every 3rd possible $\Delta\Omega$, for a total of 13 different simulations. Of this set, the two simulations with the lowest temporal aliasing errors corresponded to $\Delta\Omega \approx 84°$ and $\Delta\Omega \approx 98°$. At this point, I considered two extra simulations corresponding to the in-between values of 89° and 93°.

The obtained temporal aliasing errors are shown in the in Figure 7.27. Here, the lowest errors found are for the $\Delta\Omega \approx 84°$ and 98°. The possible values of $\Delta\Omega$ in-between these two did not yield lower errors. The error for $\Delta\Omega \approx 180°$ is also shown for comparison.

Based on the same considerations, I also analyzed temporal aliasing errors for missions consisting of three formations. The task now is to search for the minimum error over two shifts $\Delta\Omega_1$ and $\Delta\Omega_2$, which are defined as the orbital shifts between the first and the second, and the first and the third formations' orbital planes, respectively. In order to reduce the domain of possible ($\Delta\Omega_1$, $\Delta\Omega_2$) pairs, the following symmetries can be used. Two ($\Delta\Omega_1$, $\Delta\Omega_2$) pairs are equivalent when,

- *Symmetry 1-3:* the second plane is symmetric with respect to the plane located in the middle of the first and third orbital planes

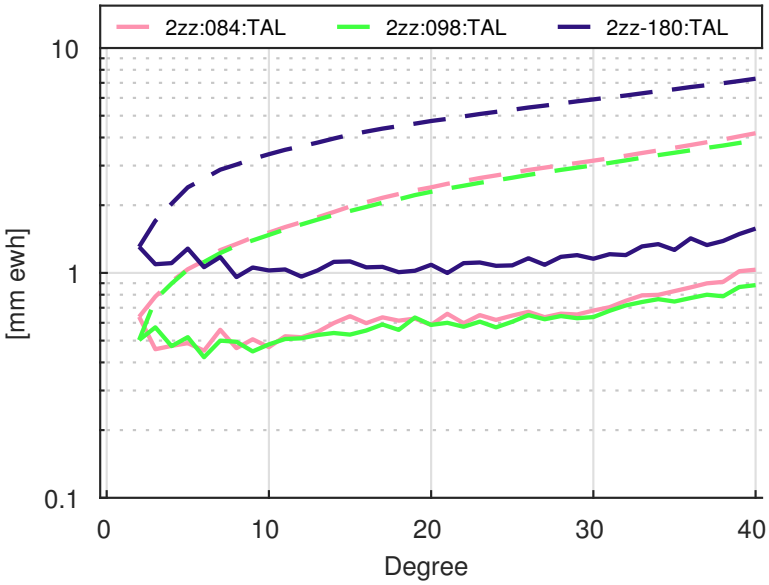

Figure 7.27: DV (solid) and CDV (dashed) for a selection of 2-formation missions with different $\Delta\Omega$ in 79/5 repeat orbits with the lowest temporal aliasing errors.

- *Symmetry 1-2:* the third plane is symmetric with respect to the plane located in the middle of the first and second orbital planes
- *Symmetry 2-3:* the first plane is symmetric with respect to the plane located in the middle of the second and third orbital planes

Let us start from the first case. It prescribes that it is sufficient to consider only those positions of the third orbital plane that satisfy the condition $\Delta\Omega_2 > 2\Delta\Omega_1$. For instance, scenario (28°,42°) is symmetric to (14°,42°). This condition defines the lower limit of $\Delta\Omega_2$. The second symmetry prescribes the upper limit for $\Delta\Omega_2 < \frac{\Delta\Omega_1}{2} + 180°$: Finally, the third symmetry prescribes another upper limit for $\Delta\Omega_2 < 360 - \Delta\Omega_1$. These symmetries and the resulting domain of three orbital plane configurations is shown in the left panel of Figure 7.28.

Given the groundtrack spacing of $\frac{79}{360}^\circ$, I considered every other possible $\Delta\Omega_1$ and $\Delta\Omega_2$, yielding a total of 120 pairs. I computed the global RMS of total temporal aliasing errors for $l_{\text{max}} = 40$ for these 120 configurations and plotted them in the right panel of Fig. 7.28.

Some insights can be gathered from this plot. The lower left and lower right regions with $\Delta\Omega_1 < 50°$ seem to be less desirable. These correspond to configurations where the second orbital plane is relatively close to the first one. A few configurations can be found which yield low temporal aliasing errors. They seem to be scattered in the region $60° < \Delta\Omega_2 - \Delta\Omega_1 < 90°$. The upper bound of this region is consistent with the finding that two orbital planes should be nearly perpendicular

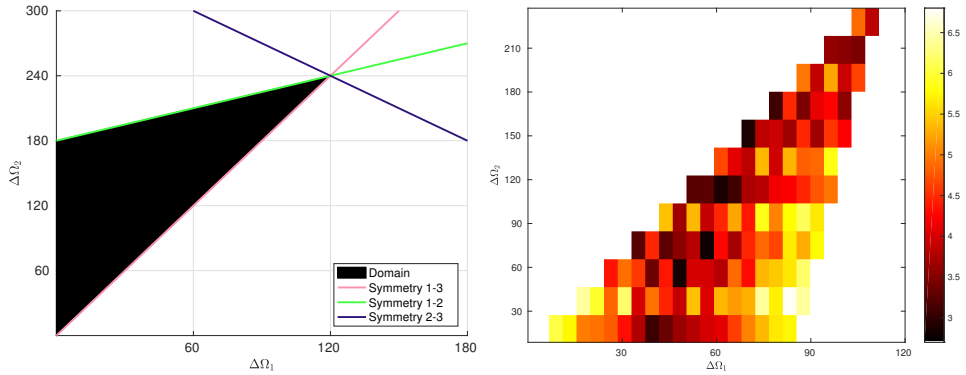

Figure 7.28: In the left panel are presented the symmetries in the relative orientation of three orbital planes and the minimum domain to be sampled. In the right panel, global RMS of total temporal aliasing errors up to $l_{\text{max}} = 40$ for different relative orientation of three orbital planes [mm ewh].

to each other. The most promising area, with four adjacent configurations which yield relatively low errors, is around (60°,120°). I considered all possible configurations neighboring this point in addition to the previously considered ones. Table 7.3 shows the six configurations with the lower global RMS of temporal aliasing errors with $l_{\text{max}} = 40$. The (59.2°,118.5°) pair yielded the lowest error with a significant difference compared to the other ones. This configuration is the closest to angles (60°,120°), which corresponds to three vertical planes that equally trisect 3D space. This is the configuration which maximizes the temporal resolution of the considered configuration.

Table 7.3: Six configurations of three orbital planes with the lowest global RMS of total temporal aliasing errors for $l_{\text{max}} = 40$ [mm ewh].

$\Delta\Omega_1$	$\Delta\Omega_2$	TAL
59.2°	118.5°	2.53
36.5°	118.5°	2.84
27.3°	100.3°	2.84
54.7°	127.6°	2.86
72.9°	145.8°	2.88
9.1°	82.0°	3.07

To close this section, one interesting way to present the discussed results is to compare the obtained reductions in temporal aliasing errors from extending the mission data accumulation period vs. the addition of satellite formations. In Figure 7.29, the improvements obtained after increasing the data accumulation period from 5 to 40-days are compared to the best 2- and 3-formation missions at 5 days. The plot reveals that the 5-day 2-formation mission results in a similar level of temporal aliasing errors as a 40-day single-formation mission. Furthermore consideration of a 3-formation mission leads to an additional reduction of about 35% compared to the single formation 40-day mission (cumulative error at SH deg 40 is

2.5 instead of 4 mm ehw).

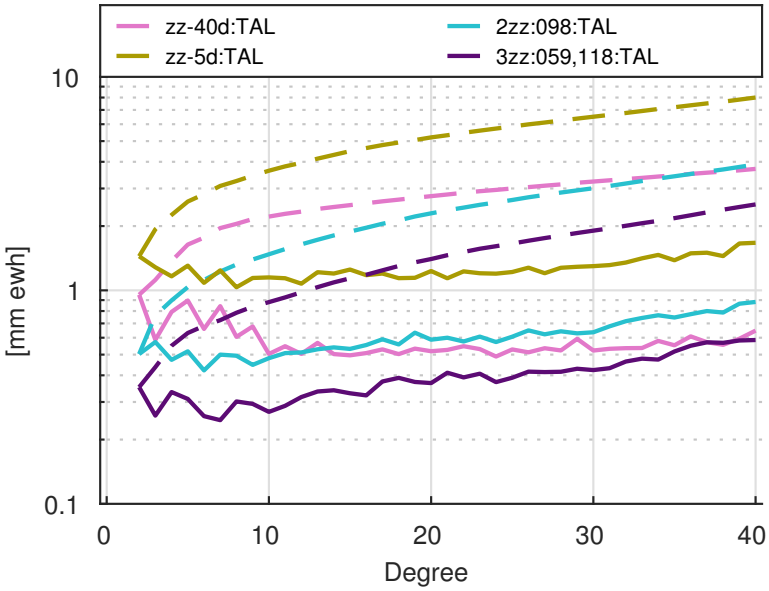

Figure 7.29: A comparison of total temporal aliasing errors for different mission in terms of DV.

7

7.6. Conclusion

In Section 7.1, parameters that make up a satellite gravimetry mission have been discussed and a small set of the most relevant parameters has been defined.

Sections 7.3, 7.4 and 7.5 were dedicated to explore spatial aliasing, spatial instability and temporal aliasing errors, respectively, using a set of small-scale simulations. They were carried out using gravity gradient observations instead of ll-SST observations. The rationale is that, conceptually, an ll-SST satellite pair is equivalent to a gradiometer instrument with a very long arm. So, a link between different ll-SST observations and the gravity gradients measured by a gradiometer instrument could be made (cf. Section 7.2).

In Section 7.3, it was shown that xx and yy gravity gradients are more sensitive to spatial aliasing errors than the zz. It was shown that, in general, spatial aliasing errors are mostly determined by signals at the SH degrees immediately above the selected $l_{\max}$. Since the mass transport signal slowly decays with increasing SH degree (in terms of ewh), it is beneficial to choose relatively high $l_{\max}$. Furthermore, it was observed that the bulk of spatial aliasing errors in the solutions is confined to the few SH degrees just below $l_{\max}$. In turn, this also proves that selecting a reasonably high $l_{\max}$ coupled with adequate filtering should be effective at removing spatial aliasing errors.

Spatial instability errors were discussed in Section 7.4. These errors arise as existing noise in the data gets amplified in the computation of a gravity field so-

lution. These errors limit the achievable spatial resolution in terms of maximum spherical harmonic degree. In practice, spatial instability errors were evaluated by inverting white noise realizations into gravity field solutions to increasingly higher SH degrees. It was shown that, with increasing $l_{\max}$, spatial instability errors increase by a limited amount for low values of $l_{\max}$, while above a certain threshold they grow exponentially up to the point where the LS system of equations can no longer be solved.

The described procedure has also lead to a number of other interesting results. For a given DAP, the spatial resolution of a mission can be improved by considering additional observables on a single-formation mission and/or by adding more satellite formations. When considering a single gradiometer component, I have shown that solutions could safely be computed up to the number of orbital revolution of the repeat period orbit $l_{max} = \beta$, twice of what is predicted by the Colombo-Nyquist rule. Furthermore, not all gradiometer components yielded the same level of spatial instability errors. The zz-component has shown a lower noise level in terms of ewh per degree than the xx and yy components. I concluded, therefore, that zz has the potential to deliver the highest spatial resolution. It was also found that by combining more components within the same mission, its spatial resolution is effectively improved far beyond the predictions made by the Colombo-Nyquist rule. For instance, when two observables are combined, the spatial resolution of the mission may be doubled. Combinations of three observables were shown to further increase the spatial resolution compared to the two-observable case.

Visser et al. (2012) proposed a reformulation of the Colombo-Nyquist rule, predicting that the maximum SH degree of a mission is to be $l_{\max} = kn_r + 1$, where k represent the number of observations combined in the gravity field inversion and n_r represents the number of satellite revolutions in the DAP. To validate this expression, three simulations were considered for which the predicted $l_{\max}$ was the same. They were shown, however, to have significantly different levels of spatial instability errors. This lead to the proposal of a new empirical predictor $l_{\max} = n_r\left(1 + \frac{k-1}{c}\right)$, where c is a constant between 1.6 and 2. At the same time, it is important to state that such expressions are an oversimplification of the problem of gravity field recovery and are no replacement for adequate simulations.

A distinction is made between even and odd repeat period orbits regarding whether their ascending groundtracks overlap at the equator or not, respectively. I have found only marginal differences between the spatial resolution of missions which consider odd and even repeat period orbits. Therefore, I concluded that both types of orbits are useful to consider in the design of future satellite gravimetry missions. In practice, this meant that I could use the lowest available repeat orbit above the selected 260 km minimum altitude threshold for all the DAPs I considered. This is relevant because, for DAPs with an odd number of days, the lowest available repeat orbit is even. If the decision was made to avoid even parity orbits, then all odd numbered DAPs would have to consider orbits roughly 20 km higher, which would bias the odd numbered DAPs to yield relatively lower performance than the rest.

Another way to increase the spatial resolution of a mission was to consider addi-

tional satellite formations. In multi-formation missions, two aspects were identified that may play a role in terms of spatial resolution: how to interleave groundtracks of multiple formations and which observables are to be considered in each formation. Different ways to interleave groundtracks of multi-formation missions were analyzed and it was shown that there are only marginal differences in terms of spatial instability errors between them. Therefore, in the multi-formation missions considered in Section 8.4, I shift all multi-formation orbits according to Eq. (7.3), which I showed to have a more homogeneous groundtrack spacing over all latitudes. Regarding the choice of observables, it was shown that two formations observing the same zz component, yielded lower temporal aliasing errors than other combinations. This finding will later be used in Section 8.6.

Examples can be found in the literature where a comparison of missions of different complexity disregards the potential of the more complex missions to achieve higher l_{max}. For example, Elsaka et al. (2013) and Wiese et al. (2009) compared single- and two-formation missions up to the same l_{max} and over the same DAP. In light of the findings of this section, one could argue that such comparisons are not fair. For a given DAP, concepts which combine multiple observables should be able to compute solutions up to a higher SH degree than single-observable ones. Alternatively, multi-observable concepts might be able to compute solutions up to the same maximum SH over smaller DAPs. These considerations will be further addressed in Chapter 8.

In Section 7.5, a similar analysis using small-scale simulations was carried out in order to find the parameters that influence temporal aliasing errors. When considered individually, single-component gradiometer observations affect differently the level of temporal aliasing errors. The zz gradient was shown to yield the lowest level of errors, followed by yy and xx. A closer look into the zz component error budget shows that the major contributors are a combination of AOD and ocean tide model errors (OTE). The smallest error component is the dynamic mass transport signal Given the substantially different geographic distribution of AOD and OTE error sources, it is interesting to notice that they yielded very similar magnitudes at most SH degrees. Therefore, in order to significantly reduce the level of temporal aliasing errors by better background models requires both OTE and AOD models to be improved.

Starting with the zz component, the best single observable, simply combining a greater number of observables was shown *not to* lead to any reduction in the level of temporal aliasing errors. This finding is in contrast with what was shown for spatial instability errors, which are significantly reduced by combining additional observables, cf. Section 7.4. On the other hand, when I start from the xx or yy component, the addition of another observable does lead to significant error reductions. The xx+yy combination shows the same level of errors as zz, the best single observable. In fact, the zz-component simultaneously yields the lowest level of temporal and spatial instability errors. Previously, in Section 7.4.1, it was shown that the xx+yy combination is equivalent to the zz-component. Given that no ll-SST formation concept is capable of continuously observing the zz-component, the equivalent xx+yy combination seems desirable. This finding will be applied in the

design of future satellite missions in Chapter 8.

Another possible way to mitigate temporal aliasing errors is the addition of satellite formations to the mission, as presented in Section 7.5. The most relevant parameter in this context is the relative RAAN $\Delta\Omega$ describing the relative orientation of the orbital planes. A search in the possible interleaved ground track configurations of two-formation missions has shown that the lowest temporal aliasing errors corresponded to a $\Delta\Omega = 98°$, while similar search made for a three-formation mission yielded $\Delta\Omega_1 = 62°$ and $\Delta\Omega_2 = 122°$. These configurations hint at the idea that the orbital planes of the intervening formations should be evenly distributed in space in order to minimize temporal aliasing errors. I explain this finding as follows. Considering a single orbital plane, the satellites will visit (the vicinity of) a given location, in average, every 12 hours. This is not enough to properly observe the dynamic processes in the atmosphere and oceans. Considering 2 or 3 orbital planes, the average re-visit time reduces to 6 and 4 hours, respectively, so that atmospheric and oceanic processes can be captured much better. It was shown that the addition of satellite formations in the optimal way leads to a substantial reduction of temporal aliasing errors. On the basis of this finding, two-formation missions presented in Section 8.4 will be set in perpendicular planes. In Section 8.6, the orbital planes of up to three formations will also be evenly distributed in space in order to minimize temporal aliasing errors.

8

Comparison of satellite formations

In this chapter, I design various ll-SST mission geometries (in line with the findings in the previous chapter) and assess their performance to select the best candidate for the future ll-SST mission. As discussed in Section 4.6, the way in which indirect effect errors propagate into observations and into gravity field solutions likely depends on the considered functional model. Even if one assumes that indirect effect errors affect all approaches, it is still unknown to what extent each approach is affected. Therefore, I opted to disregard indirect effect errors in order to present results which are not biased to any particular gravity field retrieval algorithm. The simulations presented in this chapter were computed in the simplified mode (cf. Section 4.6) meaning that no indirect effect errors were taken into account. The results presented in this manner may be interpreted as a best-case scenario for future satellite missions.

In Section 8.1, I present the error budgets of a set of elementary ll-SST formation configurations (cf. Section 2.2.3). Then, in Section 8.2, I discuss how the findings in Chapter 7 can be used to design a set of advanced mission concepts. In Section 8.3, three concepts for hybrid-formation missions consisting of three satellites are presented. Afterwards, in Section 8.4, four mission concepts consisting of 4 satellites arranged in two formations are proposed. Similarly to the elementary formations, the performance of these missions is presented and maximized over the relevant set of parameters. The comparison between the missions presented in the previous sections is deferred until Section 8.5, the missions with the lowest errors from each of the considered concepts are compared both globally and over a selection of regions where specific mass transport signals are expected to occur.

In Section 8.6, I focus on the mission concept which I found to be the most desirable at the end of Section 8.5. Noticing that temporal aliasing errors set limit on the performance of this mission, I show how to substantially improve the performance of this mission concept by considering additional formations in up to three

orbital planes which are evenly distributed in space. In Section 8.7, the conclusions of this chapter are presented.

8.1. Elementary Satellite Formations

I begin by looking at the performance of the elementary satellite formations. According to the findings in Chapter 7 several predictions can be made about the performance of the elementary satellite formations. Recall that the along-track concept is (roughly) equivalent to the xx gravity gradient mission, the pendulum concept to the yy gradient mission and the cartwheel concept alternates between the xx and zz gradient missions (cf. Section 7.2). The gravity gradients could be ranked in ascending magnitude of errors as zz, yy and xx both in terms of spatial instability and temporal aliasing errors. Therefore, the along-track concept is expected to show a higher level of errors than the other two concepts. The cartwheel's inter-satellite baseline oscillates between alignment with the most desirable zz and least desirable xx gravity gradient. Therefore, it is expected that it performs better than the along-track, however, it is hard to predict whether it will outperform the pendulum.

Temporal aliasing errors (as opposed to instrumentation errors) are likely to be dominant in the error budget of the missions, as was shown for the GRACE and GFO missions (cf. Chapter 6). When plotted on a map, the temporal aliasing error of the along-track concept is expected to have a north-south striation pattern, while that of the pendulum is expected to have some mild horizontal striations. Due to the baseline orientation oscillations of the cartwheel mission, mild north-south striations are expected in that case.

8.1.1. Along-Track

In order to tune the performance of the along-track mission concept, I start from an analysis of its limitations. The considered baseline mission follows a polar 255/16 repeat orbit at an altitude of 278 km. The top panel in Figure 8.15 (page 184) shows the corresponding $\mathrm{PSD}^{\frac{1}{2}}$ spectra of instrumentation and temporal aliasing errors propagated into inter-satellite accelerations. Instrumentation errors are very small and only become relevant in the high-frequency part of the spectrum, above 10 mHz. In Figure 8.1, total instrumentation and temporal aliasing errors are compared with the mass transport signal in terms of error per SH degree. It is clear that temporal aliasing errors are the dominant error source for all spherical harmonic degrees, being larger than the mass transport signal above degree 30.

In the top panel of Figure 8.16 (page 185), a breakdown of the temporal aliasing errors is shown. Here, it can be seen that the largest error source is the AOD model error. This error source is dominant for all SH degrees above 40. Below degree 40, the contributions of ocean tide model errors (OTE) and AOD errors are comparable.

The total temporal aliasing errors of the baseline along-track mission are shown in terms of magnitude of SH coefficients in the top panel of Figure 8.17 (page 186). The plot shows a vertical stripe, 30 SH orders wide, around the zonal coefficients,

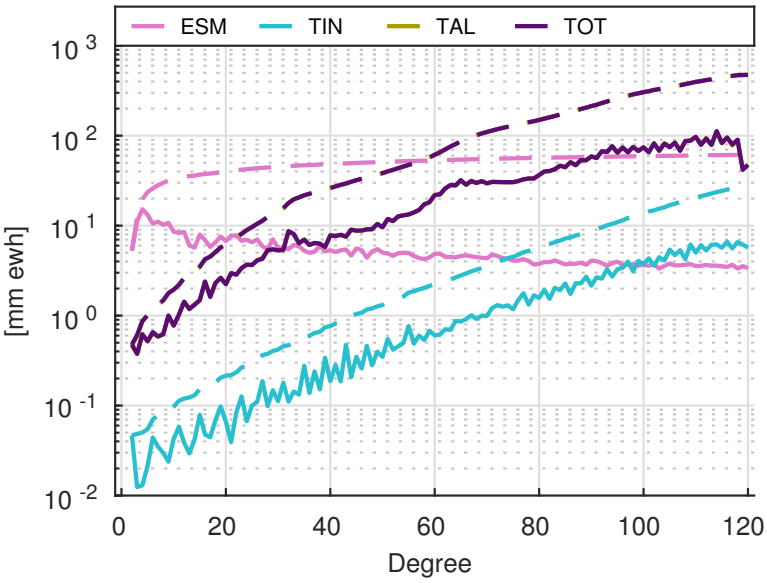

Figure 8.1: Temporal aliasing errors (TAL) and instrumentation errors (TIN) w.r.t. the mass transport signal (ESM) for the baseline along-track mission in terms of DV of unregularized solutions.

with very low errors, while the remaining coefficients show relatively large errors. This is because the along-track concept is sensitive to spatial variations in the north-south direction and is fairly blind to variations in the cross-track direction. The map of TAL errors in the top panel of Figure 8.18 (page 187) shows strong north-south striations, a well-known error pattern of along-track missions, which highlights their anisotropic sensitivity.

As discussed in Section 7.5, temporal aliasing errors can be minimized by increasing the data accumulation period (DAP) of the mission. Figure 8.2 shows the evolution of the total error with increasing DAP. It can be seen that temporal aliasing errors monotonically decrease with increasing DAP. Notice that the differences in the cumulative total errors for the 16- and 24-day DAPs are very similar, so that potential improvements of considering longer DAPs are likely negligible.

The error budget for a selection of DAPs for the along-track concept is shown in Table 8.1 (page 188). It can be seen that the longer timespans reduce the total error by an order of magnitude. However, even at the long timespans, the total error is still much larger than the mass transport signal. The large level of errors is explained by the anisotropic sensitivity of the mission and is consistent with the north-south stripes observed in GRACE solutions.

In order to improve the performance of the mission, the regularization procedure can be used to compute constrained solutions. The regularization procedure was introduced in Section 6.1.4. In Figure 8.3, total instrumentation error (TIN), total temporal aliasing error (TAL), regularization bias (REG) and total error (TOT) are compared with the mean mass transport signal (ESM) for the baseline along-

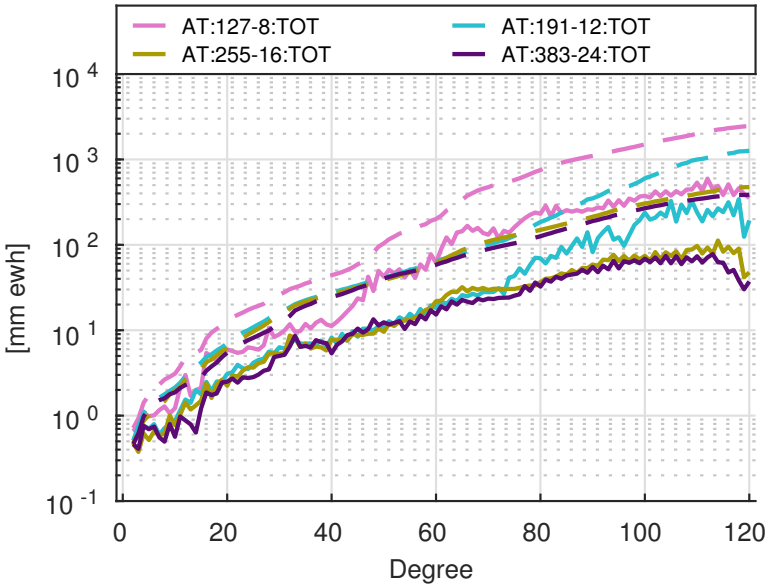

Figure 8.2: Total error (TOT) for a selection of along-track missions (AT) with increasing DAPs.

track mission. The total error is now below the mass transport signal at all SH degrees, which is a great improvement compared to the unregularized solutions (cf. Figure 8.1). The total error results from a combination of temporal aliasing and regularization bias up to SH degree 60, and by the regularization bias alone above SH degree 60.

The total temporal aliasing error for the regularized solution is shown as a triangular plot in Figure 8.4. The previously large errors seen in the non-zonal coefficients of the unregularized solution (Figure 8.17 (page 186)) are now much smaller due to the regularization procedure applied.

Figure 8.5 shows total temporal aliasing errors as a map in terms of regularized solutions. A comparison of this map with the top panel of Figure 8.18 (page 187) highlights the large reduction of the error features in the regularized solutions w.r.t. to the unregularized case. Remaining error features can be identified as segmented north-south stripes over South America, Central Africa, Northern Australia, South East Asia and a few other locations.

Figure 8.6 shows the contribution of each temporal aliasing error source over the South America. It can be seen that the major error features are caused by the dynamic mass transport signal. This is interesting because this error source cannot be reduced by improvements in existing background models.

One can also check how the total error evolves over different DAPs. This is shown in Figure 8.7. It can be seen that after regularization, the total error remains constant at different mission timespans. The difference between the 8-day and 24-day repeat missions is negligible above SH degree 60, where the regularization bias

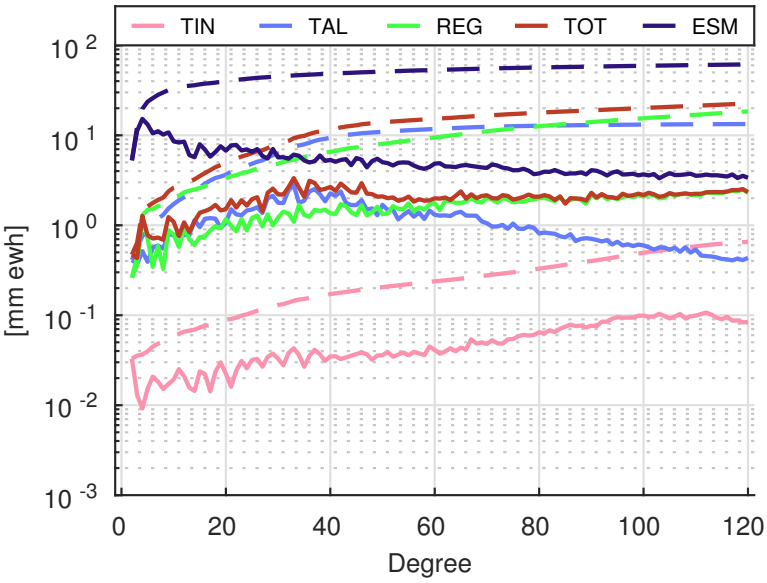

Figure 8.3: Breakdown of errors for the 255/16 along-track mission in terms of DV of *unregularized* solutions. The explanation of the used acronyms can be found in Table 4.4 in page 75.

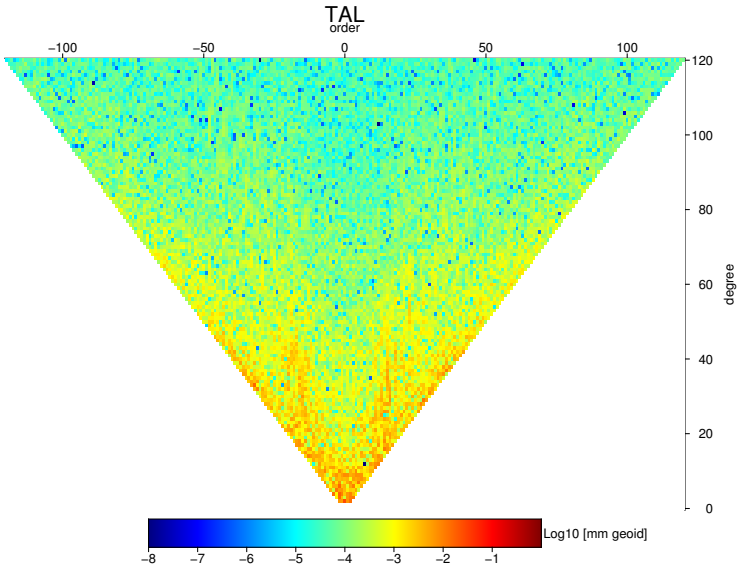

Figure 8.4: Triangular plot with the magnitude of SH coefficients of the total temporal aliasing error source (TAL) for the 255/16 along-track mission in terms regularized solutions up to $l_{max} = 120$.

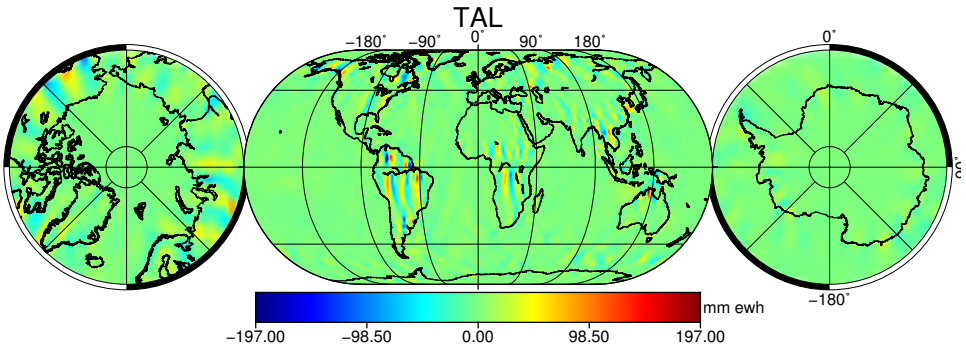

Figure 8.5: Map of total temporal aliasing error (TAL) for the 16-day along-track mission in terms of regularized solutions.

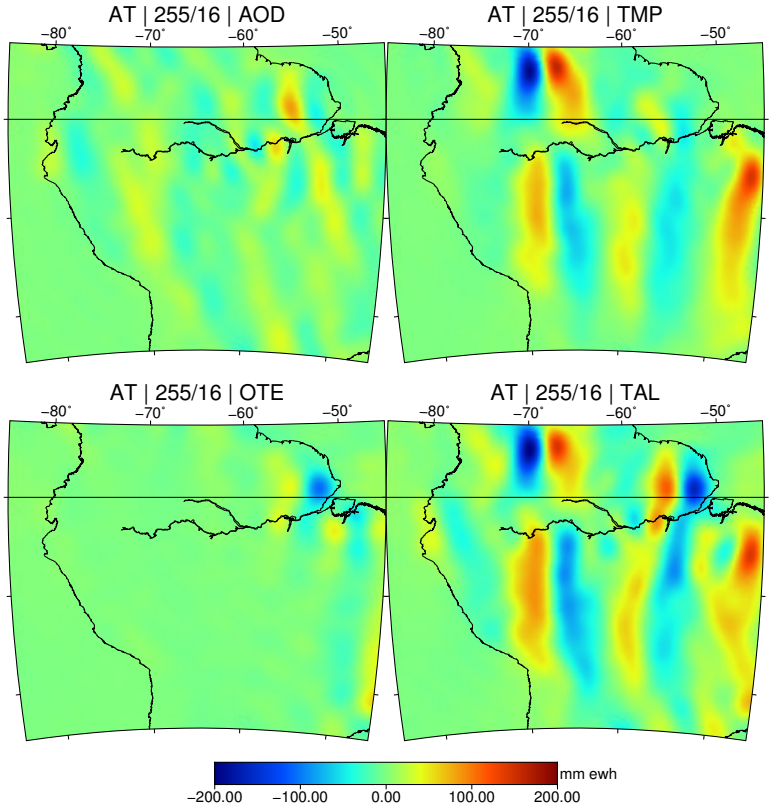

Figure 8.6: Temporal aliasing errors over the Amazon river basin for the 255/16 Along-Track mission in terms of *unregularized* solutions. The explanation of the used acronyms can be found in Table 4.4 in page 75.

is dominant.

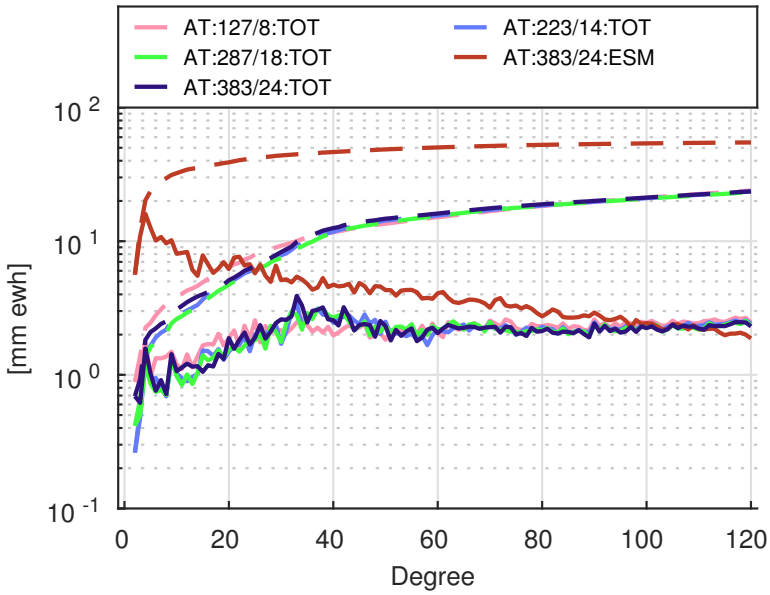

Figure 8.7: Total error (TOT) for the along-track mission with different DAPs in terms of *unregularized* solutions. Also shown is the ESM signal for the 24-day DAP.

A breakdown of error budgets for a selection of DAPs in terms of global RMS for the along-track missions is shown in Table 8.4 (page 189). It can be seen that total error is fairly constant for all considered DAPs. The total error is always explained by a combination of total temporal aliasing (TAL) error and regularization bias (REG). For the short DAPs, the total error is dominated by the regularization bias (REG) while for the longer DAP's the total temporal aliasing (TAL) errors becomes larger than REG.

Regarding the temporal aliasing errors, for the short DAPs below 16 days, TAL is driven by equal contributions of OTE and AOD errors. For the longer DAPs above 16 days, TAL error is dominated by the dynamic mass transport signal (TMP). All considered DAPs show a very similar performance, with the lowest total error being found for the 16-day along-track mission (23 mm ewh).

8.1.2. Pendulum

The pendulum formation is defined by a pair of satellites in polar orbits that slightly differ in their RAAN (cf. Section 2.2.3). The LOS is oriented in the east-west direction and is relatively static in inertial space. The relative motion between the two pendulum satellites is confined to the cross-track direction. From the equator towards the pole, the satellites travel towards each other, meeting in close proximity at the highest latitude point. At this point, the left and right satellites swap their positions in the horizontal plane and start to drift away from each other up until the

equator, where the cycle restarts.

In the vicinity of this point where the satellites swap their positions, large peaks in the RRC are observed in perturb the gravity field recovery. To tackle this problem, I defined a minimum inter-satellite distance threshold of of 40 km below which measurements are flagged as outliers.

The baseline mission follows polar 255/16 repeat orbits at an altitude of 278 km and a maximum inter-satellite distance over the equator of 200 km. The $\mathrm{PSD}^{\frac{1}{2}}$ of the error sources for the pendulum mission are shown in the middle plot of Figure 8.15 (page 184). In the $\mathrm{PSD}^{\frac{1}{2}}$ plot, one can see that total temporal aliasing errors are smaller (by roughly 50% between 1 and 10 mHz) than the mean mass transport signal.

The DV plot in Figure 8.8 shows that, up to SH degree 70, the performance of the pendulum mission is limited by temporal aliasing errors and, above degree 70, by instrumentation errors. From SH degree 80 onwards, instrumentation and total errors become larger than the mass transport signal.

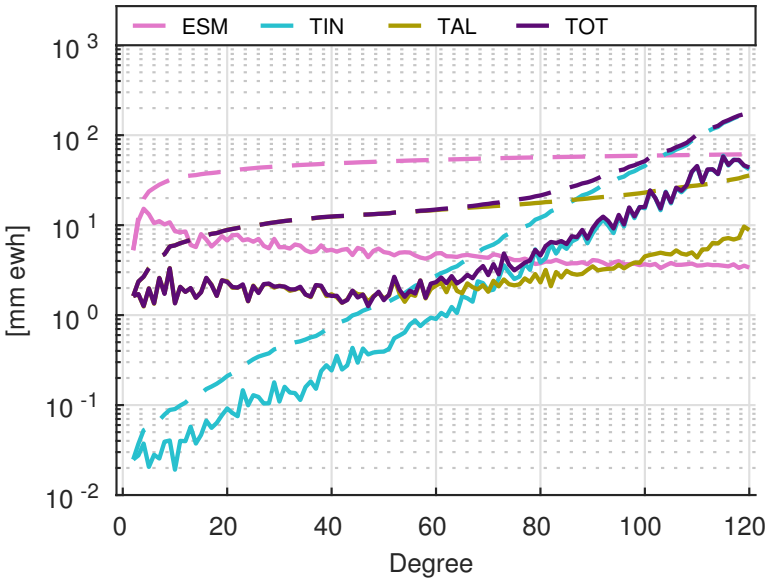

Figure 8.8: General overview of errors in the 255/16 pendulum mission in terms of DV. The explanation of the used acronyms can be found in Table 4.4 in page 75.

Looking into the total temporal aliasing errors, shown in the middle plot of Figure 8.16 (page 185), one can see that all errors are significantly lower in magnitude in comparison with the along-track mission errors shown top panel. The total temporal aliasing error is explained by a combination of atmosphere and ocean de-aliasing model (AOD) and ocean tide model (OTE) error up to SH degree 60. From SH degree 60 on, the AOD error becomes the largest contributor. The dynamic mass transport signal (TMP) is smaller than the other two errors.

Instrumentation errors-per-degree are plotted in Figure 8.9. Here, it can be seen that up to SH degree 40, the levels of accelerometer and ranging errors are comparable. Above degree 40, ranging error becomes the largest instrumentation error source.

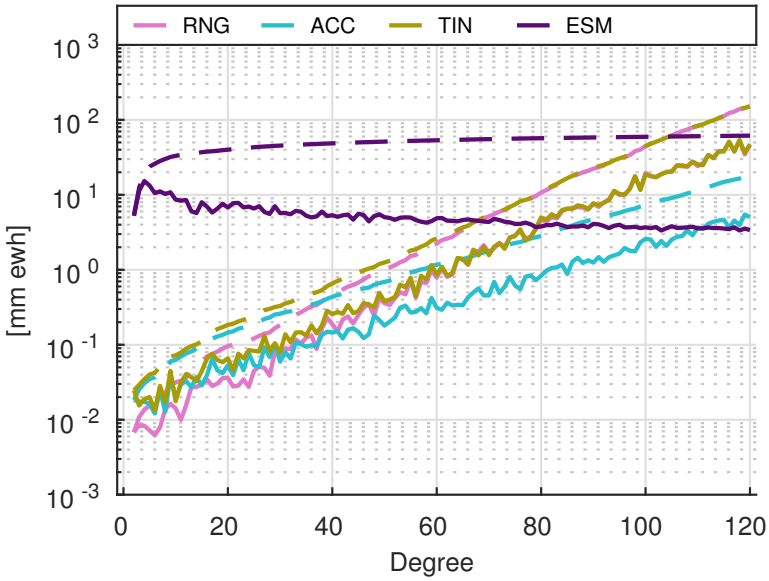

Figure 8.9: DV of instrumentation errors for the 255/15 pendulum mission. The explanation of the used acronyms can be found in Table 4.4 in page 75.

In Table 8.2 (page 188) a breakdown of the error budget for the pendulum mission at different DAPs is shown. In line with the previous plots, indeed ranging errors are the largest error source. The overall level of errors is significantly smaller than that of the along-track mission (cf. Table 8.1 in page 188).

Similarly to the along-track mission, total temporal aliasing errors are shown in a triangle plot in the middle panel of Figure 8.17 (page 186) for the baseline 255/16 Pendulum mission. The triangular plot shows that the larger temporal aliasing errors pile up in the near-zonal coefficients up to relatively high degrees. This error pattern also reveals the anisotropic sensitivity of the pendulum formation which is complementary to the one of the along-track mission. The orientation of the inter-satellite baseline of the pendulum mission makes is rather insensitive to north-south variations which are mostly described by near-zonal SH coefficients.

The along-track mission performance was significantly improved when the regularization procedure was introduced, therefore the regularization is applied in the context of pendulum mission as well. The error budget of the baseline 255/16 pendulum mission in terms of regularized solutions is shown in Table 8.5 (page 190). Once regularization is applied, instrumentation errors drop dramatically, which particularly concerns ranging errors. Not only is the ranging error no longer dominant, it is now a negligible error source. Temporal aliasing errors are dominant (apart

from the regularization bias) and these are explained by a combination of AOD and OTE errors with similar magnitudes.

As was shown in Section 7.5, extending the DAP of the mission is likely to reduce temporal aliasing errors. Therefore, similarly to what was done for the along-track mission, different DAPs were also considered for the pendulum mission. The corresponding results are also shown in Tables 8.2 (page 188) and 8.5 (page 190) in terms of unregularized and regularized solutions, respectively. Considering unregularized solutions, the total error shows significant differences depending on the DAP of the mission, especially at the shorter periods; the lowest level of cumulative errors is about 120 mm ewh for the 351/22 pendulum mission. Regarding regularized solutions, the differences in total errors between different DAPs are now significantly smaller. The lowest total error is found for the 351/22 orbit with 19 mm ewh. The DV of the total error for the considered DAPs is shown in terms of unregularized solutions in Figure 8.10, and regularized solutions in Figure 8.11.

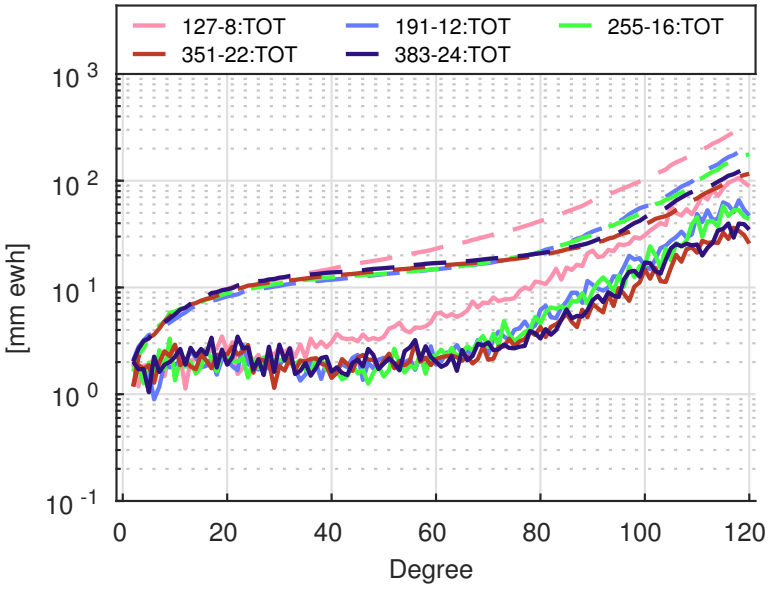

Figure 8.10: Total errors (TOT) of pendulum formation over different DAPs in terms of DV of *unregularized* solutions.

8.1.3. Cartwheel

The cartwheel mission consists of a two-satellite formation where both satellites are placed in similar, slightly eccentric orbits (cf. Section 2.2.3). By setting the two orbits on the same orbital plane such that their relative argument of periapsis is $\delta\omega = 180^\circ$, the relative motion of the satellites forms an ellipse. The aspect ratio of this ellipse is fixed, but its size is defined by the eccentricity of the orbits.

As mentioned in Section 7.1.1, one of the parameters relevant for the cartwheel

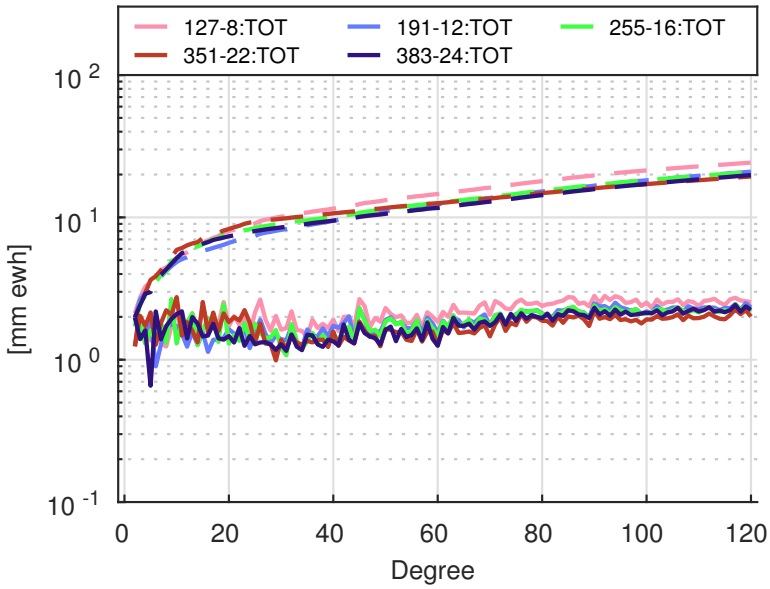

Figure 8.11: Total errors (TOT) of pendulum formation over different DAPs in terms of DV of *unregularized* solutions.

mission is the formation phase angle α, which defines the LOS elevation angle over the equator. A value of $\alpha = 0°$ corresponds to the radial direction at the equator, while a value of $\alpha = 90°$ corresponds to the along-track direction. Similarly to the previous sections, the baseline missions is on a 255/16 repeat orbit. Four cartwheel formations with different α values were simulated. Figure 8.12 shows the LOS elevation angle as a function of latitude for each of the four considered formations. The total errors are shown in Figure 8.13. Here, it can be seen that the lowest total error is obtained for $\alpha = 30°$.

Having selected $\alpha = 30°$, I show an overview of the errors in terms of $\text{PSD}^{\frac{1}{2}}$ of inter-satellite accelerations in the bottom panel of Figure 8.15 (page 184). Here, it can be seen that up to 10 mHz, temporal aliasing errors are dominant, being lower than the mass transport signal. Above this frequency, instrumentation errors become dominant. Overall, the $\text{PSD}^{\frac{1}{2}}$ errors in terms of inter-satellite accelerations share similar features in all three elementary formations. The same errors propagated into DV are shown in Figure 8.14. Temporal aliasing errors are dominant for all SH degrees; they are below the mass transport signal up to SH degree 75.

A breakdown of temporal aliasing errors in terms of DV is shown in the bottom panel of Figure 8.16 (page 185). Up to SH degree 40, the contribution of AOD error and OTE errors is comparable. Above SH degree 40, the AOD error becomes dominant. The dynamic mass transport signal (TMP) is small for all SH degrees.

Tables 8.3 (page 189) shows the error budget of the cartwheel mission for different timespans in terms of global RMS of unregularized solutions. The table shows

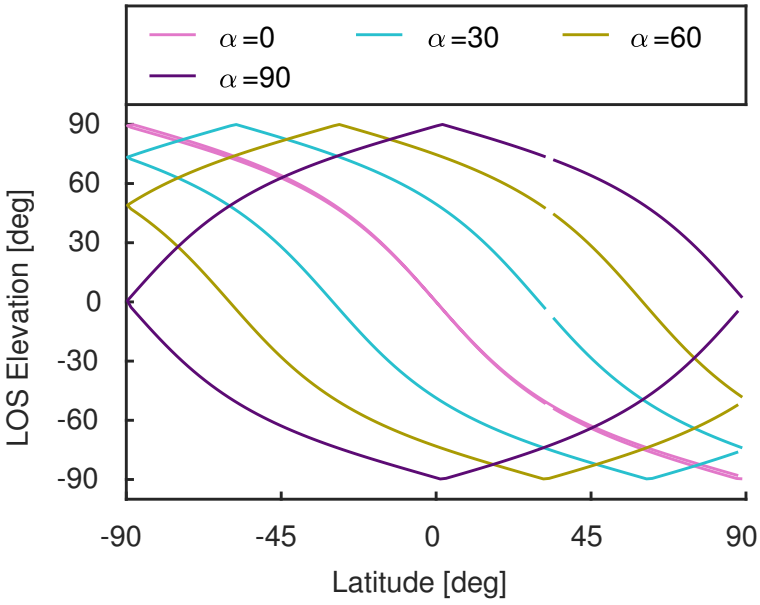

Figure 8.12: LOS elevation angle as a function of latitude (LOS elevation angle of 0° means that the LOS is aligned with the local vertical direction, while 90° means aligning with the local horizontal one).

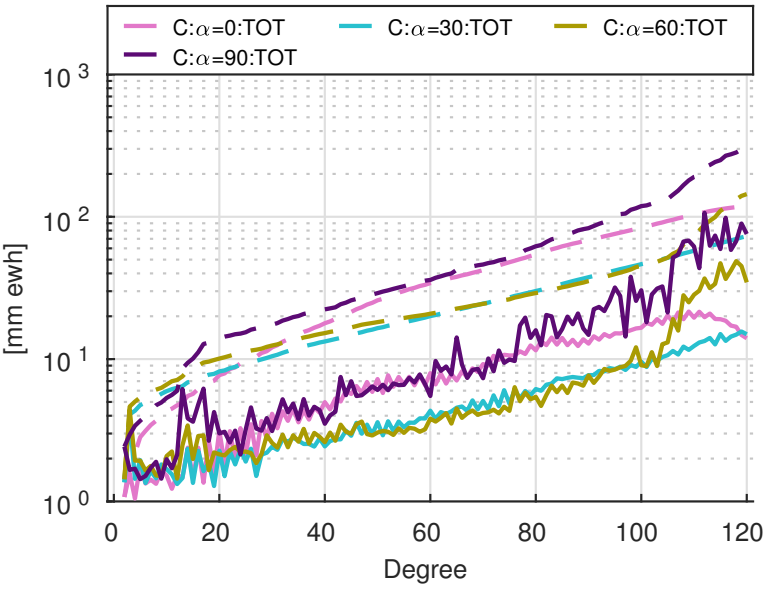

Figure 8.13: Total error (TOT) for the 255/16 cartwheel formations with different phase angles α in terms of DV.

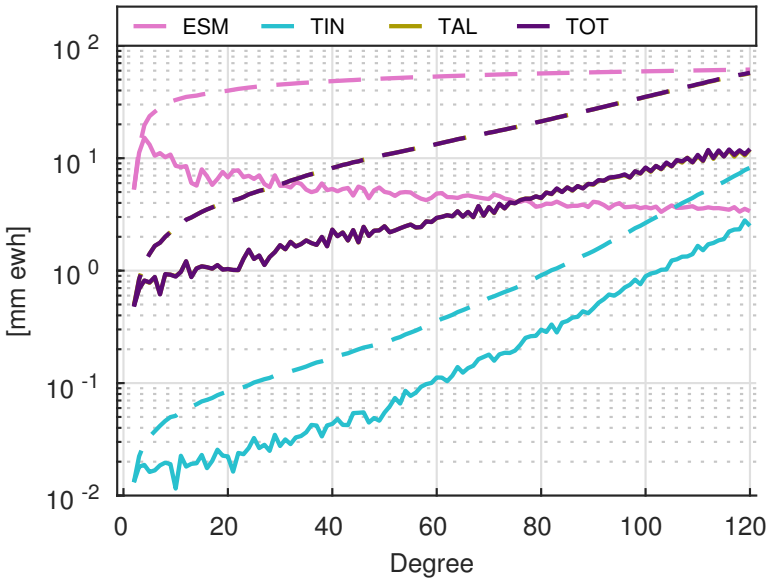

Figure 8.14: General overview of errors for the baseline cartwheel mission in terms of DV, with $\alpha = 30°$. The explanation of the used acronyms can be found in Table 4.4 in page 75.

that the minimum total error is obtained at the longest considered timespan of 24 days. The dominant error for DAPs above and including 16-days is the AOD error.

Similarly to the previous sections, total temporal aliasing errors are also presented as a triangular plot in the bottom panel of Figure 8.17 (page 186). The triangular plot shows that the cartwheel mission yields very low errors in the near-zonal coefficients, similarly to the along-track mission, and also from fairly low errors in the near-sectorial coefficients. The bulk of the AOD error piles up in the tesseral coefficients above SH degree 60.

The map of total temporal aliasing errors in the bottom panel Figure 8.18 (page 187) shows a single prominent feature in the Southern Ocean close to 0° longitude, as well as a meridional stripe pattern around both poles.

Table 8.6 (page 190) shows the error budget in terms of regularized solutions. One can see that the difference between different timespans is now again much smaller. The lowest total error is obtained for the baseline mission with a 16-day repeat orbit. The total error is now explained by a combination of regularization bias (13 mm ewh) and total temporal aliasing errors (16 mm ewq). In turn, the total temporal aliasing error is no longer dominated by AOD; both AOD and OTE errors have comparable levels, while the dynamic mass transport signal (TMP) is smaller than those two.

8.1.4. Discussion

The error budget of the elementary satellite missions was presented in the previous sections. Regarding spatial instability errors, the along-track mission is affected the most. Remember spatial instability errors arise when solving an ill-posed system of

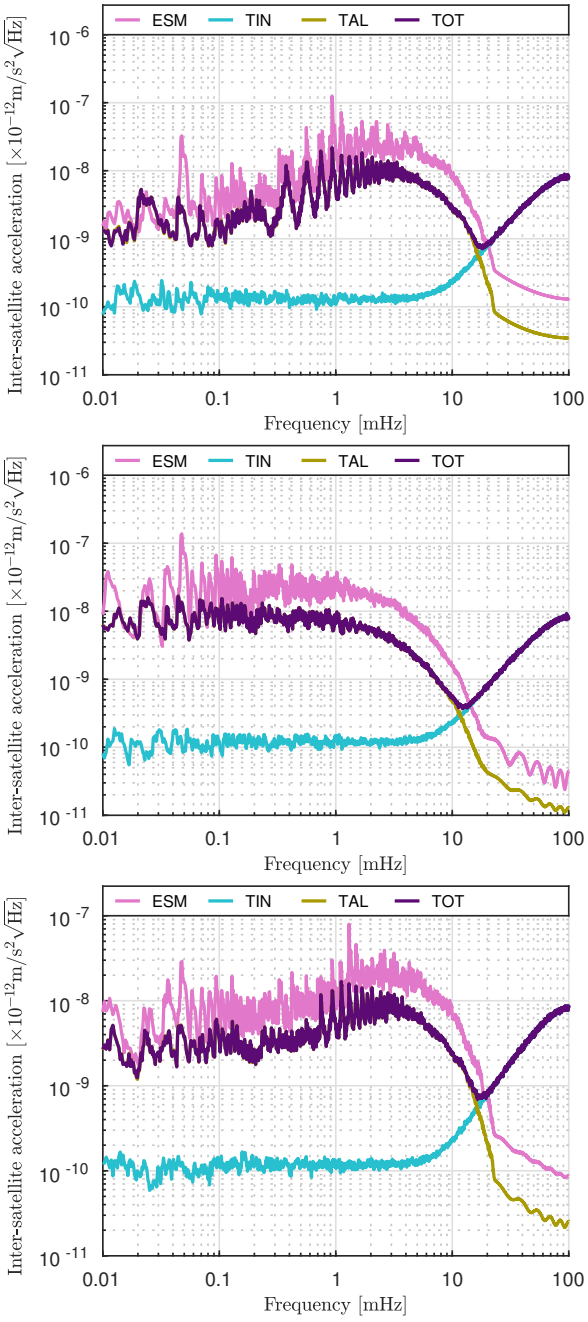

Figure 8.15: Temporal aliasing errors (TAL) and instrumentation errors (TIN) w.r.t. to the mass transport signal (ESM) in terms of PSD$^{\frac{1}{2}}$ of inter-satellite accelerations for the 255/16 along-track (top), 255/16 pendulum (middle), and 255/16 cartwheel (bottom) missions.

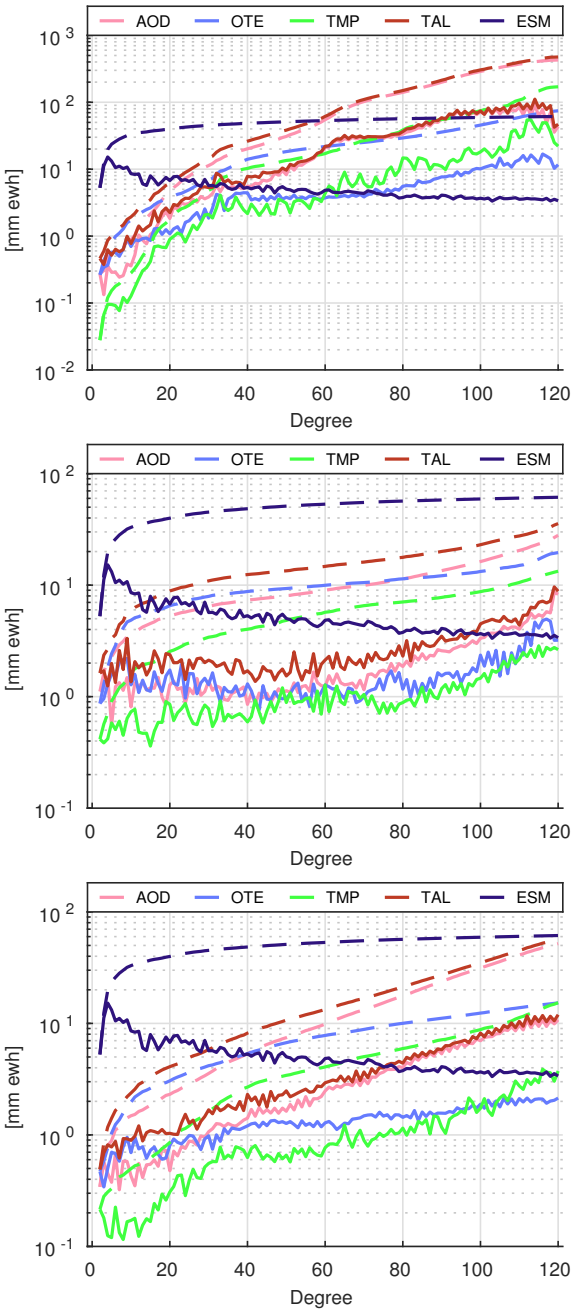

Figure 8.16: Breakdown of temporal aliasing errors in terms of DV for the 255/16 along-track (top), 255/16 pendulum (middle), and 255/16 cartwheel (bottom) missions. The explanation of the used acronyms can be found in Table 4.4 in page 75.

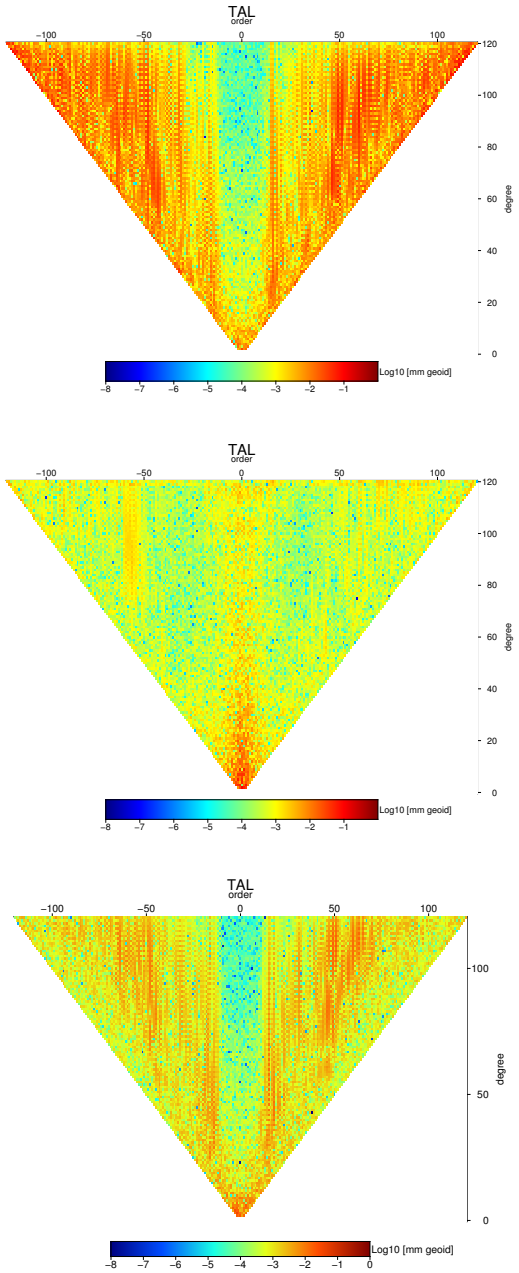

Figure 8.17: Triangular plot with the magnitude of SH coefficients of the total temporal aliasing error source (TAL) for the 255/16 along-track (top), 255/16 pendulum (middle) and 255/16 cartwheel (bottom) missions in terms of unregularized solutions.

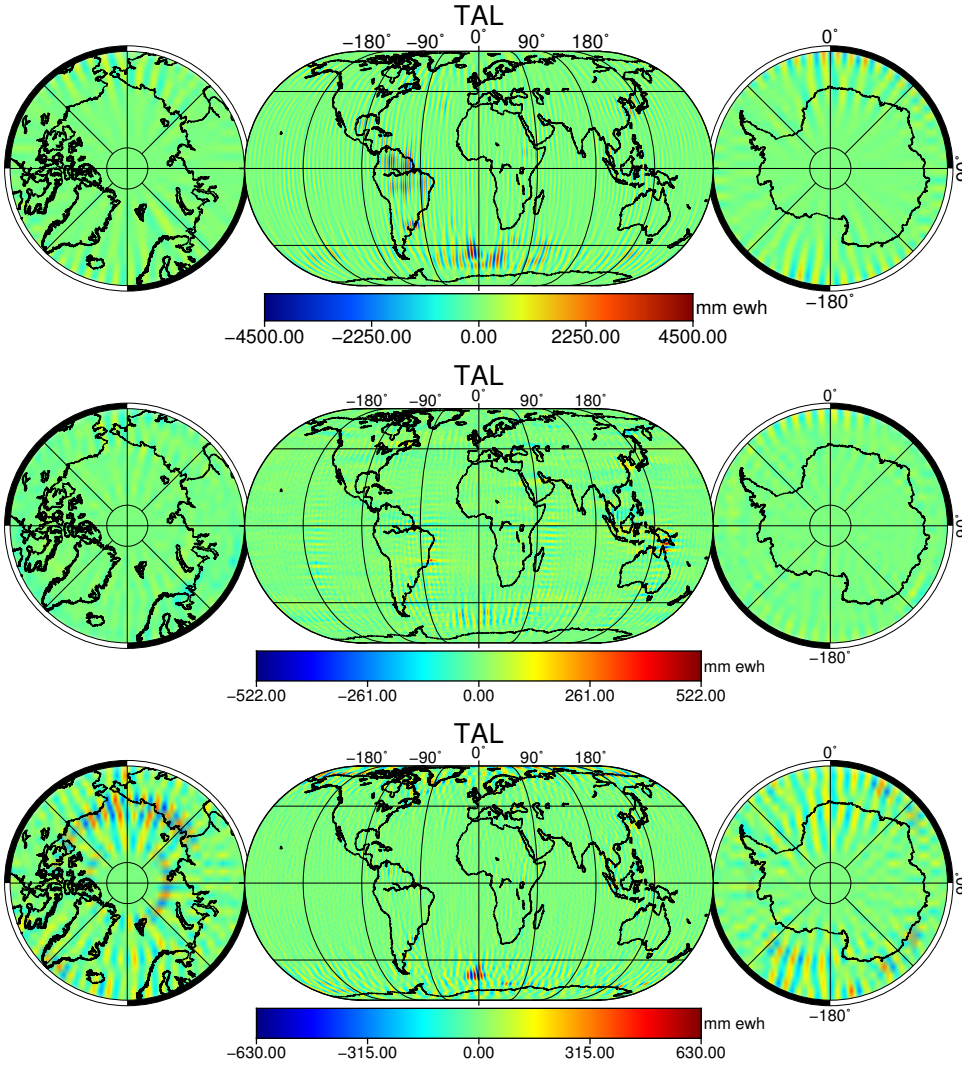

Figure 8.18: Map of total temporal aliasing error (TAL) for the 255/16 along-track (top), 255/16 pendulum (middle) and 255/16 cartwheel (bottom) mission in terms of unregularized solutions. Notice the different magnitude of the colorbar limits.

Table 8.1: Error budget of the along-track mission for a selection of DAPs in terms of global RMS [mm ewh] solved to maximum SH degree 120. The explanation of the used acronyms can be found in Table 4.4 in page 75.

AlongTrack	127/8	191/12	255/16	351/22	383/24
RNG	115.13	57.41	26.34	5.85	5.95
ACC	49.13	49.76	10.12	6.35	6.09
TIN	124.85	80.15	27.90	8.58	8.56
AOD	1867.54	1194.55	428.29	311.73	343.64
OTE	1310.50	324.18	74.51	84.86	91.30
TMP	759.47	482.84	170.31	117.74	139.37
TAL	2455.81	1257.89	474.68	354.37	385.43
SPT	27.13	26.41	12.20	12.85	12.68
TOT	2460.94	1262.14	475.01	355.92	385.65
ESM	62.78	62.14	61.36	60.12	59.70

Table 8.2: Error budget of the pendulum mission over a selection of DAPs in terms of global RMS [mm ewh] of *unregularized* solutions solved to SH degree 120. The explanation of the used acronyms can be found in Table 4.4 in page 75.

Pendulum	127/8	191/12	255/16	351/22	383/24
RNG	301.47	191.10	172.28	111.43	128.83
ACC	36.54	23.81	20.48	13.21	15.57
TIN	301.49	194.17	173.85	112.47	128.41
AOD	102.16	41.88	27.99	22.66	24.11
OTE	86.10	20.58	19.57	15.32	16.09
TMP	36.49	14.51	13.33	14.00	14.32
TAL	135.90	45.43	35.64	30.36	33.43
SPT	12.49	6.89	5.46	4.28	5.10
TOT	331.26	199.15	176.99	116.00	132.63
ESM	62.78	62.14	61.36	60.12	59.70

Table 8.3: Error budget of the cartwheel mission with $\alpha = 30°$ over a selection of DAPs in terms of global RMS [mm ewh] of solutions solved up to SH degree 120. The explanation of the used acronyms can be found in Table 4.4 in page 75.

Cartwheel	127/8	159/10	255/16	319/20	383/24
RNG	44.77	22.84	7.94	5.51	4.91
ACC	30.08	19.16	1.97	1.35	1.16
TIN	54.88	29.27	8.23	5.65	5.04
AOD	385.96	156.14	51.90	43.16	40.76
OTE	175.80	59.98	15.27	18.33	20.51
TMP	387.46	199.38	15.33	13.50	14.48
TAL	446.51	173.58	56.94	50.31	48.17
SPT	7.26	7.51	2.23	1.83	1.90
TOT	447.71	175.00	57.49	50.64	48.42
ESM	62.78	62.47	61.36	60.53	59.70

Table 8.4: Error budget of the along-track mission for a selection of DAPs in terms of global RMS of *regularized solutions* [mm ewh] solved to maximum SH degree 120. The explanation of the used acronyms can be found in Table 4.4 in page 75.

AlongTrack	127/8	191/12	255/16	351/22	383/24
RNG	0.67	0.57	0.65	0.61	0.59
ACC	0.21	0.21	0.19	0.19	0.19
TIN	0.69	0.61	0.67	0.64	0.61
AOD	6.62	7.19	6.92	7.70	7.56
OTE	6.95	7.79	7.65	8.55	7.61
TMP	4.92	7.18	8.70	12.56	15.40
TAL	10.93	12.92	13.57	17.00	18.69
REG	22.00	19.70	18.25	16.27	15.99
SPT	0.56	0.90	0.26	0.25	0.27
TOT	24.26	23.64	22.58	22.90	25.07
ESM	62.78	62.14	61.36	60.12	59.70

Table 8.5: Error budget of the pendulum mission over a selection of DAPs in terms of global RMS of *regularized* solutions [mm ewh] solved to SH degree 120. The explanation of the used acronyms can be found in Table 4.4 in page 75.

Pendulum	127/8	191/12	255/16	351/22	383/24
RNG	0.55	0.70	0.68	0.72	0.84
ACC	0.32	0.33	0.30	0.30	0.33
TIN	0.63	0.76	0.73	0.77	0.89
AOD	7.41	6.94	6.62	6.52	6.92
OTE	6.51	6.22	6.59	7.86	7.68
TMP	3.32	3.56	4.18	5.89	7.03
TAL	10.50	9.77	10.27	12.04	13.01
REG	21.75	18.87	18.05	15.23	15.36
SPT	0.74	1.53	0.29	0.24	0.32
TOT	24.24	20.94	20.81	19.38	19.82
ESM	62.78	62.14	61.36	60.12	59.70

Table 8.6: Error budget of the cartwheel mission with $\alpha = 30°$ over a selection of DAPs in terms of global RMS of *regularized* solutions [mm ewh] solved up to SH degree 120. The explanation of the used acronyms can be found in Table 4.4 in page 75.

Cartwheel	127/8	159/10	255/16	319/20	383/24
RNG	0.99	1.08	1.05	0.83	0.74
ACC	0.29	0.31	0.28	0.22	0.20
TIN	1.01	1.13	1.09	0.86	0.77
AOD	8.98	10.03	10.39	9.34	8.71
OTE	7.59	9.04	9.48	9.24	8.98
TMP	4.13	4.15	5.77	6.92	7.66
TAL	12.48	14.35	16.01	16.13	16.30
REG	17.30	14.71	12.69	11.94	11.90
SPT	0.54	0.99	0.35	0.31	0.30
TOT	21.46	20.52	19.87	20.11	20.34
ESM	62.78	62.47	61.36	60.53	59.70

equations (cf. Section 7.4). Therefore, at the short DAPs, these errors are expected to manifest with large magnitudes across all error sources, while the long DAPs are expected to stabilize the solutions to yield relatively small spatial instability errors. The along-track mission shows this behavior: large error magnitudes in all error sources for the short DAPs compared with the long ones (cf. Table 8.1 in page 188). Similar reasoning leads to the conclusion that the cartwheel concept is more sensitive to spatial instability errors than the pendulum concept.

Regarding the temporal aliasing errors, the along-track mission is also the most sensitive to them. This can be concluded by comparing Tables 8.1 (page 188), 8.2 (page 188) and 8.3 (page 189) at the longest DAPs, where spatial instability errors are minimal. For the 22-day DAP, for instance, temporal aliasing errors are at the level of 355, 50 and 30 mm ewh for the along-track, cartwheel and pendulum mission, respectively.

When the total temporal aliasing error (TAL) is plotted in terms of magnitude per SH, the along-track and cartwheel formations show a similar error distribution (cf. top and bottom panels of Figure 8.17 in page 186). There is a clear low-error stripe in the near-zonal coefficients, while the remaining ones show larger magnitudes. The cartwheel mission however shows significantly lower errors in the near-sectorial SH coefficients. Also, the tesseral coefficients show somewhat lower errors compared to the along-track concept. This is consistent with the fact that the orientation of the inter-satellite baseline in the cartwheel concept oscillates between the z and x directions. The error distribution of the zz gradient is more homogeneous than of the xx. This likely contributes to the error reduction in the tesseral and near-sectorial coefficients in the cartwheel case, as compared to the along-track one. The pendulum concept, in the middle panel of the same figure, shows a significantly different TAL error distribution, complementary to the one of the along-track concept. There is a region of comparatively large errors around the near-zonal SH coefficients, while the remaining ones show lower error magnitudes.

Plotting the TAL error on a map leads to similar conclusions. The along-track concept suffers from large north-south striations (top panel of Figure 8.18) (page 187). The cartwheel mission, in the bottom panel, shows a significant reduction of errors, which are fairly homogeneously distributed now; only at high latitudes, there are some patches of visible north-south striation errors. A comparison between the two maps illustrates the added value of the zz component observed by the cartwheel formation. The pendulum TAL error map, in the middle panel, shows a rather homogeneous error pattern with some east-west striations, though some north-south stripes gather around the Southern Ocean. The presence of both north-south and east-west stripes in the same map is interesting. I claim that it illustrates two different error propagation mechanisms at play. The east-west stripes can be attributed to the anisotropic sensitivity of the pendulum mission and the consequent emergence of spatial instability errors. The north-south stripes are common in the TAL error maps of all three considered formations. They are likely caused by a relatively low accuracy of the AOD model in this geographic region.

The dominant error source for the along-track and cartwheel configurations is the AOD error, while ranging error is the largest for the pendulum case. The total

error for the cartwheel mission in the case of 24-day DAP (48 mm ewh, cf. Table 8.3 in page 189) is smaller than the corresponding errors for the along-track (386 mm ewh, cf. Table 8.1 in page 188) and pendulum (133 mm ewh, cf. Table 8.2 in page 188) missions.

The presented results are consistent with the predictions made at the beginning of Section 8.1 on the basis of the findings presented in Sections 7.4 and 7.5. From the latter sections, it was concluded that both in terms of spatial instability and temporal aliasing errors, the zz gravity gradient component is the most favourable, while the xx is the least favourable one. The results presented above confirm that the inclusion of "oscillating" zz component, as it takes place in the cartwheel mission, greatly improves the performance compared to the along-track mission. Now, the elementary mission concepts can be ranked from best to worst as follows: cartwheel, pendulum and along-track. Similar conclusions were also presented in M. A. Sharifi et al. (2007) and Sneeuw et al. (2008), on the basis of a much simpler set of simulations.

The differences between the considered formations, as discussed in the previous paragraphs, become much smaller when regularization is applied. The regularization procedure if very effective at reducing the level errors from all the considered sources at the expense of introducing a regularization bias. This bias is the dominant error above SH degree 40 for the along-track mission, and above SH degree 60 for the pendulum and cartwheel missions. The regularization bias is particularly effective at reducing the ranging error in the pendulum mission, which makes it the best one in terms of regularized solutions. The pendulum 351/22 (19 mm ewh) has the lowest total errors, followed by the cartwheel 255/16 (20 mm ewh) and the along-track 255/16 (23 mm ewh).

A final important caveat is that the presented results did not take the indirect effect errors into account, as discussed in Section 4.6. Given that the cartwheel mission was found to be very sensitive to indirect effect errors (cf. Section 3.7), it is likely that the inclusion of those errors would change the relative performance of the considered formations. Similar findings are reported in Encarnação (2015).

8.2. Advanced Mission Design

In the previous sections, I have shown the expected performance of the elementary ll-SST formations. Taking into account the results obtained in Sections 7.4 and 7.5, one can now map the likely ways in which the performance of the elementary missions can be enhanced.

The performance of the along-track and cartwheel formations was limited by temporal aliasing errors. The largest error source for the pendulum formations in terms of unregularized solutions was the ranging error. Ranging errors will likely be solved by new technological developments in the future decades. On the other hand, the magnitude of temporal aliasing errors in future missions will depend on significant developments of background models which will likely be a challenge. Therefore I propose that mitigating temporal aliasing errors by way of mission design is likely the best way to enhance the performance of future missions. It was shown in Section 7.5, that the best way to reduce temporal aliasing errors is to

place additional formations on different orbital planes. This can be accomplished with 4 satellites grouped into two different formations. Placing the two formations' orbital planes perpendicular to each other was shown to minimize temporal aliasing errors.

However, one may also consider missions consisting of 3 satellites grouped in a single formation. For example, the Swarm mission has deployed a three-satellite formations with a single launcher, which may result in a significant reduction of mission costs compared to a dual-formation mission. In Section 7.5, it was shown that considering different gradiometer components, the single zz observable already yielded the lowest level of temporal aliasing errors. The cartwheel mission observations oscillate between xx and zz gravity gradient components. And, indeed, in Section 8.1.3 this concept was shown to result in the lowest level of errors of the elementary set of satellite formations. However, the cartwheel configuration is the most difficult to implement in practice due to the very dynamic inter-satellite baseline orientation. At the same time, it was shown in Section 7.5.1 that the xx+yy combinations yielded the same level of temporal aliasing errors as the single zz observable. This means that for a single-formation mission, a combination of along-track and pendulum observations is likely simpler to implement. Additionally, because the direction of the cartwheel formation observations oscillate between xx and the more desirable zz, the along-track + pendulum (AP) combination has the potential to significantly reduce the level of temporal aliasing errors w.r.t. cartwheel, since it observes the xx+yy combination almost continuously (except for the vicinity of the poles). Finally, as was shown in Section 7.4.1, the AP combination is likely to double the spatial resolution of the mission compared to the single-observable cartwheel configuration.

While the AP combination seems desirable, there are other combinations which could be taken into consideration. In the following sections, I will consider the cartwheel configuration as a valid combination element, too. A point of concern is that, among the elementary satellite formations considered, only the along-track concept has been proven, while the cartwheel and pendulum concepts remain theoretical alternatives (particularly, the cartwheel one). Given that the cartwheel configuration is particularly hard to implement, priority will be given, under other conditions being equal, to combinations which do not include a cartwheel pair of satellites.

Considering three satellites grouped into a single formation, the idea is to merge any two possible elementary formations by selecting one satellite to simultaneously take part in two formations. There are 6 different hybrid combinations: PP, AA, CC, PA, PC and AC, where the letters P, A and C correspond to the pendulum, along-track and cartwheel concepts, respectively. For example, the AA concept would consist of three satellites co-linearly arranged in a north-south direction such that the middle satellite takes part in both along-track formations. The most promising are the PA and the CP concepts, since they combine ll-SST observations along orthogonal orientations. The PA concept is a xx+yy combination, while the CP combines a xx/zz oscillating component with the yy component. The AA and PP concepts are the least interesting, since the additional satellite brings relatively little added value

to the base elementary satellite formation. Similarly, the AC concept is also of little interest since there is an overlap in the orientation of the measurements made by the formation. The most interesting concepts are then the PA, which will be named "gamma" (proposed in Elsaka (2010) as GRACE-Pendulum-type), the CP, named "sigma", and the CC, named "delta" (proposed in Wiese et al. (2009) as three-satellite cartwheel).

Regarding missions consisting of two elementary formations in different orbital planes, there are again the same 6 possible combinations: P+P, A+A, C+C, P+A, P+C and A+C. Similarly, the most promising are the P+A and C+P concepts, which will be called "dual gamma" and "dual sigma", respectively. Given that the cartwheel mission was shown to have the best performance among the elementary satellite formations, the C+C concept, consisting of two cartwheel formations might be interesting as well. Because both formations collect observations which oscillate between the xx and zz gravity gradients, the α angles of the two participating formations can be adjusted such that they collect orthogonal observations over all latitudes. The C+C mission will be called "dual cartwheel".

The A+A concept combines two formations observing the xx- gravity gradient, which is not the most desirable combination in light of what was found in Section 7.5. This deficiency can be mitigated by lowering the orbital inclination of one of the formations in order to introduce the yy-component into the combination. Such a variant of the A+A concept has been proposed before; it is known as the "Bender mission" (P. L. Bender et al., 2008) and has been later refined in (Wiese, 2011). This configuration will be called below "dual along-track".

On the other hand, the P+P and the A+C are the least interesting concepts since they combine similar observations; the yy component is observed twice in the P+P combination, while the A+C combines an oscillating xx/zz component with another xx component. For these reasons, these concepts will not be taken into consideration.

In the following sections, each of the concepts addressed above will be presented in detail and benchmarked.

8.3. Hybrid Formation Missions

8.3.1. Gamma

The gamma mission consists of a single formation with three satellites which can be imagined as arranged in a Γ shape. The gamma mission can be thought of as a 3-satellite combination of an along-track and pendulum formations. One of the satellites is the formation leader taking part in the measurement of two range observations made to the other two satellites. One of the observations is made in the along-track direction, while the other one in the cross-track direction.

Taking as baseline the 16-day gamma mission, I show a general overview of the errors of the mission in the top panel in Figure 8.23 (page 201). Temporal aliasing errors are the dominant error source, becoming larger than the mass transport signal at SH degree 100. A breakdown of temporal aliasing errors in the right panel

of Figure 8.24 (page 202) shows that up to SH degree 60, the performance of the mission is limited by a combination of ocean tide model (OTE) error and AOD error. From SH degree 60 onwards, AOD becomes the largest error source.

Total temporal aliasing errors shown in the triangular plot in the top panel of Figure 8.25) (page 203) shows a relatively homogeneous error distribution over the SH coefficients compared to the elementary formations (cf. Figure 8.17 in page 186). In the form of a map, the error is presented in the top-left panel of Figure 8.26 (page 204), where I zoom in on the Amazon river basin. A north-south striation pattern can still can be seen, but its magnitude is relatively low, as compared to the elementary satellite formations.

Table 8.7 (page 200) presents the error budgets for the gamma mission over different DAPs in terms of unregularized solutions. The gamma mission shows a large improvement relative to the previously considered two-satellite missions. At the longest DAP of 24 days, the gamma mission, with a total error of 22 mm ewh, is significantly better than the elementary formations, with 386, 132 and 48 mm ewh for the along-track, pendulum and cartwheel formations, respectively. At the shortest 8-day DAP, the performance gap increases even further; the total error of the gamma mission with a total error of 69 mm ewh, is at least 5x better than the elementary formations, with 2460, 331 and 447 mm ewh for the along-track, pendulum and cartwheel formations, respectively.

An unregularized recovery of mean mass transport signals up to d/o 120 with sufficient accuracy over relatively short periods of 10 or even less days is possible now. Even for the 127/8 gamma mission, the global signal-to-noise ratio (TOT divided by ESM) is about 1, since the total error is roughly of the same magnitude as the mass transport signal.

A good performance of the gamma mission can be explained as follows. On the one hand, errors in the gamma mission are mitigated by the relatively high spatial resolution, which is a consequence of combining multiple observations, as was shown in Section 7.4. On the other hand, the performance of the gamma concept is enhanced by the synergy between the pendulum and along-track pairs of satellites; the along-track pair of satellites provides the observability of the zonal and near-zonal coefficients, while the pendulum pair provides the observability of the sectorial and near-sectorial ones.

Similarly to the previously considered mission concepts, an attempt to reduce the temporal aliasing errors is done by considering different DAPs. In Figure 8.19, a comparison of the total error for gamma missions for a selection of different DAPs is shown in terms of unregularized solutions. There are small differences in the total error up to SH degree 60 for the considered DAPs. At higher SH degrees, these differences become larger, with the longer periods leading to smaller total errors. Table 8.7 (page 200) shows the error breakdown of the gamma mission for the considered DAPs. The longest considered mission with the 24-day DAP shows the lowest total error of 22 mm ewh. Temporal aliasing errors are the largest contributor for all the considered periods and of these, the AOD error is the largest component.

The regularization procedure was also applied to the gamma mission. A break-

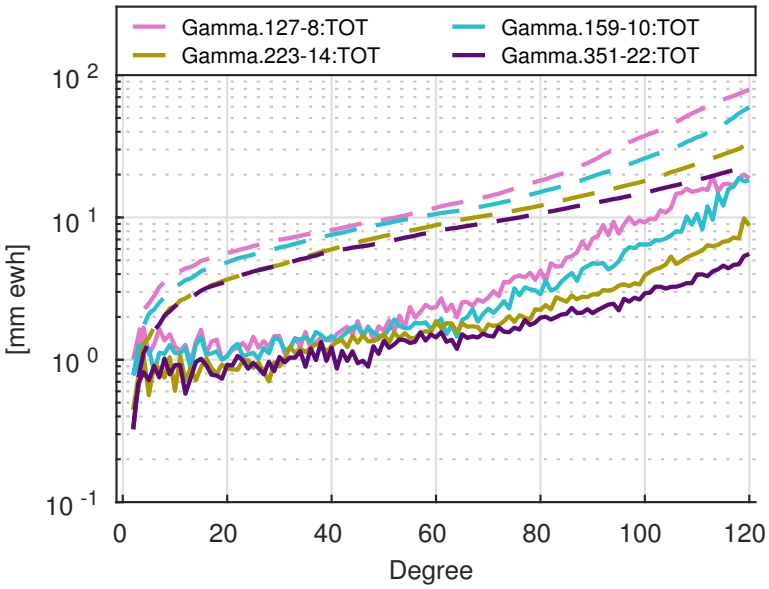

Figure 8.19: Comparison of the total error (TOT) over a selection of DAPs for the gamma mission in terms of *unregularized* solutions.

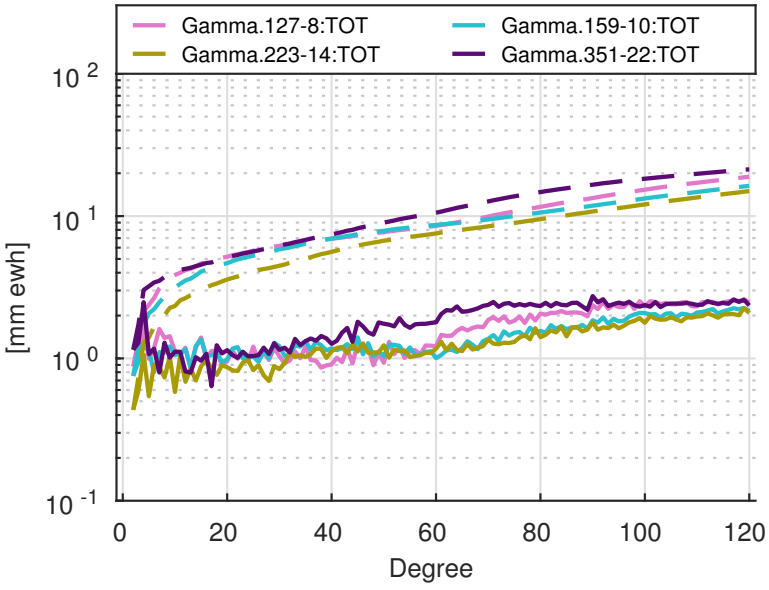

Figure 8.20: Comparison of the total error (TOT) over a selection of DAPs for the gamma mission in terms of and *regularized*.

down of the temporal aliasing errors is shown in that case for the 255/16 gamma mission in Figure 8.21. It can be seen that, overall, the total temporal aliasing error is explained by the combination of OTE and AOD model errors. OTE errors are larger below SH degree 60, while AOD errors are larger above SH degree 80.

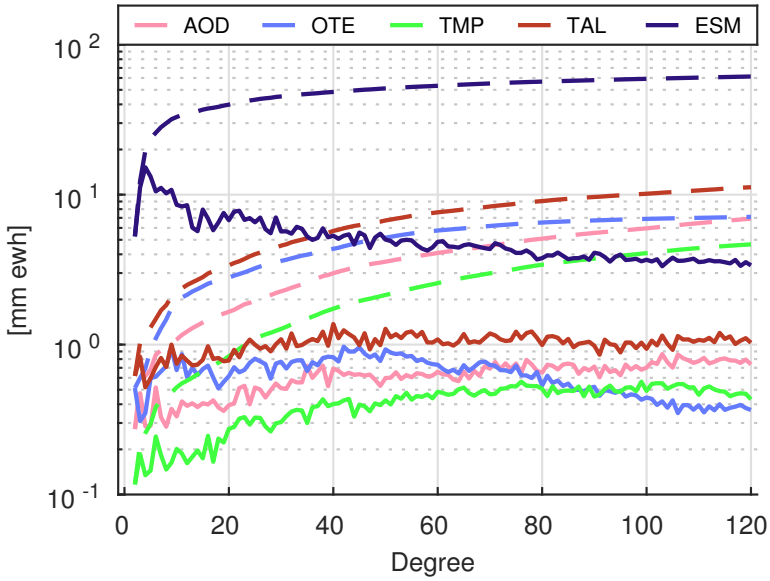

Figure 8.21: Breakdown of temporal aliasing errors in DV for the 255/16 gamma mission in terms of *regularized* solutions. The explanation of the used acronyms can be found in Table 4.4 in page 75.

A map of regularized total temporal aliasing error is shown in the top-right panel of Figure 8.26 (page 204). In comparison with the unregularized version shown in the top-left panel, the striation has been reduced. The reduction of errors due to the regularization is, however, small in comparison with the elementary satellite formations. This highlights the fact that the gamma concept displays very low errors in terms of unregularized solutions so that a filtering or regularization of the solutions complete to degree 120 may not even be required.

Figure 8.20 shows the evolution of the total error for a selection of DAPs in terms of regularized solutions. While in the unregularized case, one could observe noticeable differences between different DAPs at the SH degrees above 80, once regularization is applied, the differences become fairly small.

The error budget for the gamma mission for different repeat orbits in the presence of regularization is shown in Table 8.10 (page 206). The difference in total error for different DAPs is now much smaller than in the case of the unregularized solutions. The total error for the longest 24-day mission (14 mm ewh) is no longer significantly smaller than for the 16-day mission (also 14 mm ewh) or even for the 8-day mission (18 mm ewh).

8.3.2. Sigma

The sigma mission is a three-satellite hybrid formation consisting of a chief satellite taking part in both pendulum and cartwheel formations. The cartwheel pair of satellites collects ll-SST raging data in the vertical plane, oscillating between the xx and zz gradients, while the pendulum pair delivers ranging data in the orthogonal yy-direction.

The general error DV plot, in the middle panel of Figure 8.23 (page 201), shows that temporal aliasing errors are again the largest contributor to the error budget, becoming larger than the mass transport signal around SH degree 100. The middle panel of Figure 8.24 (page 202) shows a breakdown of temporal aliasing errors. Here, one can see that up to around SH degree 60, temporal aliasing errors are dominated by a combination of ocean tide model errors and AOD errors. From SH degree 60 upwards, AOD model errors become the largest contributor.

The total temporal aliasing error is shown per SH coefficient in a triangular plot in Figure 8.25 (page 203) and as a map over the Amazon river basin in the middle-left panel of Figure 8.26 (page 204). The triangular plot demonstrates a fairly even error distribution apart from a clear band with lower errors at the high-degree near-zonal coefficients. The map shows some relatively large error features in the form of short north-south stripes around the Amazon river basin.

Table 8.8 (page 205) presents an error breakdown for a selection of DAPs of the sigma mission in terms of global RMS. The lowest total error is seen at the longest 24-day period (21 mm ewh), while the largest one at the shortest considered DAP of 8-days (49 mm ewh).

In terms of regularized solutions, a map of the total temporal aliasing error over the Amazon basin is shown in the middle-right panel of Figure 8.26 (page 204). The regularization has removed some of the north-south striations, however the magnitude of the largest features remains almost unchanged.

An overview of the temporal aliasing errors in terms of regularized solutions is shown in Figure 8.22. Similar to the gamma mission, the overall total temporal aliasing error is explained by a combination of ocean tide model (OTE) and AOD model errors. OTE error is larger below SH deg 60, while AOD model error is larger above SH degree 80.

The error budget for a selection of periods in terms of regularized solutions is shown in Table 8.11 (page 206). In comparison with the unregularized solutions, the errors are significantly smaller and the differences between errors for different DAPs are small as well. The lowest error is found for the 22-day mission (13 mm ewh) while the worst performance is found for the shortest considered period of 8 days (17 mm ewh).

8.3.3. Delta

The delta mission is a three-satellite extension of the cartwheel mission, proposed in Wiese et al. (2009). In the traditional cartwheel concept, two satellites follow a relative elliptical motion around the center of an ellipse. The two satellites are placed on the ellipse at a 180° phase angle difference from each other. The delta formation adds one more satellite to this configuration, such that now the three satellites are placed at a 120° phase angle differences from each other. With

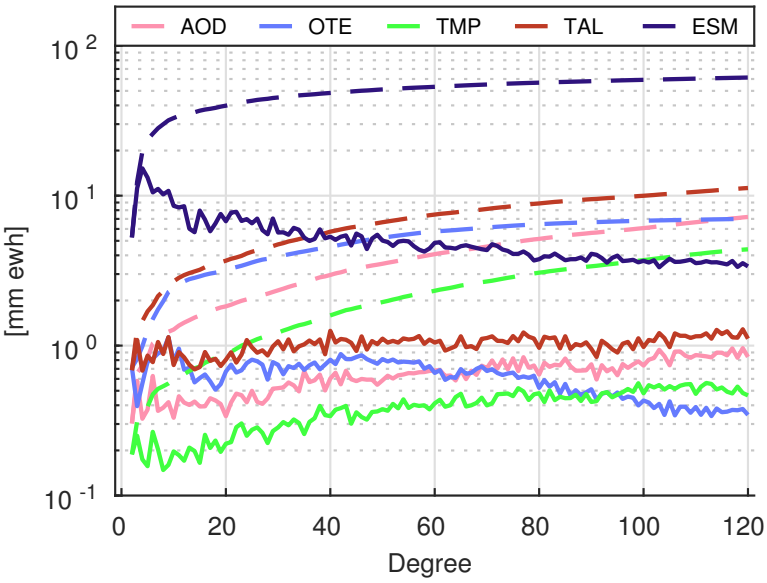

Figure 8.22: Overview of temporal aliasing errors for the 255/16 sigma mission in terms of *regularized* solutions [mm ewh]. The explanation of the used acronyms can be found in Table 4.4 in page 75.

the additional satellite, a total of three inter-satellite ranging links are considered between the satellites. This configuration ensures that the zz, xx and xz gravity gradients can be continuously resolved (Wiese et al., 2009).

The baseline delta mission, similarly to the previous sections is on a 255/16 repeat orbit. The virtual point in the middle of the formation is at an altitude of 278 km. The bottom panel in Figure 8.23 (page 201) shows an overview of the errors for the delta mission in terms of error per degree. Temporal aliasing is again the major error source. A breakdown of temporal aliasing errors, shown in the bottom panel of Figure 8.24 (page 202) shows that a combination of AOD model errors and ocean tide model errors is dominant up to SH degree 50. From SH degree 50 onwards, the AOD model error becomes larger and dominates the error budget.

In the bottom panel of Figure 8.25 (page 203), the magnitude of the total temporal aliasing error is shown per SH coefficient for the baseline 255/16 delta mission. It can be seen that the band consisting of the near-zonal coefficients shows lower errors than the rest of coefficients. Otherwise, the errors are fairly evenly distributed.

The map of the total temporal aliasing error over the Amazon river basin is shown in the bottom-left panel of Figure 8.26 (page 204). The error pattern is formed by predominantly north-south stripes, although shorter and more curved than the ones typically seen for the along-track concept (cf. top panel of Figure 8.18 in page 187).

Inspecting the error budget for the delta mission over different DAPs in terms of unregularized solutions (Table 8.9 in page (page 205)), one can see that the

lowest errors are obtained for the 22-day mission (26 mm ewh), while the shortest considered 8-day period results in the largest error (93 mm ewh).

In the bottom-right panel of Figure 8.26 (page 204), a map of the total temporal aliasing error for the 255/16 delta mission is shown over the Amazon river basin for the case of the regularized solutions. There is a clear reduction in the number and magnitude of the error features, as compared to the unregularized solution. In Table 8.12 (page 207), the error budget of regularized solutions is presented for different DAPs. As expected, there is a significant reduction of errors, compared the unregularized case. The lowest error is obtained for the 22-day period (14 mm ewh), while the highest one is again for the 8-day period (17 mm ewh).

Table 8.7: Error budget of the gamma mission over a selection of DAPs in terms of global RMS [mm ewh]. The explanation of the used acronyms can be found in Table 4.4 in page 75.

Gamma	127/8	191/12	255/16	383/24
RNG	9.76	6.46	5.34	3.24
ACC	2.31	1.70	1.06	0.64
TIN	9.99	6.66	5.44	3.30
AOD	55.77	38.21	21.16	16.57
OTE	33.75	15.28	10.30	10.06
TMP	20.10	14.03	8.80	10.02
TAL	68.63	43.25	25.90	21.89
SPT	2.78	4.13	1.74	1.20
TOT	69.46	43.72	26.43	22.11
ESM	62.78	62.14	61.36	59.70

8.3.4. Discussion

In the previous sections I analyzed the performance of three hybrid satellite formations. These formations were designed to combine ll-SST pairs of satellite with differently oriented inter-satellite baselines. All considered hybrid formations have shown significant performance improvements compared to the elementary formations. For the 24-day DAP, in terms of unregularized solutions, the global RMS of total error for the hybrid missions was between 21 and 27 mm ewh, while it was between 48 and 385 mm ewh for the elementary formations.

Overall, the performance of all hybrid formations is limited by temporal aliasing errors. Looking at the longer DAPs, temporal aliasing errors for all hybrid formations were found to be significantly smaller than those of the elementary formations. For the 24-day DAP, temporal aliasing error of the hybrid formations was between 21 and 27 mm ewh, while it was between 33 and 385 mm ewh for the elementary formations. This is consistent with the findings of Section 7.5.1, where it was shown that any combination of observables should yield lower temporal aliasing errors that either xx or yy gravity gradient alone.

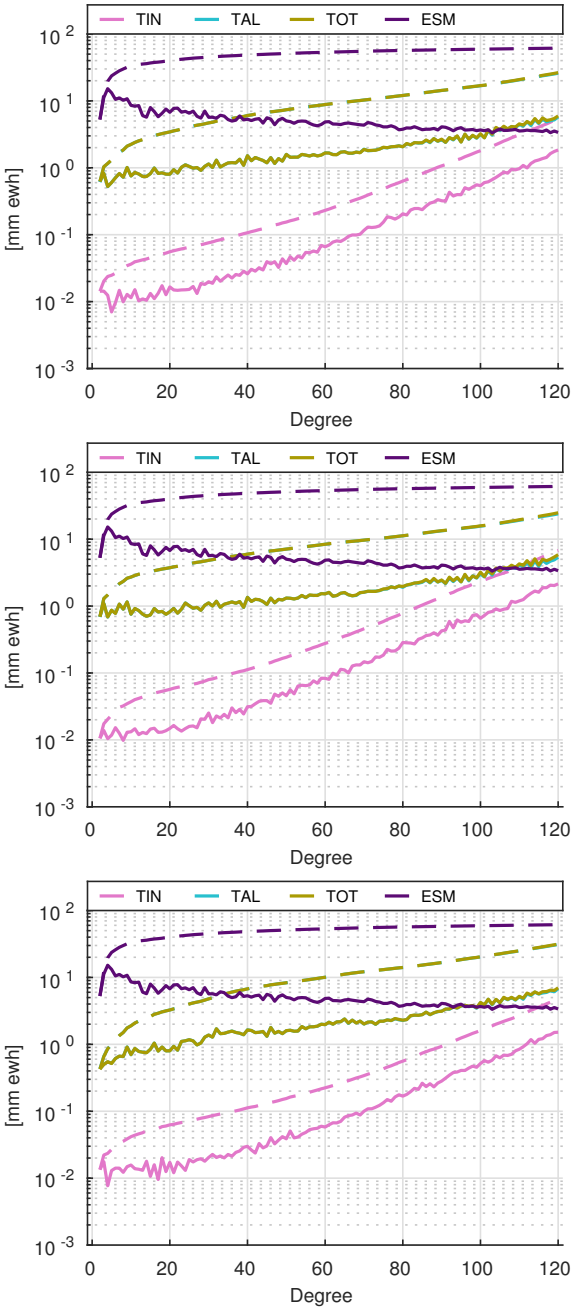

Figure 8.23: General overview of errors for the 255/16 gamma (top), 255/16 sigma (middle) and 255/16 delta (bottom) missions. The explanation of the used acronyms can be found in Table 4.4 in page 75.

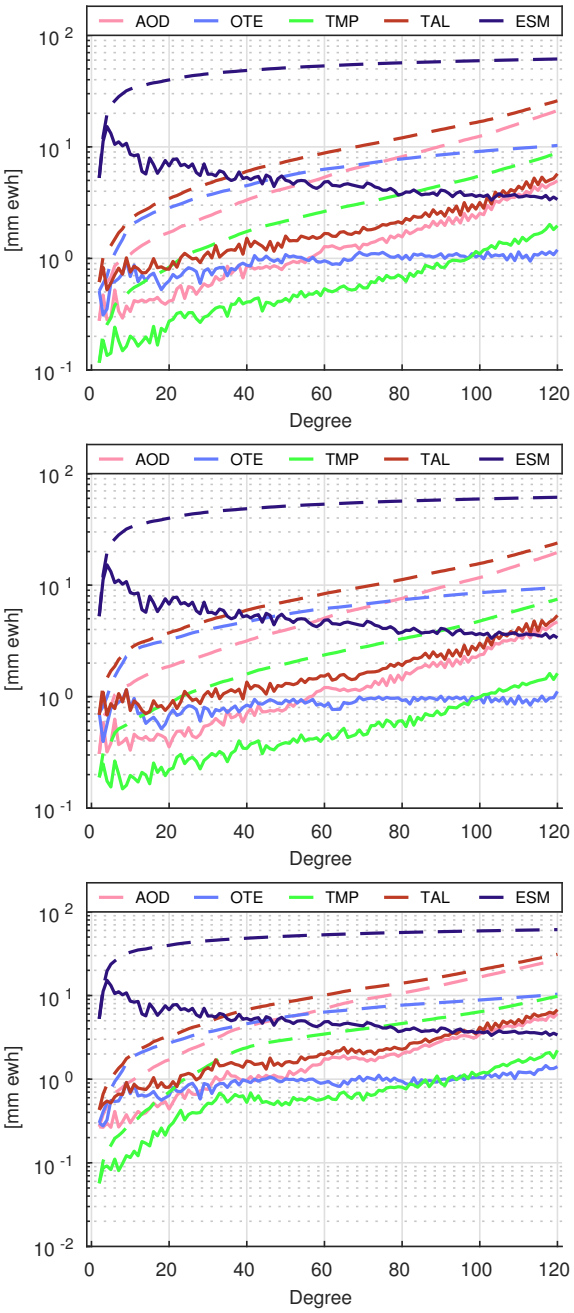

Figure 8.24: Breakdown of temporal aliasing errors for the 255/16 gamma (top), 255/16 sigma (middle) and 255/16 delta (bottom) missions. The explanation of the used acronyms can be found in Table 4.4 in page 75.

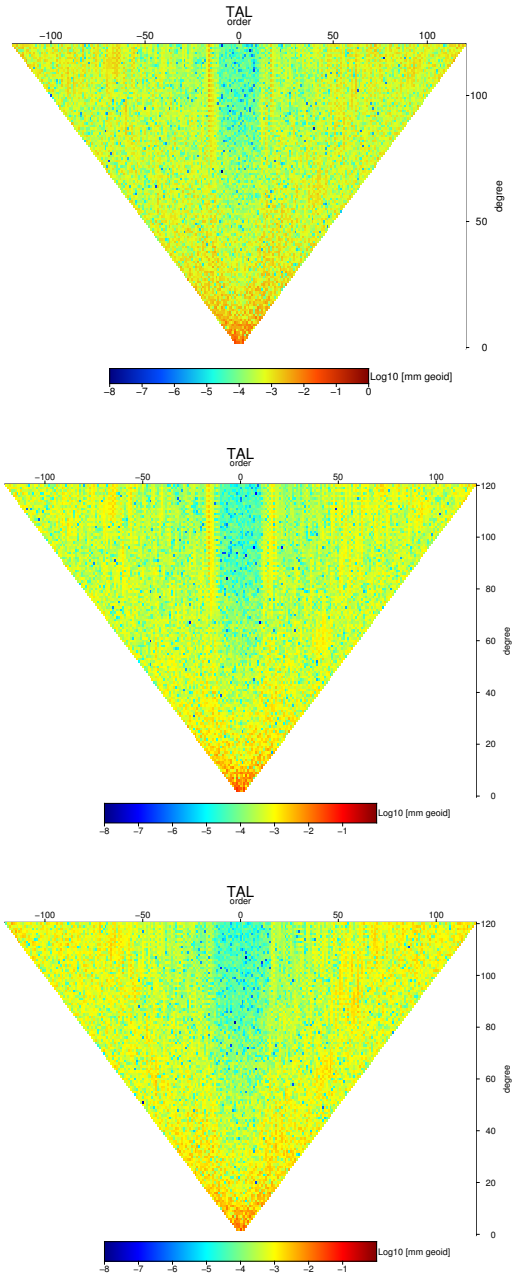

Figure 8.25: Magnitude of SH coefficients of the total temporal aliasing error (TAL) for the 255/16 gamma (top), 255/16 sigma (middle) and 255/16 (bottom) missions.

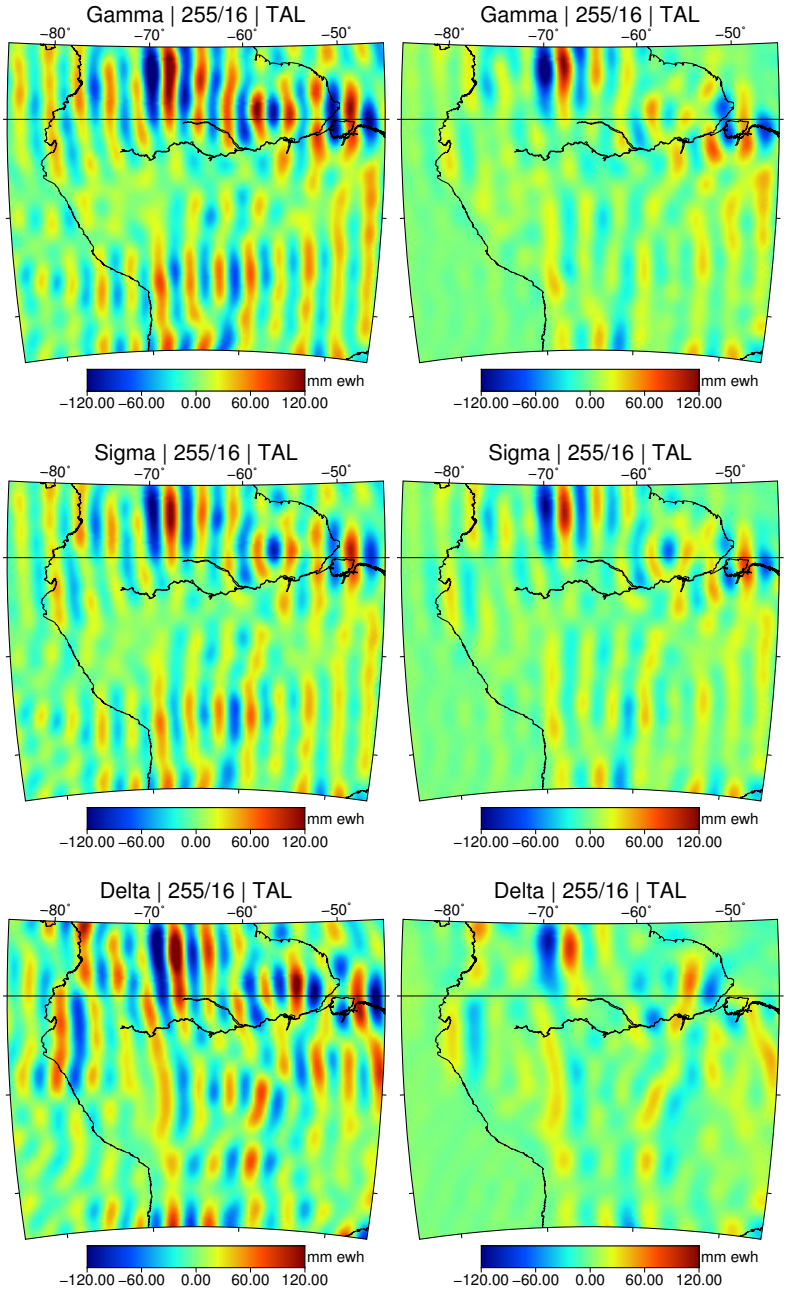

Figure 8.26: Map of the total temporal aliasing error (TAL) for the 255/16 gamma (top), 255/16 sigma (middle) and 255/16 delta (bottom) missions in terms of unregularized (left) and regularized (right) solutions over the Amazon river basin up to $l_{\max} = 120$.

Table 8.8: Error budget of the sigma mission over a selection of DAPs in terms of global RMS [mm ewh] solved up to SH degree 120. The explanation of the used acronyms can be found in Table 4.4 in page 75.

Sigma	127/8	191/12	255/16	351/22	383/24
RNG	12.08	8.08	6.69	4.15	3.99
ACC	2.31	1.50	1.17	0.73	0.72
TIN	12.33	8.20	6.78	4.22	4.05
AOD	37.60	22.23	19.65	15.58	16.22
OTE	21.86	10.25	9.54	10.30	9.71
TMP	14.23	8.12	7.48	7.65	8.99
TAL	47.60	26.51	23.88	20.51	21.03
SPT	2.44	3.06	1.61	1.35	1.35
TOT	49.30	27.78	24.81	20.95	21.45
ESM	62.78	62.14	61.36	60.12	59.70

Table 8.9: Error budget of the delta mission over a selection of DAPs in terms of global RMS [mm ewh] solved up to SH degree 120. The explanation of the used acronyms can be found in Table 4.4 in page 75.

Delta	127/8	191/12	255/16	351/22	383/24
RNG	11.20	6.14	4.57	2.90	2.78
ACC	3.38	2.02	1.22	0.80	0.76
TIN	11.68	6.52	4.77	3.01	2.88
AOD	76.33	43.81	26.77	20.79	20.92
OTE	43.17	14.18	10.37	12.33	13.41
TMP	24.89	15.06	9.81	9.80	11.47
TAL	92.00	48.63	31.05	25.84	27.28
SPT	3.81	5.10	1.65	1.28	1.27
TOT	92.68	49.28	31.51	26.04	27.41
ESM	62.78	62.14	61.36	60.12	59.70

Table 8.10: Error budget of the gamma mission over a selection of DAPs in terms of global RMS of *regularized* solutions [mm ewh]. The explanation of the used acronyms can be found in Table 4.4 in page 75.

Gamma	127/8	191/12	255/16	383/24
RNG	0.73	0.83	0.98	0.65
ACC	0.22	0.24	0.23	0.18
TIN	0.75	0.87	1.00	0.67
AOD	6.10	6.53	6.91	6.05
OTE	6.93	7.55	7.11	6.41
TMP	3.64	4.18	4.66	6.97
TAL	10.38	10.95	11.21	11.18
REG	14.63	10.77	9.09	7.89
SPT	0.66	1.43	0.49	0.22
TOT	17.83	15.23	14.35	13.69
ESM	62.78	62.14	61.36	59.70

Table 8.11: Error budget of the sigma mission over a selection of DAPs in terms of global RMS of *regularized* solutions [mm ewh] solved up to SH degree 120. The explanation of the used acronyms can be found in Table 4.4 in page 75.

Sigma	127/8	191/12	255/16	351/22	383/24
RNG	0.99	1.27	1.20	0.96	0.94
ACC	0.28	0.31	0.29	0.23	0.22
TIN	1.04	1.31	1.23	0.98	0.96
AOD	6.63	7.32	7.21	6.22	6.37
OTE	6.70	7.45	7.01	7.31	6.55
TMP	4.19	4.25	4.39	5.29	6.54
TAL	10.86	11.36	11.25	11.07	11.18
REG	13.29	9.51	8.44	7.04	6.99
SPT	0.82	1.58	0.49	0.35	0.36
TOT	17.18	14.83	14.06	13.11	13.26
ESM	62.78	62.14	61.36	60.12	59.70

Table 8.12: Error budget of the delta mission over a selection of DAPs in terms of global RMS of *regularized* solutions [mm ewh] solved up to SH degree 120. The explanation of the used acronyms can be found in Table 4.4 in page 75.

Delta	127/8	191/12	255/16	351/22	383/24
RNG	0.95	0.90	0.89	0.72	0.61
ACC	0.28	0.26	0.24	0.19	0.17
TIN	0.99	0.94	0.94	0.75	0.63
AOD	7.31	6.92	7.04	6.44	5.88
OTE	6.71	7.11	6.48	6.93	6.70
TMP	4.20	4.43	5.09	6.34	7.09
TAL	11.06	11.16	11.01	11.41	11.14
REG	13.76	11.46	9.71	8.24	8.85
SPT	0.60	1.50	0.52	0.48	0.40
TOT	17.39	15.86	14.82	13.93	14.29
ESM	62.78	62.14	61.36	60.12	59.70

The hybrid missions also yielded significantly lower spatial instability errors. These can be estimated from the differences in the overall error level between the shortest and the longest considered DAPs. The differences in the total error of the hybrid missions between 8 and 24-day DAPs in terms of unregularized solutions were between 28 (sigma) and 65 mm ewh (delta). Regarding the elementary formations, these differences were found to be between 200 (pendulum) and 2000 (along-track) mm ewh. This indicates that the spatial resolution of the hybrid missions is significantly better than that of the elementary ones. In fact, unregularized solutions of the hybrid formations at DAPs between 8 and 12 days were shown to have a signal-to-noise ratio close to 1. High resolution ($l_{\text{max}} \geq 120$) gravity field solutions at short DAPs (≤ 10 days) may be possible for the considered hybrid missions. Furthermore, due to the overall low level of errors, especially in the larger considered DAPs, it was shown that the regularization procedure leads to a relatively small error reduction and may even be considered optional. These improvements can be attributed to the synergy between two orthogonal observables which was shown in Section 7.4.1 to approximately double the spatial resolution of the mission.

At the shortest DAP considered (8 days) there are significant differences in the total error between the three hybrid missions, in terms of unregularized solutions. The delta mission has the highest level of total error (92 mm ewh, cf. Table 8.9), followed by the gamma mission (69 mm ewh, cf. Table 8.7). The sigma missions has the lowest level of errors (48 mm ewh, cf. Table 8.7). At the longest considered DAP (24 days) the missions these differences in terms of total error are small, with 27, 22 and 21 mm ewh for the sigma, gamma and delta missions respectively. The differences between the three missions are much smaller for the longest DAP

compared to the shortest one. This indicates that the delta and gamma missions suffer from a higher level of spatial instability errors w.r.t. the sigma mission.

For all three considered hybrid missions, temporal aliasing errors were found to be dominant and of those, the AOD error was consistently the largest component. Temporal aliasing errors were found to have similar structure in terms of magnitude of SH degrees for all three hybrid missions. In terms of unregularized solutions, when these errors are plotted over South America (Figure 8.26 in page 204), the major errors features are also common to all three missions. Nonetheless, the sigma mission, in the middle panel, seems to have the lowest errors. The gamma mission, in the top panel, has comparatively higher errors in the southern part of this region, while the delta mission, in the bottom panel, has larger errors in the central part.

8.4. Dual-formation Missions

In Section 7.5, I have shown that a mission observing two gravity gradient components in perpendicular orbital planes leads to a reduction of temporal aliasing errors compared to a mission observing the same components from the same orbital plane. Therefore, the performance of a single-formation mission may be enhanced by splitting it into two independent formations in different orbital planes. In the following sections, the dual-formation missions will be presented and benchmarked.

In line with the findings of Section 7.5, the two formations will be placed in nearly perpendicular orbital planes in order to minimize temporal aliasing errors. A small deviation from perpendicularity is used to ensure that the ground tracks of both formations are interleaved with each other, such that the overall ground track geometry is sufficiently homogeneous.

8.4.1. Dual Along-Track

The dual along-track mission consists of two independent along-track satellite formations. The Bender mission (P. L. Bender et al., 2008) is the most popular variant of this configuration. The design parameters of the Bender mission have been optimized in Wiese (2011). Wiese proposed two along-track pairs at 13-day repeat orbits, one polar pair and another one at a lower inclination of 73°.

The dual along-track concept is an attractive option as it relies on proven technology, already used for the GRACE and GFO missions. The addition of another pair of satellites results in increased spatio-temporal resolution, while the lower inclination of the second pair orbit allows one to collect information in the east-west direction. Regarding the inclination of the lower-inclined pair, there is a trade-off between the isotropic sensitivity of the mission and the spatial coverage of the second pair. Increasingly lower inclinations improve the east-west information content but also increase the size of the polar gap where the inclined pair does not collect observations.

As before, the 16-day DAP was chosen as a baseline. Similarly to the other dual-formation concepts, the orbital planes of the two formations were set nearly perpendicular in order to interleave their groundtracks. Figure 8.27 shows the im-

pact of inclination of the lower-inclined pair on the total error per SH coefficient. One can see significant differences between the error distributions over the SH coefficients. The 90° and 45° inclinations seem to have the highest errors. The 90° inclination shows the same error pattern as the single along-track formation: very low errors in the near-zonal coefficients and large errors in the remaining ones. The 45° inclination shows very low errors in the near-zonal and near-sectorial coefficients, and large errors in the remaining ones. The error pattern of the in-between inclinations gradually shifts between these two configurations, where the 60° and 70° inclinations seem to have relatively low errors.

Figure 8.28 presents the same total error for different inclinations of the lower-inclined pair, but now in terms of DV and CDV. The plots show that the total error becomes smaller with decreasing inclination until 70°. Cumulatively, both 70° and 60° inclinations yield similar levels of errors. At the inclination of 60°, the total error is larger between SH degrees 40 and 70 and slightly lower from degree 100 onwards, as compared to the inclination of 70°. Due to the better performance between degrees 40 and 70, the 70° inclination seems more desirable. This is in line with the findings of Wiese (2011), who concluded that the 73° inclination of the lower-inclined pair delivers the best performance. In the rest of this section, an inclination of 70° has been selected for the lower-inclined pair of the presented dual along-track simulations.

A general overview of the errors for the selected 255/16 dual along-track mission is shown in the top-left panel of Figure 8.29 (page 215). Temporal aliasing errors are dominant at all SH degrees, becoming larger than the signal around SH degree 70. In the top-left panel of Figure 8.30 (page 216), a breakdown of the temporal aliasing error is shown. Below SH degree 40 and above SH degree 80, temporal aliasing is explained by a combination of AOD model error and ocean tide model (OTE) error. Between SH degrees 40 and 80, AOD errors are the largest contributor.

The total temporal aliasing error for the selected 255/16 dual along-track mission is shown as a triangular plot in the top-left panel of Figure 8.31 (page 217) and as a map in the top-left panel of Figure 8.32 (page 218). In the triangular plot, one can see that the total error is not fully homogeneous. Above SH degree 50, increased errors are visible as two stripes between orders 15 and 30 and for near-sectorial coefficients. The map shows a pronounced striation pattern over the Amazon river basin, with a larger magnitude w.r.t. the gamma and sigma missions (cf. top and middle panels of Figure 8.26 in page 204, respectively).

Table 8.13 (page 215) reports propagated errors in terms of global RMS. It can be seen that the lowest total error is unexpectedly obtained for the fairly short period of 10 days (43 mm ewh), while the worst performance is found at the 12-day period (134 mm ewh).

The top-right panel of Figure 8.32 (page 218) shows the total temporal aliasing error for the selected 255/16 mission in terms of regularized solutions. In comparison with the top-left panel, there is a clear reduction of the striation pattern. In terms of regularized solutions, the performance of the dual along-track mission is fairly homogeneous over all the considered DAPs (cf. Table 8.17 in page 220). The best results are obtained for the 20-day period (13 mm ewh), while the worst

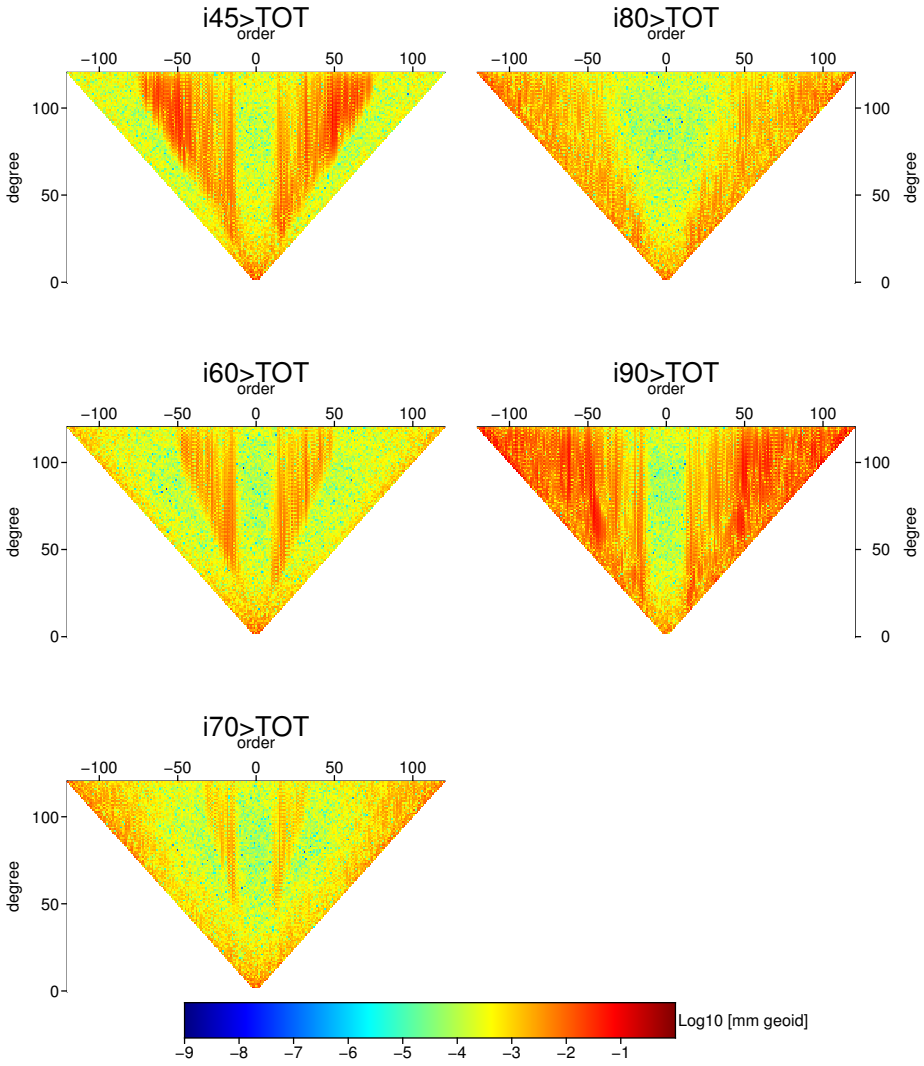

Figure 8.27: The total error (TOT) in terms of magnitude per SH coefficient for 255/16 dual along-track missions with different orbit inclination of the lower-inclined pair.

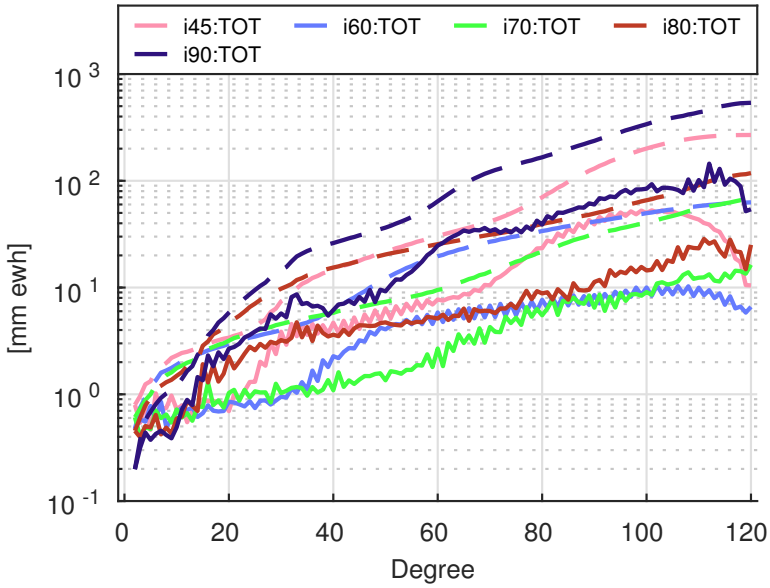

Figure 8.28: The total error (TOT) in terms of DV and CDV for 255/16 dual along-track missions with different orbit inclinations of the lower-inclined pair.

performance is observed again for the 12-day period (17 mm ewh).

8.4.2. Dual Gamma

The dual gamma mission consists of one along-track formation and one pendulum formation set in two roughly perpendicular orbital planes. Taking the 255/16 dual gamma mission as a baseline, I present a general overview of the mission errors in the top-right panel of Figure 8.29 (page 215). One can see that temporal aliasing errors are the largest at all SH degrees. At SH degree 100, temporal aliasing errors become larger that the mass transport signal. In the top-right panel of Figure 8.30 (page 216), a breakdown of temporal aliasing errors shows that AOD model errors are the dominant source above SH degree 50. Below HS degree 50, ocean tide model errors are as large as AOD model errors.

The total temporal aliasing error for the 255/16 dual gamma mission is shown as a triangular plot in the top-right panel of Figure 8.31 (page 217) and as map over the Amazon river basin in the upper-middle-left panel of Figure 8.32 (page 218). The triangular plot demonstrates that temporal aliasing errors are fairly homogeneous, apart from the low-error band at the high-degree near-zonal coefficients. The map shows a set of short north-south stripes where the largest magnitude is observed north of the equator.

Table 8.14 (page 216) shows the total error of the dual gamma mission in terms of unregularized solutions for several DAPs. One can see that the lowest errors are obtained for the 22-day DAP (22 mm ewh), while the largest error for the shortest

8-day DAP (84 mm ewh).

In terms of regularized solutions, the total temporal aliasing errors over the Amazon river basin are shown as a map in the upper-middle-right panel of Figure 8.32 (page 218). The large-error features are somewhat reduced in magnitude. Error features over the oceans can hardly be seen now.

The error budget in terms of regularized solutions is shown for several DAPs in Table 8.18 (page 220). It shows that the lowest total error is found at the 22-day period (13 mm ewh) while the largest errors at the shortest 8-day period (18 mm ewh).

8.4.3. Dual Cartwheel

The dual cartwheel mission combines two cartwheel formations in nearly perpendicular orbital planes. One important aspect in the configuration of the dual cartwheel mission is the relative orientation of the inter-satellite baselines of the two formations. While the inter-satellite baseline of one formation is oriented in the along-track direction over the equator, the second formation is oriented radially, such that both formations have roughly perpendicular baselines over all latitudes. This ensures that the maximum information is collected with the dual cartwheel concept.

Similarly to the results presented for the other mission concepts, a general overview of the errors for the 255/16 dual cartwheel mission is shown in the bottom-left panel of Figure 8.29 (page 215). The plot shows that the error budget of the dual cartwheel mission is, similarly to the other mission concepts, dominated by temporal aliasing errors. The total temporal aliasing error becomes as large as the signal at around SH degree 90. The bottom-left panel of Figure 8.30 (page 216) shows the breakdown of temporal aliasing errors. It can be seen that, above SH degree 20, AOD model errors are the dominant error source, especially above SH degree 40.

The triangular plot in the bottom-left panel of Figure 8.31 (page 217) shows the magnitude of the total temporal aliasing error per SH coefficient. The dual cartwheel mission has fairly low errors for all near-zonal coefficients up to SH order 15.

A map of the total temporal aliasing error over the Amazon river basin is presented in the lower-middle-left panel of Figure 8.32 (page 218). The error shows a pattern of short north-south stripes, with the largest-magnitude features located north of the equator.

A table with the error budget of the dual cartwheel missions for different DAPs is shown in Table 8.15 (page 219). It demonstrates that temporal aliasing errors dominate at all the considered timespans. In all the cases, AOD errors are the largest contributor to the error budget, followed by ocean tide model error and the dynamic mass transport signal. With increasing DAP, the total error decreases. The lowest total error is obtained for the 24-day period (33 mm ewh).

Concerning regularized solutions, a map of the total temporal aliasing error over the Amazon river basin is presented in the lower-middle-right panel of Figure 8.32 (page 218). The map shows a significant reduction of the error features compared

to the unregularized solution, most of the large-magnitude ones being removed almost entirely.

The error budget of regularized solutions is shown in Table 8.19 (page 221). The level of errors is significantly reduced compared to the unregularized solutions. The total error tends to decrease with increasing DAP. The lowest total error is obtained again for the 22-day period (14 mm ewh), while the highest error for the shortest, 8-day period (17 mm ewh). The total error differences between different timespans are, however, much smaller, as compared to the unregularized solutions. For instance, the performance of the 16-day mission is very close to that of the 22-day mission.

8.4.4. Dual Sigma

The dual sigma mission combines a cartwheel and a pendulum formation in different orbital planes. The cartwheel formation provides observations in the radial and along-track directions, oscillating between the two, while the pendulum formation provides observations oriented in the cross-track direction. An overview of the errors for the 255/16 dual sigma mission is shown in the bottom-left panel of Figure 8.29 (page 215). Once again, the largest error source is temporal aliasing error, which is dominant for all SH degrees and becomes larger than the mass transport signal at about SH degree 100. The breakdown of temporal aliasing errors is shown in the bottom-right panel of Figure 8.30 (page 216). It shows that temporal aliasing errors are explained by a combination of ocean tide model errors and AOD model errors up to SH degree 60. From SH degree 60 onwards, AOD model errors become the dominant source.

The magnitude of the total temporal aliasing error per SH coefficient is shown in the bottom-right panel of in Figure 8.31 (page 217). The dual sigma mission has a relatively even error distribution compared to other mission concepts. A low-error stripe can be seen for the near-zonal coefficients, nonetheless the errors are fairly low for other SH coefficients as well.

In the bottom-left panel of Figure 8.32 (page 218), the total temporal aliasing errors over the Amazon river basin are shown in the spatial domain. The error patterns shows short north-south stripes with the largest magnitude features located to the north of the equator.

Table 8.16 (page 219), shows the error budget for a selection of DAPs for the dual sigma mission. The lowest errors are obtained for the 22-day period (19.6 mm ewh), which is slightly lower than for the 24-day one (20.2 mm ewh). The major contributor for all considered intervals is the AOD model error.

Regarding regularized solutions, total temporal aliasing errors are shown over the Amazon river basin in the bottom-right panel of Figure 8.32 (page 218). In comparison with the unregularized solutions (bottom-left panel of the same figure), there is, as expected, an overall reduction in the magnitude of the error features, especially in the regions where no significant mass transport signal is expected, such as the ocean. Still, some large-magnitude features remain visible in the regularized solution.

Table 8.20 (page 221) shows the error budget for the dual sigma mission in

terms of regularized solutions. The results are consistent with the ones obtained for the unregularized solutions: the 22-day period exhibits the lowest total error (12.0 mm ewh), which is slightly below the 24-day period (12.5 mm ewh). The 12-day period, despite being almost half as short as the 22-day period, shows a total error of 14.0 mm ewh, which is only about 15% larger than in the 22-day case. For the 22-day period, the largest single contributor to the error budget is the regularization bias (6.7 mm ewh), which is nonetheless below the aggregate total temporal aliasing error (10 mm ewh).

8.4.5. Discussion

In the previous section, four mission concepts consisting of two satellite formations were presented. The dual along-track and dual cartwheel missions augmented the corresponding single formation missions by adding a second formation of the same type as the first one. Regarding the dual-along track mission, the second formation was tilted by 70° in order to improve the observability of the east-west variations of the gravity field. Similarly, the dual cartwheel mission was designed so that the inter-satellite baselines of both cartwheel formations are (approximately) perpendicular over all latitudes.

The dual along-track and dual cartwheel formations were successful at improving the performance of the corresponding single-formation mission. Curiously, the dual along-track formation yielded the lowest level of errors in terms of unregularized solutions for the relatively short 10-day DAP. Because the single formation along-track mission suffered from such high degree of spatial instability errors, the total errors of the dual along-track mission were found to be about one order of magnitude smaller (cf. Tables 8.1 in page 218 and 8.13 in page 215 for the along-track and dual along-track missions, respectively). Temporal aliasing errors were the largest error source and of those, the AOD error was the largest component. In terms of magnitude of SH coefficients, temporal aliasing errors were found to be significantly more isotropic for the dual along-track mission. Nonetheless, despite the large reduction of errors, the total temporal aliasing error plotted on a map still showed a north-south striation pattern (cf. top-left panel of Figure 8.32 in page 218).

Similar remarks can be made about the improvements obtained by the dual cartwheel mission compared to the single formation cartwheel. The sensitivity of the dual formation configuration is more isotropic and as a consequence spatial instability errors are significantly smaller at the shorter DAPs for the dual cartwheel mission (101 mm ewh, cf. Table 8.15 in page 219) w.r.t. the single formation cartwheel (447 mm ewh, cf. Table 8.3 in page 189). Further evidence of this can be concluded from comparing the total temporal aliasing error in terms of magnitude of SH coefficients. These errors, shown in the bottom panel of Figure 8.17 (page 186 for single formation cartwheel mission, are relatively high in the tesseral coefficients above SH degree 40. On the other hand, the dual cartwheel formation shown in the bottom-left panel of Figure 8.31 (page 217), shows a significant reduction of errors in the tesseral and near-sectorial SH coefficients

One important aspect when comparing the dual along-track and dual cartwheel with the along-track and cartwheel missions, respectively, is that the dual formation

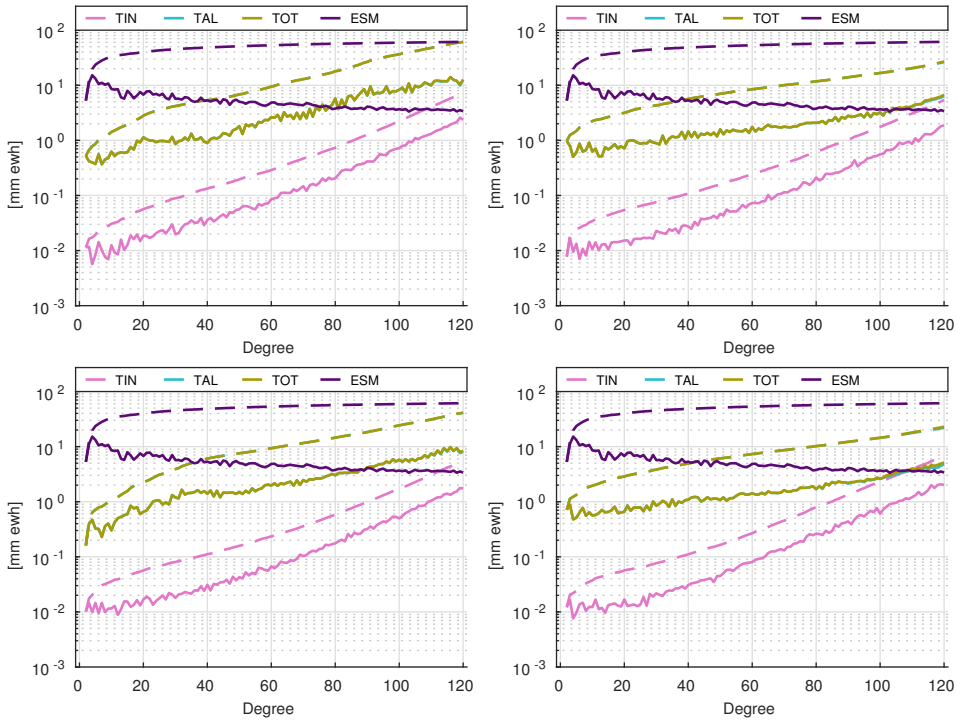

Figure 8.29: General overview of errors for the 255/16 dual along-track (top-left), 255/16 dual gamma (top-right), 255/16 dual cartwheel (bottom-left) and 255/16 dual sigma (bottom-right) missions in terms of DV and CDV. The explanation of the used acronyms can be found in Table 4.4 in page 75.

Table 8.13: Error budget of the dual along-track missions (70° inclination of the inclined orbit) over a selection of DAPs in terms of global RMS [mm ewh] of solutions solved up to SH degree 120. The explanation of the used acronyms can be found in Table 4.4 in page 75.

2AT	127/8	159/10	191/12	255/16	319/20	383/24
RNG	9.94	7.42	14.42	7.05	5.24	5.37
ACC	2.47	1.84	5.74	1.93	1.49	1.73
TIN	10.26	7.62	15.32	7.37	5.50	5.67
AOD	46.23	36.37	91.13	37.88	29.48	32.37
OTE	37.99	16.96	91.20	42.04	29.78	31.93
TMP	16.52	12.76	58.14	27.91	32.50	35.68
TAL	61.74	42.50	132.92	60.87	53.38	61.48
SPT	3.96	3.85	3.51	2.63	2.69	2.65
TOT	62.71	43.24	134.25	61.31	53.85	61.85
ESM	62.78	62.47	62.14	61.36	60.53	59.70

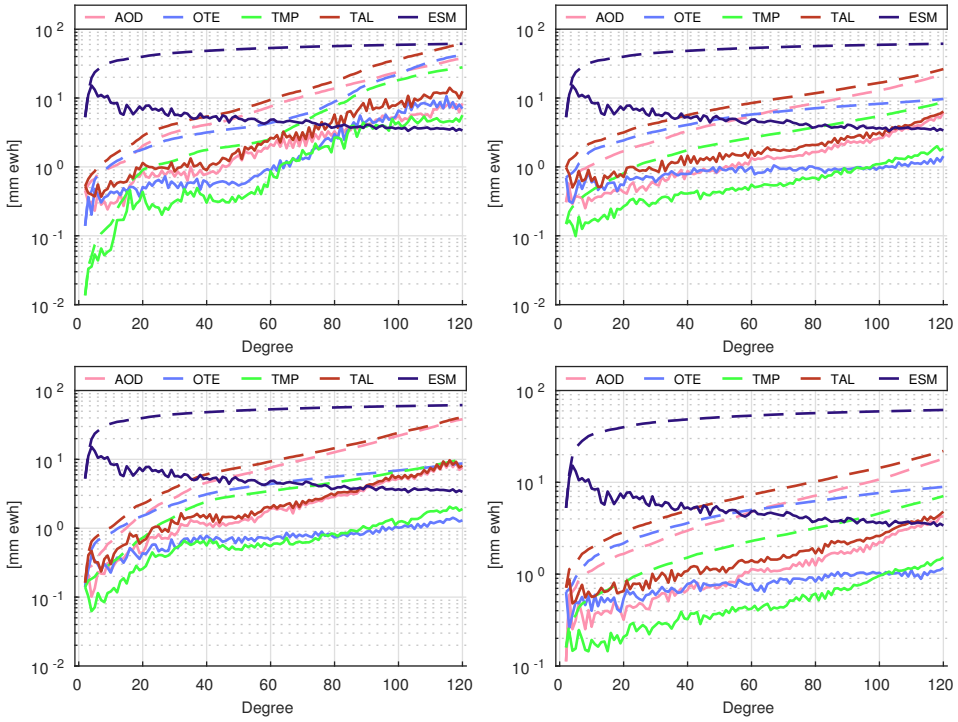

Figure 8.30: DV and CDV of temporal aliasing errors for the for the 255/16 dual along-track (top-left), 255/16 dual gamma (top-right), 255/16 dual cartwheel (bottom-left) and 255/16 dual sigma (bottom-right) missions. The explanation of the used acronyms can be found in Table 4.4 in page 75.

8

Table 8.14: Error budget of the dual gamma mission over a selection of DAPs in terms of global RMS [mm ewh] solved up to SH degree 120. The explanation of the used acronyms can be found in Table 4.4 in page 75.

2Γ	127/8	191/12	255/16	351/22	383/24
RNG	10.57	6.88	5.29	3.18	3.17
ACC	2.55	2.16	1.06	0.64	0.63
TIN	10.85	7.14	5.40	3.24	3.23
AOD	64.89	41.30	22.41	16.99	17.43
OTE	46.83	19.56	9.68	9.94	9.45
TMP	21.23	14.02	8.64	8.92	10.35
TAL	83.13	46.71	26.31	21.57	22.36
SPT	3.03	5.23	1.81	1.35	1.34
TOT	84.11	47.46	26.93	21.83	22.68
ESM	62.78	62.14	61.36	60.12	59.70

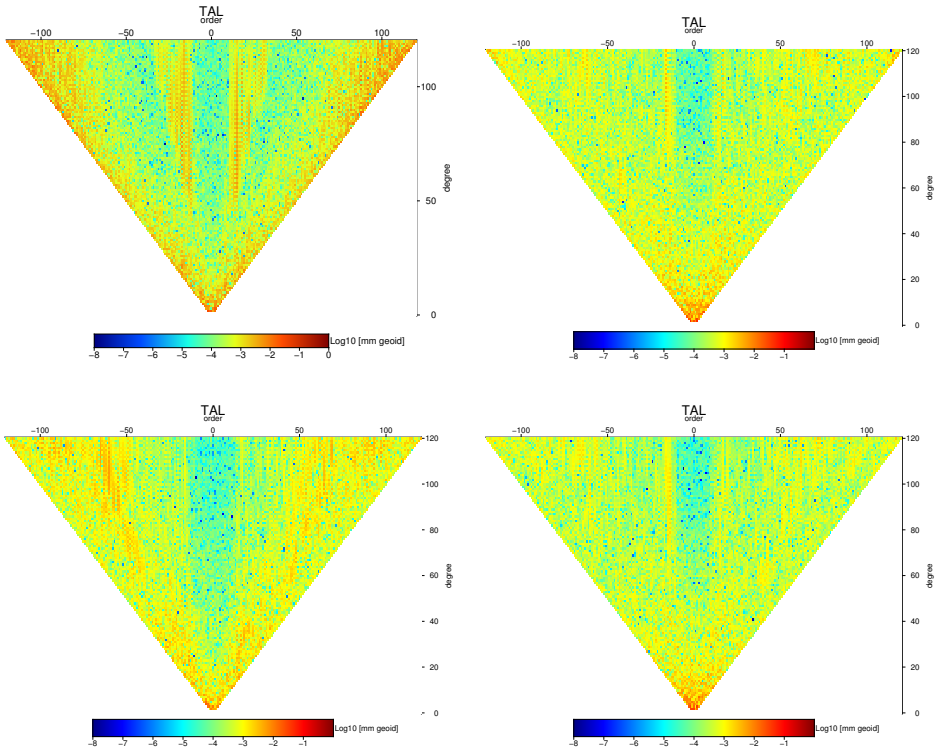

Figure 8.31: Magnitude of the total temporal aliasing error (TAL) per SH coefficient for the 255/16 dual along-track (top-left), 255/16 dual gamma (top-right), 255/16 dual cartwheel (bottom-left) and 255/16 dual sigma (bottom-right) missions.

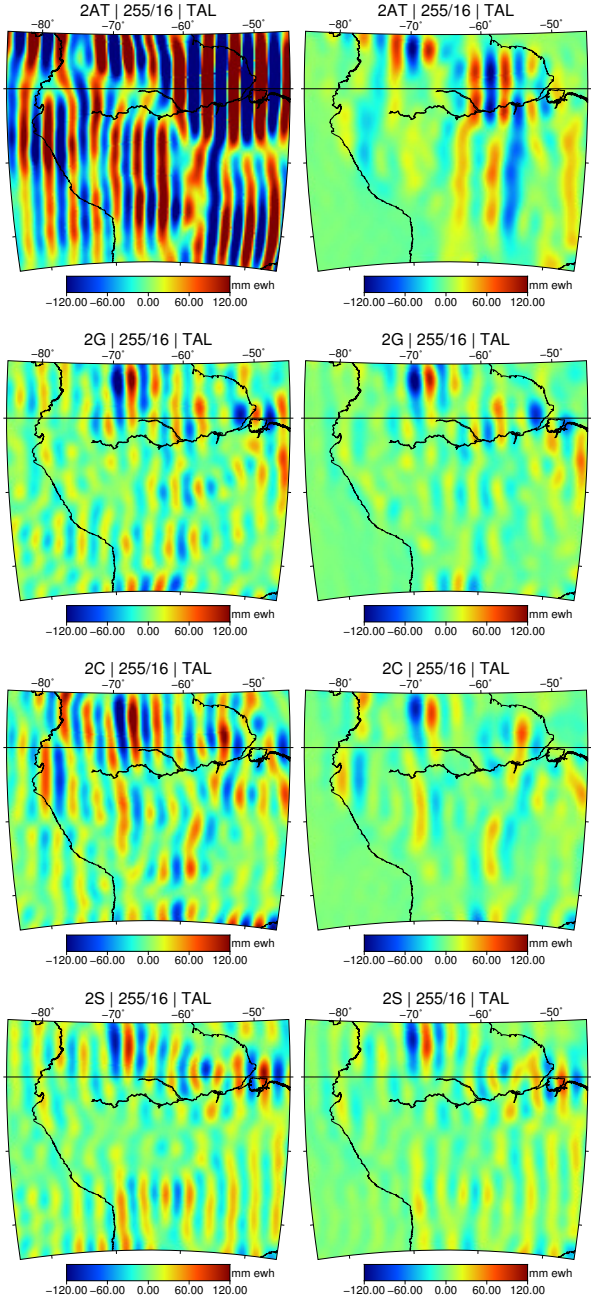

Figure 8.32: Map of the temporal aliasing error (TAL) for the 255/16 dual along-track (top), 255/16 dual gamma (upper-middle), 255/16 dual cartwheel (lower-middle) and 255/16 dual sigma (bottom) missions over the Amazon river basin in terms of unregularized (left) and regularized (right) solutions up to $l_{max} = 120$.

Table 8.15: Error budget of the dual cartwheel mission over a selection of DAPs in terms of global RMS [mm ewh] of *unregularized* solutions solved up to SH degree 120. The explanation of the used acronyms can be found in Table 4.4 in page 75.

2C	127/8	191/12	255/16	351/22	383/24
RNG	9.43	6.51	5.27	3.21	3.14
ACC	2.84	2.03	1.42	0.90	0.90
TIN	9.83	6.81	5.45	3.34	3.27
AOD	67.36	46.25	38.25	28.20	27.33
OTE	63.38	12.02	8.74	11.56	12.56
TMP	26.20	13.85	9.94	10.78	12.13
TAL	100.54	49.81	40.81	32.96	32.86
SPT	2.06	3.11	1.83	1.52	1.52
TOT	101.10	50.56	41.23	33.13	33.05
ESM	62.78	62.14	61.36	60.12	59.70

Table 8.16: Error budget of the dual sigma mission over a selection of DAPs in terms of global RMS [mm ewh] of *unregularized* solutions solved up to SH degree 120. The explanation of the used acronyms can be found in Table 4.4 in page 75.

2σ	127/8	191/12	255/16	351/22	383/24
RNG	12.36	8.21	6.62	4.12	4.11
ACC	2.53	1.70	1.18	0.74	0.72
TIN	12.59	8.38	6.73	4.17	4.17
AOD	40.87	26.54	18.18	14.91	15.39
OTE	34.41	12.11	8.94	8.82	8.44
TMP	14.66	10.67	7.08	7.43	8.64
TAL	57.39	30.26	21.92	19.15	19.66
SPT	2.79	5.36	1.65	1.35	1.33
TOT	58.73	31.89	22.95	19.56	20.20
ESM	62.78	62.14	61.36	60.12	59.70

Table 8.17: Error budget of the dual along-track missions (70° inclination of the inclined orbit) over a selection of DAPs in terms of global RMS of *regularized* solutions [mm ewh] solved up to SH degree 120. The explanation of the used acronyms can be found in Table 4.4 in page 75.

2AT	127/8	159/10	191/12	255/16	319/20	383/24
RNG	1.22	0.99	1.16	0.87	0.80	0.68
ACC	0.31	0.25	0.34	0.22	0.21	0.20
TIN	1.27	1.00	1.20	0.90	0.83	0.71
AOD	8.18	7.08	7.23	5.70	5.90	4.96
OTE	5.59	5.60	4.99	4.27	4.37	4.06
TMP	3.82	4.13	5.71	5.14	5.13	6.39
TAL	10.48	9.85	10.16	8.68	8.82	9.10
REG	11.34	11.38	13.17	11.58	10.02	11.05
SPT	1.10	0.76	0.67	0.31	0.45	0.29
TOT	15.63	14.99	16.67	14.52	13.46	14.42
ESM	62.78	62.47	62.14	61.36	60.53	59.70

Table 8.18: Error budget of the dual gamma mission over a selection of DAPs in terms of global RMS of *regularized* solutions [mm ewh] solved up to SH degree 120. The explanation of the used acronyms can be found in Table 4.4 in page 75.

2Γ	127/8	191/12	255/16	351/22	383/24
RNG	0.87	0.94	0.99	0.82	0.76
ACC	0.24	0.26	0.23	0.20	0.19
TIN	0.89	0.98	1.02	0.85	0.78
AOD	6.67	6.74	7.13	6.53	6.66
OTE	7.53	6.46	6.46	6.61	5.70
TMP	4.04	4.31	4.60	5.93	7.28
TAL	10.77	10.18	10.84	11.10	11.60
REG	14.30	10.35	9.02	6.98	7.19
SPT	0.83	2.56	0.55	0.29	0.31
TOT	17.91	14.54	14.12	13.17	13.70
ESM	62.78	62.14	61.36	60.12	59.70

Table 8.19: Error budget of the dual cartwheel mission over a selection of DAPs in terms of global RMS of *regularized* solutions [mm ewh] solved up to SH degree 120. The explanation of the used acronyms can be found in Table 4.4 in page 75.

2C	127/8	191/12	255/16	351/22	383/24
RNG	1.12	0.93	0.84	0.66	0.61
ACC	0.31	0.27	0.23	0.18	0.18
TIN	1.17	0.96	0.87	0.68	0.64
AOD	7.32	6.89	6.16	5.90	5.67
OTE	4.45	4.53	4.07	4.14	4.17
TMP	4.18	4.35	4.71	6.18	6.81
TAL	9.74	9.56	8.82	9.57	9.65
REG	13.30	11.64	10.99	9.50	9.44
SPT	0.35	0.95	0.39	0.35	0.36
TOT	16.57	15.20	14.21	13.50	13.68
ESM	62.78	62.14	61.36	60.12	59.70

Table 8.20: Error budget of the dual sigma mission over a selection of DAPs in terms of global RMS of *regularized* solutions [mm ewh] solved up to SH degree 120. The explanation of the used acronyms can be found in Table 4.4 in page 75.

2σ	127/8	191/12	255/16	351/22	383/24
RNG	1.23	1.42	1.35	1.05	0.97
ACC	0.30	0.33	0.29	0.23	0.23
TIN	1.25	1.45	1.40	1.07	0.99
AOD	6.56	7.16	6.84	5.98	6.27
OTE	7.04	6.04	5.95	5.71	5.34
TMP	3.64	4.10	4.16	5.19	6.36
TAL	10.38	10.45	10.30	9.99	10.38
REG	13.24	9.12	8.22	6.72	6.69
SPT	0.83	2.51	0.56	0.38	0.37
TOT	16.98	14.01	13.17	12.04	12.51
ESM	62.78	62.14	61.36	60.12	59.70

missions collect twice as many data as the single formation ones. Therefore, having remarked on the improvements brought in by the second formation, it is not possible from this comparison alone, to independently attribute the observed improvements to the different orientation of the inter-satellite baselines in each formation and to the additional data collected by the second formation.

Despite the improvements obtained by the dual along-track and dual cartwheel missions, their performance did not surpass that of the single-formation hybrid missions. For the longest DAP of 24-days, the dual along track (61 mm ewh, cf. 8.13 in page 215) and dual cartwheel (33 mm ewh, cf. 8.15 in page 219), were still significantly worse than the delta (27 mm ewh, cf. Table 8.9 in page 205), gamma (22 mm ewh, cf. Table 8.7 in page 200) and sigma missions (21 mm ewh, cf. Table 8.8 in page 205). This shows that the combination of orthogonal observables is more desirable than repeating the same observable over interleaving groundtracks. It is also interesting to notice that the delta mission, effectively a 3-satellite cartwheel formations, was found to be significantly better than the dual cartwheel mission with two independent cartwheel formations. The additional satellite in a single cartwheel formation and the consequent larger amount of data gathered from the three inter-satellite baselines of the delta mission proves to be more valuable than an additional pair on interleaved groundtracks.

It was shown in Section 7.5.3 that two perpendicular orbital planes are effective at reducing temporal aliasing errors. The comparison of the dual along-track and dual cartwheel missions and the corresponding single formation may be consistent with this finding, with the caveat that the dual formation missions collect twice the data of the single formation ones. On the other hand, the dual gamma and dual sigma (which collect the same amount of data as the single formation gamma and sigma) did not significantly reduce the temporal aliasing errors of the corresponding single formations mission. I propose that this is explained by the fact that when orthogonally oriented observations are considered, as in the case of the gamma and sigma concepts, they collect mutually complementary information. Therefore it makes little difference whether these observation are placed in a single or in a dual-formation configuration. Splitting orthogonal observables in two different formations does not seem to be effective at significantly improving the performance of the single-formation configuration.

Further evidence of this can be seen in the differences between the solutions of the sigma and dual sigma missions. Both sigma and dual sigma missions yielded the lowest total error at the 22-day DAP in terms of unregularized solutions. The errors budgets of these two simulations are presented in Tables 8.8 and 8.16 for the sigma and dual sigma missions, respectively. In terms of global RMS, the dual sigma mission reduced the total error by about 1.4 mm ewh. In turn, this reduction results from a small decrease of 0.7 mm ewh in terms of AOD errors and, more significantly, by a 1.5 mm ewh reduction in terms of OTE. The difference between the total error gravity field solutions of the 22-day sigma and dual sigma missions should provide an illustration of the impact of splitting the sigma combination in two different formations. These differences are shown in Figure 8.33. Major features are gathered around the coastal areas where tidal model errors are the largest.

However, the global RMS of the differences between the sigma and dual sigma missions is about 12 mm ewh, a much larger value than the improvements obtained by the dual sigma mission compared to sigma. This means that the differences between the two missions do not represent improvements brought by the dual sigma mission, they rather show the combined errors of the two missions.

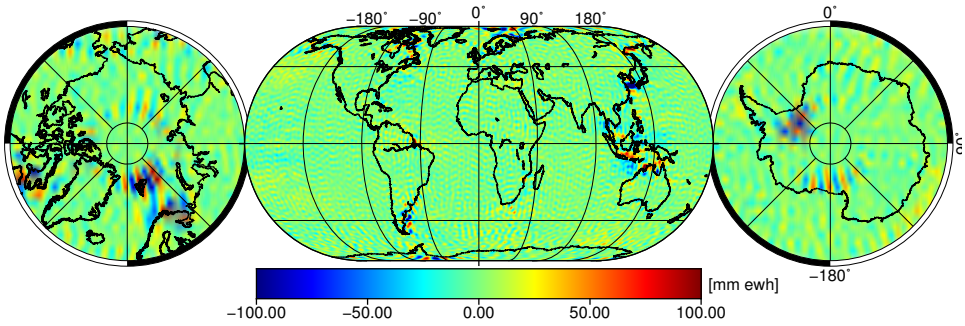

Figure 8.33: Difference between the total error of the dual sigma and sigma missions in terms of *unregularized* solutions for the 22-DAP.

8.5. Comparison

In this Section, the best performing DAPs are selected to compare the previously presented concepts. First, I will show a comparison of the elementary satellite formations. Then, a comparison of three-satellite hybrid single-formation missions is shown. Finally, a comparison of four-satellite mission concepts arranged in two formations is discussed.

GRACE/GFO solutions are used by hydrologists, glaciologists and geophysicists in different regions. Therefore, it is reasonable to compare the performance of different missions over 10 selected geographical regions where mass transport signals of different origins occur. I made this choice such that both large and small regions are considered at various (polar, mid- and equatorial) latitudes. Another consideration taken was to include regions that are predominantly stretched in both the east-west and north-south directions. The diversity of the geographical characteristics in the set of chosen regions is important, as it allows me to pinpoint the potential weaknesses in some of the considered concepts.

In the context of hydrology, I have selected four different regions. I consider the Amazon and the Nile river basins, since these two rivers are the two longest rivers on our planet. The Nile river basin is of further interest due to its predominantly north-south orientation. I analyze also the Orinoco river basin in South America. Being a neighbor of the Amazon river basin, it is not only smaller, but also has a out-of-phase hydrological cycle. Finally, the Ob river in Siberia has also been selected due to its higher latitude and a peculiar seasonal cycle driven by the accumulation

and melting of snow.

In the context of glaciology, four regions have also been chosen. Antarctica and Greenland have been selected as large ice-covered areas at high latitudes. Furthermore, I zoom in on the Amundsen Sea Embayment in West Antarctica due to its strong ice mass loss signal. Finally, the Alps have been selected as a small mid-latitude region of interest.

Regarding solid earth applications, the region of Fennoscandia has been selected due to the presence of strong glacial isostatic adjustment (GIA) signal there. The Sumatra region has also been chosen due to the massive tectonic displacement caused by the 2004 Sumatra-Andaman earthquake (Park et al., 2005), the largest in recorded history.

In the following sections, regional RMS errors of mass anomalies for different mission concepts will be presented in several tables. In these tables a simple scoring system will be used to rank the considered missions in order to quantify the performance of each mission concept relative to the other ones. When comparing N missions, for each region of interest, the best performing concept is given a maximum score of $N-1$ points; the worst mission the minimum score of 0 points and the remaining according to their rank. Adding up all the regional scores for a given mission gives its total score. In this way, I make an attempt at providing an simple measure of the overall performance of different mission concepts.

The best performing DAP will be selected for each mission. Notice that for a given mission, the best DAP may be different for regularized and unregularized solutions.

8.5.1. Single-formation missions

In Table 8.21, the regional RMS of the total error for the best three single-formation missions are compared in terms of unregularized solutions. All three considered mission concepts span similar DAPs, only the cartwheel's DAP being slightly longer with 24 days instead of 22. The table shows that the cartwheel mission is the best performing mission. It yields the lowest errors in the majority of the considered regions. Only over Fennoscandia and Greenland, the pendulum mission outperforms the cartwheel one.

Two examples of large differences between the mission performances are the Amazon and Greenland regions. A comparison of the total error over these regions is shown in Figure 8.34 and 8.35, respectively. Figure 8.34 clearly shows that the along-track mission's solution is severely affected by north-south striations, while the pendulum's and cartwheel's ones are much cleaner. A mild horizontal striation pattern is seen for the pendulum mission. The cartwheel mission is clearly the best over the Amazon river basin. However, this is no longer the case over Greenland, as can be seen in Figure 8.35. Here, the along-track mission again shows the largest errors, but now the cartwheel mission also suffers from significant north-south striations over the North Atlantic. The pendulum missions demonstrates relatively mild and homogeneous horizontal striation pattern over the whole region, so that its performance is the best among the three considered mission concepts. This could be explained by a larger east-west variability of the temporal aliasing error sources in

Table 8.21: Comparison of the total error in terms of regional RMS of mass anomalies for the best single-formation missions over the regions of interest in terms of *unregularized* solutions [mm ewh] solved up to SH degree 120.

Region	Signal	P|351/22	C|383/24	AT|351/22
Global	60.10	116.00	**48.42**	355.89
Amazon	150.97	101.52	**41.94**	556.09
Nile	176.69	88.58	**49.05**	209.72
Orinoco	96.74	136.35	**42.09**	921.00
Ob	70.01	108.07	**56.03**	182.64
Antarctica	40.48	105.04	**83.38**	334.46
Greenland	166.20	**70.97**	79.57	246.74
Amundsen S.E.	112.61	109.22	**58.36**	94.58
Alps	39.10	123.13	**38.16**	332.49
Sumatra	185.62	113.72	**24.74**	520.76
Fennoscandia	44.52	**78.86**	107.41	348.06
Score		12/22	**20/22**	1/22

this region, which are better captured by the pendulum mission.

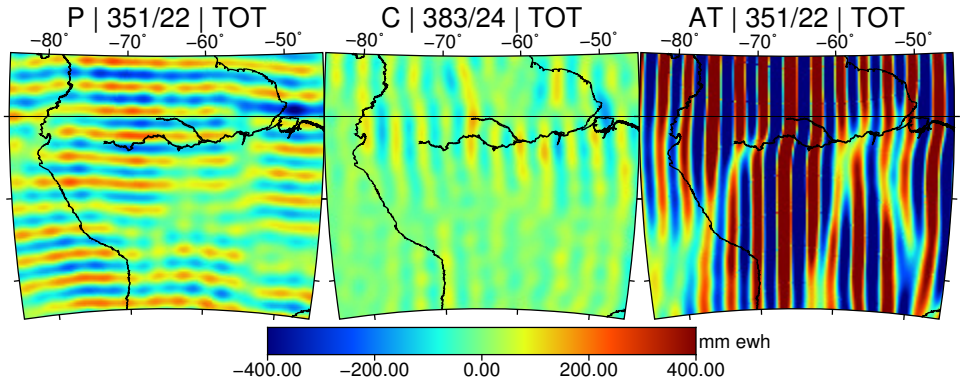

Figure 8.34: Total error as regional RMS of mass anomalies over the Amazon river basin for the pendulum 351/22 (left), along-track 383/24 (middle) and cartwheel 383/24 (right) missions, in terms of *unregularized* solutions [mm ewh].

Overall, taking into account all the considered regions, the cartwheel mission has the best score with 20/22 points, the pendulum mission comes in second with 12/22, while the along-track is clearly the worst with 1/22 points (Table 8.21).

In terms of regularized solutions, the corresponding results are presented in Table 8.22. As expected, the differences between the concepts are much smaller in this case. Overall, the pendulum mission is now the one with highest score 17/22. The cartwheel is now second with 9/22 points, while the along-track, still the worst, but now with 7/22 points, even outperforming the other two concepts over Antarctica and the Amundsen Sea.

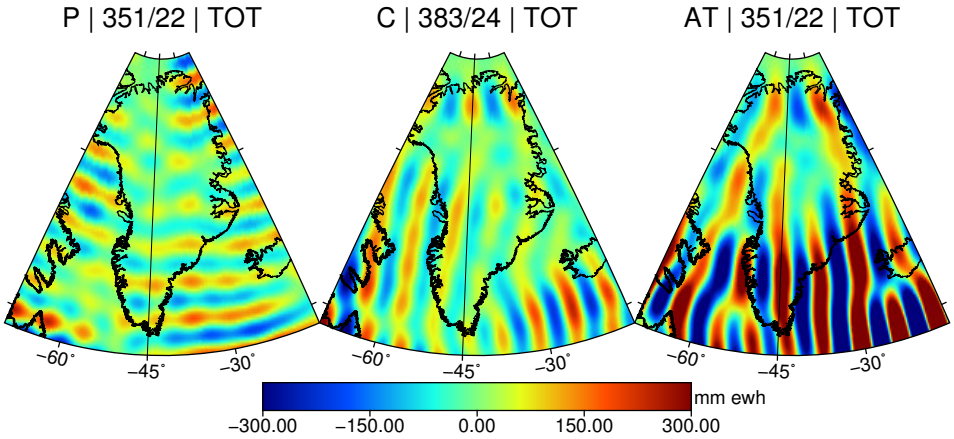

Figure 8.35: Total error as regional RMS of mass anomalies over Greenland for the pendulum 351/22 (left), along-track 383/24 (middle) and cartwheel 383/24 (right) missions, in terms of *unregularized* solutions [mm ewh].

Table 8.22: Comparison of total error in terms of regional RMS of mass anomalies for the best single formation missions over different regions of interest in terms of *regularized* solutions [mm ewh] solved up to SH degree 120.

Region	Signal	P|351/22	C|255/16	AT|255/16
Global	60.10	**19.37**	19.87	22.57
Amazon	150.97	39.38	**24.50**	45.56
Nile	176.69	**20.71**	24.33	41.46
Orinoco	96.74	28.26	**25.62**	53.95
Ob	70.01	**26.46**	43.50	32.30
Antarctica	40.48	17.90	19.16	**15.44**
Greenland	166.20	**35.94**	45.58	63.37
Amundsen S.E.	112.61	38.52	40.59	**29.20**
Alps	39.10	**15.68**	26.15	18.84
Sumatra	185.62	33.50	**20.82**	39.55
Fennoscandia	44.52	**22.13**	35.66	26.81
Score		**17/22**	9/22	7/22

It is interesting to revisit the Amazon and Greenland regions to compare the three missions again, but now in terms of regularized solutions. Over the Amazon river basin, shown in Figure 8.36, the regularization procedure has lead to a significant decrease in the errors for all the missions. Their levels appears to be similar for the along-track and pendulum formations; the along-track has a predominantly north-south error pattern, while the pendulum formation predominantly east-west. The largest errors in the pendulum case coincide with the Amazon river stream. The error pattern of the pendulum mission is hardly distinguishable from the mass transport signal in this region. Therefore, the regularization procedure dampens the input signal and introduces the observed error in the form of regularization bias. In comparison with the other two missions, the cartwheel shows the lowest total error and a fairly even error distribution over the whole region.

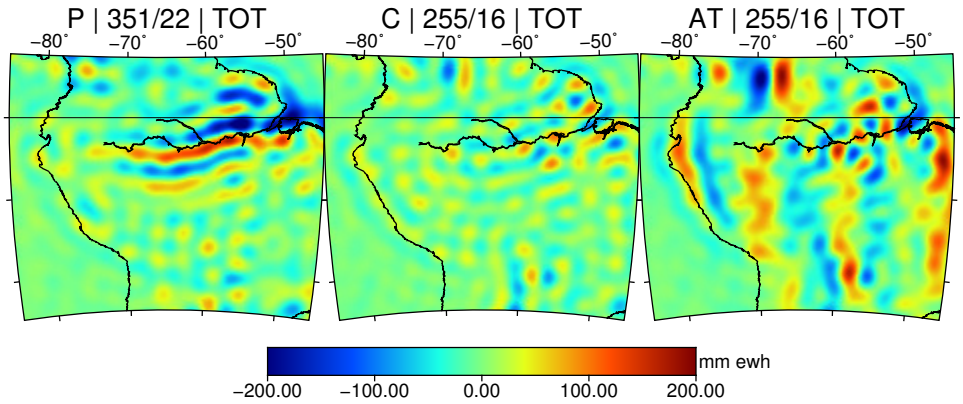

Figure 8.36: Comparison of the total error (TOT) over the Amazon river basin for the along-track 255/16, pendulum 351/22 and cartwheel 255/16 missions in terms of *regularized* solutions [mm ewh].

Regarding Greenland (Figure 8.37), the cartwheel and along-track missions yield a similar error pattern. Both missions show north-south striations along the East coast of Greenland. The along-track mission has comparatively large magnitude striations and is noticeably the worst in this region. The similarity between the two mission errors can be explained by the fact that as the cartwheel formation orbits, the inter-satellite baseline shifts between the radial and along-track directions. The baseline of the considered cartwheel mission, with a $\alpha = 30^\circ$, is in the vicinity of the along-track direction at high-latitudes (cf. Figure 8.12 in page 182). Nonetheless, the presence of radial component in the cartwheel mission observations is seen to significantly reduce the total error over this region. The pendulum mission shows a slightly different error pattern, with multiple relatively large features in the southern part of Greenland.

8.5.2. Hybrid-formation missions

Several single-hybrid-formation missions have been considered in the previous sections. In terms of unregularized solutions, the best performing scenarios were found

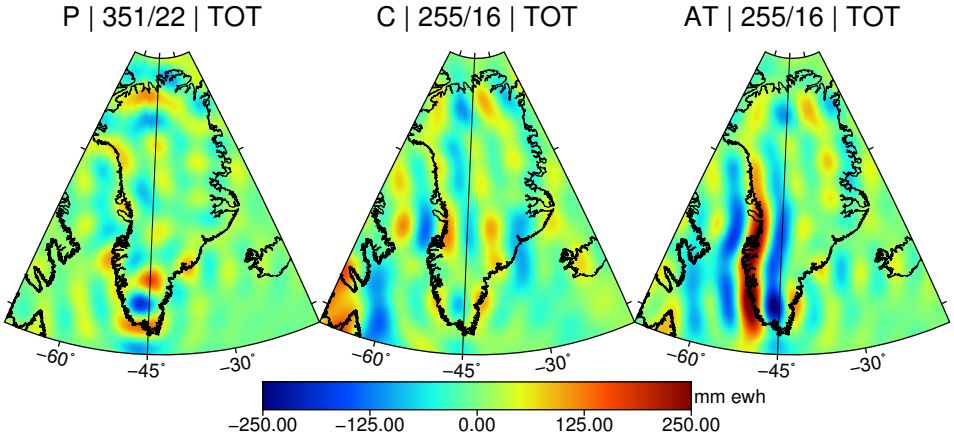

Figure 8.37: Comparison of the total error over Greenland for the along-track 255/16, pendulum 351/22 and cartwheel 255/16 missions in terms of *regularized* solutions [mm ewh].

to be the 22-day delta, the 22-day sigma and the 24-day gamma missions. The regional RMS values of the total error for these missions are shown in Table 8.23. For a comparison, I have included also the best 2-satellite single-formation missions: the 24-day cartwheel and the 16-day pendulum for unregularized and regularized solutions, respectively. This helps in establishing the added value of a 3-satellite hybrid-formation over a two-satellite one.

The results show that the sigma and gamma missions are the top performing ones, with the sigma mission being the best. The sigma mission has the lowest total error in the majority of the considered regions and gets a score of 30/33 points. The gamma mission follows with 21/33 points, while the delta and cartwheel missions fall considerably behind with 14/33 and 1/33 points, respectively. Expectedly, the regional RMS values for the three hybrid formations are significantly lower than that for the cartwheel mission. The results also show that the three considered hybrid formations are all able to reduce the total error by a factor of at least 2 in terms of global RMS of unregularized solutions, as compared to 2-satellite formations.

There are particularly large differences between the considered mission concepts over the Nile river basin. The total errors over this region are shown in the form of maps in Figure 8.38. It can be seen that the sigma mission yields the lowest level of errors, slightly lower than delta, while the gamma and cartwheel missions show comparatively high errors.

Table 8.24 presents the results of a similar comparison but now in terms of regularized solutions. The relative performance of the missions is consistent with what was found from the unregularized solutions. The sigma mission shows the best performance with 26/33 points, followed by the gamma mission with 21/33 points. The delta and pendulum missions lag behind with 18/33 and 1/33 points, respectively. It should be noticed, however, that the differences in the regional RMS values between the considered missions are now much smaller. Furthermore, while

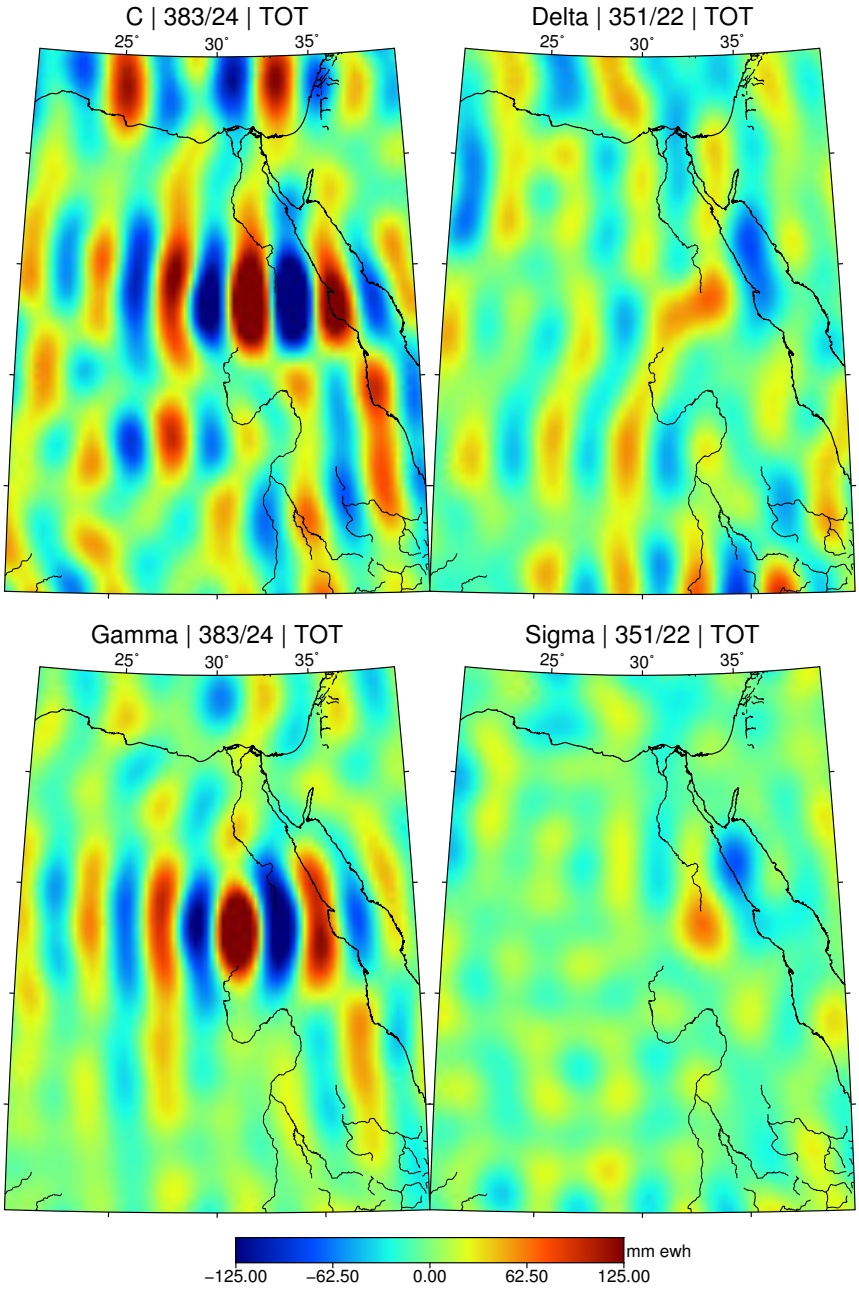

Figure 8.38: Total error over the Nile river basin for the cartwheel 383/24, delta 351/22, gamma 383/24 and sigma 351/22 missions in terms of *unregularized* solutions [mm ewh].

Table 8.23: Total error in terms of regional RMS of mass anomalies for the three hybrid formation missions over different regions of interest in terms of *unregularized* solutions [mm ewh]. The cartwheel (the best single-formation mission) is also included in the comparison for reference.

Region	Signal	C|383/24	Γ|383-24	Δ|351/22	σ|351/22
Global	59.68	48.42	22.11	26.03	**20.94**
Amazon	150.06	41.94	25.08	26.86	**19.88**
Nile	174.62	49.05	35.48	24.86	**15.17**
Orinoco	94.41	42.09	19.07	29.51	**18.52**
Ob	70.59	56.03	23.83	27.24	**21.98**
Antarctica	40.48	83.38	**20.78**	22.73	21.23
Greenland	166.54	79.57	30.60	28.92	**28.65**
Amundsen S.E.	112.31	58.36	19.08	**17.20**	19.01
Alps	38.38	38.16	20.40	30.44	**18.25**
Sumatra	185.86	24.74	**18.98**	27.30	23.92
Fennoscandia	42.86	107.41	32.07	42.95	**31.59**
Score		1/33	21/33	14/33	**30/33**

the total error was reduced threefold by the hybrid formation missions compared to the cartwheel, that is no longer the case when considering regularized solutions. The sigma mission has now a total error of 13 mm ewh, which about 32% better than the 19 mm ewh error for the pendulum mission.

The largest difference between the hybrid formations in terms of the regional RMS of the total error is again observed over the Nile river basin. The maps of total error over this region are presented in Figure 8.39. Here, the gamma and pendulum missions show relatively large errors, while the delta and sigma missions result is much less prominent error features.

Regarding the analyzed hybrid-formation missions, the 22-day sigma mission is the best option in terms of both regularized and unregularized solutions. The gamma mission is a close second. The best overall performance of the sigma and gamma missions may be attributed to the synergy in the inter-satellite ranging directions exploited in the formations. Both the gamma and sigma missions collect cross-track information from the pendulum inter-satellite link.

In Section 7.5.1, it was shown that the xx+yy combination was equally effective as the zz gradient alone at minimizing the level of temporal aliasing errors for $l_{\max} = 40$. Based on this finding, one would predict the gamma, sigma and delta configurations to yield a similar magnitude of temporal aliasing errors. However that is not the case. While the delta mission is able to fully resolve three gravity gradient directions (zz, xx and xz), it seems that this is less desirable than the yy+xx combination of the gamma mission or the alternating xx/zz+yy combination of the sigma mission. One possible explanation for this discrepancy could be that the zz gradient becomes less effective than xx+yy combination for SH degrees above 40 at mitigating temporal aliasing errors. Figure 8.40 shows DV plot of total temporal aliasing errors for these three configurations. Temporal aliasing errors of the delta configuration are slightly higher than gamma and sigma between SH degrees 40

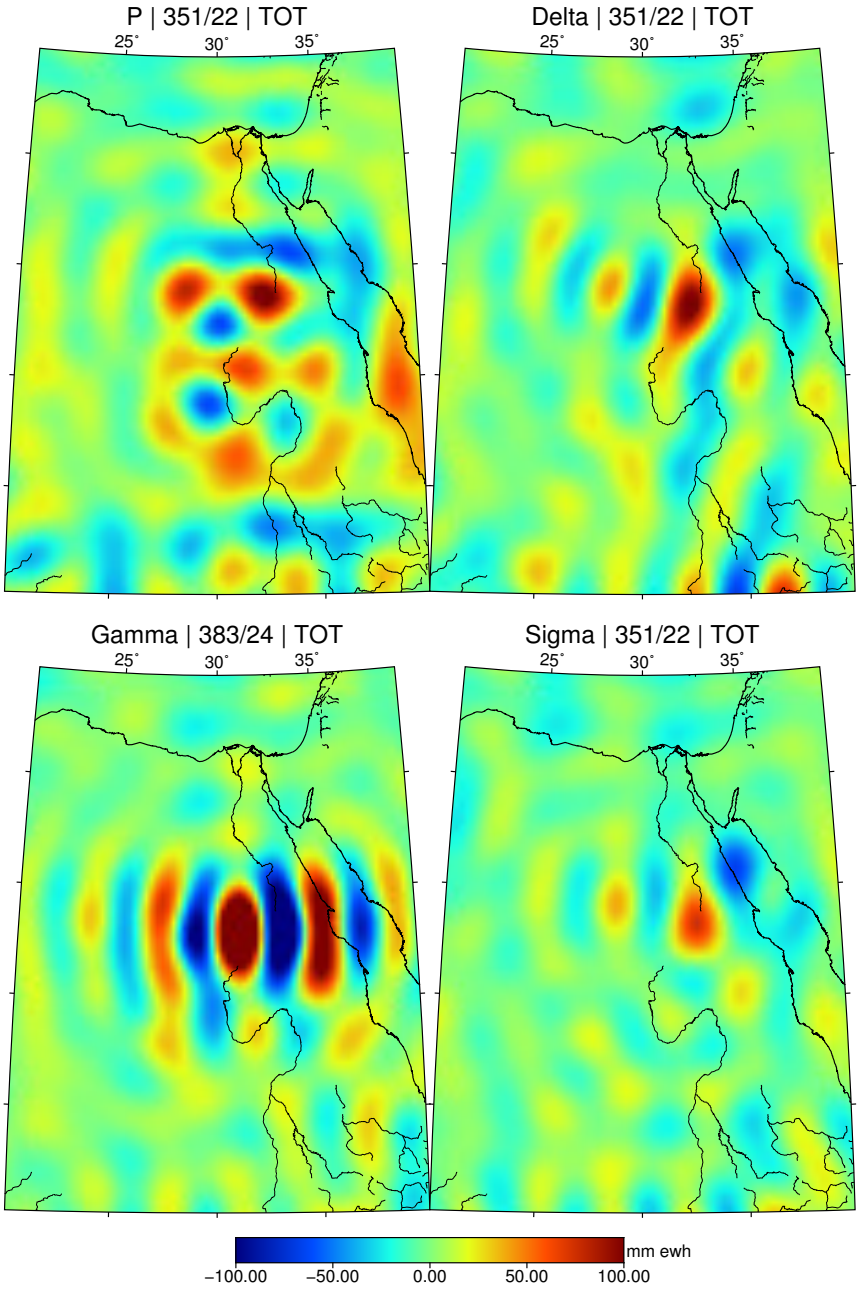

Figure 8.39: Total error over the Nile river basic for the pendulum 351/22, delta 351/22, gamma 383/24 and sigma 351/22 missions in terms of *regularized* solutions [mm ewh].

Table 8.24: Total error for the best three satellite hybrid formation missions over different regions of interest in terms of *regularized* solutions [mm ewh]. The cartwheel (the best single-formation mission) is also included in the comparison for reference.

Region	Signal	P|351/22	Γ|383-24	Δ|351/22	σ|351/22
Global	60.10	19.37	13.69	13.93	**13.11**
Amazon	150.97	39.38	20.18	21.91	**18.78**
Nile	176.69	20.71	30.04	16.97	**12.90**
Orinoco	96.74	28.26	**15.46**	23.29	18.96
Ob	70.01	26.46	18.83	19.31	**17.88**
Antarctica	40.48	17.90	11.74	**11.58**	11.81
Greenland	166.20	35.94	26.06	20.51	**19.53**
Amundsen S.E.	112.61	38.52	21.43	**17.54**	18.76
Alps	39.10	15.68	**11.44**	13.83	13.17
Sumatra	185.62	33.50	**18.40**	20.67	24.37
Fennoscandia	44.52	22.13	21.17	21.41	**19.51**
Score		1/33	21/33	18/33	**26/33**

and 80, which supports this hypothesis.

8.5.3. Dual-formation Missions

Four different dual-formation missions have been presented in the previous sections. Of those, the 10-day dual along-track, 22-day dual sigma, 22-day dual cartwheel and 22-day dual gamma missions have shown the lowest total error in terms of global RMS of unregularized solutions. Results of a regional comparison of these missions are presented in Table 8.25, along with the best performing 3-satellite mission, the 22-day sigma formation. The best performance is obtained for the 22-day dual-sigma mission with a score of 39/44. The dual sigma mission has the lowest total error globally and in most regions of interest.

Despite consisting of only one satellite formation, the second best performing mission is the single-formation sigma mission with a total score of 29/44. The remaining mission concepts – the dual gamma, dual cartwheel and dual along-track – get scores 24/44, 12/44 and 6/44, respectively. The dual along-track mission fares the worst. It shows large errors in the equatorial regions (Amazon, Orinoco and Nile river basins). This is not unexpected, since in these lower latitudes, the two along-track pairs are nearly co-linear and, therefore, comparatively less capable of observing spatial variations of mass anomalies in the east-west direction.

Maps of the total error over Antarctica for different mission concepts are shown in Figure 8.41. This figure is quite interesting, as it reveals many typical features of the considered missions. There is a clear polar cap region with larger errors for the dual along-track mission; this is the region where the lower-inclined pair does not collect any measurements. There is also a circular error feature around the pole common to the dual gamma, dual sigma and sigma missions. This area corresponds to when the satellites taking part in the pendulum pair swap their relative positions in the formation. In this process, the inter-satellite baseline shrinks to nearly zero

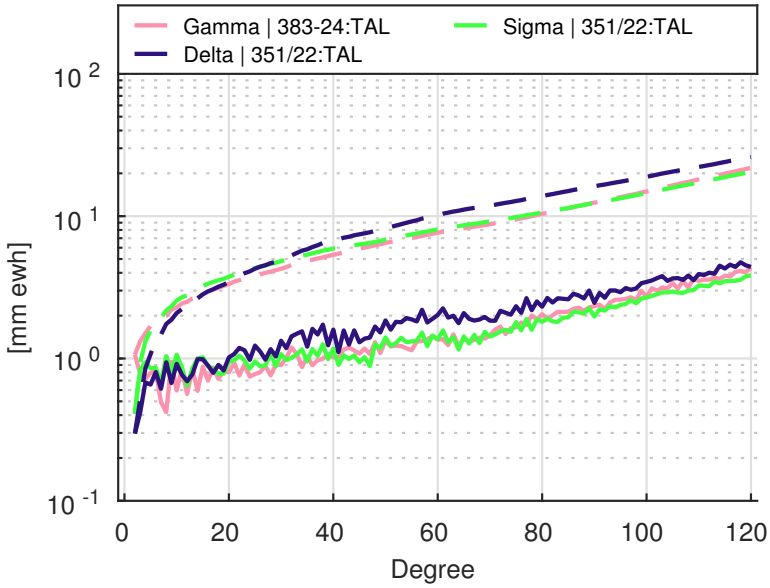

Figure 8.40: DV and CDV of the total temporal aliasing error for the sigma, gamma and delta missions in terms of *unregularized* solutions.

Table 8.25: Total error in terms of regional RMS of mass anomalies for the best dual-formation missions over different regions of interest in terms of *unregularized* solutions [mm ewh]. The sigma formation (the best hybrid-formation mission) is also included in the comparison for reference.

Region	Signal	σ:351/22	2Γ:351/22	2C:351-22	2AT:159/10	2σ:351/22
Global	60.10	20.94	21.82	33.12	43.23	**19.56**
Amazon	150.97	19.88	19.75	25.80	57.20	**15.76**
Nile	176.69	15.17	19.31	23.96	60.60	**13.67**
Orinoco	96.74	18.52	23.72	29.74	49.45	**17.31**
Ob	70.01	21.98	25.59	31.84	**18.61**	22.96
Antarctica	40.48	21.23	23.27	26.55	45.67	**21.05**
Greenland	166.20	28.65	**27.74**	35.01	57.55	28.84
Amundsen S.E.	112.61	19.01	20.34	**16.21**	78.94	17.59
Alps	39.10	18.25	21.19	39.35	22.76	**17.03**
Sumatra	185.62	23.92	21.55	22.17	75.61	**16.32**
Fennoscandia	44.52	31.59	32.18	43.63	36.17	**28.88**
Score		29/44	24/44	12/44	6/44	**39/44**

not allowing inter-satellite ranging data to be collected (cf. Section 8.1.2). This results in an increased error level, as shown in the plots. Finally, the dual cartwheel mission shows a comparatively low errors in Antarctica compared to the other missions. This can be attributed to the synergy between the cartwheel pairs in the formation, which collect orthogonal measurements over this region.

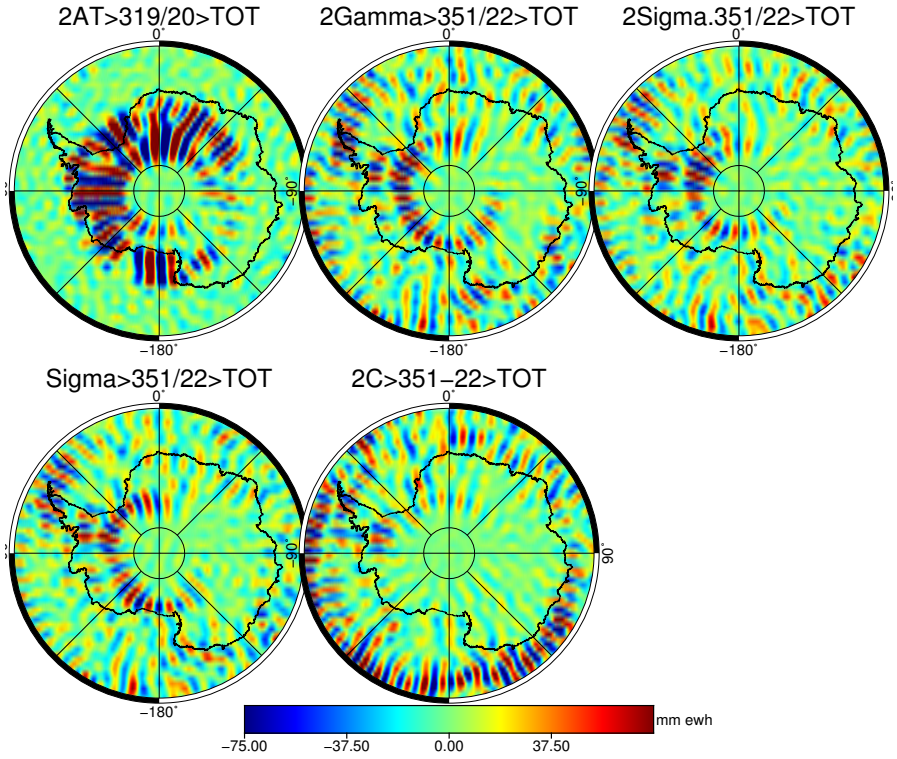

Figure 8.41: Total error in terms of regional RMS of mass anomalies over Antarctica for the sigma 351/22, dual sigma 351/22, dual gamma 351/22, dual along-track 319/20 and dual cartwheel 351/22 missions in terms of *unregularized* solutions [mm ewh].

Next, I consider the total error in terms of regularized solutions. Table 8.26 shows its breakdown over the regions of interest for the considered missions. The best performing mission is again the dual sigma mission with a total score of 34/44, followed by the dual gamma mission with a score of 26/44. The single-formation sigma mission now ranks third with a score of 24/44, which has dropped significantly compared to the unregularized case. The dual cartwheel and dual along-track missions rank fourth and fifth with a score of 18/44 and 8/44 points, respectively. Despite the large differences in the scores, the differences in the regional RMS values between the considered formations over several considered regions are relatively small (often between 10% and 20%). Even the worst performing dual along-track

Table 8.26: Total error in terms of regional RMS of mass anomalies for the best performing dual-formation missions over different regions of interest in terms of *regularized* solutions [mm ewh]. The sigma formation (the best hybrid-formation mission) is also included in the comparison for reference.

Region	Signal	σ:351/22	2Γ:351/22	2C:383/24	2AT:159/10	2σ:351/22
Global	60.10	13.11	13.16	13.68	14.99	**12.04**
Amazon	150.97	18.78	18.74	23.52	28.46	**15.33**
Nile	176.69	12.90	12.38	23.45	27.60	**11.08**
Orinoco	96.74	18.96	22.88	23.91	25.87	**16.91**
Ob	70.01	17.88	20.18	23.43	**13.07**	18.74
Antarctica	40.48	11.81	11.91	**11.08**	13.19	11.72
Greenland	166.20	19.53	22.28	21.63	26.71	**19.15**
Amundsen S.E.	112.61	18.76	18.88	**18.75**	34.37	18.88
Alps	39.10	13.17	**10.73**	13.40	15.35	12.08
Sumatra	185.62	24.37	**17.86**	20.21	24.75	17.90
Fennoscandia	44.52	19.51	17.90	19.47	**17.35**	18.13
Score		24/44	26/44	18/44	8/44	**34/44**

mission shows the best performance in some of the considered regions.

It is interesting that the dual along-track mission is significantly better than all others over Scandinavia and over the Ob river. Both of these locations are at about the same 60° latitude. Since the inclination of the second along-track formation is 70°, at these latitudes, there is a greater density of observations (w.r.t. gamma) and the inter-satellite baselines of both satellite formations are roughly perpendicular. The total errors over the Ob are shown as maps in Figure 8.42. The dual along-track mission shows the smallest magnitude features. The sigma, dual sigma and dual gamma missions show a large positive magnitude feature with similar magnitudes, while the dual cartwheel shows an error feature at the same location with opposite sign.

It seems that the dual sigma mission is consistently the best at the low latitudes while it is not at the higher latitude (except for Greenland). Similarly the sigma and dual gamma missions seem to have a somewhat better performance (i.e. closer to the mission with the lowest error) at low latitudes than in the higher latitudes. This indicates a deficiency in the gamma and sigma concepts. The pendulum pair considered these formations lacks sensitivity in the high latitudes. This is explained as the inter-satellite distance shrinks with the increasing latitude up to a minimum threshold where the pendulum observations are discarded.

8.5.4. Discussion

In the previous sections, several single- and dual-formation mission concepts were presented and their performance was analyzed. In light of the obtained results several considerations can be made.

Differences in the performance of the presented missions are most significant in terms of unregularized solutions. The overall differences in terms of regularized solutions are relatively small, the regularization bias becoming typically the largest error type. In general, unregularized solutions, where a large difference in the performance of different concepts was shown, are more useful to analyze the

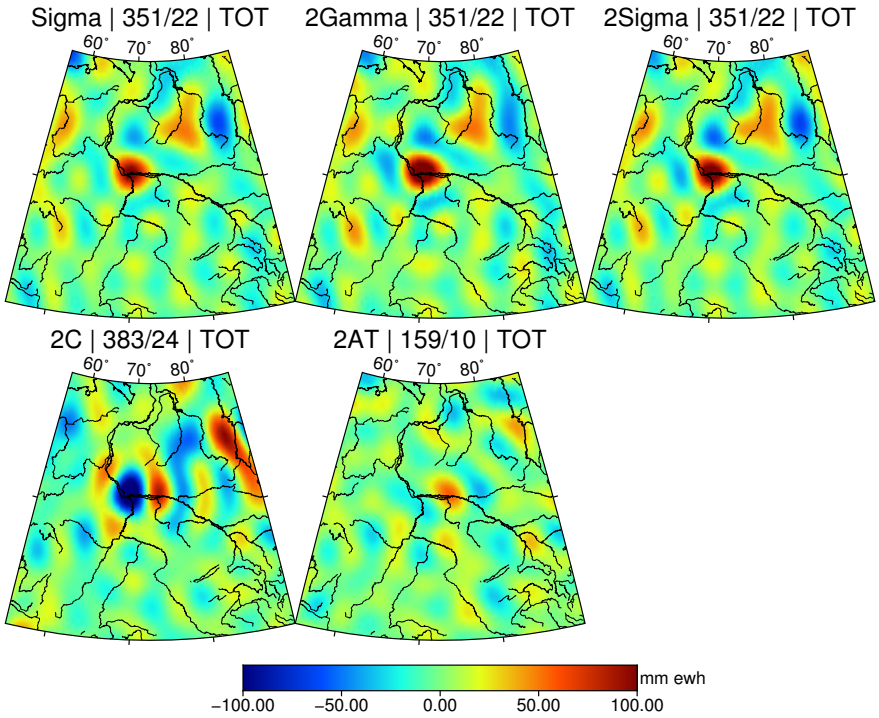

Figure 8.42: Total error in terms of regional RMS of mass anomalies over the Ob river basin for the sigma 351/22, dual sigma 351/22, dual gamma 351/22, dual along-track 319/20 and dual cartwheel 351/22 missions in terms of *regularized* solutions [mm ewh].

performance of a satellite mission as they are not biased towards the considered gravity field model.

One important conclusion of the presented study is that the dual along-track concept, often discussed in the literature, is greatly outperformed by all considered single-hybrid-formation concepts (see Table 8.25). Moreover, it requires 4 satellites arranged in 2 different formations, whereas sigma and gamma concepts require only 3 satellites in a single formation. The potential cost reductions and superior performance of the single-hybrid-formation concepts are two major advantages of these concepts.

It was shown that dual gamma and dual sigma missions, designed to improve the spatial and temporal coverage, result in only mild performance improvements, as compared to the corresponding single-formation missions. Notice that both gamma and sigma missions collect the same amount of measurements as dual gamma and dual sigma. The only difference is that the dual missions consist of two distinct formations, while the former combines both satellite pairs in a single formation. The dual gamma mission showed a total error reduction of 1% compared to the single-formation gamma mission (21.8 mm ewh instead of 22.1 mm ewh) in terms of unregularized solutions. The dual sigma showed an error reduction of 7% compared to the single-formation sigma mission (19.6 mm ewh instead of 20.9 mm ewh). It is likely that the costs associated with the additional formation are not worth the corresponding mild performance gain.

Overall, the best mission concepts can be ranked in order of their performance as: (i) dual sigma, (ii) sigma, (iii) dual gamma and (iv) gamma missions. Both sigma and dual sigma missions include a cartwheel formation, which is likely very challenging to implement. On the other hand, even in terms of unregularized solutions up to $l_{\text{max}} = 120$, the best dual gamma mission performed only about 10% worse than the best dual sigma mission, with a difference of only about 2 mm ewh in terms of global RMS. Furthermore, as mentioned before, the single-formation gamma mission is only 1% worse than the dual gamma formation. Thus, for a small performance handicap of 11%, the gamma mission refrains from cartwheel pairs of satellites (and their inherent complexity) and, at the same time, requires only three satellites in a single formation (as opposed to four satellite arranged in two formations). Therefore, the gamma mission sits in an attractive sweet spot regarding complexity, performance and cost, representing a very promising concept for future ll-SST missions. One final comparison is helpful at emphasizing the performance level of the proposed gamma mission compared to existing missions. The current GFO mission is an along-track type of mission; the best unregularized solutions of the gamma mission (22 mm ewh) show a 95% reduction in total error compared to the best along-track solutions (385 mm ewh). Even considering regularized solutions, the gamma mission (13.6 mm ewh) still shows a 45% total error reduction w.r.t. to corresponding along-track solutions (25 mm ewh).

The performance of most mission concepts shown is limited by the level of temporal aliasing errors. This observation can also be interpreted from a different perspective, i.e., that instrumentation errors play a relatively minor role. In turn, this can be used to optimize the design of the presented missions in several ways.

First, it may be possible to use relax the requirements on the accuracy of the ranging and accelerometer instruments without compromising the performance of the mission. This could allow for less expensive instruments and offset mission funds for additional satellite platforms. Similarly, less demanding requirements may allow miniaturization of these instruments in order to significantly cut on the launch costs of the mission. The second way is to raise the satellites' altitude in order to extend the mission lifetime while maintaining comparable performance. This is possible because the signal-to-noise ratio of instrumentation errors degrades as the satellite altitude increases, and instrumentation errors are magnified in the computed solutions. On the other hand, temporal aliasing errors are damped with altitude in the same way as the signal itself, so that the signal-to-noise ratio does not change with increasing altitude. Therefore, increasing the satellites' altitude will only result in an increase of instrumentation errors. Since the performance of most missions is not limited by those errors, increasing the satellite altitude should not worsen the obtained results up to the point where instrumentation errors become comparable. Allowing the satellites' altitudes to raise up to this point will maximize the mission lifespan without trading off the performance of the mission. Finally, another interesting aspect is the possibility to reduce inter-satellite distances. In general, shorter inter-satellite baselines increase the formation sensitivity to short-wavelength signals. Instead of increasing the altitude of the mission to extend the mission timespan, it may be feasible to observe mass transport signal at significantly finer spatial scales compared to existing missions. This is more relevant for the pendulum mission, where smaller inter-satellite distances will lead to lower relative velocities which may facilitate an implementation of this concept from a technical point of view. Regarding multi-formation missions, also it may also be interesting to combine different inter-satellite distances in order to maximize the bandwidth of the mission.

8.6. Beyond 4 satellites

One of the important findings of Section 7.5.3 was that placing satellite formations arranged in near-polar orbital planes such that they equally divide 3D space seems to lead to a minimum in terms of temporal aliasing errors. Given that temporal aliasing errors limit the performance of most considered concepts, an important question is whether this finding can be used to further improve the performance of the resulting concepts. Up to this point all the considered concepts have been limited to a maximum of 4 satellites which limits the number of formations and corresponding orbital planes to 2. In this section, I will no longer restrict the maximum number of satellites to 4. Instead, I will consider a maximum of three orbital planes and I will consider all the different ways of filling up these planes with along-track (A), pendulum (P) and gamma (Γ) formations. I will consider the longest data accumulation period with a 383/24 orbit.

The results are presented in Table 8.27. Two of the configurations in the table were already addressed in previous sections. They are the gamma (Γ) (cf. Section 8.3.1) and dual gamma (A/P) (cf. Section 8.4.2) concepts, respectively. The A/A concept in the second row of the table corresponds to a dual along-track mis-

Table 8.27: Comparison of several mission concepts consisting of up to three formations in three orbital planes. The table shows different configurations of along-track (A), pendulum (P) and gamma (Γ) formations that can be used to fill up the three orbital planes. The first column shows the required number of satellites. The next three columns of the table explain how the three orbital planes are filled in. The last two columns show the total error in terms of unregularized and regularized solutions [mm ewh] solved up to SH degree 120.

#s	Ω_{0°	Ω_{60°	Ω_{120°	TOT U.	TOT R.
3	Γ	✗	✗	22.11	13.69
	A	A	✗	61.85	14.42
4	A	P	✗	22.68	13.70
5	Γ	A	✗	23.03	13.94
	Γ	P	✗	19.36	12.75
6	Γ	Γ	✗	19.52	12.64
	A	P	A	20.34	10.98
	P	A	P	15.64	10.39
7	Γ	P	A	15.10	9.88
8	Γ	Γ	A	15.08	9.59
	Γ	Γ	P	13.24	8.87
9	Γ	Γ	Γ	12.68	8.34

sion with two along-track formations in near-polar orbits. It is slightly different from the dual along-track mission presented in Section 8.4.1 since the second formation of that one was on a 70° inclination orbit.

Overall, the table shows a tendency of a reduction of the total error with increasing number orbital planes and satellites. There are nonetheless several exceptions where increasing the number of orbital planes or the number of satellites does not lead to a reduction of the total error. The best configuration is the Γ/Γ/Γ consisting of three gamma formations in three different orbital planes. In terms of unregularized solutions, it yields a total error of 12.7 mm ewh, which is 43% smaller than that of the single-formation gamma mission (22.1 mm ewh). Perhaps, the most interesting result shown in the table is the error reduction accomplished by the P/A/P configuration. With 6 satellites arranged in three formations, this configuration yields an improvement of 29% compared to the single formation gamma mission. Such configuration is interesting because is relies on three independent elementary formations and is significantly better than the alternative A/P/A configuration. I interpret this finding as follows. Polar regions are problematic for pendulum formations. It is likely, however, that a single along-track pair is sufficient to adequately sample these regions. Then, it is likely that the performance of missions with a single along-track pair and multiple pendulums is significantly better compared to configurations with more than one along-track pair.

A comparison of the total error RMS over different regions for the Γ, P/A/P and Γ/Γ/Γ missions is shown in Table 8.28. The three considered missions clearly show different performance levels. A map of the total error for each of the three missions is shown over Greenland (Figure 8.43) and over the Amundsen Sea Embayment (Figure 8.44). In both figures, one can see the incremental improvements brought

in by the use of a more complex mission. The P/A/P mission is able to remove some of the error features seen in the Γ mission, while Γ/Γ/Γ removes all major error features seen in the other two concepts.

Table 8.28: Regional RMS of the total error (TOT) for the Γ, P/A/P and Γ/Γ/Γ missions on a 383/24 orbit over different regions in terms of *unregularized* solutions [mm ewh].

Region	Signal	Γ	P+A+P	Γ+Γ+Γ
Global	59.68	22.85	15.63	**12.67**
Amazon	150.06	25.39	16.39	**11.47**
Nile	174.62	36.14	19.03	**14.54**
Orinoco	94.41	19.56	19.34	**12.59**
Ob	70.59	25.20	21.49	**14.72**
Antarctica	40.48	22.30	16.41	**12.80**
Greenland	166.54	32.53	25.42	**18.04**
Amundsen S.E.	112.31	21.18	15.67	**8.18**
Alps	38.38	20.92	**15.58**	16.28
Sumatra	185.86	19.09	18.11	**13.45**
Fennoscandia	42.86	33.43	24.86	**20.87**
Score		0/22	12/22	**21/22**

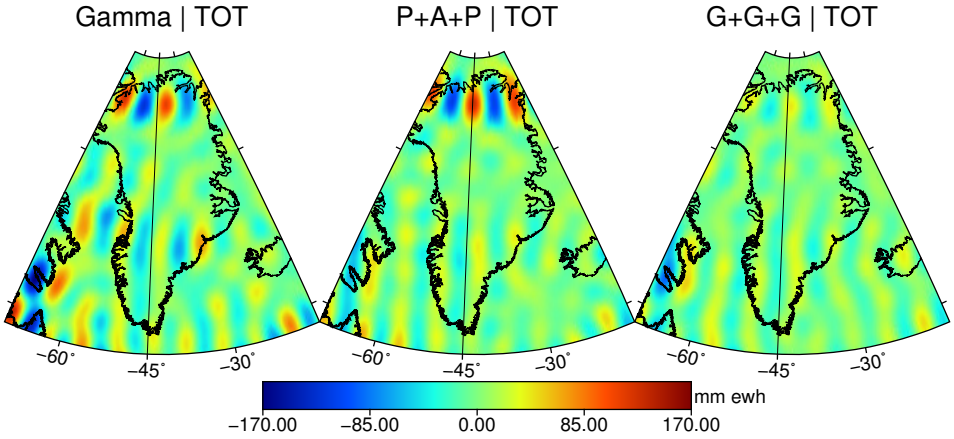

Figure 8.43: Comparison of total error (TOT) over Greenland for the Γ, P/A/P and Γ/Γ/Γ missions on a 383/24 orbit in terms of *unregularized* solutions [mm ewh].

Apart from showing the potential performance improvements of considering larger missions, an interesting realization is that there is no requirement for, e.g. the full Γ/Γ/Γ (or P/A/P) mission to be launched at once. Any presented configuration may be launched and operated independently over time and even by different organizations within an international venture. This idea also opens the door for a long-term continuous mass monitoring system where various, e.g. Γ formations are continuously launched to replace the ones reaching the end of their lifetimes.

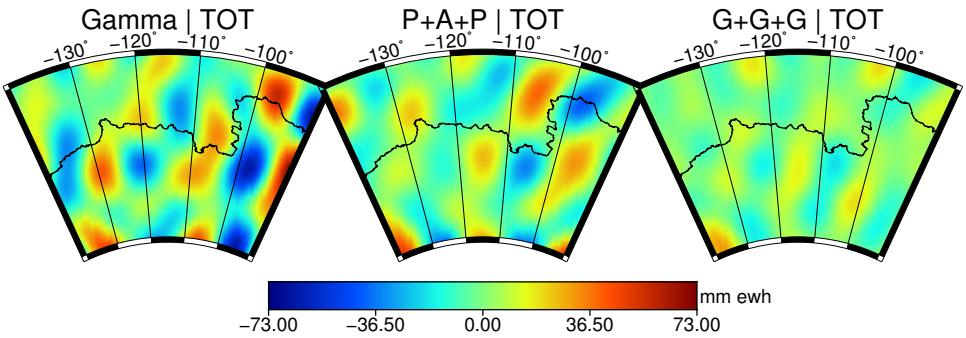

Figure 8.44: Comparison of total error (TOT) over the Amundsen Sea Embayment for the Γ, P/A/P and Γ/Γ/Γ missions on a 383/24 orbit in terms of *unregularized* solutions [mm ewh].

8.7. Conclusion

In this Chapter, a number of important findings have been documented. Initially, only missions consisting of up to 4 satellites were considered, grouped in one or two formations. The general mission objective was stated to be the recovery of mass transport signals up to $l_{\text{max}} = 120$ over DAPs between 8 and 24-days. The orbits of the chief satellites were restricted to circular, near-polar, low-altitude repeat ground track orbits. Formation parameters were limited to three topologies: along-track, pendulum and cartwheel, with maximum inter-satellite distances of 200 km. Dual-formation missions were designed with interleaved ground tracks at near-perpendicular orbital planes in order to minimize temporal aliasing errors.

Then, by making a correspondence between the orientation of the inter-satellite baselines in the elementary formations and the gravity gradient components analyzed in Sections 7.4 and 7.5, a number of missions consisting of combinations of elementary ll-SST satellite pairs was proposed. A set of three-satellite hybrid formation missions was presented that included the gamma, delta and sigma missions. The gamma mission is a single-formation mission consisting of an along-track and a pendulum pair of satellites. The sigma mission is a combination of a cartwheel and a pendulum pair. The delta mission is a three-satellite variant of the cartwheel mission which is capable of continuously resolving three gravity gradient directions (xx, xz and zz). In addition, a set of concepts consisting of two formations was also presented: the dual along-track, dual sigma, dual gamma and dual cartwheel concepts.

In Section 8.5, a comparison between all the proposed mission concepts was presented. To that end, I selected a number of regions which are of interest in different applications of satellite gravimetry. The setup with the lowest total error was selected within each concept and benchmarked over the regions under consideration. A simple scoring system based on the regional RMS of the total error was used as a metric for the relative performance of each mission concept. A common trait of most presented concepts was that their performance is limited by temporal aliasing errors. Starting with the elementary satellite missions, I showed that

there are significant differences in the distribution and magnitude of errors. The comparison between the elementary satellite formations showed that, in terms of unregularized solutions, the 383/24 cartwheel mission (20/22 points) is the best, being followed by the 351/22 pendulum mission (12/22 points) and the 351/22 along-track (1/22 points) scoring the worst.

The along-track concept yielded the largest amount of spatial instability and temporal aliasing errors, while the cartwheel mission was the best. This shows that the radial component of the measurements made by the cartwheel mission leads to significant improvements w.r.t. the along-track mission. These findings were found to be consistent with the results presented in Chapter 7. They show that the yy gradient direction, and, preferably, the zz gradient directions are more desirable than xx. These findings are also consistent with exiting literature on the topic (M. A. Sharifi et al., 2007; Sneeuw et al., 2008).

Regarding the hybrid-formation missions, the 351/22 sigma mission was the best one, both in terms of regularized (26/33 points) and unregularized (30/33 points) solutions, followed by the 383/24 gamma (22/33 and 22/33) and 351/22 delta (12/33 and 15/33) missions. The performance of all hybrid missions was significantly better than all the elementary satellite formations. Regarding unregularized solutions, the 383/24 cartwheel mission only scored 2/33 points, while in terms of regularized solutions the 351/22 pendulum only scored 3/33 points. Regarding the sigma and gamma mission, the higher performance of these concepts is for the most part explained by synergy between the orthogonal baselines used as observables of the formation and the consequent reduction in spatial instability and temporal aliasing errors. The delta concept too showed large improvement compared to the cartwheel mission. However, it failed to reach the performance level of the other two hybrid formations.

The sigma mission, as the best performing one, was also benchmarked against all dual formation missions, and the results were somewhat unexpected. While the best mission overall was the 351/22 dual sigma (39/44 points), the single-formation 351/22 sigma (29/44) was shown to perform better than all other dual-formation missions, in terms of unregularized solutions. However, the differences in terms of global RMS of the total errors between the sigma (20.9 mm ewh) and dual sigma (19.6 mm ewh) missions were small (7%, cf. Table 8.25). Similarly, the differences between the best gamma (22.1) and dual gamma (21.8 mm ewh) missions were also small (1%). This leads to the conclusion that splitting the considered orthogonal combinations in two orbital planes results in marginal improvements. This can be explained by the fact that the orthogonal observations collect mutually complementary information. As a consequence, it makes little difference whether these observations are collected from a single or from two different orbital planes.

As argued in Section 8.5.4, the gamma mission seems hold the most potential, despite ranking worse than the dual sigma, sigma and dual gamma concepts. It suffers from a performance handicap of 11%, 5% and 1% compared to the dual sigma, sigma and dual gamma, respectively, but it avoids the complexities of cartwheel formations. Furthermore, it requires only three satellites grouped in a single formation, as opposed to 4 satellites grouped in 2 formations, as required by

the dual sigma and dual gamma missions. I propose, therefore, that the gamma mission is a very promising concept for future ll-SST missions. To highlight the performance level of the gamma mission compared to existing ones, notice that the current GFO mission is an along-track type mission. A comparison between the total error of the gamma (22 mm ewh) and along-track (385 mm ewh) concepts shows a error reduction of 95%. Even when regularized solutions are considered, the gamma (13.6 mm ewh) yields a 45% error reduction w.r.t the along-track (25 mm ewh).

In the final Section 8.6, using the gamma mission as a starting point, I showed the potential of extending the number of formations in different orbital planes to three. I have shown that the $\Gamma/\Gamma/\Gamma$ concept consisting of three gamma formations reduces the total error by 43% compared to the single-formation gamma mission. Furthermore, I have shown that the 6-satellite P/A/P[1] configuration is also promising one, with rather high performance. It shows an error reduction of 29% w.r.t. the single-formation gamma mission, and it manages to do so with only 6 satellites instead of 9 satellites required for the best $\Gamma/\Gamma/\Gamma$. This concept only requires three elementary formations without the likely complexities introduced by the Γ formations.

The P/A/P (15.6 mm ewh) configuration is also significantly better than the Γ/Γ (19.5 mm ewh) one, which also consists of 6-satellites (cf. Table 8.28). The enhanced performance is likely explained by the better global observability provided by the three orbital planes of the P/A/P configuration. Finally, the P/A/P concept also showed significant improvements relative to an alternative A/P/A[2] (20.3 mm ewh) formation. One can conclude that pendulum formations are more valuable than along-track ones, as long as one along-track formation is present to enhance the constellation sensitivity to signals in the polar regions.

[1] pendulum/along-track/pendulum
[2] along-track/pendulum/along-track

9

Conclusion

The following sections gather the concluding remarks of this thesis. In Section 9.1, a summary of the major findings in this thesis is presented and I answer the research questions of this study. In Section 9.2, a number of recommendations are presented.

9.1. Summary

In this thesis, I undertook the challenge of designing future ll-SST missions with the potential to improve on the performance of the current ones. The approach that I took was to find the performance limitations which current missions face and to identify the mission parameters which can be used to overcome these limitations. The major findings of the thesis are summarized in the next sections, each referring to one of the research objectives outlined in Section 1.2.

9.1.1. Build a simulation tool and a realistic noise model to assess the performance of satellite gravimetry missions

In order to study the performance of future missions through simulations, a simulator was required. The existing software used to process GRACE data was available, and my work focused on expanding it to generate and process all the required data of any ll-SST mission. The major milestone in the development of this tool was the validation of the noise model. This validation was based on its ability to correctly reproduce the errors of the GRACE mission. Another important motivation existed to undertake this validation step. Our current understanding of errors in the GRACE data time-series was not complete. Observed errors in the frequency range between 1 and 9 mHz in inter-satellite accelerations of the GRACE data were not understood well. By comparing the simulated errors against errors in the real data from the GRACE mission, I was not only able to ensure the validation of the noise model, but also to close the existing knowledge gap. In turn, a better understanding of the errors in the GRACE data may lead to improvements to the quality

of the gravity field solutions produced on their basis.

Undertaking this task meant that several research lines had to be pursued simultaneously in order to find explanation for the observed errors in GRACE data. From this process, two different topics were identified which ultimately resulted in two different chapters in this thesis: indirect effect errors and star-camera errors.

9.1.2. Describe and predict the propagation of indirect effect errors

Indirect effect errors arise when force model perturbations are propagated via the numerical integration into the reference orbits. This non-linear and non-local error propagation mechanism had previously not been fully understood. In Section 6.3, it was estimated that indirect effect errors account for 9% of the total error in terms of global RMS in mm ewh, and that this number may increase to 14% for future along-track type of missions.

In Chapter 3, the indirect effect error was formalized in the context of the RRC approach. In the rest of that chapter, simple simulations were used to show how a point mass perturbation maps into observations of different ll-SST concepts. It was shown that the pendulum formation is the most resilient to indirect effect errors. This is because, in the pendulum formation, the relative satellite motion is confined to the inter-satellite baseline direction. Therefore, most of indirect effect errors are monitored by the ranging sensors and can be corrected for. This is in contrast with the along-track and cartwheel concepts. The along-track concept was shown to be rather sensitive to these errors, while the cartwheel concept was found to be the most sensitive one. The presented findings offer a complete picture of what indirect effect errors are, how to compute them and why they matter. Those findings represent a step forward in understanding indirect effect errors, while being consistent with previous work (Encarnação, 2015).

9.1.3. Quantify the impact of star camera errors in the GRACE data

Star cameras are space-borne instruments which compute the attitude of the spacecraft by measuring the positions of the stars and collating them with an on-board catalog. In Chapter 5, I analyzed star-camera errors and their propagation into inter-satellite acceleration measurements of the GRACE mission. Two distinct types of star-camera errors were found in the data: harmonic and stochastic errors. Harmonic errors were found to be highly correlated with the satellite's true anomaly. The contents of this chapter were originally published in Inácio et al. (2015). Later on, Harvey (2016) showed that the documented harmonic errors were caused by an error in the software used to process the star-camera data.

The analysis of the star-camera errors showed that the error levels of the star-camera instruments are close to the nominal values. The ratio between the accuracy of the cross- and boresight axes is within the expected value of 8, except for primary SC boresight axis where this ratio was found to be between 11.7 and 12.2 µrad for GRACE-A and 8.9 and 9.4 µrad for GRACE-B. The SCs on board GRACE-A and GRACE-B have about the same accuracy except for the primary SC boresight axes,

where GRACE-A (158-164 µrad) is less accurate than GRACE-B (131-143 µrad). A close-to-nominal error level of the star cameras meant that those errors did not provide a significant contribution to the error budget in terms of gravity field solutions. However, there were two issues with the potential to compound and amplify existing star-camera errors: data gaps and periods of poor attitude control.

A data gap occurs when one of the star-camera instruments is blinded by a very bright celestial body (i.e., the Sun or the Moon). During these periods, only one star camera is active. As a result, the measured satellite attitudes are significantly less accurate: the errors in measured pitch and yaw angles increase by up to a factor of 4.

Both spacecraft are kept pointing at each other by the attitude and orbit control system (AOCS). However, an analysis of the inter-satellite pointing angle showed that, for a few months in the GRACE data series, the AOCS did not keep this angle within the required values. It was found that, in the worst-case scenario, large inter-satellite pointing angles can result in a magnification of the impact of star-camera errors on computed inter-satellite accelerations by a factor of 5. The analysis of star-camera errors in terms of regularized solutions of the GRACE mission revealed that they may account for 18% of the total error. As argued, this figure may become significantly larger in months with poor attitude control and/or with large amount of single-star-camera activity. Unfortunately, star-camera errors alone could not completely explain the observed errors in the GRACE data.

9.1.4. Explain the error budget of the GRACE mission

In Chapter 6, the noise budget of the GRACE mission was presented. The errors were divided into instrumentation errors and temporal aliasing errors. The instrumentation noise model for GRACE was presented in Table 4.1. A comparison of the total error with the observed errors in real GRACE data showed a good agreement between the two. The total error in real GRACE data was explained by a combination of accelerometer errors and positioning errors up to the frequency of 0.8 mHz. From this point on, the AOD error becomes dominant up until about 5 mHz, at which point ranging errors become dominant.

An in-depth analysis of the error budget in terms of monthly gravity field solutions followed. The importance of the high-pass filtering of inter-satellite accelerations and regularization of gravity field solutions in the mitigation of noise was illustrated. Only by employing both procedures, it was possible to reduce noise in the solutions with $l_{\max} = 120$ to a reasonable level. The dominant error in the simulated GRACE solutions in terms of global RMS was the ranging error. Total instrumentation errors were found to be slightly larger than temporal aliasing errors. Regularization bias and filtering errors were found to be large contributors to the error budget of regularized solutions. It is important to notice that these errors are not visible in real data processing. Furthermore, notice that the regularization bias is for the most part determined by the high-resolution components of the input ESM model which are not adequately observed by GRACE.

9.1.5. Quantify the performance of future GRACE-type missions

The GFO mission was recently launched and, apart from the new LRI and star-camera assembly, it replicates for the most part the design of the previous GRACE mission. Once the GRACE error budget was presented, it became interesting to evaluate the potential of future GRACE-type missions (FGT) which are to replicate GRACE. Assuming a conservative baseline for the performance of the instrumentation on future missions and the same simulation set-up as used in Sec. 9.1.4, I computed the error budget of the FGT mission. Large improvements in the (assumed) performance of the accelerometer and ranging sensors lead to a great reduction of instrumentation errors. Temporal aliasing errors became dominant, and of those, AOD model error was the largest component. Despite large improvements in the instrumentation errors, the total error of the FGT mission was found to be only 12% smaller than in the case of GRACE. These results show that temporal aliasing errors place a limit on the performance of FGT missions. In the first instance, this could mean that more accurate background models are required in order to improve the performance of satellite gravimetry missions. However, it is not likely that substantial improvements in background models will be readily attainable. The fact that temporal aliasing errors are dominant sends a clear message that future ll-SST missions will have to be designed in order to reduce these errors. In turn, a new generation of satellite gravimetry missions will provide the required data to improve the accuracy of existing background models.

Propagation of indirect effect errors into gravity field solutions is likely to depend on the adopted functional model. In that case, the presented results could be regarded as conditioned to the choice of methodology. On the other hand, a comparison of indirect effect errors in all different functional models is beyond the scope of this thesis. In order to address this issue, an additional comparison between the two missions was made where no indirect effect errors were considered. This scenario implies a best-case scenario, where the impact of indirect effect errors is reduced to zero. It was shown that the simulated GFO mission was 17% better than GRACE in terms of global RMS. This comparison also revealed that indirect effect errors, which account for between 9% and 14% of the total error, make a relatively small contribution to the error budget.

9.1.6. Identify the set of mission design parameters that have the largest impact on spatial and temporal aliasing errors

Evaluating the performance of a multitude of different possible ll-SST mission concepts is a computationally demanding task. Therefore, in Chapter 7, my approach has been to reduce the complexity of the simulated missions to a minimum (ensuring they are realistic nonetheless) in order to effectively study their performance limitations. Any ll-SST satellite pair is conceptually the same as a gradiometer with a very long-arm. Therefore, in Section 7.2, a correspondence was made between different types of ll-SST missions and different components of a gradiometer instrument flying in a single satellite. This allowed for a set of simple gradiometer

simulations to be carried out instead of more complex ll-SST simulations. To speed up the computations, I considered short timespans and computed solutions up to relatively small SH degrees. By systematically analyzing the performance limitations of simple gravity gradient simulations, it became possible to infer how to design ll-SST missions with the maximum potential performance. In this way, I could quickly research the different errors that affect ll-SST mission data.

First, I looked at the propagation of spatial aliasing errors in different gravity gradient components. Spatial aliasing errors were found to be dominated by signals at the SH degrees that are immediately above the considered maximum degree l_{max}. I have shown that there are significant differences in terms of spatial aliasing errors between the different gravity gradient components. The zz gradient yielded significantly lower errors than both xx and yy gravity gradients. Therefore, it is expected that both along-track and pendulum formations suffer from larger spatial aliasing errors than the cartwheel. Notice that the magnitude of the mass transport signal decreases with increasing SH degree. Therefore, in order to minimize spatial aliasing errors, a high l_{max} is desirable. A caveat is that a too high l_{max} will result in a high level of spatial instability errors, which were afterwards analyzed.

Besides spatial aliasing errors, I have found that spatial instability errors also limit the spatial resolution of the mission. Spatial instability errors are most pronounced when a too high l_{max} is chosen. When this happens, the set of linear equations to be solved becomes ill-posed, and the existing noise in the data is greatly magnified in the obtained solutions. In the considered simulations, I introduced white noise in the gradiometer instrument with a $\text{PSD}^{\frac{1}{2}}$ of $1 \times 10^{-5}\,\text{E}/\sqrt{\text{Hz}}$ in order to trigger spatial instability errors in the solutions. It was shown that the three considered gradiometer components (xx, yy and zz) yielded different error levels. The zz component was found to be the one showing the lowest errors. Additionally, it is was found that combining multiple components in a single formation may double or almost triple the spatial resolution of the mission. This finding is very important; it implies that the Colombo-Nyquist rule is not valid when combinations of observations from the same formation are considered. Thus, a combination of multiple observations in a single formation is an effective way to extend the spatial resolution of a mission.

Finally, regarding single-formation missions, it was shown that there are no significant differences in terms of spatial resolution for even and odd repeat period orbits. Repeat orbits with even parity are characterized by an overlap of the ascending and descending groundtrack over the equator, whereas for odd orbits the ascending and descending tracks are interleaved over the equator. As a consequence, even-parity repeat period orbits have larger distance between the groundtracks at the Equator compared to odd-parity orbits. Because of this, it has been argued in the literature that even repeat period orbits are less desirable as they result in a lower spatial resolution compared to odd-parity ones. However, I have found no supporting evidence for this claim. I have shown that the spatial resolution of even- and odd-parity repeat orbits is actually similar. Consequently, when analyzing the performance of satellite missions over different data accumulation periods (DAP), I could always select the lowest altitude repeat orbit available irregardless of its

parity. This was important regarding the odd DAPs (9, 11, 13 ... days), for which the lowest altitude orbit available is of even parity. These DAPs would otherwise suffer from a performance penalty from the need to select a comparatively higher altitude odd-parity orbit.

Looking into missions consisting of two formations, I showed that interleaving the groundtracks of multi-formation missions which consider different observables *does not* significantly improve the spatial resolution of the missions. Additionally, no significant differences were found either for different possible ways to interleave groundtracks of multi-formations missions which consider different observables.

A similar setup was used to investigate the level of temporal aliasing errors. For single-formation missions, it was shown that different gradiometer observation components yielded different levels of temporal aliasing errors. Observation of the zz component resulted in the lowest temporal aliasing errors; it was followed by yy, while the xx component was found to be the worst. It was also demonstrated that the xx+yy combination provided the same level of errors as the zz component alone. Furthermore, it was shown that combinations of zz with other components does not lead to a further error reduction.

Dependence of temporal aliasing errors on the DAP, which was set equal to the orbit repeat period, was also analyzed. As argued in Section 7.5.2, for a given DAP, temporal aliasing errors depend not only on the amount of data considered in that DAP. Temporal aliasing errors will also depend on how the measurements are distributed over the globe within the DAP, on the rate at which the non-stationary temporal aliasing errors may average out and on the combination and orientation of observables considered. Due to all the factors that play a role, I considered the possibility that a given DAP could exist that would yield minimum temporal aliasing errors. In general, it was found that longer DAPs are beneficial; no evidence was found for the existence of a short DAP which would yield a relatively low amount of temporal aliasing errors.

The temporal resolution of a mission is intrinsically linked to the concept of revisit time. The revisit time is defined as the time interval between two passes over the same geographic region. When two satellite formations are considered, the second formation's orbit may be time-shifted in order to half the revisit time. In turn, this should double the temporal resolution of the mission. A time-shift is applied by setting the second formation to pass over the same geographic region as the first one at half of the repeat orbit period. Applying a time-shift to the orbit of the second formation results in two nearly co-linear orbital planes. I have shown that two formations observing the zz/xz combination in nearly co-planar orbital planes *did not* lead to any error reduction compared to a single formation observing the same zz+xz combination. I concluded that co-planar orbital planes are not effective at improving the temporal resolution of a mission.

Unlike other direct measurement techniques (like radar altimetry or satellite imagery), gravimetry measurements are not local in nature. They carry information about the Earth's gravity field as a whole. Therefore I hypothesize that the concept of *exact revisit time*, where the satellite formations are required to fly over exactly the same location is of little use. Instead, I proposed a more flexible concept

of *wide revisit time* where it is sufficient that the satellite formations fly over the vicinity of the same location. On the basis of this concept, one can half the wide revisit time by considering nearly perpendicular orbital planes. I have shown that two satellite formations in nearly perpendicular orbital planes observing the same zz/xz combination yielded lower temporal aliasing errors compared to the single formation zz+xz combination and the zz/xz combination in two nearly co-planar orbital planes. Similarly, the zz/zz combination in two near-perpendicular planes was significantly better than the same combination in two nearly co-planar orbital planes. Both results seem to confirm that the concept of wide revisit time is useful and that two perpendicular planes are likely to maximize the temporal resolution of missions consisting of two formations. In order to further confirm this hypothesis, I proceeded to search the space of relative orientation of near-polar orbital planes to find the lowest level of temporal aliasing errors. I considered missions consisting of two and three formations, all of them exploiting the most desirable zz-gravity gradient. I showed that, in order to minimize temporal aliasing errors, the polar orbital planes of the considered formations must be arranged such that they equipartition 3D-space. Specifically, for two formations the orbital planes should be perpendicular and for three formations the relative RAAN of the orbital planes should be set $\approx 60°$ apart.

Still considering two-formation missions, I showed that a zz/xz combination of orthogonal observables split over two formations in near perpendicular orbital planes *does not* lead to any significant reduction of temporal aliasing errors, compared to the same combination collected from a single formation. This can be explained by the fact that the orthogonal observations in a single formation are able to collect mutually complementary information. Therefore, there is no added value in distributing the observables over two different formations. A significant reduction of temporal aliasing errors was achieved when the zz/zz combination was considered by two formations in nearly perpendicular planes. Given that the zz-gravity gradient was found to yield the lowest temporal aliasing errors of the single gradient components, one can conclude that it is more desirable to combine multiple zz/../zz observables in multiple formations than to consider an equal number of orthogonal components in a single formation.

The Heisenberg-like rule of satellite gravimetry (Reubelt et al., 2010) makes (at least) two testable predictions for missions consisting of two formations: i) that interleaving groundtracks of two formations should double the spatial resolution, and ii) that a time-shift of the second formation should double the temporal resolution. I showed that splitting the combination yy/xz over two formations with interleaved groundtracks yields the same spatial resolution as the single formation yy+xz combination. Furthermore, in Section 7.5.3, I have shown that splitting the zz+xz combination from a single formation into a two-formation mission, where a time-shift is applied to the second formation, does not yield any significant reduction of temporal aliasing errors. On the basis of the arguments presented above, I conclude that the Heisenberg-rule is inadequate to predict the spatial and temporal resolutions of multi-formation missions.

9.1.7. Compare the performance of a comprehensive set of mission concepts to identify the best candidate for next-generation satellite gravimetry missions

In Chapter 8, I proposed a set of missions with the potential to deliver the highest performance. I then benchmarked this set of missions in order to identify the most promising concept for the next generation of ll-SST gravimetry missions.

At first, the proposed mission concepts were restricted to a maximum of 4 satellites which were grouped into 1 or 2 formations in different orbital planes. The satellite formations were placed in near-polar circular orbits, with a repeat period between 8 and 24 days, and the lowest altitude above 260 km. The satellites in the formations were placed with maximum inter-satellite distances of 200 km. The assumed objective of the missions was to recover the mean mass transport signal up to $l_{\text{max}} = 120$ within the given DAP matching the repeat period of the orbit.

I started with the elementary satellite formations. The analysis of their error budgets revealed significant differences between them. As expected, it was shown that the along-track concepts are plagued by spatial instability errors and simultaneously suffer from relatively large temporal aliasing errors. In terms of unregularized solutions, the cartwheel mission was found to be the best; it had 48 mm ewh as opposed to 116 and 356 mm ewh in terms of global RMS of total error for the pendulum and along-track, respectively The better performance of the cartwheel configuration was attributed to the inclusion of measurements with a radial component. In terms of regularized solutions, the pendulum (19.4 mm ewh) mission was the best in comparison with the cartwheel (19.9 mm ewh) and along-track (22.6 mm ewh) configurations. The good performance of the pendulum is explained by the regularization procedure, which was very effective at reducing the large magnitude of ranging errors affecting this configuration.

Next, various combined ll-SST concepts were introduced based on the findings of the previous Chapter. I considered combining multiple observables in order to significantly enhance the spatial and temporal resolution of the proposed missions. Considering a single formation, I focused on the possible combinations of two orthogonal observables. Firstly, a set of three-satellite hybrid formations was considered: the gamma, sigma and delta missions. All these hybrid missions consist of single three-satellite formations. In gamma and sigma missions, two elementary satellite formations are combined with the chief satellite taking part in both. The gamma mission consists of a pendulum and along-track combination, while sigma combines a pendulum and cartwheel. The delta mission is a three-satellite extension of a cartwheel formation with three inter-satellite links considered between the satellites. Considering two formations, I similarly considered combinations of two observables split in two formations in nearly perpendicular planes. The set of two-formation concepts proposed was: the dual along-track, the dual gamma, dual cartwheel and the dual sigma. The dual along-track consists of two along-track pairs where one of the pairs may have lower inclination. The most popular variant of this concept is the Bender mission. The dual gamma and dual sigma missions split the corresponding single formation mission in two different formations. Finally the dual cartwheel mission considers two cartwheel formations where the inter-

satellite baselines of both formations are defined to be perpendicular over all the latitudes. For each considered mission concept, the corresponding error budget for each considered DAP was presented.

It was found that, in general, temporal aliasing errors are the dominant error source for most of these missions. Overall, the hybrid and dual formation missions were able to reduce these errors by about 50% compared to the elementary satellite formations. Furthermore, they yielded a total error reduction of about 70 to 80% in terms of unregularized solutions at relatively short DAPs of 12 days or less. I interpret this as a reduction of spatial instability error, which can be attributed to the improved spatial resolution of the more complex missions. These results show that the combination of two observables in these missions successfully lead to better temporal and spatial resolution w.r.t. the single-formation ones. Better results accomplished by the more complex concepts are a consequence of two factors: the synergy between the combination of orthogonal observations and the inclusion of observations aligned with the most desirable zz gradient (where applicable).

In Section 8.5, the best DAP for each concept was selected and general comparison between all the considered mission concepts was presented. The comparison was made over a selected set of regions where hydrological, glaciological and solid earth phenomena are expected. The top four concepts were ranked in descending order as follows: dual sigma, sigma, dual gamma and gamma. In terms of global RMS of total errors in unregularized solutions they yielded 19.6, 20.9, 21.8 and 22.1 mm ewh, respectively, at similar DAPs of 22 and 24 days. The differences between these four mission concepts are small and become even smaller when regularized solutions are considered. Then, the performance of the two-formation missions is only marginally better (between 1% and 6%) than that of single-formation ones. This confirms the earlier findings that interleaving groundtracks of multiple formations which consider different observables *does not lead* to significant improvements in the performance of the mission. Similarly, it also shows that splitting orthogonal observables collected from a single formation over two formations in near-polar perpendicular planes is not effective at reducing temporal aliasing errors.

Regarding the single-formation missions, the performance gap between the sigma and gamma missions is only about 5%. The sigma mission relies on a cartwheel pair of satellites, which are the most challenging to implement. Furthermore, in line with the findings in Chapter 3, the cartwheel formation is very sensitive to indirect effect errors, which were not taken into account in the comparison. At the same time, the gamma mission does not rely on cartwheel pairs of satellites and consists of a single three-satellite formation, as opposed to the more complex two-formation missions. It combines orthogonal observations oriented in the xx and yy gradient directions, which greatly increases the isotropy of the mission sensitivity and consequently extends its spatial resolution compared to the standalone along-track and pendulum concepts. Additionally, the xx+yy combination also ensures that the level of temporal aliasing errors is significantly reduced. For all these reasons, I argued that the gamma mission, with a very small performance penalty w.r.t. the sigma mission, is the right choice for the next generation of ll-SST gravimetry missions. To set the performance level of the gamma mission in

perspective, noticing that the current GFO mission is a along-track type mission, a comparison between the total error of the gamma and along-track concepts shows a error reduction of up to 95%.

Several of the analyzed mission concepts rely on cartwheel formations. However, there is an important caveat regarding the presented results. As previously argued, no indirect effect errors were taken into account in the presented results for these formations. As was shown in Chapter 3 (as well as in Encarnação (2015)), cartwheel formations are extremely sensitive to indirect effect errors. At the same time, pendulum formations are rather insensitive to them. This means that, for those gravity field estimation approaches that are (particularly) sensitive to indirect effect errors, the gamma concept is very likely to outperform the sigma mission. More broadly, all the considered concepts which include cartwheel formations, i.e., the sigma, dual sigma, delta and dual cartwheel missions, are likely to limit the applicability of many gravity field estimation approaches.

Recalling one of the findings in Section 7.5, placing three formations (all observing the zz gradient) in three polar orbital planes such that they trisect 3D space leads to minimum temporal aliasing errors. Temporal aliasing errors were systematically found to be the limit in the performance of the analyzed missions. Since the gamma mission is a combination of a pendulum and along-track satellite pairs, I looked into different possible ways of distributing these formations in up to three orbital planes. The results clearly showed the benefits of increasing the number of optimally aligned orbital planes. The $\Gamma/\Gamma/\Gamma$, a constellation of three gamma missions was able to reduce the total error (i.e., the level of temporal aliasing errors) by 43% compared to the stand-alone gamma mission. The different combinations considered also revealed another interesting configuration. The P/A/P configuration with two pendulum and one along-track formations is less complex and consists of three less satellites than the $\Gamma/\Gamma/\Gamma$ mission. Nonetheless, the P/A/P combination yielded a reduction of 29% in terms of temporal aliasing errors w.r.t. the stand-alone gamma mission.

9.2. Recommendations

As was shown for most proposed future ll-SST mission concepts, their performance is limited by temporal aliasing errors. I have analyzed several mission design options which I found to be effective in reducing the level of these errors. Nonetheless, the most obvious way to reduce these errors is to improve the corresponding background models. However, significant improvements in the accuracy of background models are likely not readily available. In order to make that possible, a larger quantity and quality of data is required. If a background model is expected to be accurate in terms of mass anomalies, mass anomaly data, as measured by satellite gravimetry missions, is the best input for that purpose. Therefore, satellite gravimetry will likely prove to be indispensable in achieving those improvements. Satellite gravimetry data should be used to observe and better understand the physical processes which will allow for a new generation of refined background models. In turn, a new generation of background models will allow for large advances in the accuracy of satellite gravimetry. Ideally, in the limit, gravimetric observations

would be accumulated so quickly (daily?) that a temporal de-aliasing model would no longer be required.

In the proposed mission concepts, I have consistently chosen an inclination of 89.5° for all near-polar orbits. From a limited analysis not preset in this thesis, I have found some indication that slightly lower inclination values for near-polar orbits may lead to a small performance increase. Therefore, I propose the performance of the proposed concepts may be tweaked by searching for an optimal inclination value. Similarly, regarding the dual along-track mission, I have assumed that setting the near-polar orbital planes of the formations close to perpendicular is the most desirable configuration in order to minimize temporal aliasing errors. While that has been shown for near-polar orbits, it is not necessarily true when a lower-inclined satellite pair is considered.

In Section 8.6, I have shown that three satellite formations in different polar orbital planes, positioned such that they equipartition 3-D space, are successful at mitigating temporal aliasing errors compared to the case with a lower number of orbital planes. Then one may wonder if there are limits of this approach? How low can temporal aliasing errors become with additional orbital planes? Unfortunately, in this thesis I could not go beyond considering three orbital planes. The considered input AOD and TMP error sources are modeled as 6-hour piecewise constant sets of SH coefficients. Considering more than three orbital planes in this configuration would mean that the satellite revisit time would be below the temporal resolution of the models. Therefore, to assess the performance of missions which consider more than three orbital planes requires background models defined with shorter sampling intervals in order to provide realistic results.

One of the difficulties to implement a pendulum pair of satellites are the large inter-satellite velocities that this formation experiences. Elsaka (2010) argues that the magnitude of these velocities excludes the possibility of existing laser ranging technology to measure the inter-satellite ranges. A possible way out is as follows. Instead of a simple pendulum, one may consider a double pendulum arrangement, where a central chief satellite takes part in two pendulum formations on either side. In this configuration, the left pair has inter-satellite velocity in the opposite direction and close in magnitude to the other pair. While the inter-satellite velocities of a single pendulum pair is high, the differential velocity between the two pairs is not. This may allow for some differential velocity measurements to be made within the limitations of existing laser ranging technology. Of course, this idea requires further elaboration.

The standard parameterization that is typically used in satellite gravimetry considers a single set of SH coefficients up to $l_{\max}$ which are estimated on the basis of the data collected over the whole DAP. I propose that alternative parameterizations should be considered as a way to effectively enhance the temporal resolution and likely to improve the accuracy of the recovered fields. A couple of examples can be used to illustrate this idea. An along-track pair of satellites continuously samples the near-zonal coefficients up to a high degree, while a relatively long DAP is required in order to adequately sample the near-sectorial coefficients of the similar degree. In fact, it is well known that SH models can be solved for along-track

missions to fairly large $l_{max} > 120$ as long as the maximum order is truncated to a sufficiently low value. Alternative parameterizations may consider solving some subset of SH coefficient over DAPs shorter than the complete set of coefficients. Such an approach has been previously shown to benefit the accuracy of the resulting gravity field models (Daras et al., 2017; Wiese, 2011). I propose that it can be applied to other mission concepts as well, though this will require careful analysis. It may be desirable to tune the selection of SH coefficients in the subset to the particularities of a specific gravimetry mission. Such types of parameterizations are likely to come with a new set of challenges. For example, it is not clear whether signal will leak from some SH coefficients into the subset which is estimated more frequently. Alternative parameterizations might even avoid SH coefficients entirely. In the literature one readily finds gravity field solutions parametrized in terms of mascons (Loomis et al., 2011). For specific applications, regional gravity field solutions may yield better performance than the standard parametrization. Kalman filters have been used to estimate daily gravity fields from GRACE data (Kurtenbach et al., 2009); application of this technique to more sensitive missions may yield even more accurate daily solutions. Lastly, one may consider applying neural networks to the processing of satellite gravimetry data. These networks are at the basis of the latest developments in the field of the artificial intelligence. They are currently been applied to numerous scientific domains, sometimes with great success. Therefore, my recommendation is to tailor the mathematical approaches and algorithms to ensure the best performance of the future missions before they are launched.

In this thesis, I have considered constellations consisting of up to 9 satellites. There are ways to realistically extend the number of satellites beyond 9, though these concepts are left for future studies. One idea is to offset the high costs of a mission consisting of a large number of satellites by considering micro- or nano-satellite platforms. These have considerably lower launch costs since they can be launched in large quantities from a single booster. However, taking advantage of this approach would require a paradigm shift in satellite development. Up until now, satellite gravimetry instruments have been specifically built for a single mission using cutting-edge technology. In order to target the small-satellite sector, the emphasis has to shift from developing state-of-the-art instrumentation into miniaturization and replication of proven technologies. Another important aspect to consider is that launching multiple satellites on a single booster is confines them all to a narrow orbital region which may not be ideal in terms of temporal resolutions. Certainly, the deployed satellites may be maneuvered into desired orbits, however there are certainly various considerations which limit what is achievable.

On a similar note, it is also noteworthy to point out that the business of LEO satellite launches has been experiencing a shift in the past few years. Multiple new companies all over the world started operating in recent years whose entire business model revolves around, substantially lowering the launch costs. In the past, the extremely high costs associated with the launch of a scientific payload into LEO meant that there would be a single opportunity for success. In turn, this meant that a tremendous amount of resources was placed on the development, testing

and preparation of a single spacecraft. Considering the shift towards lower costs observed in recent years, it is important to consider the new opportunities offered by the lower-cost access to LEO. Resources may be shifted towards building a larger number of cheaper spacecraft, which may be advantageous for the field of gravimetry. Specifically, this may allow for multiple satellite formations to be launched, which was shown to significantly reduce the level of temporal aliasing errors. The concept of wide revisit time, which leads to less strict orbital requirements, may allow for multiple micro-satellite formations to piggyback on the boosters of other missions. The performance of a sub-optimal orbital configuration of a large number of micro-satellite formations may prove better than an optimal configuration of a small number of large-satellite formations lifted in dedicated boosters.

An alternative approach is to design satellite gravimetry missions that rely on non-dedicated satellites or constellations. Some work has been published in this direction (Ditmar et al., 2009; B. C. Gunter et al., 2011). One noteworthy monumental constellation is the upcoming SpaceX's Starlink (Foust, 2019), which is planned to have nearly 12000 LEO satellites. The sheer number of satellites only in this constellation provides an exciting opportunity for satellite gravimetry. Assuming that the satellites in this massive constellation will have some communication link with the neighboring satellites and assuming that the elapsed time between the neighboring satellites can be known with sufficient accuracy, it becomes possible to compute the inter-satellite ranges between neighboring satellites. If that is the case, then, in practice, a 12000 satellite ll-SST mesh constellation will be effectively deployed potentially providing nearly continuous monitoring of the whole Earth's gravity field. Given the specific details of this (and other) upcoming constellations, it remains to be shown what is their real potential for gravity field recovery.

A

Rotations

Relative orientations between two arbitrary reference frames can be defined as a set of three consecutive rotations. Consider the roll angle α, the pitch angle β and the yaw angle γ, denoting rotations around the x-, y- and z-axes, respectively. This set of angles is also known as Cardan angles. I follow the *zyx* convention, stating the order and the axis along which each of the intrinsic rotations is applied and I define rotations to be *active* transformations. Let $\mathbf{R}_a^b$, be the matrix which rotates vectors from frame *a* into frame *b*, written as (Jekeli, 2001),

$$\begin{aligned}\mathbf{R}_a^b &= \mathbf{R}_z(\gamma)\mathbf{R}_y(\beta)\mathbf{R}_x(\alpha) \\ &= \begin{bmatrix}\cos\gamma & -\sin\gamma & 0\\ \sin\gamma & \cos\gamma & 0\\ 0 & 0 & 1\end{bmatrix}\begin{bmatrix}\cos\beta & 0 & \sin\beta\\ 0 & 1 & 0\\ -\sin\beta & 0 & \cos\beta\end{bmatrix}\begin{bmatrix}1 & 0 & 0\\ 0 & \cos\alpha & -\sin\alpha\\ 0 & \sin\alpha & \cos\alpha\end{bmatrix} \\ &= \begin{bmatrix}\cos\gamma\cos\beta & \cos\gamma\sin\beta\sin\alpha - \sin\gamma\cos\alpha & \cos\gamma\sin\beta\cos\alpha + \sin\gamma\sin\alpha\\ \sin\gamma\cos\beta & \sin\gamma\sin\beta\sin\alpha + \cos\gamma\cos\alpha & \sin\gamma\sin\beta\cos\alpha - \cos\gamma\sin\alpha\\ -\sin\beta & \cos\beta\sin\alpha & \cos\beta\cos\alpha\end{bmatrix}.\end{aligned} \tag{A.1}$$

This type of matrix is known as direction cosine matrix (DCM). The DCM can also be represented as a vectorial function $\mathbf{R}(\boldsymbol{\psi})$, where $\boldsymbol{\psi} \equiv \begin{bmatrix}\alpha & \beta & \gamma\end{bmatrix}^T$ is an *axial* vector consisting of the ordered triple of Cardan angles representing the rotation between two arbitrary frames. Axial vectors are not true vectors because they do not fulfil all the properties of vectors. It can be shown however (Jekeli, 2001, chap. 1) that for small rotation angles, axial vectors do behave like true vectors and under this assumption it becomes possible to add, subtract and rotate small rotation angles between different reference frames. Assuming that ψ represents a small angle rotation, Eq. (A.1), $R(\boldsymbol{\psi})$ can be approximated to,

$$\mathbf{R}_{\boldsymbol{\psi}} = \begin{bmatrix}1 & -\gamma & \beta\\ \gamma & 1 & -\alpha\\ -\beta & \alpha & 1\end{bmatrix} = \mathbf{I} - \boldsymbol{\Psi}, \tag{A.2}$$

where,

$$\boldsymbol{\Psi} = \begin{bmatrix} 0 & \gamma & -\beta \\ -\gamma & 0 & \alpha \\ \beta & -\alpha & 0 \end{bmatrix}$$

The DCM, cf., Eq. (A.1) and (A.2), are orthogonal matrices, with the property that,

$$\mathbf{R}_a^b \left(\mathbf{R}_a^b\right)^T = \mathbf{I} \Rightarrow \mathbf{R}_b^a = \left(\mathbf{R}_a^b\right)^{-1} = \left(\mathbf{R}_a^b\right)^T. \tag{A.3}$$

Multiplication of a given vector $\mathbf{v}^a$ defined in frame *a* with matrix $\mathbf{R}_a^b$ transforms it to frame *b*,

$$\mathbf{v}^b = \mathbf{R}_a^b \mathbf{v}^a, \tag{A.4}$$

and for a given tensor $\mathbf{A}^a$ defined in frame *a*, the following operation also transforms it to frame *b*,

$$\mathbf{A}^b = \mathbf{R}_a^b \mathbf{A}^a \mathbf{R}_b^a. \tag{A.5}$$

Consecutive rotations are achieved by successive multiplication of rotations matrices, as seen in Eq. (A.1),

$$\mathbf{R}_a^c = \mathbf{R}_b^c \mathbf{R}_a^b. \tag{A.6}$$

B

Optimal SC combination

In this Appendix, I formulate the combination of multiple SC measurements, on board a single satellite. The result of this method is the set of Cardan angles which minimizes the square differences w.r.t. all SC measurements. Furthermore, this combination also takes into account the inherent anisotropy of the SC instruments. This combination is originally presented in Romans (2003) in terms of attitude quaternions.

In the presence of multiple SCs, one wishes to combine all measurements in an optimal manner. Let $\boldsymbol{\varepsilon}_{\psi,\text{opt}}$ be the set of small angle rotations which minimizes the differences w.r.t. the errors in all SCs. It is obtained by minimizing the quadratic error function J,

$$J = \sum_i (\boldsymbol{\varepsilon}_{\psi,\text{opt}}^{S_i} - \boldsymbol{\varepsilon}_{\psi,i}^{S_i})^T \boldsymbol{\Lambda}_i (\boldsymbol{\varepsilon}_{\psi,\text{opt}}^{S_i} - \boldsymbol{\varepsilon}_{\psi,i}^{S_i}), \tag{B.1}$$

where $\boldsymbol{\varepsilon}_{\psi,i} \equiv \begin{bmatrix} \varepsilon_{\alpha,i} & \varepsilon_{\beta,i} & \varepsilon_{\gamma,i} \end{bmatrix}^T$ is the vector representing the errors in the roll ($\varepsilon_{\alpha,i}$), pitch ($\varepsilon_{\beta,i}$) and yaw ($\varepsilon_{\gamma,i}$) angles in the rotation measured by the i-th star camera and $\boldsymbol{\Lambda}_i$ is the inverse of the covariance matrix or information matrix,

$$\boldsymbol{\Lambda}_i = \mathbf{C}_i^{-1} \tag{B.2}$$

Equation (5.5) shows that, for small measurement errors, the differential rotation between any pair of SCs is linearly dependent on the error of each SC. This allows us to write an expression for the errors in each SC w.r.t. a single one,

$$\boldsymbol{\varepsilon}_{\psi,j}^C = \boldsymbol{\varepsilon}_{\psi,1}^C - \Delta\boldsymbol{\varepsilon}_{\psi,1j}^C. \tag{B.3}$$

Let $\boldsymbol{\Lambda}_i^C \equiv \mathbf{R}_{S_i}^C \, \boldsymbol{\Lambda}_i \, \mathbf{R}_C^{S_i}$ be the information matrix rotated to the C frame. The cost function can be written in the C frame as,

$$J = \sum_i \left(\boldsymbol{\varepsilon}_{\psi,\text{opt}}^C - \boldsymbol{\varepsilon}_{\psi,i}^C\right)^T \boldsymbol{\Lambda}_i^C \left(\boldsymbol{\varepsilon}_{\psi,\text{opt}}^C - \boldsymbol{\varepsilon}_{\psi,i}^C\right). \tag{B.4}$$

With N SC measurements, minimization of J would require the knowledge of the errors $\boldsymbol{\varepsilon}_{\psi,i}$ in each SC measurement. This knowledge is not available, so we must tackle the problem differently using the differences between pairs of SC measurements. Let us choose the first star camera, $i = 1$, and making use of Eq. (B.3), one can relate all SC errors to this one, so that the objective function becomes,

$$J = \sum_i \left(\boldsymbol{\varepsilon}^C_{\psi,\text{opt}} - \boldsymbol{\varepsilon}^C_{\psi,1} + \Delta\boldsymbol{\varepsilon}^C_{\psi,1i}\right)^T \boldsymbol{\Lambda}^C_i \left(\boldsymbol{\varepsilon}^C_{\psi,\text{opt}} - \boldsymbol{\varepsilon}^C_{\psi,1} + \Delta\boldsymbol{\varepsilon}^C_{\psi,1i}\right), \tag{B.5}$$

where,

$$\Delta\boldsymbol{\varepsilon}^C_{\psi,11} = 0$$

Let $\boldsymbol{\varepsilon}_{\text{opt}} \equiv \boldsymbol{\varepsilon}^C_{\psi,\text{opt}} - \boldsymbol{\varepsilon}^C_{\psi,1}$, be defined as the optimal correction to the first SC measurement. One can rewrite,

$$\begin{aligned} J &= \sum_i \left(\boldsymbol{\varepsilon}_{\text{opt}} + \Delta\boldsymbol{\varepsilon}^C_{\psi,1i}\right)^T \boldsymbol{\Lambda}^C_i \left(\boldsymbol{\varepsilon}_{\text{opt}} + \Delta\boldsymbol{\varepsilon}^C_{\psi,1i}\right), \\ &= \boldsymbol{\varepsilon}_{\text{opt}}\boldsymbol{\Lambda}^C_1 \boldsymbol{\varepsilon}_{\text{opt}} + \sum_{i\neq 1} \left(\boldsymbol{\varepsilon}_{\text{opt}} + \Delta\boldsymbol{\varepsilon}^C_{\psi,1i}\right)^T \boldsymbol{\Lambda}^C_i \left(\boldsymbol{\varepsilon}_{\text{opt}} + \Delta\boldsymbol{\varepsilon}^C_{\psi,1i}\right). \end{aligned} \tag{B.6}$$

Minimization of the cost function J w.r.t. $\boldsymbol{\varepsilon}_{\text{opt}}$ yields,

$$\boldsymbol{\varepsilon}_{\text{opt}} = -\left(\boldsymbol{\Lambda}^C_{\text{total}}\right)^{-1} \sum_{i\neq 1} \boldsymbol{\Lambda}^C_i \, \Delta\boldsymbol{\varepsilon}^C_{\psi,1i}\,, \tag{B.7}$$

where $\boldsymbol{\Lambda}^C_{\text{total}} = \sum_i \boldsymbol{\Lambda}^C_i$. It can be shown that the solution does not depend on the choice of the camera w.r.t. which all errors are defined in Eq. (B.5).

The optimal combination of multiple SC measurements is then obtained by applying the optimal correction $\boldsymbol{\varepsilon}_{\text{opt}}$ to the measurement of the first one,

$$\mathbf{R}^C_{I,\text{opt}} = \mathbf{R}(\boldsymbol{\varepsilon}_{\text{opt}})\,\tilde{\mathbf{R}}^C_{I,1}. \tag{B.8}$$

References

(HSO-OEG), G. F. T. (Feb. 2014). *GOCE End-of-Mission Operations Report*. Tech. rep.

Abich, K. et al. (July 2019). "On orbit performance of the GRACE Follow-On Laser Ranging Interferometer". In: *Physical Review Letters* 123.3. arXiv: 1907.00104, p. 031101.

Bandikova, T., J. Flury, and U.-D. Ko (July 2012). "Characteristics and accuracies of the GRACE inter-satellite pointing". In: *Advances in Space Research* 50.1, pp. 123–135.

Battaglia, M. et al. (Nov. 2008). "4D volcano gravimetry". In: *GEOPHYSICS* 73.6, WA3–WA18.

Bender, P. L., D. N. Wiese, and R. S. Nerem (2008). "A possible Dual-GRACE mission with 90 degree and 63 degree inclination orbits". In: *in Proceedings, 3rd International Symposium on Formation Flying, Missions and Technologies. European Space Agency Symposium Proceedings, ESA SP-654.* Noordwijk, The Netherlands: ESA.

Bender, P. et al. (2003). "Satellite-Satellite Laser Links for Future Gravity Missions". In: *Space Science Reviews* 108.1-2, pp. 377–384.

Bergmann-Wolf, I. et al. (2014). "Updating ESA's Earth System Model for Gravity Mission Simulation Studies : 2. Comparison with the Original Model". In:

Bergmann-Wolf, I. et al. (2015). *Updating ESA's Earth System Model for Gravity Mission Simulation Studies : 3. A Realistically Perturbed Non-Tidal Atmosphere and Ocean De-Aliasing Model*. Tech. rep.

Beutler, G. et al. (Nov. 2010). "The celestial mechanics approach: application to data of the GRACE mission". In: *Journal of Geodesy* 84.11, pp. 661–681.

Bosch, W. et al. (2009). "Residual ocean tide signals from satellite altimetry, GRACE gravity fields, and hydrodynamic modelling". In: *Geophysical Journal International* 178.3, pp. 1185–1192.

Bouman, J. et al. (Mar. 2015). "GOCE gravity gradient data for lithospheric modeling". In: *International Journal of Applied Earth Observation and Geoinformation* 35, pp. 16–30.

Broerse, T., R. Riva, and B. Vermeersen (Sept. 2014). "Ocean contribution to seismic gravity changes: the sea level equation for seismic perturbations revisited". In: *Geophysical Journal International* 199.2, pp. 1094–1109.

Carrère, L. et al. (2016). "FES 2014, a new tidal model—Validation results and perspectives for improvements". In: *Proceedings of the ESA living planet symposium*, pp. 9–13.

Case, K., G. Kruizinga, and S.-C. Wu (2010). *GRACE Level-1b Data Product User Handbook*. Tech. rep. JPL D-22027. Jet Propulsion Laboratory.

Chinnasamy, P. and G. Agoramoorthy (May 2015). "Groundwater Storage and Depletion Trends in Tamil Nadu State, India". In: *Water Resources Management* 29.7, pp. 2139–2152.

Colombo, O. L. (1983). "The Global Mapping of Gravity with Two Satellites". PhD Thesis. Delft.

Curtis, H. D. (2008). *Orbital mechanics for engineering students*. 1. ed., reprinted. Elsevier Aerospace engineering series. OCLC: 552116374. Amsterdam: Elsevier/Butterworth Heinemann.

Dangendorf, S. et al. (June 2017). "Reassessment of 20th century global mean sea level rise". In: *Proceedings of the National Academy of Sciences* 114.23, pp. 5946–5951.

Daras, I. and R. Pail (Sept. 2017). "Treatment of temporal aliasing effects in the context of next generation satellite gravimetry missions: TEMPORAL ALIASING FOR NGGM". In: *Journal of Geophysical Research: Solid Earth* 122.9, pp. 7343–7362.

Davis, E. et al. (1999). *The GRACE Mission: Meeting the Technical Challenges*. Tech. rep. IAF-99-I3.2.05. Jet Propulsion Laboratory.

Dehne, M. et al. (Mar. 2009). "Laser interferometer for spaceborne mapping of the Earth's gravity field". In: *Journal of Physics: Conference Series* 154, p. 012023.

Didova, O. (2017). *Separating glacial isostatic adjustment and ice-mass change signals in Antarctica using satellite data*. OCLC: 7792858960.

Ditmar, P. and A. A. van Eck van der Sluijs (2004). "A technique for modeling the Earth's gravity field on the basis of satellite accelerations". In: *Journal of Geodesy* 78.1, pp. 12–33.

Ditmar, P., R. Klees, and X. Liu (Dec. 2006). "Frequency-dependent data weighting in global gravity field modeling from satellite data contaminated by non-stationary noise". In: *Journal of Geodesy* 81.1, pp. 81–96.

Ditmar, P., J. Teixeira da Encarnação, and H. H. Farahani (2012). "Understanding data noise in gravity field recovery on the basis of inter-satellite ranging measurements acquired by the satellite gravimetry mission GRACE". In: *Journal of Geodesy*, pp. 1–25.

Ditmar, P. et al. (2009). "On a feasibility of modeling temporal gravity field variations from orbits of non-dedicated satellites". In: *Observing our changing earth*. Springer, pp. 307–313.

Dobslaw, Henryk et al. (Aug. 2016). *Product Description Document for AOD1B Release 06*. Tech. rep. GRACE 327-750. GFZ.

Dobslaw, H. et al. (2014a). *Supplement to: The Updated ESA Earth System Model for Gravity Mission Simulation Studies*.

Dobslaw, H. et al. (2014b). *Updating ESA's Earth System Model for Gravity Mission Simulation Studies : 1. Model Description and Validation*. Tech. rep.

Dobslaw, H. et al. (May 2015). "The updated ESA Earth System Model for future gravity mission simulation studies". In: *Journal of Geodesy* 89.5, pp. 505–513.

Doodson, A. T. (1921). "The Harmonic Development of the Tide-Generating Potential". In: *Proceedings of the Royal Society of London. Series A* 100.704, pp. 305–329.

Drinkwater, M. R. et al. (2007). "The GOCE Gravity Mission: ESA's First Core Earth Explorer". In: *Proceedings of 3rd International GOCE User Workshop, 6-8 November, 2006, Frascati, Italy, ESA Special Publication, SP-627, ISBN 92-9092-938-3, pp.1-8*.

Drinkwater, M. R. et al. (2006). "The GOCE gravity mission: ESA's first core Earth explorer". In: *Proceedings of the 3rd international GOCE user workshop*. European Space Agency Noordwijk, The Netherlands, pp. 6–8.

Elsaka, B. (2010). "Simulated Satellite Formation Flights for Detecting the Temporal Variations of the Earth's Gravity Field". PhD Thesis. University Bonn.

Elsaka, B. et al. (2013). "Comparing seven candidate mission configurations for temporal gravity field retrieval through full-scale numerical simulation". In: *Journal of Ge*.

Encarnação, J. (2015). "Next-generation satellite gravimetry for measuring mass transport in the Earth system". PhD thesis. Delft: Technische Universiteit Delft.

Farahani, H. H. (2013). *Modelling the Earth's static and time-varying gravity field using a combination of GRACE and GOCE data*. Delft University of Technology.

Farahani, H. H. et al. (2013). "The static gravity field model DGM-1S from GRACE and GOCE data: computation, validation and an analysis of GOCE mission's added value". In: *Journal of Geodesy* 87.9, pp. 843–867.

Flechtner, F., H. Dobslaw, and E. Fagiolini (2014a). *AOD1B Product Description Document for Product Release 05*. Tech. rep. GRACE 327-750. GFZ German Research Centre for Geosciences.

Flechtner, F. et al. (2014b). "Status of the GRACE Follow-On Mission". In: *Gravity, Geoid and Height Systems*. Ed. by U. Marti. Vol. 141. Cham: Springer International Publishing, pp. 117–121.

Flechtner, F. et al. (Mar. 2016). "What Can be Expected from the GRACE-FO Laser Ranging Interferometer for Earth Science Applications?" In: *Surveys in Geophysics* 37.2, pp. 453–470.

Flury, J., S. Bettadpur, and B. D. Tapley (Oct. 2008). "Precise accelerometry onboard the GRACE gravity field satellite mission". In: *Advances in Space Research* 42.8, pp. 1414–1423.

Förste, Christoph et al. (2014). *EIGEN-6C4 The latest combined global gravity field model including GOCE data up to degree and order 2190 of GFZ Potsdam and GRGS Toulouse*. GFZ Data Services.

Foust, J. (Jan. 2019). "SpaceX's space-Internet woes: Despite technical glitches, the company plans to launch the first of nearly 12,000 satellites in 2019". In: *IEEE Spectrum* 56.1, pp. 50–51.

Frederikse, T. et al. (July 2017). "The sea-level budget along the Northwest Atlantic coast: GIA, mass changes, and large-scale ocean dynamics". In: *Journal of Geophysical Research: Oceans* 122.7, pp. 5486–5501.

Frommknecht, B., U. Fackler, and J. Flury (2006). "Integrated sensor analysis GRACE". In: *Observation of the Earth System from Space*. Springer, pp. 99–113.

Frommknecht, B. et al. (2011). "GOCE level 1b data processing". In: *Journal of Geodesy* 85.11, pp. 759–775.

Fuchs, M. J. et al. (Oct. 2013). "Observing coseismic gravity change from the Japan Tohoku-Oki 2011 earthquake with GOCE gravity gradiometry". In: *Journal of Geophysical Research: Solid Earth* 118.10, pp. 5712–5721.

Gerlach, C. et al. (Oct. 2003). "A CHAMP-only gravity field model from kinematic orbits using the energy integral: CHAMP GRAVITY FIELD MODEL FROM KINEMATIC ORBIT". In: *Geophysical Research Letters* 30.20, n/a–n/a.

Gerlach, C. et al. (2004). "GRACE Performance Study and Sensor Analysis". In:

Gunter, B. C. et al. (Apr. 2014). "Empirical estimation of present-day Antarctic glacial isostatic adjustment and ice mass change". In: *The Cryosphere* 8.2, pp. 743–760.

Gunter, B. et al. (2011). "Deriving global time-variable gravity from precise orbits of the iridium next constellation". In: *Advances in the astronautical sciences* 142.

Gunter, B. C. et al. (Mar. 2011). "Using Satellite Constellations for Improved Determination of Earth's Time-Variable Gravity". In: *Journal of Spacecraft and Rockets* 48.2, pp. 368–377.

Han, S.-C. (2004). "Efficient Determination of Global Gravity Field from Satellite-to-satellite Tracking Mission". In: *Celestial Mechanics and Dynamical Astronomy* 88.1, pp. 69–102.

Han, S.-C., C. K. Shum, and K. Matsumoto (2005). "GRACE observations of M_2 and S_2 ocean tides underneath the Filchner-Ronne and Larsen ice shelves, Antarctica". In: *Geophysical Research Letters* 32.20.

Harvey, N. (Aug. 2016). "GRACE star camera noise". In: *Advances in Space Research* 58.3, pp. 408–414.

Hauk, M. and D. N. Wiese (Mar. 2020). "New Methods for Linking Science Objectives to Remote Sensing Observations: A Concept Study Using Single- and Dual-Pair Satellite Gravimetry Architectures". In: *Earth and Space Science* 7.3.

Heiskanen, W. and H. Moritz (1967). *Physical Geodesy*.

Herceg, M., P. Jørgensen, and J. Jørgensen (Aug. 2017). "Characterization and compensation of thermo-elastic instability of SWARM optical bench on micro Advanced Stellar Compass attitude observations". In: *Acta Astronautica* 137, pp. 205–213.

Herman, J. et al. (2004). "Attitude Control for GRACE". In: *18th International Symposium on Space Flight Dynamics*. Vol. 548. ESA Special Publication, p. 27.

Hill, G. W. (1878). "Researches in the Lunar Theory". In: *American Journal of Mathematics* 1.1, p. 5.

Horwath, M. et al. (2011). "Improved GRACE science results after adjustment of geometric biases in the Level-1b K-band ranging data". In: *Journal of Geodesy* 85.1, pp. 23–38.

Huess, V. (2001). *Sea Level Variation in the North Sea - from Tide Gauges, Altimetry and Modelling*. Scientific Report 01-08. Danish Metereological Institute.

IERS (2010). *IERS Technical Note 36: IERS Conventions (2010)*. Ed. by G. Petit and B. L. (eds.) Frankfurt am Main: Verlag des Bundesamts für Kartographie und Geodäsie.

Inácio, P. et al. (June 2015). "Analysis of star camera errors in GRACE data and their impact on monthly gravity field models". In: *Journal of Geodesy* 89.6, pp. 551–571.

Iran Pour, S., T. Reubelt, and N. Sneeuw (Sept. 2013). "Quality assessment of sub-Nyquist recovery from future gravity satellite missions". In: *Advances in Space Research* 52.5, pp. 916–929.

Iran-Pour, S. et al. (Aug. 2018). "Impact of Groundtrack Pattern of a Single Pair Mission on the Gravity Recovery Quality". In: *Geosciences* 8.9, p. 315.

Jäggi, A., G. Beutler, and L. Mervart (2010). "GRACE Gravity Field Determination Using the Celestial Mechanics Approach – First Results". In: *Gravity, Geoid and Earth Observation*. Ed. by S. P. Mertikas. Vol. 135. Berlin, Heidelberg: Springer Berlin Heidelberg, pp. 177–184.

Jekeli, C. (2001). *Inertial Navigation Systems with Geodetic Applications*. Ed. by W. d. Gruyter. Walter de Gruyter.

Jekeli, C. (1999). "The determination of gravitational potential differences from satellite-to-satellite tracking". In: *Celestial Mechanics and Dynamical Astronomy* 75.2, pp. 85–101.

Joodaki, G., J. Wahr, and S. Swenson (Mar. 2014). "Estimating the human contribution to groundwater depletion in the Middle East, from GRACE data, land surface models, and well observations". In: *Water Resources Research* 50.3, pp. 2679–2692.

JPL (2000). *Science & Mission Requirements Document*. Tech. rep. D–15928. Jet Propulsion Laboratory.

Jungclaus, J. H. et al. (June 2013). "Characteristics of the ocean simulations in the Max Planck Institute Ocean Model (MPIOM) the ocean component of the MPI-Earth system model: Mpiom CMIP5 Ocean Simulations". In: *Journal of Advances in Modeling Earth Systems* 5.2, pp. 422–446.

Kang, Z. et al. (2006). "Precise orbit determination for the GRACE mission using only GPS data". In: *Journal of Geodesy* 80.6, pp. 322–331.

Kim, J. (2000). "Simulation study of a low-low satellite-to-satellite tracking mission". PhD Thesis. The University of Texas at Austin.

Klees, R., P. Ditmar, and P. Broersen (2003). "How to handle colored observation noise in large least-squares problems". In: *Journal of Geodesy* 76.11-12, pp. 629–640.

Klees, R. et al. (2008). "The design of an optimal filter for monthly GRACE gravity models". In: *Geophysical Journal International* 175.2, pp. 417–432.

Kleinherenbrink, M. et al. (Aug. 2017). "Trends and interannual variability of mass and steric sea level in the Tropical Asian Seas". In: *Journal of Geophysical Research: Oceans* 122.8, pp. 6254–6276.

Klokočník, J. et al. (Dec. 2008). "Variations in the accuracy of gravity recovery due to ground track variability: GRACE, CHAMP, and GOCE". In: *Journal of Geodesy* 82.12, pp. 917–927.

Knudsen, P. et al. (Nov. 2011). "A global mean dynamic topography and ocean circulation estimation using a preliminary GOCE gravity model". In: *Journal of Geodesy* 85.11, pp. 861–879.

Koop, R. (1993). *Global gravity field modelling using satellite gravity gradiometry*. Citeseer.

Kruizinga, G. et al. (2010). "GRACE Level-1 Status". In: *GRACE Science Team Meeting 2010*.

Kurtenbach, E., T. Mayer-Gurr, and A. Eicker (2009). "Deriving daily snapshots of the Earth's gravity field from GRACE L1B data using Kalman filtering". In: *Geophys. Res. Lett.* 36, p. L17102.

Kusche, J. et al. (Oct. 2009). "Decorrelated GRACE time-variable gravity solutions by GFZ, and their validation using a hydrological model". In: *Journal of Geodesy* 83.10, pp. 903–913.

Liebe, C. (2002). "Accuracy Performance of Star Trackers - A Tutorial". In: *IEEE Transactions on Aerospace and Electronic Systems* 38, pp. 587–599.

Liu, X. (2008). "Global gravity field recovery from satellite-to-satellite tracking data". PhD Thesis. Technische Universiteit Delft.

Liu, X. et al. (2010). "DEOS Mass Transport model (DMT-1) based on GRACE satellite data: methodology and validation". In: *Geophysical Journal International* 181.2, pp. 769–788.

Lombard, A. et al. (Feb. 2007). "Estimation of steric sea level variations from combined GRACE and Jason-1 data". In: *Earth and Planetary Science Letters* 254.1-2, pp. 194–202.

Long, D. et al. (July 2013). "GRACE satellite monitoring of large depletion in water storage in response to the 2011 drought in Texas". In: *Geophysical Research Letters* 40.13, pp. 3395–3401.

Loomis, B. D., R. S. Nerem, and S. B. Luthcke (Oct. 2011). "Simulation study of a follow-on gravity mission to GRACE". In: *Journal of Geodesy* 86.5, pp. 319–335.

Lyard, F. et al. (2006). "Modelling the global ocean tides: modern insights from FES2004". In: *Ocean Dynamics* 56.5, pp. 394–415.

Mayer-Gürr, T. (2006). "Gravitationsfeldbestimmung aus der Analyse kurzer Bahnbögen am Beispiel der Satellitenmissionen CHAMP und GRACE". PhD Thesis. Bonn, Germany: University of Bonn.

Mayer-Gürr, T. et al. (Mar. 2005). "ITG-CHAMP01: a CHAMP gravity field model from short kinematic arcs over a one-year observation period". In: *Journal of Geodesy* 78.7-8, pp. 462–480.

Mayer-Gürr, T. et al. (2010). "ITG-GRACE: Global Static and Temporal Gravity Field Models from GRACE Data". In: *System Earth via Geodetic-Geophysical Space Techniques*. Ed. by F. M. Flechtner et al. Berlin, Heidelberg: Springer Berlin Heidelberg, pp. 159–168.

Meissl, P. (1971). *On the linearization of the geodetic boundary value problem*. Tech. rep. 151. Department of Geodetic Science and Surv, Ohio State University Columbus.

Meyer, U., A. Jäggi, and G. Beutler (2012). "The Impact of Attitude Control on GRACE Accelerometry and Orbits". In: *Geodesy for Planet Earth*. Ed. by S. Kenyon, M. C. Pacino, and U. Marti. Vol. 136. Berlin, Heidelberg: Springer Berlin Heidelberg, pp. 139–146.

Mulder, G. et al. (Mar. 2015). "Identifying water mass depletion in northern Iraq observed by GRACE". In: *Hydrology and Earth System Sciences* 19.3, pp. 1487–1500.

Pail, R. (2005). "A parametric study on the impact of satellite attitude errors on GOCE gravity field recovery". In: *Journal of Geodesy*.

Pail, R. et al. (Oct. 2010). "Combined satellite gravity field model GOCO01S derived from GOCE and GRACE: GOCO01S COMBINED GOCE AND GRACE MODEL". In: *Geophysical Research Letters* 37.20, n/a–n/a.

Park, J. et al. (2005). "Earth's free oscillations excited by the 26 December 2004 Sumatra-Andaman earthquake". In: *Science* 308.5725, pp. 1139–1144.

Peterseim, N., J. Flury, and A. Schlicht (May 2012). "Magnetic torquer induced disturbing signals within GRACE accelerometer data". In: *Advances in Space Research* 49.9, pp. 1388–1394.

Prange, L. et al. (2008). "Gravity Field Determination at the AIUB – The Celestial Mechanics Approach". In: *Observing our Changing Earth*. Ed. by M. G. Sideris. Vol. 133. Berlin, Heidelberg: Springer Berlin Heidelberg, pp. 353–362.

Purkey, S. G., G. C. Johnson, and D. P. Chambers (Nov. 2014). "Relative contributions of ocean mass and deep steric changes to sea level rise between 1993 and 2013". In: *Journal of Geophysical Research: Oceans* 119.11, pp. 7509–7522.

Purkhauser, A. F., C. Siemes, and R. Pail (May 2020). "Consistent quantification of the impact of key mission design parameters on the performance of next-generation gravity missions". In: *Geophysical Journal International* 221.2, pp. 1190–1210.

Quinn, K. J. and R. M. Ponte (Apr. 2011). "Estimating high frequency ocean bottom pressure variability". In: *Geophys. Res. Lett.* 38.8, pp. L08611–.

Ray, R. D. and S. B. Luthcke (Dec. 2006). "Tide model errors and GRACE gravimetry: towards a more realistic assessment". In: *Geophysical Journal International* 167.3, pp. 1055–1059.

Reager, J., B. Thomas, and J. Famiglietti (2014). "River basin flood potential inferred using GRACE gravity observations at several months lead time". In: *Nature Geoscience* 7.8, p. 588.

Reigber, C. (1989). "Gravity field recovery from satellite tracking data". In: *Theory of Satellite Geodesy and Gravity Field Determination*. Ed. by F. Sansò and R. Rummel. Vol. 25. Berlin/Heidelberg: Springer-Verlag, pp. 197–234.

Reigber, C. et al. (July 2002). "A high-quality global gravity field model from CHAMP GPS tracking data and accelerometry (EIGEN-1S): A GLOBAL GRAVITY FIELD MODEL". In: *Geophysical Research Letters* 29.14, pp. 37–1–37–4.

Reigber, C. et al. (Apr. 2003). "The CHAMP-only earth gravity field model EIGEN-2". In: *Advances in Space Research* 31.8, pp. 1883–1888.

Reigber, C. et al. (1996). *Champ, Phase B: Executive Summary*. Geoforschungszentrum.

Reubelt, T., G. Austen, and E. Grafarend (Aug. 2003). "Harmonic analysis of the Earth's gravitational field by means of semi-continuous ephemerides of a low Earth orbiting GPS-tracked satellite. Case study: CHAMP". In: *Journal of Geodesy* 77.5-6, pp. 257–278.

Reubelt, T., M. Götzelmann, and E. W. Grafarend (2006). "Harmonic Analysis of the Earth's Gravitational Field from Kinematic CHAMP Orbits based on Numerically Derived Satellite Accelerations". In: *Observation of the Earth System from Space*. Ed. by J. Flury et al. Berlin/Heidelberg: Springer-Verlag, pp. 27–42.

Reubelt, T., N. Sneeuw, and M. A. Sharifi (2010). "Future Mission Design Options for Spatio-Temporal Geopotential Recovery". In: *Gravity, Geoid and Earth Observation*. Ed. by S. P. Mertikas. Vol. 135. Berlin, Heidelberg: Springer Berlin Heidelberg, pp. 163–170.

Ries, J. et al. (2016). *The Combined Gravity Model GGM05C*. GFZ Data Services.

Romans, L. (2003). *Optimal combination of quaternions from multiple star cameras*. JPL Internal Memorandum. Jet Propulsion Laboratory.

Rummel, R. (Jan. 2012). "Height unification using GOCE". In: *Journal of Geodetic Science* 2.4.

Rummel, R. et al. (2003). *Scientific Objectives for Future Geopotential Missions*. Tech. rep. Draft version 6.

Savcenko, R. and W. Bosch (2012). *EOT11a - empirical ocean tide model from multi-mission satellite altimetry*. Tech. rep. 89. DGFI.

Scargle, J. D. (Dec. 1982). "Studies in astronomical time series analysis. II - Statistical aspects of spectral analysis of unevenly spaced data". In: *The Astrophysical Journal* 263, p. 835.

Schaub, H. and J. L. Junkins (2009). *Analytical mechanics of space systems*. 2nd ed. AIAA education series. Reston, VA: American Institute of Aeronautics and Astronautics.

Schmidt, R. et al. (2008). "Hydrological Signals Observed by the GRACE Satellites". In: *Surv Geophys* 29, pp. 319–334.

Schrama, E. J. O. (Nov. 1990). *Gravity Field Error Analysis: Applications of GPS Receivers and Gradiometers on Low Orbiting Platforms*. NASA Technical Memorandum 100769.

Sharifi, M. A., N. Sneeuw, and W. Keller (2007). "Gravity recovery capability of four generic satellite formations".

Sharifi, M. and W. Keller (2005). "GRACE Gradiometer". In: *Gravity, Geoid and Space Missions*. Ed. by C. Jekeli, L. Bastos, and J. Fernandes. Berlin, Heidelberg: Springer Berlin Heidelberg, pp. 42–47.

Sheard, B. S. et al. (Dec. 2012). "Intersatellite laser ranging instrument for the GRACE follow-on mission". In: *Journal of Geodesy* 86.12, pp. 1083–1095.

Shepherd, A. et al. (Nov. 2012). "A Reconciled Estimate of Ice-Sheet Mass Balance". In: *Science* 338.6111, pp. 1183–1189.

Siemes, C., M. Rexer, and R. Haagmans (Feb. 2019). "GOCE star tracker attitude quaternion calibration and combination". In: *Advances in Space Research* 63.3, pp. 1133–1146.

Sneeuw, N., M. A. Sharifi, and W. Keller (2008). "Gravity Recovery from Formation Flight Missions". In: *VI Hotine-Marussi Symposium on Theoretical and Computational Geodesy*. Ed. by P. Xu, J. Liu, and A. Dermanis. Vol. 132. International Association of Geodesy Symposia. Springer Berlin Heidelberg, pp. 29–34.

Stammer, D. et al. (Sept. 2014). "Accuracy assessment of global barotropic ocean tide models". In: *Reviews of Geophysics* 52.3, pp. 243–282.

Stummer, C., T. Fecher, and R. Pail (2011). "Alternative method for angular rate determination within the GOCE gradiometer processing". In: *Journal of Geodesy* 85.9, pp. 585–596.

Stummer, C. et al. (2012). "Upgrade of the {GOCE} Level 1b gradiometer processor". In: *Advances in Space Research* 49.4, pp. 739–752.

Sun, Y., P. Ditmar, and R. Riva (Sept. 2015). "Observed changes in the Earth's dynamic oblateness from GRACE data and geophysical models". In: *Journal of Geodesy*.

Swenson, S., D. Chambers, and J. Wahr (Aug. 2008). "Estimating geocenter variations from a combination of GRACE and ocean model output". In: *Journal of Geophysical Research* 113.B8, B08410–.

Swenson, S. and J. Wahr (2006). "Post-processing removal of correlated errors in GRACE data". In: *Geophysical Research Letters* 33.8.

Tangdamrongsub, N. et al. (Apr. 2015). "Data assimilation of GRACE terrestrial water storage estimates into a regional hydrological model of the Rhine River basin". In: *Hydrology and Earth System Sciences* 19.4, pp. 2079–2100.

Tapley, B. (1997). "The gravity recovery and climate experiment (GRACE)". In: *Supplement to EOS Transactions of the American Geophysical Union* 78.46, p. 163.

Tapley, B. D. (2003). "Large scale ocean circulation from the GRACE GGM01 Geoid". In: *Geophysical Research Letters* 30.22.

Tapley, B. et al. (Nov. 2005). "GGM02 – An improved Earth gravity field model from GRACE". In: *Journal of Geodesy* 79.8, pp. 467–478.

Tapley, B. D. et al. (2004). "GRACE Measurements of Mass Variability in the Earth System". In: *Science* 305.5683, pp. 503–505.

Thompson, P. F. (2004). "Impact of short period, non-tidal, temporal mass variability on GRACE gravity estimates". In: *Geophysical Research Letters* 31.6.

Tikhonov, A. and V. Y. Arsenin (1977). "Solutions of ill-posed problems". In: *WH Winston, Washington, DC* 330.

Velicogna, I., T. Sutterley, and M. Van Den Broeke (2014). "Regional acceleration in ice mass loss from Greenland and Antarctica using GRACE time-variable gravity data". In: *Geophysical Research Letters* 41.22, pp. 8130–8137.

Visser, P. N. A. M. et al. (2012). "Dependency of Resolvable Gravitational Spatial Resolution on Space-Borne Observation Techniques". In: *Geodesy for Planet Earth*. Ed. by S. Kenyon, M. C. Pacino, and U. Marti. Vol. 136. Berlin, Heidelberg: Springer Berlin Heidelberg, pp. 373–379.

Wahr, J., M. Molenaar, and F. Bryan (1998). "Time variability of the Earth's gravity field: Hydrological and oceanic effects and their possible detection using GRACE". In: *J. Geophys. Res.* 103.B12, pp. 30205–30229.

Webb, F. et al. (June 2019). *GRACE Follow-On Science Data System Newsletter Report: June 2019 (No. 4)*. Tech. rep.

Weigelt, M. et al. (Feb. 2013). "An improved sampling rule for mapping geopotential functions of a planet from a near polar orbit". In: *Journal of Geodesy* 87.2, pp. 127–142.

Wiese, D. (2011). "Optimizing two pairs of GRACE-like satellites for recovering temporal gravity variations". PhD Thesis. University of Colorado.

Wiese, D., W. Folkner, and R. Nerem (2009). "Alternative mission architectures for a gravity recovery satellite mission". In: *Journal of Geodesy* 83, pp. 569–581.

Wiese, D., R. S. Nerem, and F. G. Lemoine (June 2011). "Design considerations for a dedicated gravity recovery satellite mission consisting of two pairs of satellites". In: *Journal of Geodesy* 86.2, pp. 81–98.

Wu, S.-C., G. Kruizinga, and W. Bertinger (May 2006). *Algorithm Theoretical Basis Document for GRACE Level-1B Data Processing V1.2*. Tech. rep. JPL D-27672. Jet Propulsion Laboratory.

Wu, X. et al. (Sept. 2010). "Simultaneous estimation of global present-day water transport and glacial isostatic adjustment". In: *Nature Geoscience* 3.9, pp. 642–646.

Zhang, Z.-Z. et al. (Sept. 2009). "An effective filtering for GRACE time-variable gravity: Fan filter". In: *Geophysical Research Letters* 36.17.

Zhao, Q. (2004). "Research on precise orbit determination theory and software for both GPS navigation constellation and LEO satellites". PhD Thesis. School of Geodesy and Geomatics, Wuhan University.

Zhao, Q. et al. (Jan. 2010). "Precise relative orbit determination of twin GRACE satellites". In: *Geo-spatial Information Science* 13.3, pp. 221–225.

Zhou et al. (Oct. 2019). "Improving the GRACE Kinematic Precise Orbit Determination Through Modified Clock Estimating". In: *Sensors* 19.19, p. 4347.

Nomenclature

3RC	3-point Range Combination
AOD	Atmosphere and Ocean De-Aliasing Model Errors
AOD1B	Atmosphere and Ocean De-aliasing Level-1B product
APC	Antenna Phase Centre
CDV	Cumulative Degree Variance
CHAMP	CHAllenging Minisatellite Payload
DAP	Data Accumulation Period
DMT	Delft Mass Transport model
DV	Degree Variance
ESM	Earth System Model for Gravity Mission Simulation Studies
ewh	Equivalent water height
FFT	Fast Fourier Transform
FGT	Future GRACE-type mission
GFO	GRACE Follow-On
GOCE	Gravity Field and Steady-State Ocean Explorer
GRACE	Gravity Recovery And Climate Experiment
IFFT	Inverse Fast Fourier Transform
IRF	Inertial Reference Frame
ISA	Average inter-satellite accelerations
KBR	K-band ranging
KO	Kinematic orbit
L1A	Level-1 A
L1B	Level-1 B
ll-SST	Low-low satellite-to-satellite tracking

LoS	Line-of-sight
LRI	Laser Ranging Instrument
NOI	Synthetic ranging noise
OTE	Ocean Tide Model Errors
PDO	Purely Dynamic Orbit
PSD	Power Spectral Density
RDO	Reduced dynamic orbit
RGO	Repeat ground track orbit
RRC	Residual Range Combinations
SC	Star-Camera
SGG	Satellite gravity gradiometry
SH	Spherical harmonic
SNR	Signal-to-noise ratio
SRF	Science Reference Frame

Curriculum Vitæ

Pedro Miragaia Gomes Inácio

07-06-1986 Born in Santa Maria da Feira, Portugal.

Education

2003–2007 BSc. in Aerospace Engineering
Instituto Superior Técnico, Lisboa, Portugal

2007–2010 MSc. in Aerospace Engineering
Technische Universiteit Delft, Delft, The Netherlands

List of Publications

3. Farahani, H. H. et al. (2017). *A high resolution model of linear trend in mass variations from DMT-2: Added value of accounting for coloured noise in GRACE data.* In: Journal of Geodynamics, 103, 12-25.

2. Inácio, P. et al. (2015). *Analysis of star camera errors in GRACE data and their impact on monthly gravity field models.* In: Journal of Geodesy 89.6, 551–571.

1. Francis, O. et al. (2013). *The European Comparison of Absolute Gravimeters 2011 (ECAG-2011) in Walferdange, Luxembourg: results and recommendations.* In: Metrologia, 50, 257.